Development of a Novel Air-Cored Permanent Magnet Linear Generator for Direct Drive Ocean Wave Energy Converters

by

Rieghard Vermaak

Dissertation presented for the degree Doctor of Philosophy in the Faculty of Engineering at Stellenbosch University

Supervisor: Prof. Maarten Jan Kamper
Faculty of Engineering
Department of Electrical and Electronic Engineering

March 2013

Declaration

By submitting this dissertation electronically, I declare that the entirety of the work contained therein is my own, original work, that I am the sole author thereof (save to the extent explicitly otherwise stated), that reproduction and publication thereof by Stellenbosch University will not infringe any third party rights and that I have not previously in its entirety or in part submitted it for obtaining any qualification.

March 2013

Opsomming

Ontwikkeling van ‘n Nuwe Lug-Kern Permanent Magneet Lineêre Generator vir Direk Aangedrewe Oseaan Golf Energie Omsetters

In hierdie tesis word ’n nuwe lug kern permanent magnet (PM) lineêre generator (LG) vir toepassing tot direk aangedrewe (DA) oseaan golf energie omsetters (GEO) ontwikkel. Die nuwe LG word ontwikkel vanaf die lineêre dubbel-kant topologie in ’n poging om probleme met die huidige longitudinale vloed (LV) yster kern LGs, wat tot dusvêr oorheersend voorkom in eksperimentele DA-GEOs, te oorkom. Die grootste probleem met hierdie LGs is die masiewe aantrekkings kragte tussen hul yster stators en die PM transleerders. ’n Groot hoeveelheid strukturuele staal word benodig om die luggaping te handhaaf, terwyl die las op die laars ook ’n groot probleem is. Die nuwe LG gebruik ’n lug kern stator wat alle aantrekkings kragte tussen die stator en transleerder elimineer en dus die nodige strukturuele material verminder. Die topologie van die transleerder is ook van so ’n aard dat die netto aantrekkings kragte op enige spesifieke PM ideaal nul is; dit verminder die strukturuele materiaal selfs verder. Die transleerder het ook ’n nuwe transversale vloed pad wat die sogenaamde paarwyse vloed koppeling wat in LV-LGs voorkom, en die negatiewe effekte daarvan, verhoed.

’n Aantal nuwe bydraes tot die veld van LGs vir DA-GEO word in hierdie tesis gemaak. ’n Nuwe topologie lug kern PMLG is ontwikkel soos bespreek. Dit sluit in die ontwikkeling van analitiese en eindige element modelle en ’n optimerings prosedure wat vinnig optimale dimensies vir minimum aktiewe massa van die nuwe LG vind. In die ontwerp word dit ook gevind dat die drywingsdigtheid van LGs verbeter kan word deur zero oorvleuling tussen die die stator en transleerder by die slag endte toe te laat. ’n 1 kW prototipe van die nuwe LG word ontwerp en gebou; die uitvoerbaarheid van die konstruksie vir die nuwe topologie op ’n klein skaal word dus gedemonstreer. ’n Unieke toets opstelling word ook ontwerp en is gebasseer op bestaande toerusting in die vorm van ’n wind turbine generator en rug-aan-rug spannings bron omsetters. Met die toets opstelling word ’n enkel frekwensie golf ge-emuleer om die teorie en simulasies te verifieer en word ook ’n voorspellende beheer strategie geimplementeer, wat vir die eerste keer gedemonstreer word vir LGs vir DA-GEOs. Goeie ooreenstemming tussen die gemete en gesimuleerde data bevestig die voorgestelde modellerings en ontwerps metodes.

Abstract

Development of a Novel Air-Cored Permanent Magnet Linear Generator for Direct Drive Ocean Wave Energy Converters

In this thesis, a novel air-cored permanent magnet (PM) linear generator (LG) is developed with application to direct drive (DD) wave energy converters (WECs). The novel LG is developed from the linear double-sided topology in an attempt to overcome the problems with current longitudinal flux (LF) iron-cored LGs, which have so far been dominant in experimental DD-WECs. The biggest problem with these LGs is the massive attraction forces between their iron stators and PM translators. A large amount of structural steel is required to maintain the air gap, while the load on the bearings is also a large concern. The novel LG uses an air-cored stator which eliminates any attraction forces between the stator and translator and hence reduces the required structural material. Furthermore, the topology of the translator is such that the net attraction force on any particular PM is ideally zero, which even further reduces the structural material required for the translator. A new transverse circulating flux path is also introduced in the translator which prevents pair-wise flux coupling and its negative effects as observed in LF-LGs.

A number of new contributions are made to the field of LGs for DD-WECs in this thesis. A novel topology air-cored PMLG is developed as described. This includes the development of analytical and finite element models and an exhaustive optimisation procedure for quickly finding optimal dimensions for minimum active mass of the novel LG. In the design it is also found that the power density of LGs can be improved by allowing zero overlap between the stator and translator at the stroke ends. A 1 kW prototype of the novel LG is designed and built; the feasibility of constructing the novel LG on a small scale is as such demonstrated. A unique test rig is designed based on existing equipment in the form of a wind turbine generator and back-to-back voltage source converters. The test rig allows emulation of a monochromatic wave for verifying the theory and simulations and also allows for implementation of a predictive control strategy, which is for the first time demonstrated for LGs for DD-WECs. Good agreement between measured and simulated data confirms the presented modelling and design methods.

Acknowledgements

I would like to thank:

- My Lord and Saviour, Jesus Christ, for saving me and giving me abundant life and the grace to achieve more than my own abilities will ever allow.
- My wife, Candace, for her love, support, encouragement and understanding during the project.
- Prof Maarten Kamper for conceiving the project, allowing me to be part of it and providing the necessary guidance and support for me to execute the project successfully.
- The South African National Energy Research Institute (SANERI) and the OSP Project for financing the project.
- Dr Peter Jan Randewijk for his work on the analysis of radial flux permanent magnet air-cored machines which greatly aided me in completing this work in time.
- Abri Stegmann, for advice with the stator design and construction.
- Jakkie Blom, Jos Weerdenburg and the other people from SMD who helped with the mechanical design and manufacture.
- Jaco Serdyn, Ivan Hobbs and David Groenewald for their advice and help with the power electronics and control implementation.
- Pietro Petzer, Andre Swartz and Marius Jumat at the Electrical Workshop for their valuable inputs and assistance.
- Will Esterhuizen, Masande Ngomane and the vacation work students for their help with the stator construction and assembly of the machine.
- Daleen Kleyn, for assistance with all the financial and procurement issues.
- My family and friends for their patience while I was socially not as present as I should have been.

Author Publications

International conference papers (abstract reviewed):

- R.Vermaak and M.J. Kamper, "Novel permanent magnet linear generator topology for wave energy conversion", presented at the *IET 5th International Conference on Power Electronics, Machines and Drives (PEMD)*, Brighton, UK, Apr. 2010.
- R.Vermaak and M.J. Kamper, "Construction and control of an air-cored permanent magnet linear generator for direct drive wave energy converters", presentated at the *IEEE International Electrical Machines and Drives Conference (IEMDC)*, Niagara Falls, Canada, May 2011.

International conference papers (full paper reviewed):

- R.Vermaak and M.J. Kamper, "Design of a novel air-cored permanent magnet linear generator for wave energy conversion", presented at the *19th International Conference on Electrical Machines (ICEM)*, Rome, Italy, Sep. 2010.

International journal articles:

- R.Vermaak and M.J. Kamper, "Design aspects of a novel topology air-cored permanent magnet linear generator for direct drive wave energy converters", *IEEE Transactions on Industrial Electronics*, vol. 59, no 5, pp. 2104-2115, May 2012.
- R.Vermaak and M.J. Kamper, "Experimental evaluation and predictive control of an air-cored linear generator for direct drive wave energy converters", *IEEE Transactions on Industrial Applications*, vol. 48, no 6, pp. 1817-1826, Nov/Dec 2012.

All publications are available from the IEEE Xplore Digital Library (http://ieeexplore.ieee.org).

Table of Contents

List of Figures

List of Tables

Nomenclature

Abbreviations

AWS	Archimedes Wave Swing
CAD	Computer aided design
CNC	Computer numerical control
CPT	Columbia Power Technologies
CT	Current transformer
DD-WEC	Direct drive wave energy converter
DL	Double-layer
DSC	Digital signal controller
EMF	Electro motive force
FEA	Finite element analysis
FOC	Field oriented control
IGBT	Insulated gate bipolar transistor
IRP	Integrated resource plan
LDS	Linear double-sided
LF	Longitudinal flux
LG	Linear generator
MMF	Magneto motive force
NdFeB	Neodymium Iron Boron
NO	Non-overlapping
OPT	Ocean Power Technologies
OSU	Oregon State University
OWC	Oscillating water column
PLC	Programmable logic controller
PM	Permanent magnet
PET	Polyethylene terephthalate
PEC	Power electronic converter
PTO	Power take-off
PVC	Polyvinyl chloride
PWM	Pulse width modulation
RE	Renewable energy
RF	Radial flux
SmCo	Samarium Cobalt

SV	Space vector
TF	Transverse flux
THD	Total harmonic distortion
UK	United Kingdom
VHDL-AMS	VHSIC hardware description language – analogue and mixed signals.
VHSIC	Very high speed integrated circuit
VHM	Vernier hybrid machine
VR	Variable reluctance
VSC	Voltage source converter
VSD	Variable speed drive
WEC	Wave energy converter
WTG	Wind turbine generator

Roman symbols

a	Number of parallel circuits	
A	Magnetic vector potential.	[Wb/m]
A_g	Air gap area	[m^2]
A_m	Magnet area	[m^2]
b	Mechanical circuit damping / loss resistance	[Ns/m]
b_r	Buoy radiation damping / loss resistance	[Ns/m]
b_f	Wave / buoy frictional damping / loss resistance	[Ns/m]
b_g	LG mechanical damping / loss resistance	[Ns/m]
b_w	Wave internal damping / loss resistance ($b_w = b_f + b_r$)	[Ns/m]
B	RMS air gap flux density	[T]
B_g	Air gap flux density (as a function of θ)	[T]
B_p	Peak air gap flux density	[T]
B_m	Permanent magnet flux density	[T]
B_r	Permanent magnet residual flux density	[T]
c	Mechanical circuit spring constant / stiffness	[N/m]
c_h	Hydrostatic buoyancy spring constant / stiffness	[N/m]
c_g	LG mechanical spring constant / stiffness	[N/m]
C_1	Machine constant 1	
C_2	Machine constant 2	
C_{M1}	Permanent magnet field constant 1	
C_{M2}	Permanent magnet field constant 2	

C_{M3}	Permanent magnet field constant 3	
C_{M4}	Permanent magnet field constant 4	
C_{S1}	Stator field constant 1	
C_{S2}	Stator field constant 2	
C_{S3}	Stator field constant 3	
C_{S4}	Stator field constant 4	
C_d	DC-bus capacitance	[F]
C_f	Filter capacitance	[F]
d_i	LG inner diameter	[m]
d_o	LG outer diameter	[m]
d_w	Wire diameter	[m]
e	Instantaneous voltage	[V]
e_g	Instantaneous LG internal voltage (EMF)	[V]
e_t	Instantaneous LG terminal voltage	[V]
e_r	Instantaneous active rectifier voltage	[V]
E_g	LG rms internal voltage (EMF)	[V]
E_p	LG peak internal voltage (EMF) = $2E_g$	[V]
E_d	DC-bus voltage	[V]
E_s	IGBT rated voltage	[V]
f	Electrical frequency	[Hz]
f_c	Filter cut-off frequency	[Hz]
f_n	Normal magnet attraction force	[N]
f_e	Instantaneous wave excitation force	[N]
f_g	LG instantaneous developed force	[N]
f_s	Converter switching frequency	[Hz]
F_g	LG total rms developed force	[N]
F_e	Peak wave excitation force	[N]
F_p	LG peak developed force	[N]
F_m	Magneto motive force of one magnet	[A-turns]
g	Mechanical air gap	[m]
H_w	Significant wave height	[m]
H_c	Permanent magnet coercive field strength.	[A/m]
h	Slot / winding depth / thickness	[m]
h_m	Average magnet height	[m]
h_{mi}	Inner magnet height	[m]
h_{mo}	Outer magnet height	[m]
h_s	Spacer height	[m]

i	Instantaneous LG current	[A]
i_r	Ideal reference current	[A]
i_{rc}	Calculated reference current	[A]
I	LG rms current	[A]
I	LG peak current	[A]
J	LG rms current density	[A/mm^2]
K	Electrical loading	[A/m]
K_λ	Flux linkage constant	
K_1	Additional machine constant 1	
K_2	Additional machine constant 2	
K_3	Additional machine constant 3	
k	Ratio of copper losses to total losses	
k_d	Distribution factor	
k_f	Copper fill factor	
k_p	Pitch factor	
k_r	Rated current scaling factor	
k_w	Winding factor	
L	LG active length (stator length)	[m]
L_{st}	Stroke length	[m]
L_t	LG translator length	[m]
L_s	LG synchronous inductance	[H]
L_m	LG mutual inductance	[H]
L_{xx}	LG phase self inductance	[H]
L_f	Filter inductance	[H]
ℓ	Active winding length	[m]
ℓ_e	End-winding length	[m]
ℓ_g	Total air gap length	[m]
ℓ_{ipg}	Inter polar gap	[m]
ℓ_w	Wire length	[m]
M	Total mass of a DD-WEC system in the sea	[kg]
M_{cu}	Copper mass	[kg]
M_m	Active magnet mass	[kg]
M_s	Total stator mass	[kg]
M_t	Total translator mass	[kg]
M_r	Permanent magnet residual magnetisation	[A/m]
n_c	Number of parallel strands	
n_s	Number of stator sections	

n	Conductor density	[Turns/m]
N	Number of coil turns	
N_{ph}	Total number of coil turns in series per phase	
p	number of active poles	
p_g	LG instantaneous generated power	[W]
p_t	Instantaneous power at LG terminal (transferred to load)	[W]
P_g	LG total generated power	[W]
P_c	Core losses	[W]
P_{cu}	LG total copper losses	[W]
P_{ec}	LG total stator eddy current losses	[W]
q	Number of coils per phase	
Q	Total number of coils	
R_{ec}	Eddy-current loss resistance	[Ω]
R_s	LG winding resistance	[Ω]
t	Time	[s]
T_m	Torque	[Nm]
T_s	Converter switching period	[s]
T_w	Wave period	[s]
v	LG translator / buoy instantaneous velocity	[m/s]
V	LG translator / buoy rms velocity	[m/s]
V_p	LG translator / buoy peak velocity	[m/s]
w	Coil-side width	[m]
w_1	Weighting factor 1	
w_2	Weighting factor 2	
w_s	Slot width	[m]
W_w	Specific wave energy	[J/m^2]
X_s	LG synchronous reactance	[Ω]
z	Instantaneous vertical displacement	[m]
Z	Vertical displacement amplitude	[m]

Greek symbols

α	Coil position with respect to the flux density wave	[rad]
δ	Ratio of end winding length to active winding length	
Δ	Position of a single turn within a coil	[rad]
ε_i	Current error	[A]
ζ	Mechanical damping factor	
η	LG efficiency	[%]
θ	LG translator position	[rad]
θ_d	Drive motor rotor angular position	[rad]
θ_c	Coil width	[rad]
θ_m	Magnet width	[rad]
θ_p	Pole width	[rad]
θ_r	Coil side width	[rad]
κ	Per unit coil side width ($\kappa = \theta_r / \theta_c$)	
Λ	Peak flux linkage of a single coil	[Wb-turns]
λ_c	Flux linkage of a coil	[Wb-turns]
λ_t	Flux linkage of a single coil turn	[Wb-turns]
λ_w	(Ocean) wave length	[m]
μ_{rec}	Magnet recoil permeability	
σ_s	Shear stress	[N/m^2]
σ_g	Air gap reluctance	[A-turns/Wb]
σ_m	Magnet reluctance	[A-turns/Wb]
τ	Pole pitch	[m]
τ_m	Per unit magnet width ($\tau_m = \theta_m/\theta_p$)	
τ_s	Slot pitch	[m]
φ_m	Magnet flux	[Wb]
φ	Phase shift between LG's EMF and current	[rad]
χ	Phase shift between wave excitation force and buoy displacement	[rad]
χ_m	Magnetic susceptibility	
ψ	Phase shift between wave excitation force and buoy velocity	[rad]
ω	Electrical angular frequency	[rad/s]
ω_m	Drive motor angular velocity	[rad/s]
ω_o	Natural frequency of a DD-WEC in the sea	[rad/s]
ω_w	Wave frequency	[rad/s]
ω_s	Half of the distance between successive phase coils	[m]
μ_r	Relative permeability of a material	

Matrices and vectors

$\mathbf{A}$	Magnetic vector potential	[Wb/m]
$\mathbf{B_g}$	Air gap flux density	[T]
$\mathbf{E_g}$	LG internal voltage (EMF)	[V]
$\mathbf{E_i}$	Inverter voltage	[V]
$\mathbf{E_r}$	Active rectifier voltage	[V]
$\mathbf{E_t}$	LG terminal voltage	[V]
$\mathbf{F_e}$	Wave excitation force	[N]
$\mathbf{F_g}$	Mechanical load / LG force	[N]
$\mathbf{F_w}$	Wave "terminal" force	[N]
$\mathbf{G}$	Reduced performance specifications for a single stator section	
$\mathbf{H}$	Magnetic field intensity	[A/m]
$\mathbf{I}$	LG current	[A]
$\mathbf{J}$	Current density	[A/mm^2]
$\mathbf{M}$	Magnetisation	[A/m]
$\mathbf{M_i}$	Induced magnetisation	[A/m]
$\mathbf{M_r}$	Remnant magnetisation	[A/m]
$\mathbf{U}$	LG performance specification	
$\mathbf{V}$	LG translator / buoy velocity	[m/s]
$\mathbf{X_1}$	LG dimensional parameters	
$\mathbf{X_2}$	LG additional parameters	
$\mathbf{Z_g}$	LG mechanical impedance ($\mathbf{Z_g} = b_g - \mathrm{j}c_g/\omega_w$)	[Ns/m]
$\mathbf{Z_r}$	Rectifier impedance	[Ω]
$\mathbf{Z_s}$	LG Internal electrical impedance ($\mathbf{Z_s} = R_s + \mathrm{j}\omega L_s$)	[Ω]
$\mathbf{Z_w}$	Internal mechanical wave impedance [$\mathbf{Z_w} = b_w + \mathrm{j}(\omega_w M - c_h/\omega_w)$]	[Ns/m]

Constants

g_a	Gravitational acceleration	[9.81 m/s^2]
γ_{fe}	Magnet density	[7580 kg/m^3]
γ_{cu}	Copper density	[8230 kg/m^3]
γ_{sw}	Sea water density	[1030 kg/m^3]
μ_0	Permeability of free space	[$4\pi \times 10^{-7}$ H/m]
ρ_{cu}	Resistivity of copper	[1.7×10^8 Ωm]

Subscripts

A, B	Case A or B (Chapter 4)
abc	*a*, *b* and *c*-phase components of the stationary reference frame
αβ	α and β components of the stationary reference frame
dq	*d* and *q* components of the synchronous rotating reference frame
i	Individual stator section
I, II	Region I or II in the subdomain model (Chapter 3)
1	Fundamental frequency

Chapter 1

Introduction

The rolling blackouts experienced in South Africa in late 2007 left a lasting impact on the country's economy. Due to mines slowing production, precious metal prices reached record highs early in 2008 [1]. Mining company Rio Tinto cancelled a R 24 billion aluminium smelter investment at Coega in the Eastern Cape [2]. Anglo American, on the other hand, decided to build its own power plant to ensure sustained mining operations in the country [3]. These are simply some local examples from the recent past that show the major reliance of the economy on a secure energy supply.

Now, as it is already happening all over the world, South Africa is trying to increase the share of renewable energy (RE) into its energy resource mix in order to increase energy security and reduce emissions. The 2003 Government white paper on RE sources showed one of the first signs of a noteworthy drive for RE investment in South Africa [4]. The government followed up by setting feed-in tariffs (FITs) for RE in 2009 [5]. The Department of Energy's (DOE) Integrated Resource Plan (IRP), released in May 2011, foresees that 9 % of electricity will be generated from renewables by 2030, mainly from solar and wind [6]. In order to stimulate industry to meet this target, the DOE launched a new RE procurement programme in 2011 which allows independent power producers (IPPs) to bid for a share of pre-determined generating capacities for solar, wind, hydro, biogass/mass and landfill gas energy [7].

It is noteworthy that in all of the above named initiatives, no provision has been made for any source of ocean energy, even though South Africa has a significant wave resource [8]. This is probably due to the fact that hardly any technology exists commercially at a proven level for harnessing ocean energy [9], [10]. Tidal barrages are the only long term economically proven technology [10]. Most ocean energy devices are still in the development phase. This thesis begins with a brief history of research and development done specifically for *wave* energy conversion.

1.1 A brief history of wave energy research and development

Energy can be extracted in many different ways from the ocean's waves, tides, currents and thermal and salinity gradients. The ocean *waves*, which is probably the most obvious form of energy in the ocean, has been the subject of research for many years. The first known patent for a wave energy converter was registered in 1799, with several hundred more patents being registered in the ensuing 170 years [11]. Since the 1940s, the most significant work was done by the late Yoshio Masuda from Japan, who is considered the father of modern scientific wave energy research [12]. He developed navigation buoys which were power by the waves. He used a method which would eventually become known as the oscillating water column (discussed in more detail in Section 1.3.2). The buoys were commercialised in Japan and the USA.

The oil crisis of 1973 caused a significant increase in all kinds of renewable energy research, including wave energy. Influential ocean energy research groups were established at Edinburgh University by Stephen Salter and at the (then) Norwegian University of Technology in Trondheim by Kjell Budal [13]; the first conferences and symposia around ocean energy conversion were consequently also hosted in the UK and Scandinavia [12]. In addition to Salter and Budal's groups, important research was also done by a number of other researchers as reviewed in [14], [15]. Despite a significant reduction in funding with the stabilising oil prices in the 1980s, further research did continue [12], [13].

The 1990's saw a new worldwide push for clean energy sources in order to reduce greenhouse gas emissions [13]. During this time the European Commission (EC) played an important part by initiating and funding a number of wave energy R&D projects [11] and by promoting collaboration among countries through supporting wave energy conferences and establishing of the European Wave Energy Thematic Network in 2000 and the Co-ordinated Action of Ocean Energy in 2004 [16]. A host of other, similar organisations have been established since then. Probably the most important of these bodies is the Ocean Energy Systems (OES) Implementation Agreement, launched by the International Energy Agency (IEA) in 2001 [17]. The initial implementation agreement was signed between three countries, namely Denmark, Portugal and the UK, but has since grown to 19 member countries and more countries are also likely to join soon [17]. OES publishes annual reports summarising the R&D activities of all member countries and addresses specific issues facing developers, e.g. marine spatial planning, regulatory issues and standardisation. A number of task groups exist which also look specifically at dissemination of information, recommended practice for testing devices, grid-integration and environmental issues; reports are published online [18] as and when a specific task is completed. The OES online library is hence a very comprehensive and up-to-date source for everything related to ocean energy and serves as an excellent starting point for someone who is new in the field.

For more practical research and to facilitate sea testing of ocean energy converters, the European Marine Energy Centre (EMEC) was established at Orkney in Scotland in 2003 [19]. EMEC was the first purpose built commercial test and certification centre of its kind where any developer could test their devices in the sea with facilities for grid-connection. Since its establishment, EMEC has been utilised by a number of well known developers, including Pelamis Wave Power, AW-Energy, Aquamarine Power, Seatricity and Wello [19]. From these test activities a large amount of research expertise has been developed from which a number of industry guidelines have been published. A work group (TC114) at the IEC is currently also developing international standards for industry [20] and some of the EMEC guidelines are forming the basis of these [19].

A number of books on wave energy has also been published in the last thirty years. These include McCormick [21], Shaw [22], Ross [23], [24], Falnes [25], Cruz [26] and a book published by the Engineering Committee on Oceanic Resources [14]; these serve as good sources, both for entry into the field and also as detailed references. Two non-English language books are also listed online at [27]. New research is still disseminated at a number of international conferences. These include the biannual European Wave and Tidal Energy Conference (EWTEC) and the International Conference on Ocean Energy (ICOE), which are dedicated to the ocean energy industry. A number of other conference, e.g. the International Ocean and Polar Engineering Conference (ISOPE) and the In-

ternational Conference on Offshore, Ocean and Arctic Engineering (OMAE) usually also feature a number of ocean energy papers. Research is also published in a host of different journals too numerous to discuss here.

A huge amount of research has also been done by industry in the development of WECs; some of this is discussed in more detail in Section 1.3.

1.2 The wave energy resource

The rotation of the earth in the sun and moon's gravity fields is responsible for generating waves to some extent [14]. However, the most waves appropriate for energy conversion are created by wind blowing over the ocean surface, which in turn are created by the differential heating of the earth [14], [28]. Waves are therefore indirectly created by the sun, and are as such basically a concentrated form of solar energy. Wave energy is particularly attractive because it is much more spatially concentrated than both solar and wind energy [10], [13], [14] and, although variable, it is also more persistent [13] and predictable [10], [28] than both solar and wind energy. Taking into account the fact that the world's oceans cover roughly 75 % of the earth's surface [29], wave energy is obviously a very attractive renewable energy source. It has been predicted that around 2000 TWh of energy could eventually be extracted annually from the ocean as technology develops [29]. This figure is in the range of the worldwide nuclear or hydro energy production in 2006 [30].

Waves are characterised in terms of their height H_w, period T_w and wave length λ_w. No mathematical theory can exactly describe the behaviour of sea waves, however, linear wave theory can be used with excellent accuracy in predicting the kinematic properties of waves when $H_w/\lambda_w \leq 1/50$ and when losses due to friction and turbulence are ignored [21]. An exhaustive treatment of this theory is covered in e.g. [14], [21], [22], [26]. Most waves can also be characterised as deep water waves (water depth > $\lambda_w/2$). With linear theory applied to a deep water

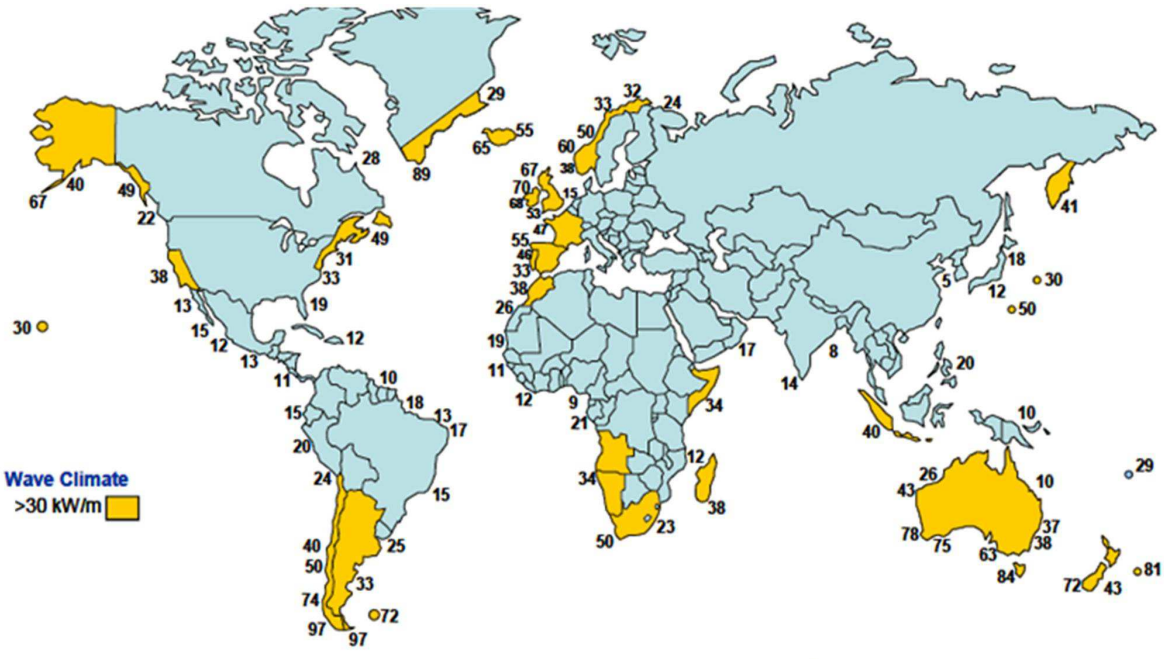

Fig. 1.1 World wave energy resource measured in kW per meter crest length [31].

waves, the power in a wave, given in kW per meter of wave crest length, is given as

$$P_e = \frac{\gamma_{sw} g_a H_w^{\,2} \lambda_w}{16 T_w}, \tag{1.1}$$

where γ_{sw} is the water density and g_a is the gravitational constant. In Fig. 1.1 an indication of the worldwide wave resource is given [31]. Figures of around 30 kW/m and above are considered as being promising for energy extraction [31]. It can be seen that countries with particularly energetic waves include the USA (Alaska), South America (Chile), the UK, Australia, and Southern Africa.

1.3 Wave energy converters

1.3.1 The wave energy conversion process

The basic principle in wave energy conversion is that a device that can effectively generate waves can also be used to effectively absorb waves [13], [21]. The law of energy conservation requires that a WEC should in effect reduce the amount of available energy in the wave; as such the WEC must be able to create a wave which destructively interferes with the incident wave. For wave energy to be useful it needs to be converted to a suitable form and transported to a place where it can satisfy demand. Apart from some isolated applications, such as seawater desalination [9], [14], the most obvious way of harnessing wave energy would be to convert it to electricity and to inject it into a utility grid [12], [14]; from there it is made available to the public.

In Fig. 1.2 the different steps in the wave energy conversion process are depicted [10]. The wave motion is absorbed by some front-end mechanical device or interface. An intermediate power conversion stage, called the power take-off (PTO), then converts the motion from the front-end device to a form suitable for driving a con-

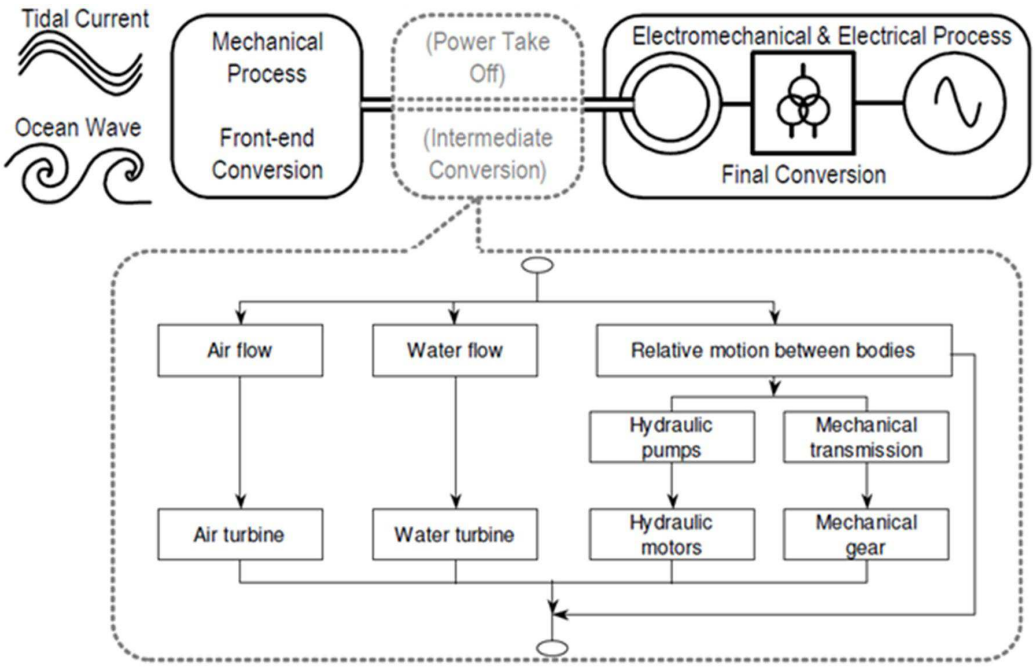

Fig. 1.2 Wave energy conversion process [10].

ventional electrical generator. The PTO usually consists of a pneumatic or hydraulic system and can include some form of energy storage mechanism to smooth out the variable power absorbed from the waves. The electrical generator forms part of the electromechanical energy conversion stage as shown in Fig. 1.2. The generator output may still be subject to further electrical processes in order to convert it to a form acceptable for utility grid connection. Mueller [32], in agreement with this, also notes that all WECs can be divided into 3 areas, namely the (i) device (primary mechanical interface), (ii) PTO (intermediate mechanical interface) and (iii) the electrical system (including the generator and the power converter). Despite this commonality found among all WECs, a massive number of different WEC concepts have been proposed. All of these can however be divided into a small number of major categories as is explained in the next section.

1.3.2 Classification of WECs

WECs can be classified according to their location as onshore, near-shore or offshore devices and also as floating, submerged or bottom-standing devices [13]. According to their horizontal extension and orientation, as shown in [13], WECs can also be classified as:

a) Point-absorbers, which have a physical extension which is small compared to a typical wavelength.
b) Line absorbers. These devices have an extension which is comparable or larger than a typical wavelength. These can be further classified as attenuators when the device is aligned parallel to the prevailing wave direction, and terminators, when the device is aligned normal to the prevailing wave direction.

For the purpose of this thesis, however, it is more useful to classify WECs according to their method of energy

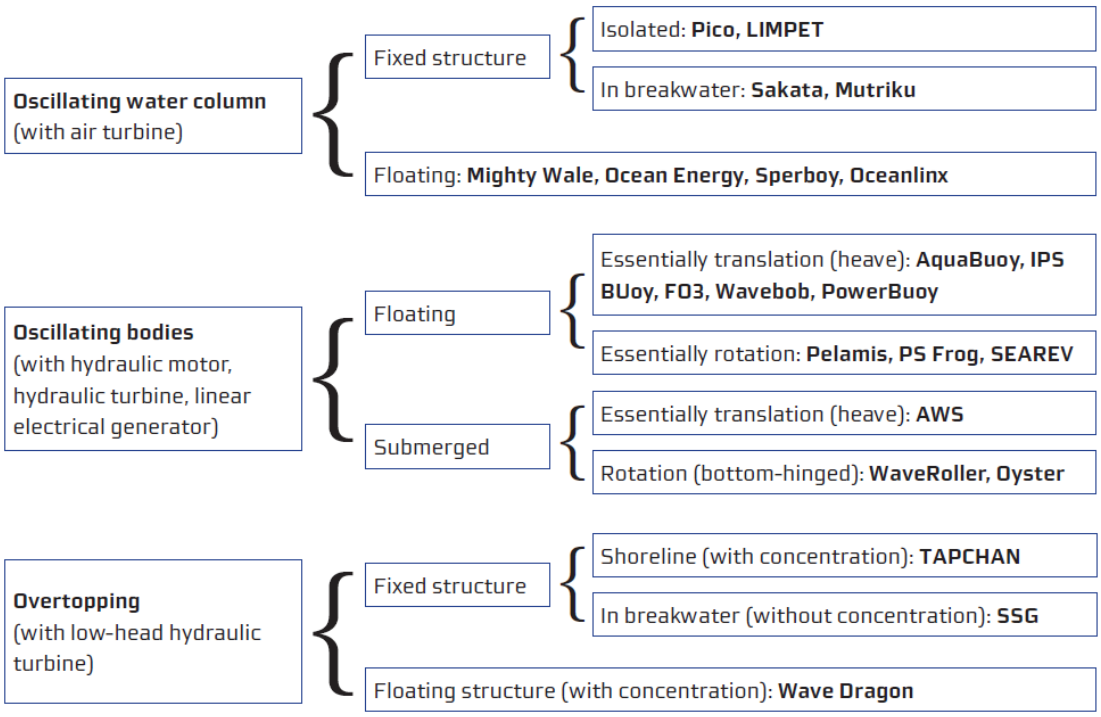

Fig. 1.3 A classification system for wave energy converters showing examples of each type [9], [12].

conversion, or working principle, as done in [9], [10], [12], [32]; these authors all categorize WECs slightly differently. In Fig. 1.3 the categories as discussed in [9], [12] are illustrated. It is noted in literature that it is still unclear which type will be the final winner. The basic operating principles of the three main categories are considered by way of examples.

a) *Oscillating Water Columns (OWCs)*: These devices have a partly submerged chamber which is open below the water surface. Inside this chamber the water level rises and falls with the waves, thus creating a bi-directional air-flow through another opening in the chamber as shown in Fig. 1.4 (a). Using an air turbine, this airflow is converted to unidirectional rotation for driving an induction generator. The typical size and rotation speed of the air turbines make it possible to store a significant amount of energy as kinetic energy with the flywheel effect. This can contribute to smoothing out the variable energy absorbed from the waves. The OWC was one of the first WEC types which were built to full-scale with ratings up to 2 MW. Oceanlinx (formerly Energetech) in Australia is an example of an OWC. It has two versions, one for shallow and one for deep water [33]. A custom turbine and a standard induction generator are used. Power conversion control is done with a standard drive and programmable logic controller (PLC). An independent study from Emerging Energy Research found Oceanlinx to currently be the most advanced OWC technology and overall the second most advanced WEC in the world today [34].

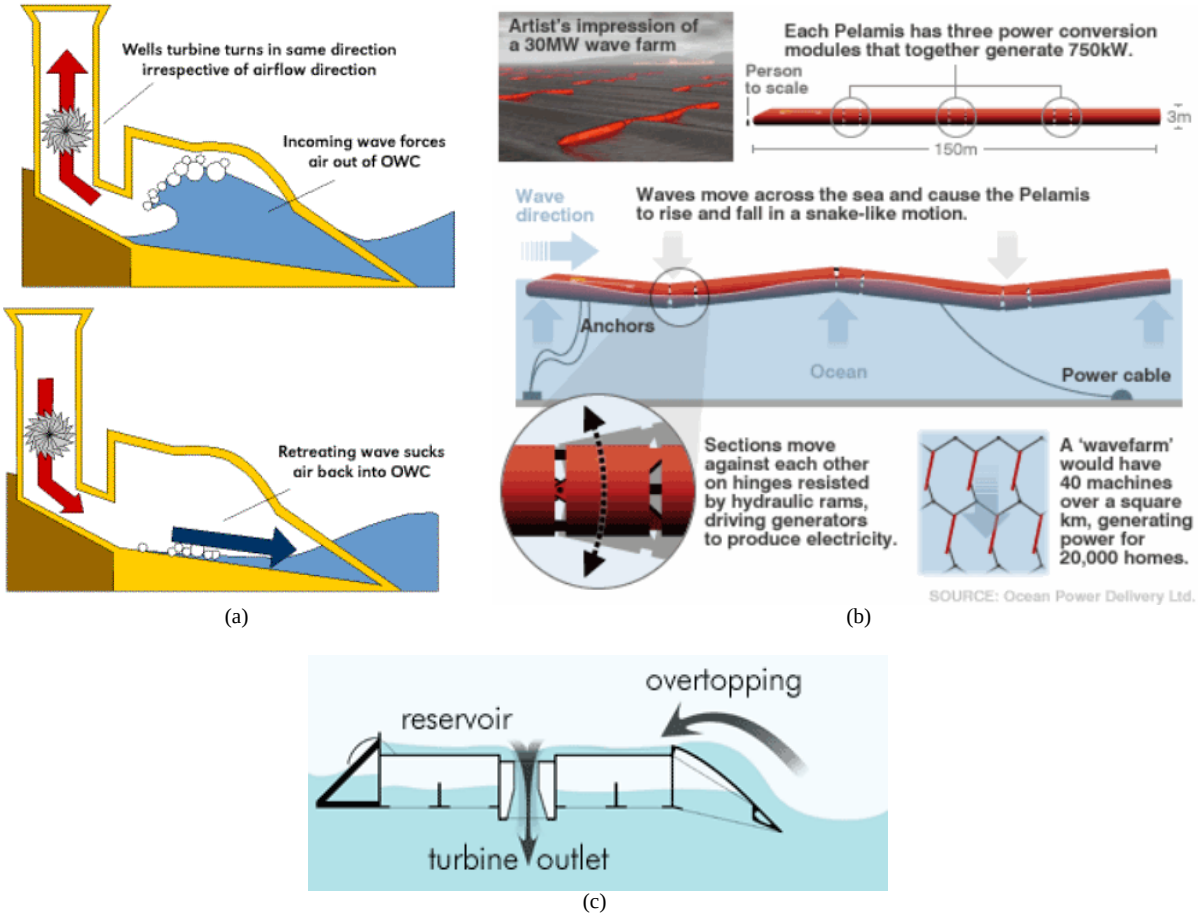

Fig. 1.4 Working principle of a typical (a) oscillating water column, (b) the Pelamis (as an example of an oscillating device) and (c) an overtopping device.

b) *Oscillating bodies*: This type of device uses some mechanism to extract energy from the relative oscillating motion between two bodies [9]. There are a large variety of devices in this category, some using rotational and some translational motion. Most of these devices use hydraulic PTOs with induction generators. The Pelamis WEC, shown in Fig. 1.4 (b), consist of 4 floating cylinders linked by hinged joints [35]. At each joint hydraulic rams resist the relative motion between the cylinders which are caused by the waves. The rams pump high pressure oil through hydraulic motors via smoothing accumulators. The motors are used to drive induction generators which supply electricity to the grid through a transformer. The accumulators achieve sufficient power smoothing to enable grid connection without a power electronics converter (PEC). Costs are further reduced by using standard components from the offshore oil and gas industry. The first and, so far, still the only ever commercial wave energy facility was commissioned in September 2008 off the coast of Portugal and consisted of three 750 kW Pelamis P1-A WECs connected to the local grid at Aguçadoura. According to the report from Emerging Energy, the Pelamis is overall the most advanced WEC in the world today [34].

c) *Overtopping devices*: Overtopping devices collect water in a reservoir and thereby convert wave energy to potential energy [9]. This reservoir is then used as a stable supply to a conventional low-head water turbine connected to a conventional electrical generator as seen in Fig. 1.4 (c). Overtopping devices have the advantage of using few moving parts and proven low head hydro technology [32]. The Wavedragon, currently the most advanced overtopping device, has two reflector arms to focus waves towards a ramp. On the other side of the ramp the water collects in a reservoir and from there standard water turbines are used to drive PM synchronous generators. The variable voltage induced by the PM generator is connected to the grid through a power electronic converter (PEC) [36]. A 1:4.5 scale prototype rated at 20 kW was tested off the coast of Nissum Bredning in Denmark between 2003 and 2005 [37].

1.3.3 Direct drive wave energy converters

To improve the efficiency and reliability of WECs, it is desirable to minimise the number of moving parts; this idea also manifests itself in the wind energy industry where the removal of the gearbox between the turbine and the generator is becoming more and more attractive. This is then called a “direct drive” system, i.e. the turbine (front-end mechanical interface) directly drives the generator without any intermediate power conversion stages (PTO). In direct drive wave energy converters (DD-WECs), the heave motion (translation) of the waves is usually employed to directly drive a linear generator (LG). These devices are usually point absorbers and classified as oscillating bodies with translation motion (from Fig. 1.3).

In concept, a floating buoy acting against a fixed reference is probably one of the most simple forms of a point absorber. This is reflected in the fact that much of the research started in the 1970s was focussed on the fundamental theory of wave energy absorption by a heaving buoy; an excellent review of this research is given in [14]. In 1983, Neuenschwander [38] filed a patent for what was one of the first DD-WECs to employ a float to directly drive a LG [39]. LGs were however considered too heavy and inefficient to be a viable option for wave energy conversion at that time [39]. It was only with the more recent advances in permanent magnet (PM) materials and also in power electronic converters (PECs) that interest in DD-WECs increased again [39].

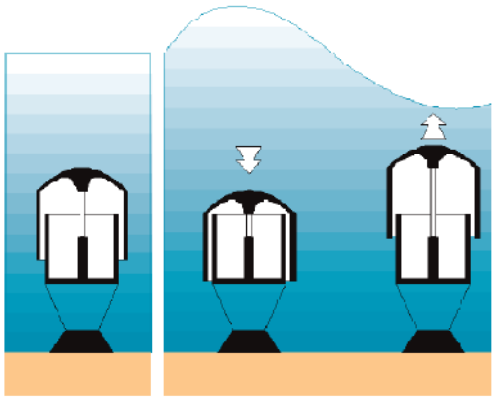

Fig. 1.5 Working principle of the original Archimedes Wave Swing.

Probably the first DD-WEC to use a PMLG is the original Archimedes Wave Swing (AWS). The first patents for the AWS was filed in the early 1990s. It was developed in the Netherlands and a full scale prototype was first tested in the sea off the coast of Portugal in 2004 [40], [41]. The AWS however does not make use of a floating buoy. It is a fully submerged device filled with air and consists of an upper part (floater) which moves against a bottom part fixed to the seafloor as shown in Fig. 1.5. The floater moves down and compresses the air under a wave crest; the pressure is then released under a wave trough and the floater is allowed to move back up again. The floater is directly connected to the translator of a PMLG and thus the AWS uses no intermediate PTO. The AWS dynamically vary the volume of air in the device to effectively change its spring constant; this way it can optimise energy transfer from the floater to the generator. At 2 MW of peak power, it is still the largest ever DD-WEC to have been built to date.

After the turn of the century a number of other DD-WECs also emerged; although different in their configurations, all are based around a floating device of some kind. The concepts as used by Uppsala University [42], Oregon State University [43] and Trident Energy Ltd [44] are depicted in Fig. 1.6. All of them also use PMLGs, although each of these is also of a different topology. All these DD-WECs are still at the development stage and not commercially available yet.

DD-WECs have no inherent energy storage mechanisms and produce a voltage with variable amplitude, frequency and phase rotation. A PEC with enough storage on the dc-bus is therefore needed to connect these devices to the grid. Aggregation of phase shifted outputs of multiple LGs onto a common dc-bus however relaxes the energy storage requirements as a natural smoothing effect occurs [45], [46]. The presence of a PEC can also be seen as an advantage as it can be used to control the generator current for maximum power transfer to the load. It is also well known that voltage source inverters (VSIs) serve as an excellent grid interface in terms of complying with grid-code requirements [47]. The PEC will be discussed in more detail in Chapter 5.

Overall, the simplicity of operation and absence of an intermediate PTO is what makes DD-WECs very attractive, especially as expected maintenance requirements are much reduced. A high efficiency is also expected and has in fact been demonstrated in DD-WECs with PMLGs at all loads [32]. In addition, DD-WECs do not contain any hydraulic fluid, like many other WECs [9]; apart from the obvious maintenance requirements it could also

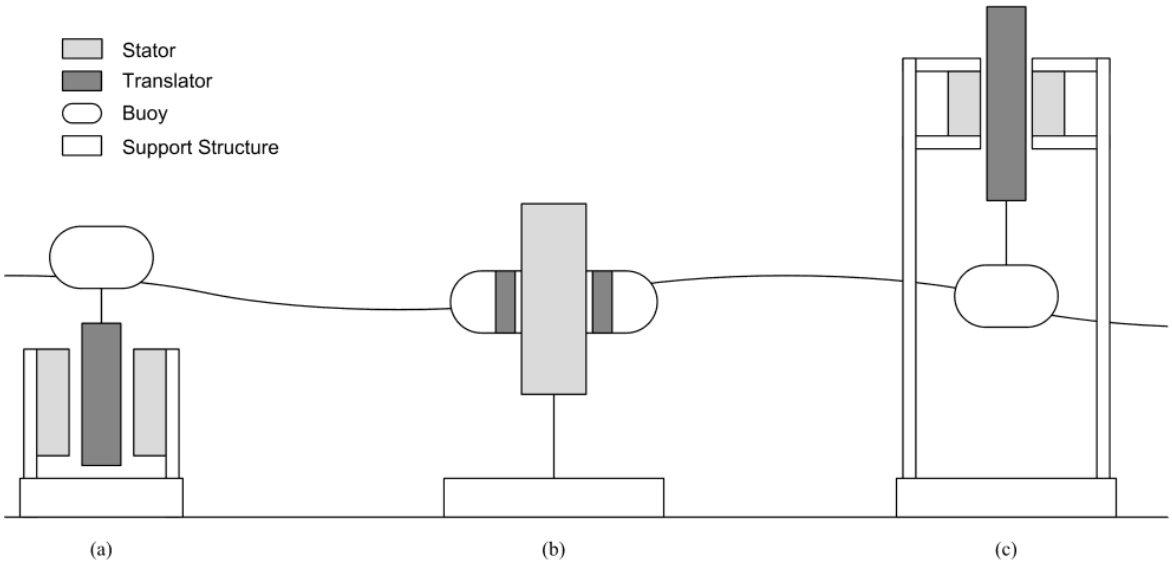

Fig. 1.6 Different configurations of WECs employing the heave motion of a buoy to drive a linear generator. The concepts are from (a) Sea-based / Uppsala University, (b) Columbia Power Technologies / Oregon State University and (c) Trident Energy.

cause concern for the environment if leakage should occur. It is therefore easy to see why DD-WECs have received much research attention in recent years and why the work in this thesis is also focussed in this area. However, as mentioned, none of these devices are commercially viable yet and this indicates that there are currently still some problems preventing progress of DD-WECs. This will be discussed next.

1.4 Problem statement

From the preceding section the advantages of DD-WECs are clear. However, the direct drive aspect of the devices is also one of their greatest drawbacks. This can be explained by observing the fact that power equals the product of force and velocity for a translating body. The velocity of ocean waves is rather slow with peaks of 1 – 2 m/s [48]. Therefore, in order to generate a significant amount of power, a large force is needed, which in turn means that a large generator is needed. One implication of this is that the generator's price per unit power becomes very large. Other implications of the large generator and further problems associated with its control and testing are explored below.

1.4.1 Linear generators

In a study, Polinder compares different types of conventional LGs for the AWS [49]; of these, the iron-cored longitudinal flux (LF) PM synchronous machine is found to be the most efficient and to also have the lowest active material cost. The other known LGs which have made it to sea trials (one from Uppsala University [42] and one from Oregon State University [43]) are also LFPM generators. In these generators, permanent attraction forces exist between the PM translator and the iron stator. In order to keep the correct clearance between the stator and translator, these normal attraction forces must be supported by a sufficient amount of structural material and by the bearings which facilitates the motion of the translator relative to the stator. As the generators get larger, these attraction forces also become larger. With larger size also comes the problem of greater deviation in

dimensions due to manufacturing tolerances [50]. Over a large area where a small air gap needs to be maintained in the presence of immense attraction forces, the difficulty and cost associated with this can be quite substantial and even insurmountable.

Further problems are inherent to the type or topology of the generator used, and not related to the size of the generator. For LFPM machines these problems are mainly pair-wise flux coupling, cogging forces and increased eddy-current losses due to the longitudinal ends of the machines [51]. These aspects are discussed in more detail in the next chapter.

Other types of generators, namely variable reluctance (VR) PM machines like transverse flux (TF) and vernier hybrid (VH) machines are investigated as high force density alternatives to LFPM machines in [49] and [52]. Unfortunately, difficult construction [49] and low power factor [52] are considerable disadvantages of these machines. Different linear tubular topologies are also investigated in [53] and [54], also as higher force density alternatives to planar LFPM machines. Large normal attraction forces are, however, still a problem in all of these machines.

Air-cored generators are also receiving increasing attention for use in DD-WECs [44], [48], [55], [56]. The elimination of cogging forces and the elimination of the attraction forces between the stator and translator make them very attractive. However, more PM material compared to a similarly rated iron-cored machine is used. By using a double-sided PM translator, a higher air gap flux density than in a single-sided air-cored machine can be maintained. However, attractive forces between the two opposing translator sides are then introduced which again creates the need for increased structural material.

1.4.2 Power conversion control

The energy conversion process in DD-WECs is similar as described in Section 2.1 for a generic WEC. Only now there is no PTO present. The process can therefore be seen firstly as mechanical energy absorbed from the waves by the front-end mechanical interface (e.g. the buoy); this energy is then directly transferred to the LG without a PTO. Secondly the process can be seen as the electrical energy absorbed from the LG by the load. Maximum energy is captured from the waves when the device velocity is in phase with the wave force and with the device's damping force equal to that of the waves; this effectively constitutes a resonance condition between the waves and the device. This condition can be achieved by controlling the device's reaction to the waves with mechanical means (e.g. the AWS [40]) or electrically by manipulating the LG current with a PEC [57], [58], [59]. Maximum energy transfer between the LG and load likewise occurs with the current in phase with the EMF and with the correct load impedance [56], [60].

Device reaction force control with a PEC has obvious advantages over mechanical actuators like in the AWS, e.g. faster operation, lower maintenance and greater flexibility. However, reaction force control with a PEC will always cause a phase difference between the LG's current and EMF as reactive power needs to be returned to the waves during part of the period [12], [57], [58] (this is explained in more detail in Chapter 5 and Appendix A); the condition for maximum power transfer between the generator and load is therefore compromised.

Assuming that mechanical or other means of device reaction force control is used leaves only the aspect of energy transfer from the generator to the load to be considered. The PEC can then be used to control the generator current at the desired amplitude and in phase with the EMF. For this method, as well as reactive force control with a PEC, the generator EMF must be measured or estimated. In [56], [60] sense coils are used to determine the EMF amplitude and phase, but the authors of [60] admit that this is a cumbersome practice and that sensorless methods should be investigated. Some control strategies also require linear position feedback in order to do coordinate transformations (*dq*-transformations) for control purposes [53]. Again, a sensorless method would be preferred; especially considering that stroke lengths (and hence linear encoders) in the order of meters would likely be required.

1.4.3 Testing

Testing of LGs in the laboratory is not straightforward as linear drive systems are not commonplace in traditional electrical machines laboratories. Custom test rigs were for instance developed for laboratory testing of LGs in [43], [48], [53], [56], [58]. This includes vertical [43] and horizontal [48] hydraulic drive systems, cable-and-pulley systems [53], [56] and a VSD with a worm-and-ball gear [58]. Control hardware and software for such drive systems are also needed to simulate wave motion under a varying generator load. Developing a drive system for testing LGs can thus become a project on its own with considerable cost.

1.5 Approach to problem

Some suggestions from Polinder et.al. [61] for overcoming problems associated with DD-WECs include: increasing generator speed, investigating higher force density generator types, investigating air-cored machines and using cheaper construction methods, like using concentrated coil windings. In order to solve or improve on some of the problems with PMLGs described in Section 1.3, it is decided to develop a novel LG topology with an air-cored stator and concentrated windings; this is in keeping with the above named suggestions and based on previous experience at Stellenbosch University with air-cored machines and concentrated windings [62], [63], [64], [65], [66]. The approach in achieving this is outlined as follows:

1) A thorough investigation of LGs used in current experimental DD-WECs as well as generator design theory is conducted.
2) Existing machine topologies are used to devise a novel machine topology.
3) Analytical and Finite Element (FE) methods are used to design a small scale prototype.
4) A suitable test rig is designed and constructed together with the prototype generator.
5) A suitable sensorless control strategy is identified and simulated using Ansys Simplorer ®.
6) A standard voltage source converter (VSC) is used to implement the control strategy.
7) The novel generator, control strategy and test rig are finally tested and evaluated in terms of the problems described in Section 1.3.

1.6 Scope and limitations

It is important to note that the novel LG developed in this study is in itself not a WEC. The LG simply fulfils the function of converting the mechanical energy captured from the waves to electrical energy as explained in Section 1.3.1. The generator would therefore still need to be installed in a WEC like the AWS in order to be installed in the sea. This approach is also followed by a leading research group in Edinburgh [48], where only the generator is considered, and not the entire WEC.

In the design of the LG, thermal and structural analyses are mostly ignored due to the small size of the prototype. The design is more focussed on the electromagnetic aspects of the generator.

Furthermore, the control strategy implemented is likewise only aimed at maximising energy transfer between the LG and the load. It is as such assumed that alternative arrangements can be made for optimising energy transfer from the waves to the WEC. In this study, the load is also considered to be the dc-bus of the PEC. Inversion of the dc-power to the grid is not considered. The reason for this is the fact that only one generator will be tested. As mentioned before, many of these devices would likely feed onto a common dc-bus in a grid-connected system. It is as such considered unnecessary to attempt grid connection of a single generator.

1.7 Research contributions

The original research contributions of this study are discussed in detail in Chapter 7 and are summarised as follows:

1) A completely novel air-cored LG topology is developed which improves on some of the problems associated with more traditional LG topologies.
2) A two dimensional analytical subdomain model is developed and used to very accurately analyse the magnetic fields in the novel LG. It is furthermore used to derive an accurate equation for the stator windings inductances, which is usually difficult to accurately calculate with analytical methods.
3) A simplified one-dimensional analytical magnetic circuit model and conditions for its use are also developed.
4) The relatively simply one-dimensional analytical model is used to develop an exhaustive optimisation procedure for quickly finding optimal dimensions for minimum active mass of the novel LG.
5) The feasibility of constructing the novel LG topology, at least on a small scale, is demonstrated. Test results from the prototype also confirm the validity of the design methods used.
6) A unique test rig which simulates ideal monochromatic wave conditions for testing the LG, under active control and a variable load, is developed.
7) It is shown that allowing zero stator-translator overlap at the stroke ends can improve the power-to-weight ratio compared to LGs designed for full stator-translator overlap during the entire stroke.
8) Dead-beat predictive control, as a position sensorless alternative to current LG control strategies, is proposed and practically evaluated for DD-WECs for the first time.

9) An important advantage of using an air-cored stator with predictive current control is established. It is shown that the negligible and constant internal reactance of the stator winding, together with accurate measurements of the LG's phase resistance and filter inductance reduces the complexity and increase the accuracy of the predictive control strategy.

1.8 Thesis layout

The layout and contents of the thesis is briefly described here:

Chapter 2: Permanent magnet linear generators. This chapter is basically a thorough literature review of PMLGs. Aspects that are covered are the different PMLG topologies, the basic theory behind them and also an overview of the generators specifically used in the most well known DD-WECs.

Chapter 3: Analysis of the novel linear generator. This chapter starts with a description of the development of the novel PMLG topology. The focus is however on the in depth analytical and finite element analysis of the magnetic fields and performance of the novel LG. A basic analysis of the novel machine's performance compared to other PMLGs is also presented.

Chapter 4: Prototype linear generator design. The design and optimisation of the prototype generator are described in this chapter.

Chapter 5: Drive system and control design. The chosen drive system and control strategy is described in this chapter. Simulation results of the control algorithm are also presented.

Chapter 6: Experimental evaluation. The construction of the prototype PMLG and the chosen test rig is described in this chapter. Measurements are presented and compared to analytical and simulated design results.

Chapter 7: Conclusion and recommendations. The conclusions derived from the research are presented in this chapter together with recommendations for further work. A detailed account of the original research contributions is also given.

Appendix A: Wave energy absorption. The basic theory behind wave energy conversion is outlined in this Appendix.

Appendix B: Electromagnetic theory. The electromagnetic theory which is relevant to the analysis and design of electrical machines is reviewed in this Appendix. This includes an overview of the theory of finite element analysis.

Appendix C: Fourier series expansions. The theory pertaining to Fourier Series expansions are reviewed and the derivation for the Fourier Series expansions of the conductor density, current density and magnetisation is given in this Appendix.

Appendix D: LG magnetic field solutions. The choice of general and particular solutions for the LG magnetic fields due to the stator current and the PM excitation is discussed and the solutions for the constant terms in the general solutions are given in this Appendix.

Appendix E: Inductance calculation. The derivation of the equations for stator winding inductances is given in this Appendix.

Appendix F: Average power derivation. The average power for a sinusoidally reciprocating three-phase LG is derived in this Appendix.

Appendix G: Comparative study calculations. The calculations done for the comparative study presented in Chapter 3 is discussed in more detail in this Appendix.

Appendix H: Simplorer simulation model. The Simplorer model used for the predictive control simulations is shown together with some explanations.

Appendix I: List of patents. A list of international patents with reference to the LGs discussed In Chapter 2 is given for reference in this Appendix.

Chapter 2

Permanent magnet linear generators

In this chapter a literature review of permanent magnet linear generators (PMLGs) is given. The different topologies and PM arrangements are first discussed, where after the issue of the longitudinal end effects of LGs are considered. Particular attention is also given to the choice of winding arrangements and methods of rating and sizing LGs. The chapter ends with an overview of the state-of-the-art in LG research.

2.1 Linear generator topologies and classification

Electrical generators are better known in their rotary version as shown in Fig. 2.1. The inside part of the generator rotates with the prime mover and is called the rotor. A magnetic field on the rotor induces an electromotive force (EMF) in windings on the stationary outside part of the generator, called the stator, according to Faraday's law of electromagnetic induction. Since the induced stator EMF is in synchronism with the revolving rotor field, the generator is called a synchronous generator. The rotor field excitation is created with either permanent magnets (PMs) or electromagnetically. For LGs the rotor is called a translator, thus referring to the linear motion of the generator as opposed to rotary motion.

Linear synchronous machines can be classified according to whether they are [67]

- flat (planar) or tubular (cylindrical);
- single-sided or double-sided;
- slotted or slotless;
- iron-cored or air-cored;
- longitudinal flux or transverse flux.

A number of different excitation options can be implemented for each of these topologies, namely PMs in the translator or stator, electromagnetic excitation and superconducting excitation [67]. This thesis focuses mainly on PM excitation which is further discussed in the next section.

The different LG topologies can all be developed from a rotary machine as explained by Boldea and Nassar in [68]. By simply unrolling a rotary machine, a flat single-sided topology can be obtained as in Fig. 2.1(a). Alternatively, by halving both the stator and rotor and flattening them, a flat double-sided topology can be obtained as shown in Fig. 2.1(b). If either of these flat machines is rerolled along their linear axis, a single- or double-sided tubular topology can also be obtained as shown in Fig. 2.2.

The ideal flux paths in a single-sided iron-cored machine can be seen in Fig. 2.3. Machines with such a flux setup where the flux flows in a plane parallel to the direction of motion are called longitudinal flux (LF) ma-

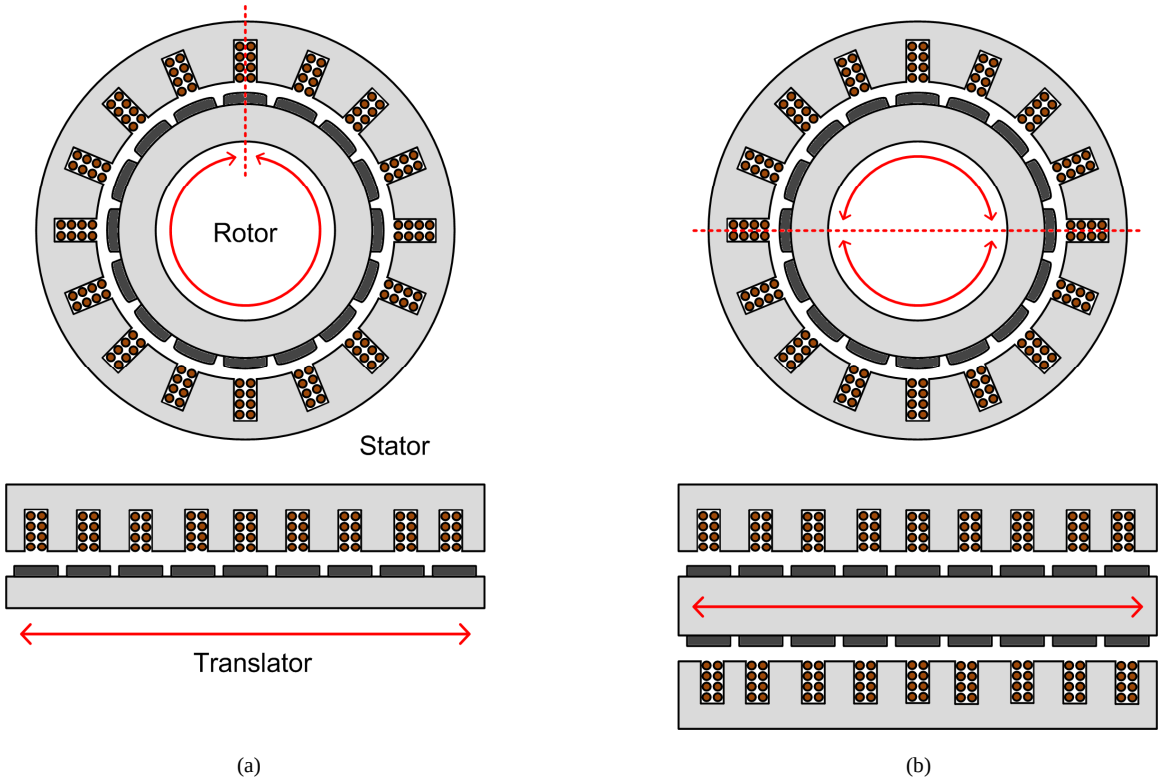

Fig. 2.1 The development of linear machines from rotary machines. (a) If this conventional rotary machine is cut and unrolled, a single-sided planar linear machine topology results. (b) If the stator and translator is halved and flattened, a double-sided planar topology results.

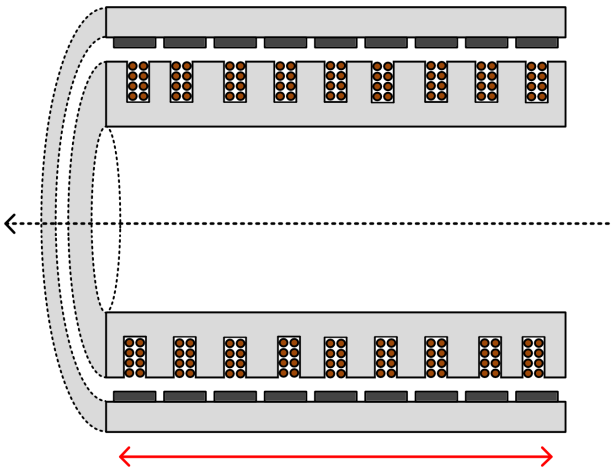

Fig. 2.2 A single-sided tubular linear machine topology formed by rotating a single-sided planar machine around its linear axis.

chines. Machines can also be designed such that the flux flows in a plane perpendicular to the direction of motion; these machines are called transverse flux (TF) machines and are not considered further in this chapter.

A slotted iron-cored stator is the most common in electrical machines. With iron slots higher air gap flux density and stator flux linkage are possible, which means that higher force densities can be achieved. The teeth, however, create a stator with variable reluctance which causes cogging forces. Attraction forces between the stator and translator can also be high. Slotless windings can either be placed on an iron yoke or can be completely

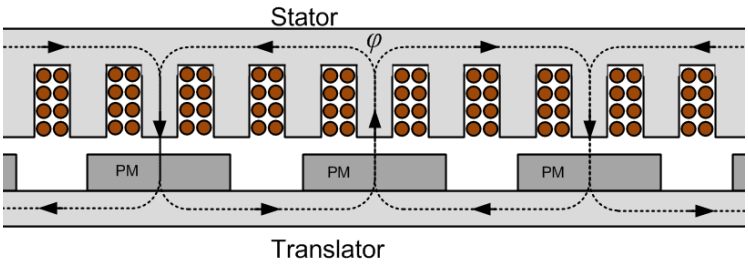

Fig. 2.3 The ideal flux paths in a longitudinal flux linear machine when the longitudinal ends are ignored.

ironless (also called 'air-cored'). In both cases the air gap flux density is much reduced and more leakage and fringing flux is present. The attraction force between the stator and translator is however eliminated. Air-cored stators also have zero cogging force which is an importance advantage, especially in terms of starting of direct drive RE generators.

While a rotary machine's rotor can move in the same direction for an unlimited amount of time, a linear machine has a finite length, and hence the motion of its translator is restricted. It is therefore obvious that the translator must change direction continuously in order to generate electricity continuously. This then implies that the generated voltage will have a continuously varying amplitude and frequency; in a three-phase generator the reversal of the direction of motion will also change the phase sequence.

2.2 Permanent magnet excitation

The magnetic field in a synchronous machine is usually created by a winding on the rotor excited through slip-rings, brushes and a dc-source; this winding is effectively an electromagnet. The field winding of a synchronous machine can of course be replaced with PMs. Although field control is sacrificed, the brushes, slip rings and field winding copper losses are eliminated [69], resulting in a simpler and more efficient machine. PMs can also occupy less space than a field winding, which means that a higher force and power density can be achieved.

PMs can be characterised in terms of their remanent flux density B_r and coercive field intensity H_c. The remanent flux density is the flux density corresponding to zero magnetic field intensity and the coercive field intensity is the field strength necessary to demagnetise the magnet (more details about PM materials are given in Appendix B). The demagnetisation curve in Fig 2.4 shows these parameters for the different PM materials used in electrical machines, which are [67]

- Alnico (alloy of aluminium, nickel, cobalt, iron and traces of other metals);
- Ferrites (or ceramics), e.g. barium ferrite and strontium ferrite;
- Rare-earth materials, e.g. samarium-cobalt (SmCo) and neodymium-iron-boron (NdFeB).

Alnico magnets have a high remanent flux density, which means higher air gap flux density can be achieved. They can also operate at very high temperatures (see Table 2.1). Unfortunately they can also easily become demagnetised due to their low coercivity and have a very non-linear demagnetisation curve. Ferrites are more resistant to demagnetisation, but have a lower remanent flux density and operating temperatures. The rare-earth mag-

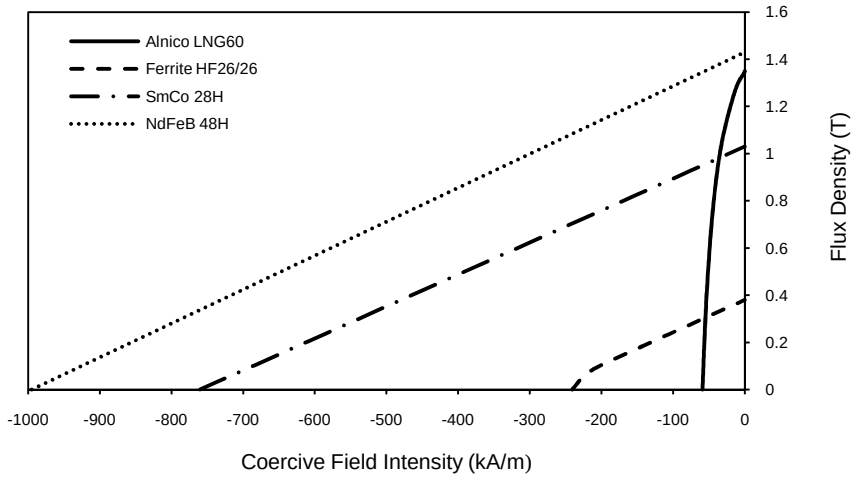

Fig 2.4 Demagnetisation curves of Alnico LNG60, Ferrite HF26/26, SmCo 28H and NdFeB 48H magnets.

Table 2.1 Properties of typical permanent magnet materials available from a supplier in China.

Magnet	Grade	B_r (T)	H_c (kA/m)	Max Energy Prod. (kJ/m^3)	Max Temp (°C)
Alnico	LNG60	1.35	59	60	525
Ferrite	HF26/26	0.38	240	27	400
SmCo	28H	1.03	760	224	300
NdFeB	48H	1.43	$\geq$ 995	390	120

nets are clearly superior in terms of magnetic properties, although not as good in terms of operating temperatures. NdFeB has better magnetic properties than SmCo and Nd is also more available than Sm [67], making NdFeB the magnet of choice nowadays. It must be noted that the magnetic properties of especially NdFeB are fairly temperature dependent and that SmCo actually perform better than NdFeB at high temperatures.

PMs can be installed in a number of different ways in a machine. When installed on the translator, the magnets can either be surface mounted and magnetised perpendicular to the air gap area as seen in Fig 2.5(a), or they can be buried and magnetised parallel to the air gap area as seen in Fig. 2.5(b). In the first case the yoke is ferromagnetic as it is part of the flux path. In the second case it is non-ferromagnetic as it is not part of the flux path. The magnets can also be arranged in a so-called Halbach array as shown in [67]. This arrangement creates a higher

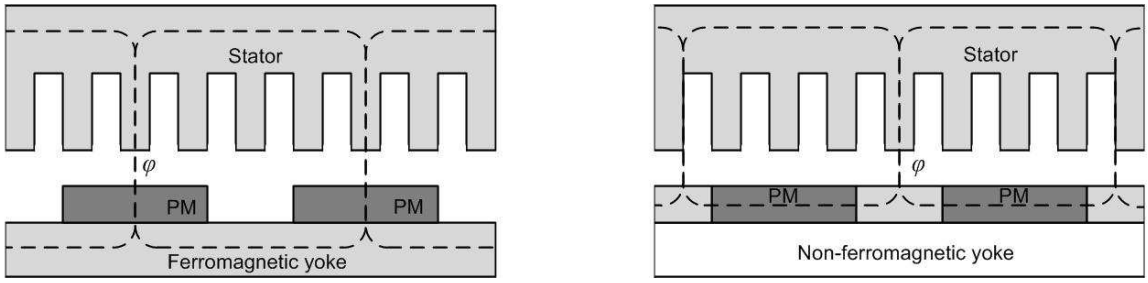

(a) (b)

Fig. 2.5 Different options for PM installation. (a) Surface mounted PMs are magnetised perpendicular to the direction of motion and have a ferromagnetic yoke. (b) Buried PMs are magnetised parallel to the direction of motion and have a non-ferromagnetic yoke.

and more sinusoidal air gap flux density than the previous two.

With the PMs on the translator, the translator length should be equal to the stator length plus the stroke length for the stator winding to be active at all times. This could mean that a huge amount of PM material is used. An alternative and cheaper option is to place the PM material on the stator as in [52]. The translator is then slotted to create a reluctance which varies with translator position; this then causes the changing stator flux linkage as the translator moves relative to the stator. These are called variable reluctance (VR) machines. An example of such a machine is further discussed in Section 7.4.

2.3 Longitudinal end-effects

In a rotary machine the magnetic circuit closes on itself and the stator and rotor fully overlap each other at all times. In LF linear machines, however, the magnetic circuit is open on both ends of the machine and all parts of the stator and translator cannot be active at all times. This causes a number of unwanted effects which are often neglected in linear machine modelling. These can be divided into static and dynamic end effects as discussed in [51], [70].

2.3.1 Static end-effects

In a rotary machine, the flux from any particular magnet pole couples equally with each of its neighbouring magnets. However, when the magnet at the end of a linear machine is considered, the flux of this magnet can only couple with its one neighbouring magnet, as shown in Fig. 2.6. The flux from the magnet third from the end in Fig. 2.6 will also then couple completely with the fourth magnet and so on. This causes a so-called pair-wise flux coupling throughout the machine and means that larger stator and translator yokes are needed to prevent saturation. It is also shown in [51], [70] that due to saturation and symmetry effects the pair-wise flux coupling approaches the ideal flux pattern (as shown in Fig. 2.3) towards the middle of the machine; this causes uneven air gap flux density along the length of the machine and can be a problem for cogging force reduction methods such as fractional slot windings, which assumes symmetrical air gap flux in order to work [51], [70].

Furthermore, in a rotary machine all the windings link an equal amount of flux caused by the current in each of the other phases. In other words, the mutual inductance of all the phases are the same and usually equal to around half of the self inductance [71]. However, in a linear machine the windings at and near the end of the machine will have no other windings to its one side and hence will link a different net flux than the windings in the middle of the stator. The effect of this is that the mutual inductances will differ among the three phases and will

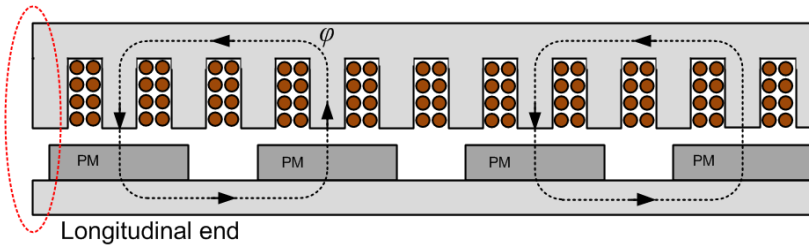

Fig. 2.6 Pair-wise flux coupling in longitudinal flux linear machines.

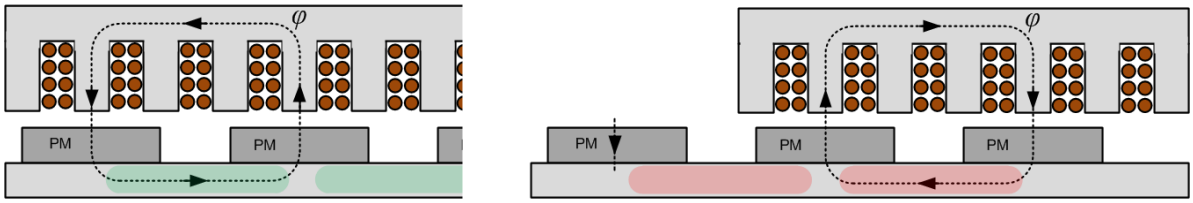

(a) (b)

Fig. 2.7 The dynamic end effects in LF linear machines are illustrated here. The flux in the green areas (a) changes when the translator moves to its position in (b); this will cause unwanted eddy-current losses in the machine. It can also be seen that a huge change in the reluctance seen by the end magnet occurs between the two positions; this will cause significant cogging forces.

cause a degree of unbalance among the phases.

2.3.2 Dynamic end-effects

The pair-wise flux pattern can only form when the two magnet poles in question are aligned with the stator (assuming an iron-cored machine) as in Fig. 2.7(a). When the end magnet moves out of the stator, as shown in Fig 2.7(b), the second magnet will change its "partner" to the third magnet, with the effect also rippling through the rest of the machine. This will cause unwanted changing flux in the translator yoke, which can cause considerable eddy-current losses in solid translator yokes. Furthermore, considerable cogging forces associated with the magnets moving into and out of the iron stator are also experienced.

2.4 Windings arrangements

Windings in linear machines are basically no different to windings in rotary machines; the only difference occurs at the longitudinal ends as explained before. The chosen winding arrangement is important as it influences the amplitude and waveform of the generated voltage and stator MMF. Details of different winding arrangements are given in classic texts such as [72], [73] and more recently developments are covered in [65], [74], [75], [76], [77]. A brief overview of the literature is given here.

Windings can be either overlapping or non-overlapping and either single or double-layer with varying numbers of slots and coils per pole and per phase. Examples of some windings are shown in Fig. 2.8 for slotted iron-cored stators. To understand how the choice of these parameters influence machine performance, consider a phase windings with a coil pitch equal to the pole pitch and with each of its coil sides concentrated in a single slot. The rms voltage E induced in this phase winding is given in classic texts [72], [73] as

$$E = \frac{2\pi}{\sqrt{2}} f N_{ph} \varphi_m, \tag{2.1}$$

where f is the electrical frequency, N_{ph} is the number of coil turns in series per phase and φ_m is the flux per pole linked by the phase winding. In practice, however, the coil sides of a winding may be distributed over several slots. The coils may also not be full-pitched, i.e. the coil pitch may be different to the pole pitch. The reason for doing this is to achieve a more sinusoidal induced voltage and MMF waveform and to decrease the end-winding length (and hence the losses). To determine the amplitude of the voltage induced in such practical windings, the vector sum of the voltages induced in all the coils must be calculated as shown in [72], [73]. This results in a

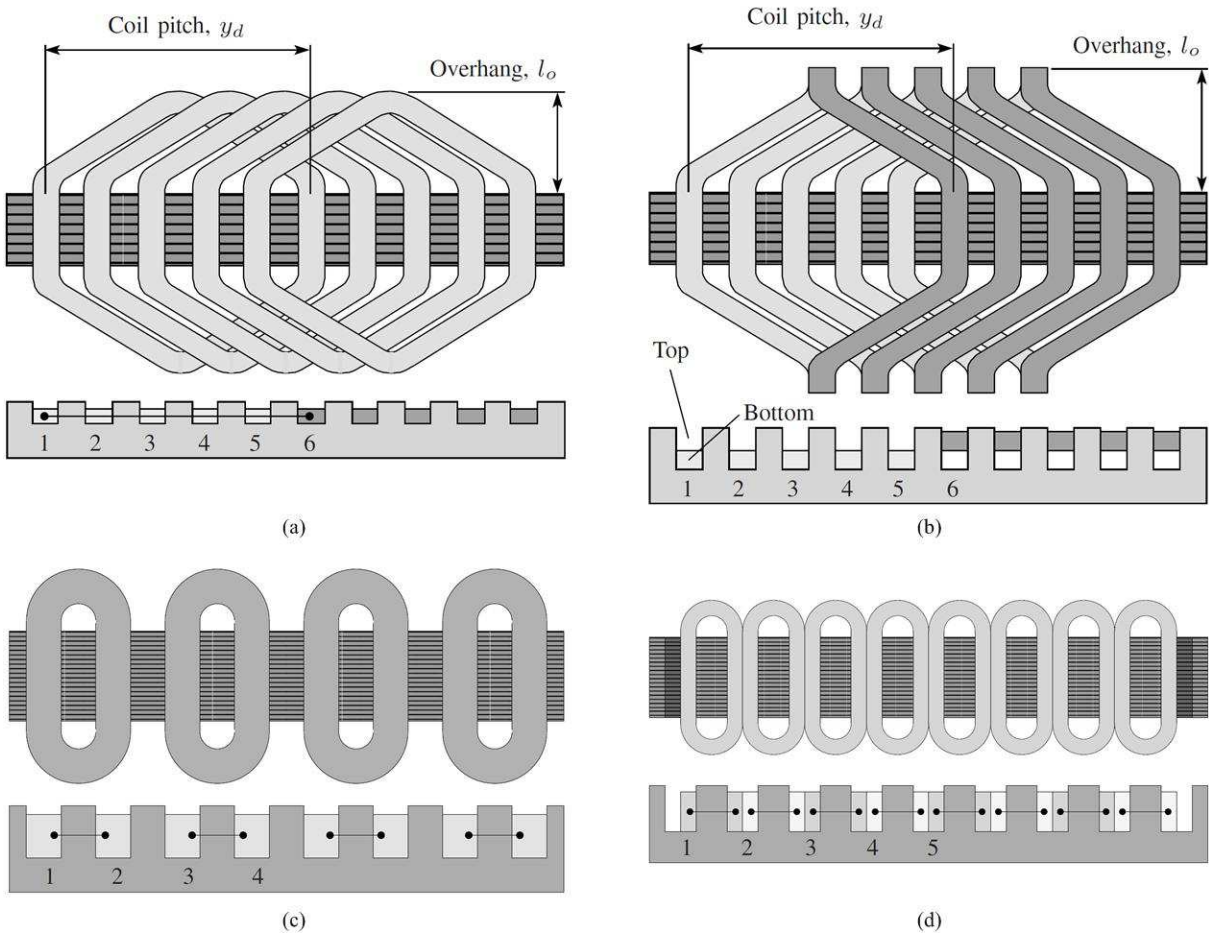

Fig. 2.8. Examples of the main types of windings, namely (a) single-layer overlapping windings, (b) double-layer overlapping windings, (c) single-layer non-overlapping windings and (d) double-layer non-overlapping windings. [77]

voltage amplitude which is less than that given in (2.1). This reduction in voltage is calculated as the winding factor k_w, such that

$$E = \frac{2\pi}{\sqrt{2}} k_w f N_{ph} \varphi_m \qquad (k_w \leq 1). \tag{2.2}$$

It is usually therefore strived to select a pole/slot and pole/coil combination which results in the highest possible winding factor subject to constraints on voltage waveform quality and losses. However, recent studies have pointed out that for air-cored windings, the winding factor alone does not determine the performance of the winding [65]. Since the flux is not concentrated in stator teeth as with iron-cored stators, the distribution of windings within a slot (imaginary "air-slot") also has a significant effect on the total stator flux linkage, and hence the induced voltage and stator MMF. It was shown in this study that the coil-side to coil-span ratio has a significant effect on the machine's thrust per copper losses, which is like the efficiency; and the best thrust per copper losses is not necessarily achieved at the best winding factor.

2.5 Rating linear generators

Rotary generators are usually designed to operate at a specific (constant) angular velocity ω_m. At this velocity the voltage amplitude E_p and frequency will also be constant and for a three-phase machine, the total instantane-

ous power $p_g(t)$ generated will be constant and equal to the average power P_g [78]. This voltage and power can be taken as the machine's rated values and can be expressed as

$$P_g = T_m \omega_m = \frac{3E_p I_p}{2} = 3EI\cos\varphi, \tag{2.3}$$

where T_m is the torque, I_p is the peak current, E and I are the rms phase voltage and current and $\cos\varphi$ is the power factor.

Linear generators are designed for reciprocating motion, and hence for continually changing velocity magnitude and direction. For direct drive wave energy applications, the translator velocity can be assumed to be sinusoidal as

$$v(t) = V_p \cos\omega t, \tag{2.4}$$

where V_p is the peak velocity. The LG developed force $f_g(t)$ is also sinusoidal with amplitude F_p and assumed to be in phase with the velocity. The instantaneous power can now be shown to be

$$p_g(t) = \frac{F_p V_p}{2}(1+\cos 2\omega t) = \frac{3E_p I_p}{4}(1+\cos 2\omega t), \tag{2.5}$$

as derived in Appendix F; the LG back-EMF and current is here assumed to be controlled to be in phase, such that $\cos\varphi$ from (2.3) is equal to unity. It is clear from (2.5) that the instantaneous power is not constant, but varying sinusoidally about an average value of

$$P_g = \frac{F_p V_p}{2} = \frac{3E_p I_p}{4}. \tag{2.6}$$

It is useful to design a LG for this constant average power P_g, with constant force F_g, velocity V, phase voltage E_g and phase current I, which are all rms values such that

$$P_g = F_g V = 3E_g I. \tag{2.7}$$

From (2.6) and (2.7),

$$F_g = \frac{F_p}{\sqrt{2}},\ V = \frac{V_p}{\sqrt{2}},\ E_g = \frac{E_p}{2} \text{ and } I = \frac{I_p}{2}. \tag{2.8}$$

In (2.5) to (2.8) it is assumed that the stator winding is active at all times, i.e. that the whole stator winding is within the PM generated field at all times.

2.6 Sizing linear generators

A method for sizing electrical machines based on the air gap tangential or shear force density (or shear stress) is often used for linear machines [32], [61], [79], [80] and is explained for rotary machines in detail by Miller [69]. The theory of Miller is here applied to linear machines.

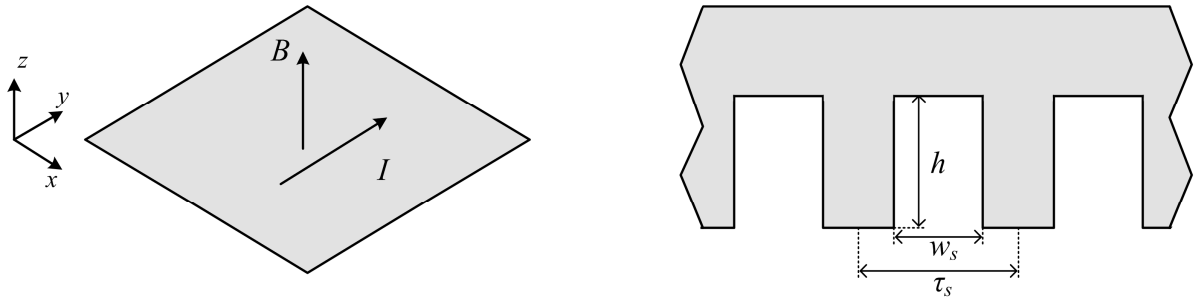

(a) (b)

Fig. 2.9 (a) A rectangular area in the air gap near a linear machine's stator winding. The current flows in the *y*-direction and the flux in the *z*-direction. (b) A section of an iron-cored stator showing the slot pitch τ_s, slot width w_s and slot depth *h*.

Consider a rectangular area in the air gap near the stator windings as in Fig 2.9(a). The normal flux density *B* is perpendicular to this surface, and the current *I* flows in the *y* direction. The electric loading *K* can now be defined as

$$K = \frac{I}{x} \ [\text{kA/m}]. \tag{2.9}$$

The shear force (LG developed force) F_g produced by the interaction of the flux and the current is

$$F_g = BIy = BKxy \ [\text{kN}], \tag{2.10}$$

and from this it follows that the shear stress σ_s (shear force per unit area) is

$$\sigma_s = BK \ [\text{kN/m}^2]. \tag{2.11}$$

For an actual electrical machine, *B* and *K* in (2.11) are rms values and *K* should also include the winding factor. The air gap flux density in electrical machines has an upper limit determined by the excitation MMF (i.e. the magnet dimensions), air gap length and saturation. The electrical loading is restricted by thermal limits, slot fill factor and stack length. From the allowable rms current density *J* and achievable slot fill factor k_f, the electrical loading can be given as

$$K = Jk_f h \frac{w_s}{\tau_s} k_w, \tag{2.12}$$

where, from Fig. 2.9(b), w_s is the slot width, τ_s is the slot pitch, *h* is the slot depth and k_w is the winding factor.

To illustrate how this helps in determining a machine's size, an example is used as follows: In order to generate 1 MW of power at an average wave velocity of 1 m/s, (2.7) shows that the necessary force is 1000 kN. Taking a peak air gap flux density of 1 T, current density of 5 A/mm^2, slot fill factor of 0.5, slot width/pitch ratio of 0.5, slot depth of 100 mm and winding factor of 0.95, the shear stress can be calculated from (2.11) and (2.12) as 84 kN/m^2. Dividing 1000 kN by this value reveals that a machine with an active air gap area of roughly 12 m^2 is needed to generate the required 1 MW. The theory of this section can therefore be used to quickly get an idea of the size of machine needed for a given rating. It also illustrates the effect the slow wave speed has on the size of LGs used in DD-WECs.

Table 2.2 State-of-the-art of LGs for DD-WECs.

LG	Flux	Shape	Sides	Core	Magnets	Rating
AWS	LF	Planar	Double	Iron	Surface mount	1 MW
Seabased	LF	Planar	Four	Iron	Surface mount	10 kW
Columbia PT.	LF	Tubular	Single	Iron	Surface mount	1 kW
VHM	LF	Planar	Double	Iron	Surface mount	-
Trident Energy	LF	Tubular	Single	Iron / Slotless	Embedded	30 kW
C-Gen	LF/TF	Planar	Double	Air	Surface mount	25 kW

2.7 State-of-the-art

The LGs which are most prominent in recent research are considered here. In Table II an overview of these LGs are given. In the following sections each of these are considered in more detail.

2.7.1 Archimedes wave swing

The design, modelling and testing of the original AWS are discussed in [40], [41], [49], [81], [82], [83], [84] and on overview of the working principle is given in Chapter 1. The intellectual property for the original AWS is protected by two patents as given in Appendix I. Interestingly, in these patents, the use of hydraulic cylinders and conventional generators are envisioned and the use of LGs is not considered. However, during the initial design it was established that this concept is not feasible and Polinder was approached to design a LG instead [84]. Details of the LG is hence not contained in any patents, but are published in the above cited references.

The LG used in the AWS is a 3 phase PM synchronous generator rated at 2 MW peak instantaneous power (1 MW average power) at a peak velocity of 2.2 m/s. It is double-sided with the two translator sides on the outside and stator on the inside as shown in Fig 2.10(a). The stator is 5 m high, has a stack length of 1 m and is iron-cored with 1 slot per pole per phase. It contains the single-layer, overlapping 3 phase winding designed for a maximum current density of 4 A/mm^2. The translator is 8 m high and hosts the surface mounted PMs which are

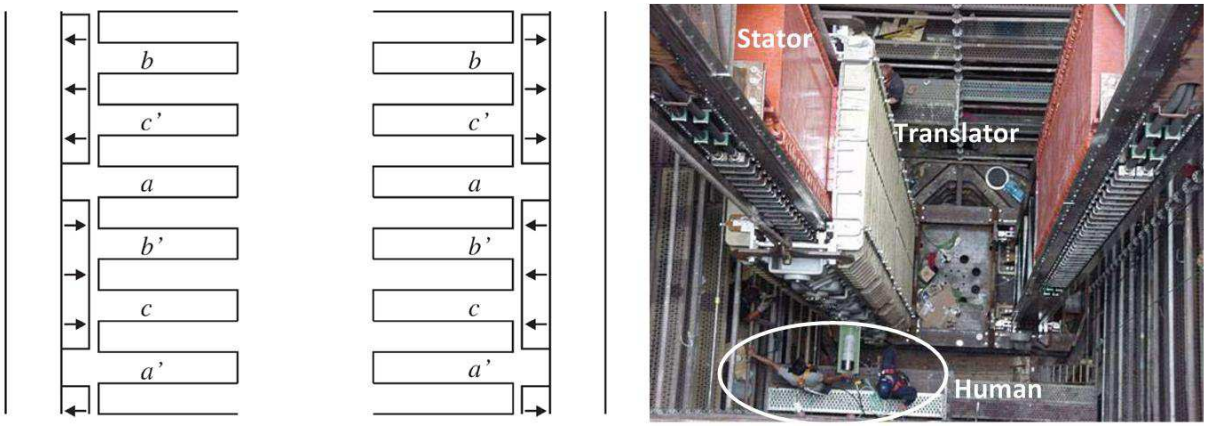

(a) (b)

Fig. 2.10 The double-sided LG of the AWS. (a) Schematic representation showing the surface mounted magnets, slots and winding arrangement [41]. (b) The inside of the actual AWS; the size of the LG compared to a human is apparent [61].

arranged for longitudinal flux. The LG has a rated stroke length of 7 m, but can be extended to 9 m. The massive size of this LG means the attraction forces between the PM translator and the iron stator is very high. In theory, the double-sided configuration serves to cancel the net attraction force. However, in practice, due to manufacturing tolerances, this only reduces the attraction force. In Fig. 2.10(b) a photo of the inside of the AWS shows the LG; its size in comparison to a human is apparent.

It should be mentioned that the current version of the AWS, the AWS-III, does not use a LG anymore; instead it has turned to a pneumatic PTO [82]. The reason for this is not stated, but it is easy to assume that the difficulty and expense of constructing such a large LG was too great.

2.7.2 Uppsala University / Seabased AB

A number of publications details the design of the LG used in the DD-WEC developed at Uppsala University [42], [51], [70], [83]. The technology is currently further developed and commercialised through a company named Seabased AB [84]. This LG is configured in a similar way to the one of the AWS, but only with four sides (two double-sided machines) and with the stator on the outside as shown in Fig. 2.11(a). The rating is also much less at 10 kW. Almost all aspects of the WEC, including the LG, PEC and the way it's envisioned to operate in a large, interconnected wave energy facility, are protected by at least 13 different international patents as given in Appendix I.

The stator is 1.3 m long, has a stack length of 0.4 m and is also iron-cored. It has 6/5 slots per pole per phase which reduces cogging forces compared to an integral winding like in the AWS. The three-phase winding configuration can be seen in Fig. 2.11(b). Standard PVC insulated cables with stranded conductors are used for the winding. Although this is unusual for machine winding, the insulated, stranded cable is easy to handle, flexible and relatively cheap which makes it ideal for winding a large machine. Furthermore, the PVC provides good in-

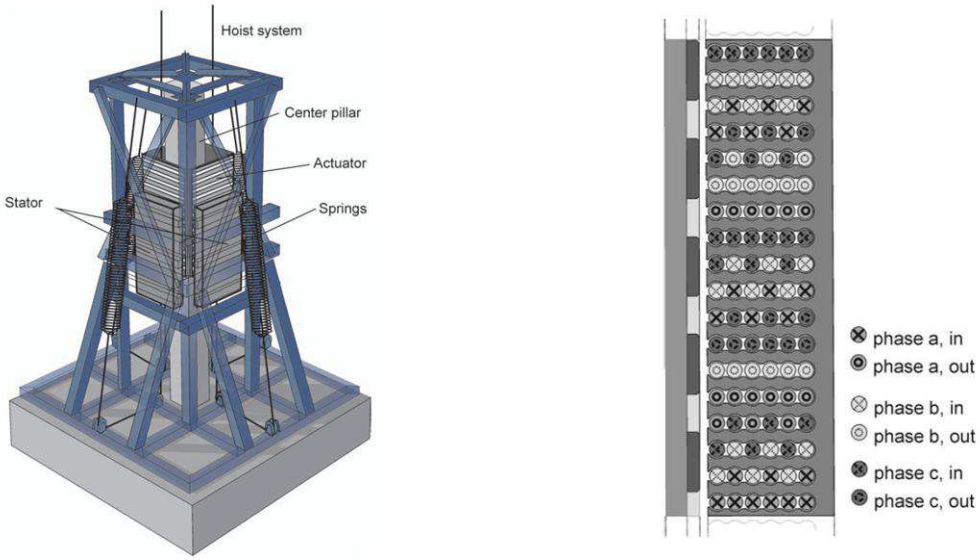

(a) (b)

Fig. 2.11 The four-sided LG of Seabased showing (a) 3D CAD model and (b) one winding segment detailing the winding arrangement [70].

sulation in the harsh marine environment.

The translator length is 1.8 m and the NdFeB PMs are surface mounted with aluminium spacers for accurate positioning of the PMs. The PMs are arranged for longitudinal flux and the attraction forces between the stator and translator are reduced by the double-sided configuration.

One of the more recent patents published by this research group (WO2011149398, Dec. 2011), shows a number of planar stator sections arranged along the inside wall of a cylindrical tube. It would hence seem like different configurations for the LG is still being considered.

2.7.3 Columbia Power Technologies

A DD-WEC developed at Oregon State University (OSU) is reported on in [43], [85]. This WEC is currently also further developed through a company named Columbia Power Technologies (CPT) [86]. The cylindrical shape of the WEC lends itself to the tubular shape of this generator, rated at 1 kW, as shown in Fig 2.12. As shown in Appendix I, two patents protect the design of this WEC, including the LG. Three more patents published since 2010 are applicable to a novel direct drive *rotary* WEC which will briefly be discussed later.

The iron-cored stator is 0.288 m high and has 1 slot per pole per phase with a single-layer 3 phase overlapping winding. Due to the tubular topology the end windings are almost completely eliminated. Shaping of the stator teeth is used to reduce cogging forces.

The translator is 1.152 m high with surface-mounted NdFeB PMs arranged for longitudinal flux and is also positioned with aluminium spacers. The tubular topology can also be seen as a double-sided planar machine with multiple pairs of opposing sides, like the latest development of the Seabased LG as discussed in the previous Section. In this case, the number of double-sided LGs is simply infinite, resulting in the tubular topology. The tubular topology therefore in theory also eliminates the attraction forces between stator and translator.

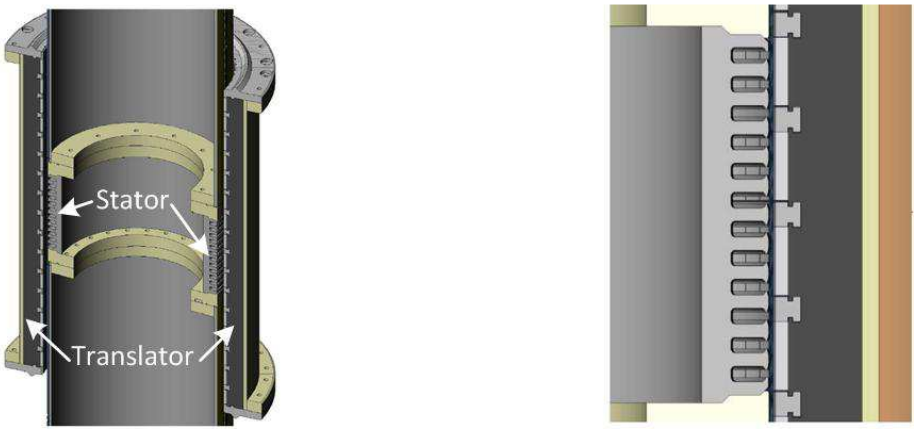

(a) (b)

Fig. 2.12 The tubular LG of Columbia Power Technology showing (a) section view a 3D CAD model and (b) a close-up of the PMs and stator slots [85].

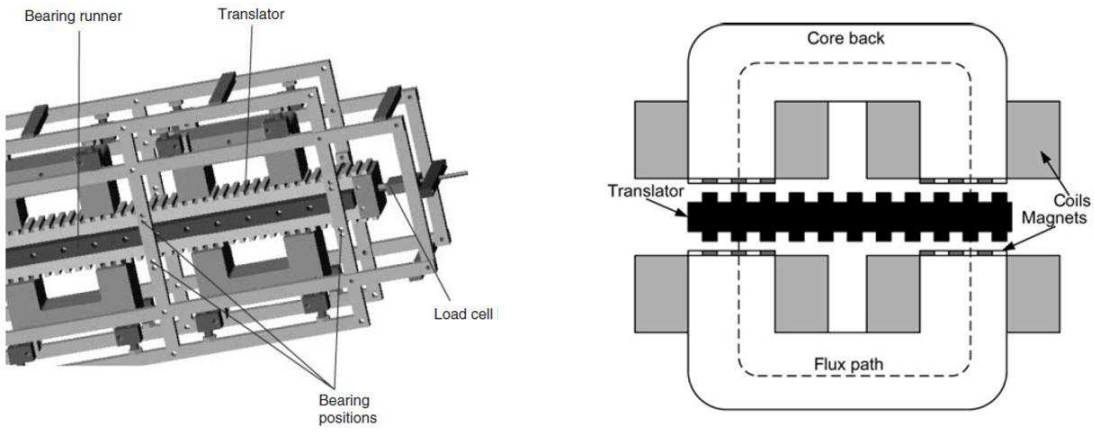

(a) (b)

Fig. 2.13 The Vernier Hybrid LG showing a (a) 3D CAD model and (b) detail of the magnetic circuit [52]

2.7.4 Vernier Hybrid Machine (VHM)

The VHM is a type of variable reluctance (VR) PM machine and is reported on in [52], [60], [90]. Research on VHMs for DD-WECs started at Durham University with the aim to find a high force density alternative to more conventional LGs. The basic topology of the LG is shown in Fig. 2.13. There are multiple magnets mounted side by side, with alternating polarisation, on a single *stator* pole face. The translator has a slot and tooth pitch of similar length to the magnet pole pitch. This enables the teeth to be alternately aligned with differently polarised magnets as it moves relative to the stator and so creates a rapidly changing flux in the stator iron. The C-core stator iron has coils wound around each of its two pole faces. These two coils are connected in series to form one phase. Two more of these modules are added and phase shifted to add the other two phases of the machine.

As with other machines from the VR family, this particular LG has a high power density, but also has a very high internal reactance. If the current is controlled in phase with the LG's EMF, a low power factor is therefore observed at the LG terminals, which means that the PEC must be overrating significantly. Furthermore, high attraction forces between the stator and translator is also present in this LG, as with all other iron-cored LGs.

2.7.5 Slotless and air-cored tubular LGs

An air-cored tubular LG is considered for DD-WECs by a group of universities in the UK [55], [56], [87], [88] and a similar LG is also used by a company named Trident Energy, also in the UK [44], [89]. The WEC concept of Trident Energy is protected by a number of international patents, as given in Appendix I.

The basic topology of these LGs is shown in Fig. 2.14. The translator is on the inside and has buried PMs arranged for longitudinal flux. The stator coils are on the outside and contain no iron. Due to this lack of iron in the stator, the flux density rapidly decreases away from the translator. The outside coil diameter (or else the coil-side thickness) is therefore limited. Trident Energy makes use of a magnetic shield around the outside to limit this decrease in flux density. This sleeve is in effect a stator yoke and makes the generator "slotless", rather than completely air-cored. The obvious advantage of both these LGs is the elimination, or at least the reduction, in attrac-

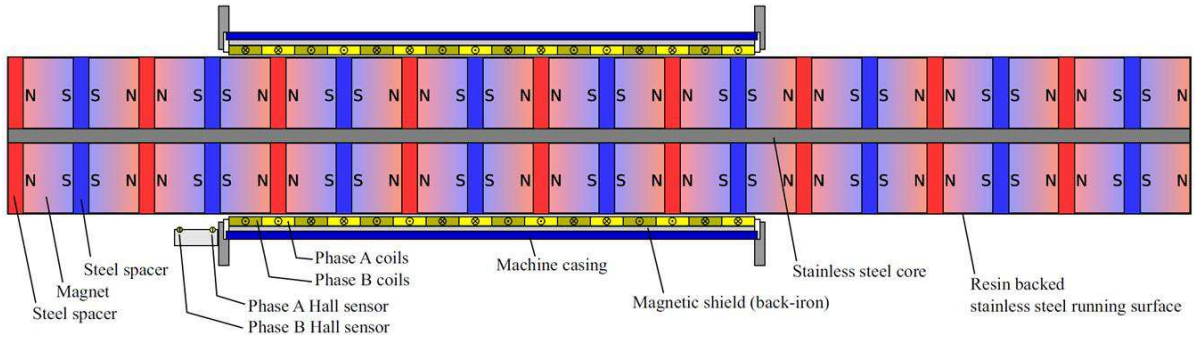

Fig. 2.14 The slotless tubular LG from Trident Energy [44].

tive forces between the stator and translator for the air-cored and slotless LGs respectively. The stator windings can also be individually machine wound, which further simplifies construction and assembly.

2.7.6 Double-sided air-cored machines

Another option for PM air-cored LGs is the double-sided translator topology shown in Fig. 2.15. This topology has widely been studied for radial and axial flux rotary machines in direct drive wind energy generators, e.g. [66], [94], [95], [96], which is also a low-speed application like DD-WECs. Both overlapping and non-overlapping stator windings can be used. Parker Hannifin Corporation currently manufactures linear double-sided air-cored motors with overlapping windings for use where low cogging forces and high precision linear positioning are paramount, e.g. certain industrial automation applications [94].

The C-Gen is a patented (see Appendix I) variation of this topology, developed at Edinburgh University and is reported on in [48], [80], [91]. The technology is being used for both rotary and linear machines and is commercially exploited through a company named NGenTec [92]. As shown in Fig. 2.16(a), a double-sided LG is separated into C-cored pole sections in order to force the flux in a transverse direction as shown in Fig. 2.16(b). Two of these C-cores are then placed head-to-head as shown in Fig. 2.16(c). This provides additional strength to the yokes and provides another flux path. The idea with this arrangement is to use the active steel of the machine as structural support as well and so reducing or eliminating the need for additional structural mass. By placing the C-core sections next to each other in the generator, the longitudinal path for the flux is again available. The multiple flux paths mean that the steel can be reduced further before the core starts to saturate.

In Fig. 2.16(d) a small scale prototype is shown. Overlapping air-cored windings can be seen. The separate pole

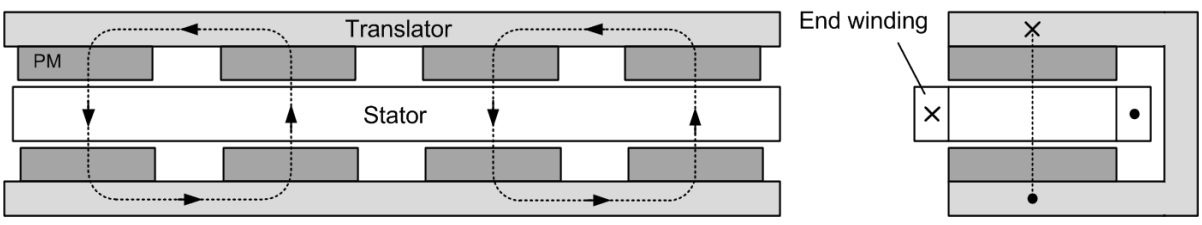

Fig. 2.15 Linear double-sided translator topology.

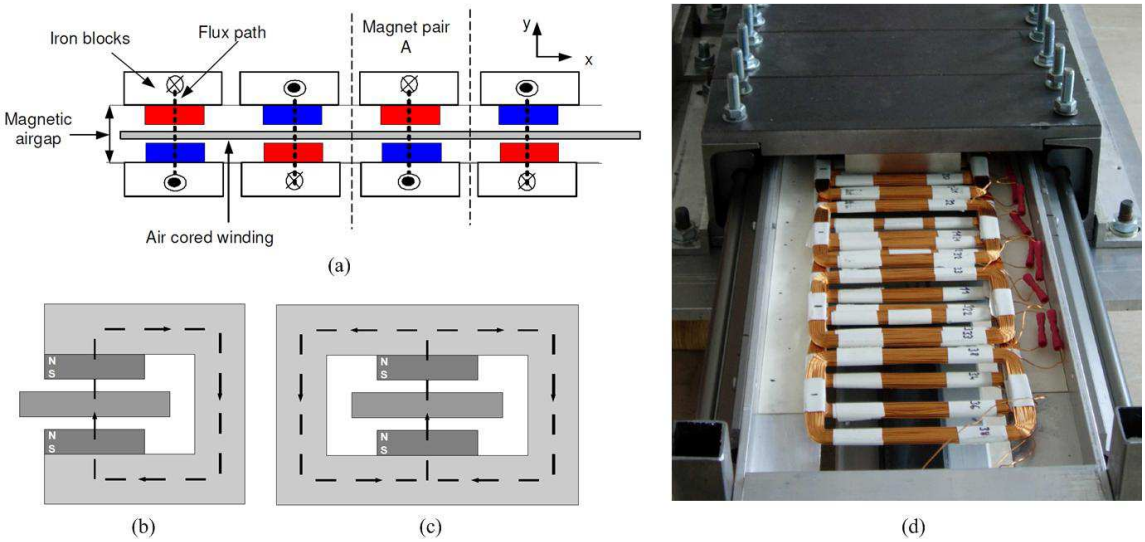

Fig. 2.16 The C-Gen air-cored linear generator developed at Edinburgh University [91].

section next to each other is also evident. More recently test results from a much larger 25 kW prototype were also published [48]. For this prototype, the stator consists of modular sections of non-overlapping windings encapsulated in epoxy. Elimination of attraction forces between the stator and translator and modularity of both the stator and translator are therefore other advantages of this LG.

2.7.7 Discussion

LFPM generators were some of the first types to be used for DD-WECs. The named problems with high attraction forces, the associated cost of the structural material and load on the bearings are however significant [61], [91], [93]; as mentioned before, the AWS have abandoned LGs in its subsequent prototypes in favour of a pneumatic PTO. Seabased and CPT have gone down much the same route by developing LFPM generators, however, their LGs are much smaller than that of the AWS and consequently it would seem easier to tolerate these issues. In a recent study done by the research group at OSU/CPT [98], it is concluded that LGs are good solutions only for low-power (<10 kW) WECs; in large-power (>10 kW) applications, air gap tolerances and linear guiding challenges for LGs become too difficult to solve in a cost-effective manner. For large power applications, CPT is looking at a novel direct drive *rotary* WEC [99], [100]. It is also interesting to note that Ocean Power Technologies [101], who develops the very advanced 150 kW PowerBuoy point absorber WEC, despite being in possession of a number of patents for LGs specifically for use in their WEC (listed in Appendix I), still rather makes use of a hydraulic PTO. It is clear that there are significant challenges with using LGs in WECs and the continued research into different LG topologies highlights the fact that alternative options are needed if DD-WECs are to be commercially viable. To solve the named issues, more attention is turning to air-cored LGs.

When considering only active material, iron-cored generators will always have a higher power density than air-cored machines and will use less PM material (which is still fairly expensive). However, when considering the saving in structural material and reduced bearing wear in air-cored LGs, they become very attractive options. Coupled with innovative, cost-saving construction methods, like pre-formed, machine-wound stators, air-cored LGs may compete very well with iron-cored LGs in terms of power density and cost (both capital and running

costs). The fact that companies like Trident Energy and NGenTec are built on air-cored (and slotless) technology, further supports the notions that air-cored LGs may indeed be the way to go for DD-WECs.

.

Chapter 3

Analysis of the novel linear generator

In this chapter the novel LG topology is developed and analysed. The stator and PM fields are analysed analytically with so-called Subdomain analysis by solving the relevant Laplace and Poisson equations for the magnetic vector potential. Finite element modelling is used to verify these calculations. A simplified analytical model and conditions for its use is also developed as a tool for conducting a comparative study and for the design of a prototype in the Chapter 4.

3.1 The novel LG topology

A novel generator topology was developed from the linear double-sided (LDS) permanent magnet air-cored topology shown in [65], [80], [94], [95] and in Fig. 2.15. An air-cored topology was chosen due to the elimination of the high attraction forces (which lead to high bearing loads and large amount of structural material), the ease of assembly and the option of using preformed non-overlapping windings. Also, with the double-sided translator topology the effective air gap is more clearly defined and much reduced compared to the single-sided translator [96]. Higher flux densities are now possible with the same amount of PM material compared to the single-sided translator. The effective air gap is however still much larger than for conventional small air gap iron-cored machines, and so fringing and leakage flux is still observed. Furthermore, the double-sided topology is already well-proven for rotary air-cored axial flux [63], [64], [97], [98] and radial flux machines [96], [99], [100] and is currently used in the C-Gen LG as discussed in Chapter 2.

The LDS topology is further developed by arranging a number of these double magnet translators in a tubular topology as in Fig. 3.1(a). The yokes are then removed as seen in Fig 3.1(b), and the magnets adjacent to each other on the same transverse plane are replaced with a single magnet as seen in Fig 3.1(c). The flux from any particular magnet now circulates around the machine in a transverse plane, instead of coupling with the adjacent poles in a longitudinal plane. The advantages of creating this arrangement are:

- The removal of the steel translator yokes, which is a source of losses and add to the structural mass.
- The flux paths of the machine are modified in such a way that the pair-wise flux coupling occurring in linear generators is eliminated.
- The resultant magnetic normal forces on any particular magnet will ideally sum to zero. In practice this would mean that a magnet must be located exactly halfway between its neighbouring magnets; this is of course not possible due to manufacturing tolerances. However, with a fair degree of manufacturing accuracy the resultant normal force on each magnet will still be close to zero, meaning that the structural mass needed to keep the magnet in place can be reduced dramatically.

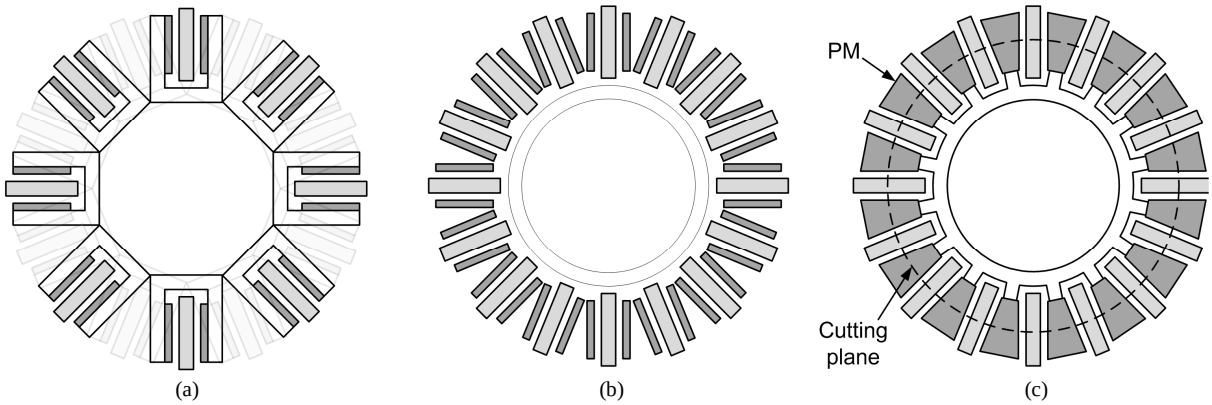

Fig. 3.1 Development of a novel linear generator topology from the LDS topology.

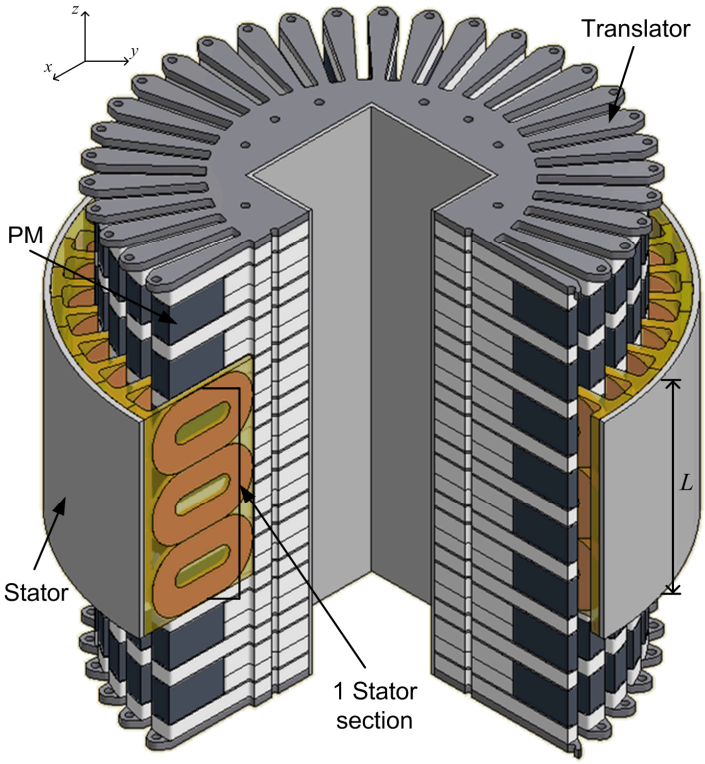

Fig. 3.2 Three dimensional cut-out view of the novel air-cored linear generator.

The stator now consists of a number of identical sections placed around the circumference of the machine as shown in Fig. 3.2. These will stay the same as for the LDS machine. In the next sections the modelling and analysis of the machine is considered, where after a comparative study is conducted to get a first idea of how the force density of the novel topology compares to other topologies.

3.2 Modelling

An air-cored machine can be represented with a classic per phase lumped parameter model as shown in Fig. 3.3 [63]. The voltage $\mathbf{E_g}$ represents the electromotive force (EMF) induced in the windings by the varying magnetic flux from the magnets, while R_s and L_s represents the phase resistance and synchronous inductance of the windings respectively. The phase resistance represents the main source of losses in the machine. In air-cored

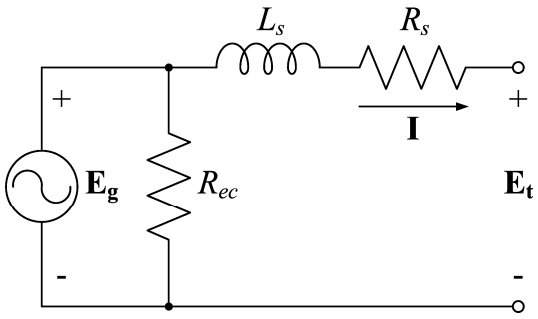

Fig. 3.3 Steady-state per phase equivalent circuit diagram of an air-cored synchronous generator.

machines the eddy-current losses in the copper conductors can also be significant, and can be represented by the shunt resistance R_{ec}. A more in-depth discussion of this equivalent circuit model, including the *dq*-equivalent circuits (in the synchronous rotating reference frame), is found in [63]. For the purposes of this thesis the equivalent circuit in Fig. 3.3 is sufficient.

It would be ideal if accurate analytical expressions for each of the parameters in Fig. 3.3 can be found in order to easily analyse the machine. Complicated geometry and non-linearity in machines however often requires the use of approximate expressions and/or numerical methods to calculate these parameters. The absence of iron in the novel topology fortunately eliminates almost all non-linear behaviour in this machine. And although the topology may look fairly complicated, it basically consists of a number of relatively simple LDS machines as discussed in the previous section. A simple 2-D model of an LDS machine is easily obtained for this machine by introducing a radial cutting plane at the average magnet thickness h_m as shown in Fig. 3.1(c). This radial plane is then rolled open into a planar 2-D model as shown in Fig. 3.4(a), as viewed from the side. This is similar to how a 2-D LDS model is developed for an axial flux rotary machine in [63]. It is hence anticipated that most of the machine parameters can be calculated fairly accurately with analytical methods already established for AF rotary and LDS machines. The rest of this chapter is devoted mostly to the discussion of these analytical expressions while a finite element package is used to verify the results. These two different methods of analysis are discussed next. Machine dimensions as used in the rest of the Chapter are shown in Fig. 3.4(a) and (b).

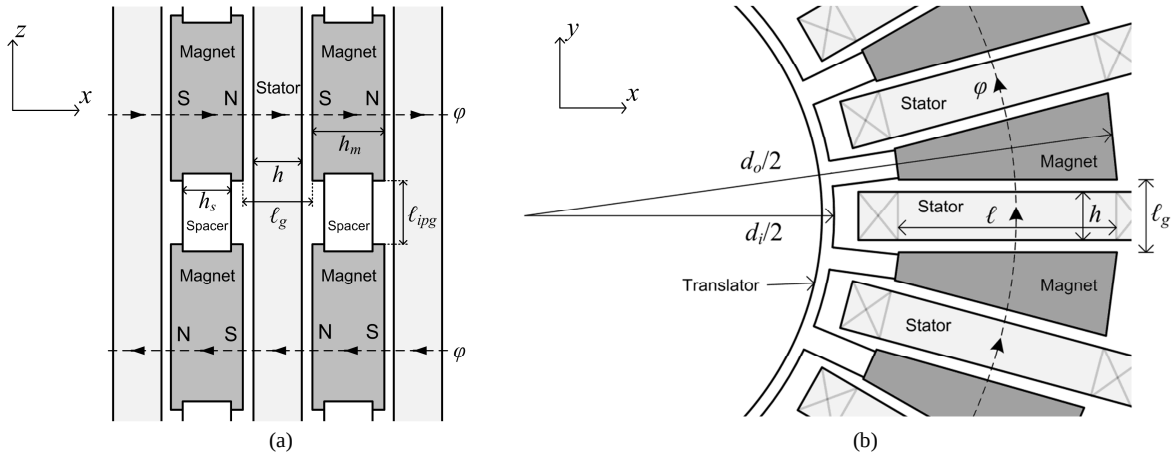

Fig. 3.4 (a) Two-dimensional model of the novel machine and (b) top view of the novel machine showing dimensions.

3.2.1 Analytical analysis

The phase resistance is easily calculated from the dimensions and resistivity of the windings as for instance done in [99]. All the other parameters require knowledge of the flux density in the air gap. Equations can be derived to calculate the eddy current resistance, back-EMF and inductance from the flux density.

Due to the large effective air gap in this machine, a higher degree of fringing and leakage flux occurs compared to iron-cored machines. Mueller mentions in [96] that increasing the air gap length will increase the winding height and as such increase the electric loading, but the air gap flux density will also significantly decrease. It is also mentioned that at some point after increasing the air gap the flux will also start to leak to neighbouring magnets rather than cross the air gap. This leads to different approaches in calculating the air gap flux density in air-cored machines.

The most straightforward way to calculate the flux density is to use a lumped parameter circuit model to represent the machine's magnetic circuit as done in [66], [80], [101]. The large effective air gap means that the magnet and air gap reluctances are dominant in the machine [101] and leakage flux can usually be ignored if machine dimensions are chosen correctly [66]. By assuming a constant reluctance for the air gap, a constant value for the air gap flux density is obtained and taken as the peak value of a trapezoidal air gap flux density distribution. Measurements generally agreed very well with this analytically approximation. Equations can then also be derived which uses the peak value of flux density to obtain the peak induced EMF [64], [65], [99], and the eddy current loss resistance [62], [66]. An accurate analytical expression for the inductance of air-cored windings is however difficult to find [63]. In [98] an analytical expression for the inductance of circular air-cored windings are derived by assuming a conical stator flux density distribution, while in [102], a simplified formula for the inductance of an AF air-cored machine is derived from the inductance formula of the Brooke's coil.

In order to find more accurate solutions to the air gap flux density and to gain a better understanding of the magnetic flux behaviour and phenomena like ripple force, subdomain analysis can be used. Subdomain analysis basically entails dividing the 2-D model into different regions, or domains, such that the magnetic vector potential in each region can be described by a single Poisson/Laplace equation; the magnetic vector potential can then be solved by applying the appropriate boundary conditions between the domains [111], [112]. With the above equations the flux density distributions, and consequently the induced back-EMF and winding inductances, can be calculated very accurately. Subdomain analysis is specifically used for air-cored LDS PM machines in [97], [98].

The subdomain model used for the analysis in this thesis is shown in Fig. 3.5. Region I consist of half of one row of PMs, Region II is the air gap region (including the stator) and Region III consist of half of the next row of PMs. There exists symmetry both about the centre of the stator and about the centre of the PMs (unlike a normal LDS topology) and hence the model could have been devised differently with a row of PMs in the middle and half of a stator section on either side. The configuration in Fig. 3.5 was however chosen to indicate the similarity to a conventional LDS topology. Analysis of region III is in fact not necessary because of the symmetry about the stator – the field solutions in Region III are simply the mirror image of the field solution in Region I. It is

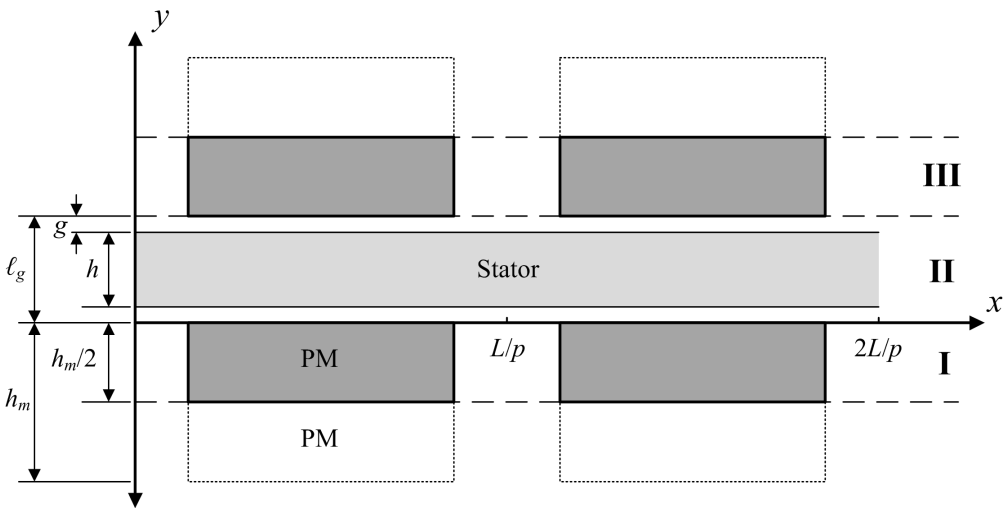

Fig. 3.5 Two-dimensional subdomain model dividing the LG into three regions.

only shown here again to correspond with the 2-D model of a LDS machine. The analysis will be discussed in more detail as the Chapter progresses.

3.2.2 Finite element analysis

As mentioned before, all the LG's circuit parameters can also be calculated with FEA. The process of FEA is explained in more detail in Appendix B. It basically entails meshing the machine model and approximating the magnetic vector potential in each element to obtain a piece-wise continuous approximation of the magnetic field in the machine. In this way complicated geometry can be analysed and by using iterative algorithms, non-linear behaviour can also be taken into account. The effect of the mesh can however introduce unacceptable inaccuracies when calculating force, especially for ripple force and unbalanced magnetic attraction forces [103]. By refining the mesh, the resulting approximation can be made more accurate, but at the expense of computation time.

Due to the above reasons, it is often still preferred to use analytical methods at the initial design stage and especially for optimisation purposes where possible. Analytical methods can also help to gain a better understanding of the fundamental physics in the machine [103]. FEA is then rather used as a verification and refinement tool and to help analyse more complicated phenomena in the machine. The same approach is used in this thesis. A commercial FEA package, Infolytica Magnet 7, is used to verify the 2-D Subdomain model. It is also further

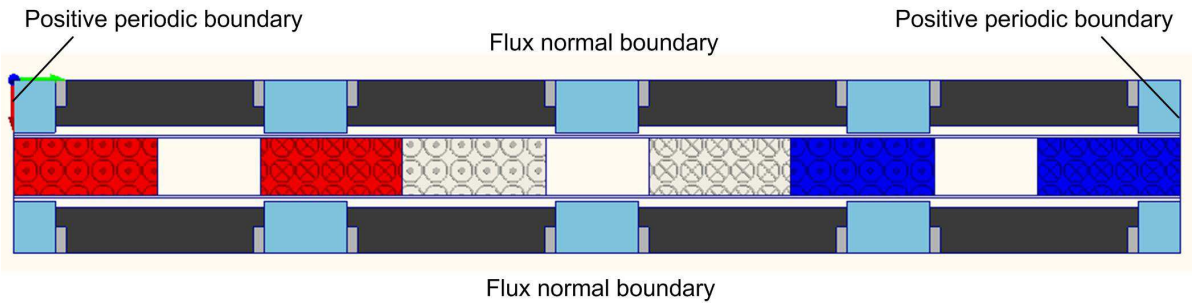

Fig. 3.6 Two-dimensional FEA model showing the different boundary conditions. The red, white and blue regions are the windings for the three phases.

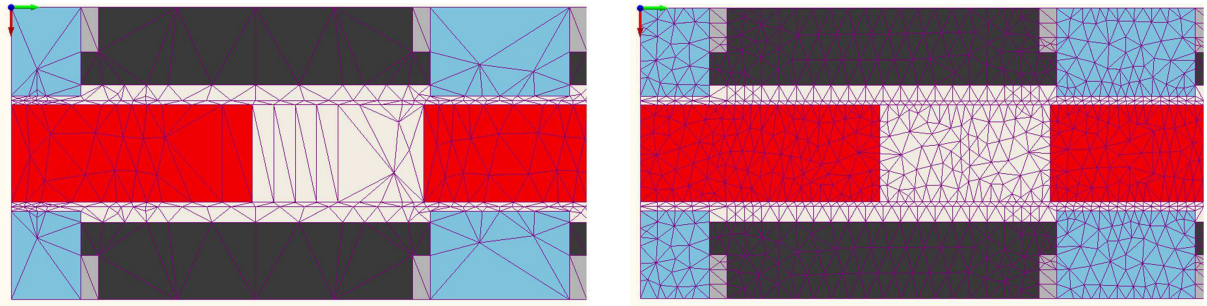

(a) (b)

Fig. 3.7 (a) Original automatically generated mesh and (b) refined mesh with smaller triangles for greater accuracy.

used to get an indication of the LG's output under sinusoidal translator displacement and to study the effects of varying stator-translator overlap.

The 2-D model as implemented in the FEA package is shown in Fig. 3.6. Due to the symmetry and repeated geometry in the machine, only this section needs to be analysed and it corresponds to the way the Subdomain model is devised in Fig 3.5. It includes one complete winding section (3 coils) and four pole pairs – this choice is explained in the next section. The light grey indentations on both sides of each PM in Fig. 3.6 are construction aids and are discussed in more detail in Chapter 4. These indentations are fairly small and are ignored in the analytical Subdomain model; this is a good example of a small geometrical intricacy which is rather analysed with FEA as it may overcomplicate the analytical model. To properly model the magnetic flux, appropriate boundary conditions should be applied to the model as explained in Appendix B. These boundary conditions are indicated in Fig. 3.6. A section of the model with the initial automatically generated mesh is shown in Fig. 3.7(a). This mesh was refined as shown in Fig. 3.7(b) to give more accurate results.

A typical flux density colour and contour plot is shown in Fig. 3.8 (a). To show the direction of the flux density

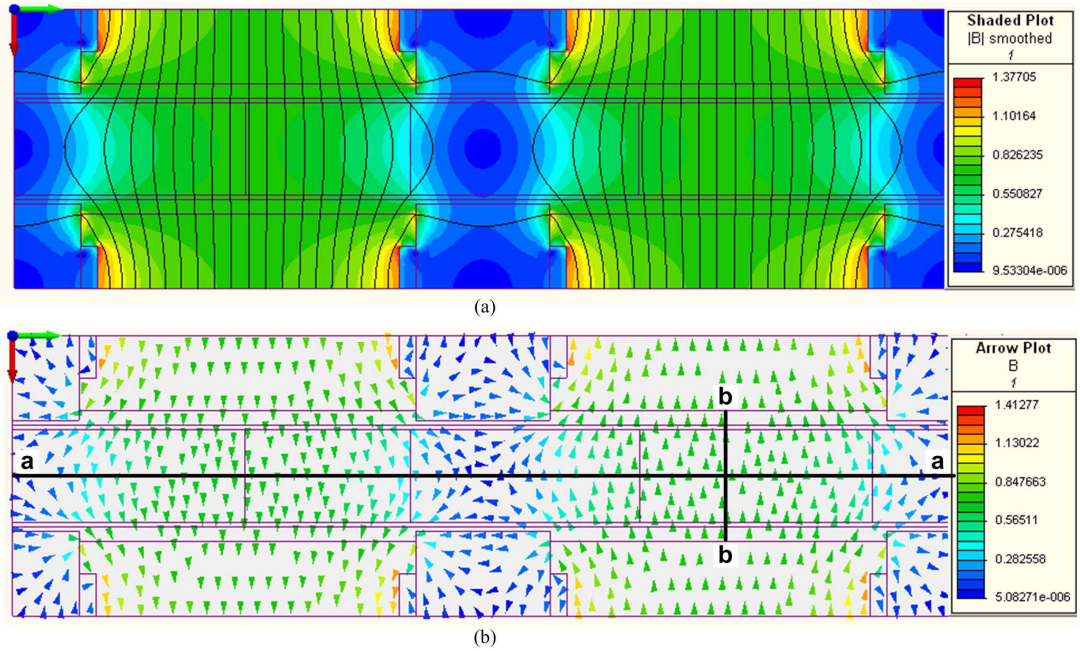

Fig. 3.8 (a) A typical flux density colour and flux contour plot and (b) arrow plot showing the flux direction.

vector, an arrow plot is also shown in Fig. 3.8(b). These results will be discussed in more detail as the Chapter progresses. It is important to note that the 2-D FEA model, the same as the 2-D analytical model, does not take any effects due to the end-windings into account.

3.3 Winding analysis

3.3.1 Winding layout selection

As discussed in Chapter 2, the air-cored stator windings can consist of overlapping or non-overlapping (NO) windings. NO windings (in literature also referred to as concentrated windings, fractional slot windings and also some other names [77]), as shown e.g. in Fig. 3.9, are especially attractive because of their ease of manufacture and short, flat end-windings [65], [74], [75]. The coils can be machine-wound and individually inserted into the stator. The shorter end-windings mean that less copper is used, which reduce costs and copper losses in the machine. In [65] it is shown that up to 50 % less copper is used for a NO air-cored winding compared to an overlapping winding. The fact that the end-winding is also flat (or the same thickness as the active part of the winding) means that the whole stator can easily be inserted and removed from the machine without dismantling the machine.

Studies in [74], [75] show that good winding factors can be obtained for NO-windings in high pole number radial flux machines. It has also been shown that the winding factor alone does not determine the performance of NO air-cored windings, but that the coil-side to coil-span ratio ($\kappa = \theta_r/\theta_c$ from Fig 3.9) also plays an important role [65], [76]; it is shown that a pole/coil combination of 4/3 with $\kappa = 0.37$, although resulting in a fundamental winding factor of only $k_{w1} = 0.875$, gives the optimal thrust per given copper losses, which is equivalent to efficiency for double-layer (DL) NO air-cored windings.

Considering the topology of the novel machine, it is clear that at the inside diameter it is essential to have an end-winding overhang as small as possible in order to fit the maximum number of stator sections into the machine. It is therefore decided to use a NO-winding. For NO-windings, DL windings also have smaller end windings compared to single-layer windings; a DLNO-winding, as shown in Fig. 3.9, is therefore selected. Only the analysis of DLNO will hence be considered in this thesis.

An in-depth analytical subdomain analysis of a double-sided RFPM rotary machine with non-overlapping air-cored windings has recently been done by Randewijk [104]; a similar approach is used here. A simplified equation is first derived for the flux linkage of the winding due to an idealised, sinusoidal PM field, similarly as derived for DLNO windings in [64], [65]. This allows for only a single, peak value of air gap flux density to be calculated from which the back-EMF can be determined, as discussed in Section 3.2.1. Equations for the conductor- and current density of the windings are derived thereafter; these equations are then used to solve the appropriate Poisson equations and hence to calculate the armature reaction fields and winding inductance.

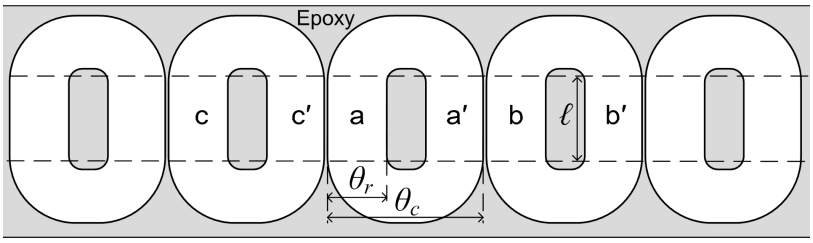

Fig. 3.9 Layout of double-layer non-overlapping air-cored stator windings.

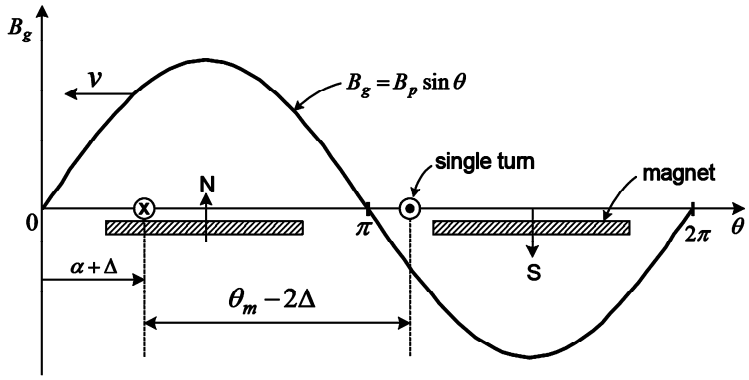

Fig. 3.10 A single coil turn in a sinusoidal field created by the alternating permanent magnets.

3.3.2 Flux linkage

The cross section of a single turn of a DLNO winding in the PM field is shown in Fig. 3.10. Since the coils are not wound around iron teeth, the distributed nature of the coil sides need to be taken into account; this means that the differences in flux linkage of each turn in the coil should be taken into account. To start with, a single turn is considered at position Δ in the coil side ($0 \le \Delta \le \theta_r$) and at position $\alpha + \Delta$ with respect to the flux density wave, as shown in Fig. 3.10. Its flux linkage can then be given as

$$\lambda_t = \int_0^{\ell} \int_{(\alpha+\Delta)}^{(\alpha+\theta_c-\Delta)} B_p \sin(\theta)\, dx dy. \tag{3.1}$$

Assuming that the flux density is uniform in the y direction and by substituting $dx = (L/p\pi)d\theta$ into (3.1), λ_t is given as

$$\lambda_t = \int_{(\alpha+\Delta)}^{(\alpha+\theta_c-\Delta)} B_p \sin(\theta)\, \ell \frac{L}{p\pi} d\theta. \tag{3.2}$$

Performing the integral and substituting $\alpha = \omega t$ gives

$$\lambda_t = \frac{2B_p \ell L}{p\pi} \sin(0.5\theta_c - \Delta).\sin(\omega t + 0.5\theta_c). \tag{3.3}$$

In order to find the total flux linkage of the coil with a continuous coil side layer of N conductors, (3.3) must be integrated with respect to Δ from 0 to θ_r. Only one factor in (3.3) contains the Δ-term and hence taking its average over the coil side width gives what is called the pitch factor as

$$\begin{aligned} k_p &= \frac{1}{\theta_r}\int_0^{\theta_r} \sin\left(0.5\theta_c - \Delta\right)d\Delta \\ &= \frac{\sin\left[0.5\theta_c\left(1-\kappa\right)\right]\sin\left(0.5\kappa\theta_c\right)}{0.5\kappa\theta_c} \end{aligned} \tag{3.4}$$

where $\kappa = \theta_r / \theta_c$ and $0 \leq \kappa \leq ½$. The total flux linkage of a coil is then given as

$$\lambda = \frac{2B_p \ell L N k_p}{p\pi}\sin\left(\omega t + 0.5\theta_c\right). \tag{3.5}$$

For a total of q coils per phase, with a parallel circuits, the induced phase voltage can now be calculated according to (B.6) and (B.7) as

$$\begin{aligned} e_g &= \frac{d\lambda}{dt} \\ &= E_p \cos\left(\omega t + 0.5\theta_m\right). \end{aligned} \tag{3.6}$$

where

$$E_p = \frac{2\omega q B_p \ell L N k_p}{p\pi a}. \tag{3.7}$$

It may be that a number of coils are arranged next to each other in a coil group. In this case, the flux linkage of these coils will not be the same; there will be a small difference in amplitude and phase between the coils due to their differing displacements relative to the flux density wave. The total flux linkage for the coil group will be the vector sum of the flux linkages for the individual coils. From this the so-called distribution factor can be calculated as [72], [73]

$$k_d = \frac{\sin\left[0.5n\left(\theta_c - \pi\right)\right]}{n\sin\left[0.5\left(\theta_c - \pi\right)\right]}, \tag{3.8}$$

where n is the number of side-by-side coils in the coil group. This term can now be included in (3.7) to give

$$E_p = \frac{2\omega q B_p \ell L N k_p k_d}{p\pi a}. \tag{3.9}$$

For the chosen winding arrangement $n = 1$ and hence $k_d = 1$.

3.3.3 Conductor density distribution

The conductor density is used to calculate the winding flux linkage due to the armature reaction directly from the magnetic vector potential in Section 3.3.6. The conductor density in the coil side can be calculated as

$$|n_a| = \frac{NQ}{\kappa L}. \tag{3.10}$$

It can be shown graphically for one phase as shown in Fig. 3.11; positive conductor density is defined as current coming out of the page and negative conductor density is defined as current going into the page. In order for this distribution to be useful it is necessary to find a mathematical expression to describe it. Due to its periodic nature it can be expressed as a Fourier series expansion. This Fourier series expansion of the current distribution as shown in Fig. 3.11 can be expressed as

$$n_a = |n_a| \sum_{m=1}^{\infty} b_{m_n} \sin\left(\frac{m\pi x}{\omega_s}\right), \tag{3.11}$$

where

$$b_{m_n} = \left(\frac{4}{m\pi}\right) \sin\left(\frac{m\pi(1-\kappa)}{3}\right) \sin\left(\frac{m\pi\kappa}{3}\right). \tag{3.12}$$

The derivation of (3.11) and (3.12) are given in Appendix C. The conductor density distribution of the other two phases are of course exactly the same, but shifted by ±2π/3 radians.

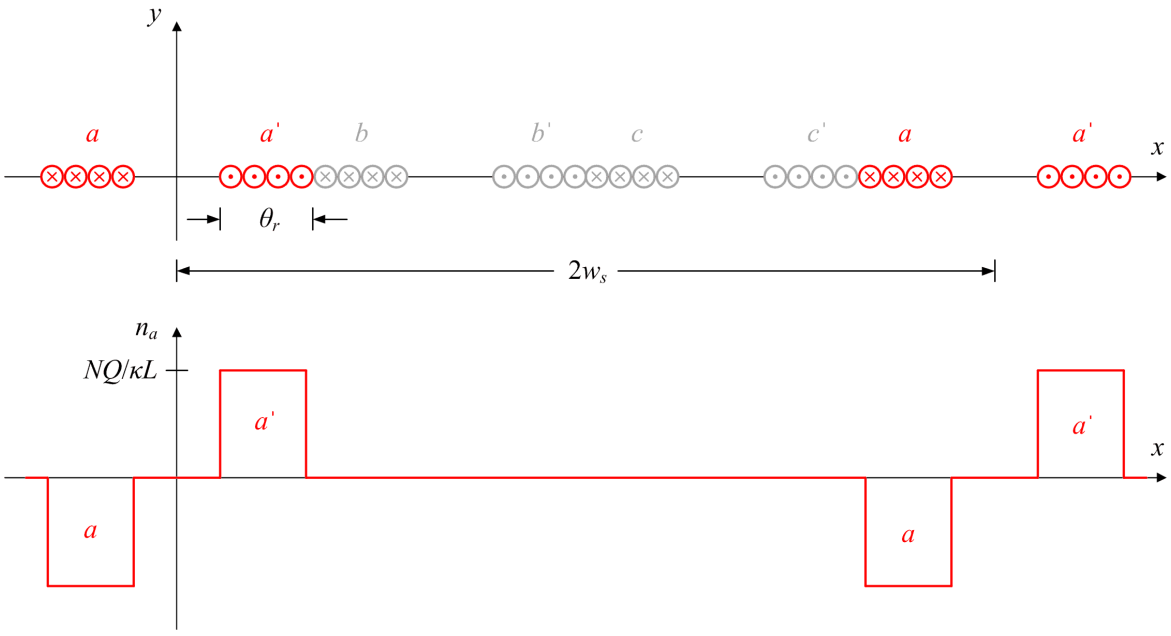

Fig. 3.11 Graphical representation of the conductor density distribution.

3.3.4 Current density distribution

The three-phase current density distribution is required to calculate the magnetic vector potential and the flux density due to the armature reaction fields (as done in Section 3.3.5). Similar to the conductor density, the current density distribution in the coil side can be calculated as

$$J_{za}(t) = \frac{i_a(t)Q}{\kappa g L}. \tag{3.13}$$

for the *a*-phase. This current density distribution can be shown graphically as shown in Fig. 3.12 and consequently its Fourier series expansion is then also given as

$$J_{za}(x) = J_{za}(t)\sum_{m=1}^{\infty} b_{m_n} \sin\left(\frac{m\pi x}{\omega_s}\right), \tag{3.14}$$

In the same way as the conductor density distribution, the current density distribution for the other two phases is displaced in space by ±2π/3 radians. The magnitudes will however be time dependent according to the current flowing in each phase. The current density distribution for the other two phases is hence given as

$$J_{zb}(x) = J_{zb}(t)\sum_{m=1}^{\infty} b_{m_n} \sin\left(\frac{m\pi\left(x - {}^{L}\!/_{Q}\right)}{\omega_s}\right), \tag{3.15}$$

$$J_{zc}(x) = J_{zc}(t)\sum_{m=1}^{\infty} b_{m_n} \sin\left(\frac{m\pi\left(x + {}^{L}\!/_{Q}\right)}{\omega_s}\right), \tag{3.16}$$

where the three-phase currents are assumed to be balanced such that their vector sum is zero. The current distribution at the instant where i_a = -2i_b = -2i_c is shown in Fig. 3.12. The total stator current density distribution is

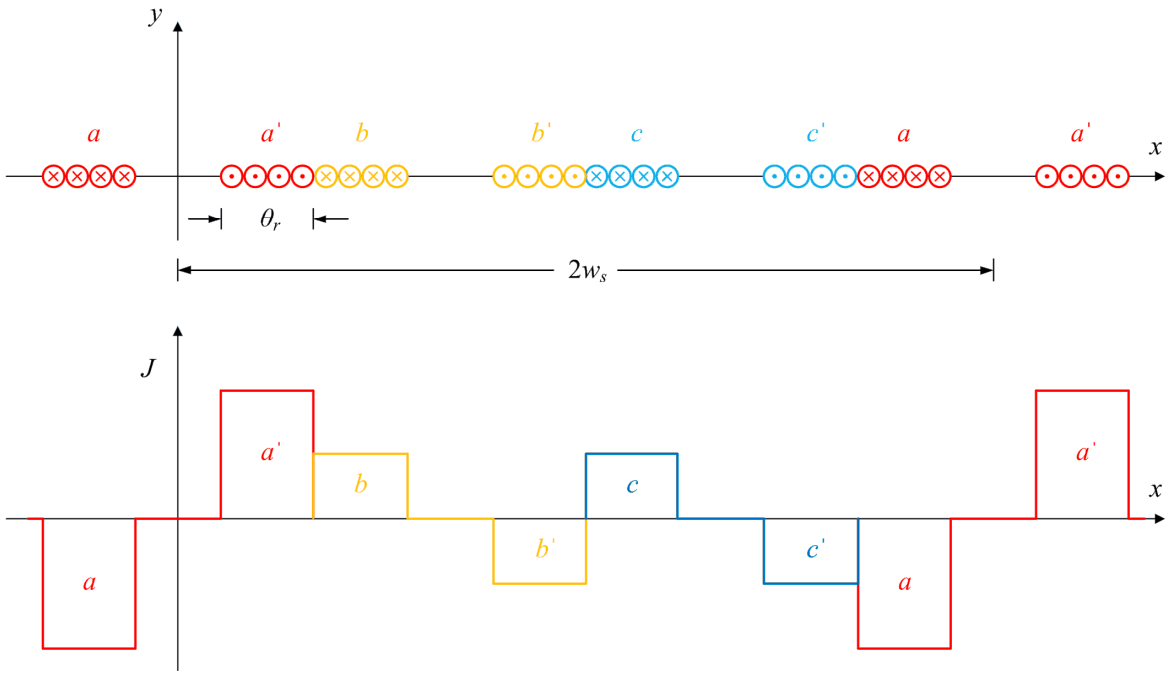

Fig. 3.12 Graphical representation of the current density distribution.

given as the sum of (3.14), (3.15) and (3.16) as

$$J_z = J_{za} + J_{zb} + J_{zc}. \tag{3.17}$$

3.3.5 Field solution

In order to calculate the magnetic fields due to the stator excitation, the Poisson equation (B.26) derived in Appendix B must be solved for each of the regions in of the Subdomain model shown in Fig. 3.5. By "switching off" the PM fields and only considering the stator excitation, (B.26) can be simplified to

$$\nabla^2 A_{zI} = 0 \tag{3.18}$$

in regions **I** and **III** (PM regions) and

$$\nabla^2 A_{zII} = \mu_0 J_z \tag{3.19}$$

in region **II** (air gap region).

The solutions to A_z in (3.18) and (3.19) are derived in Appendix D and are respectively given as

$$A_{zI} = \sum_{m=1,2,3}^{\infty} \left(C_{S3} e^{\frac{m\pi y}{\omega_s}} + C_{S4} e^{\frac{-m\pi y}{\omega_s}} \right) \sin\left(\frac{m\pi x}{\omega_s} \right) \tag{3.20}$$

and

$$A_{zII} = \sum_{m=1,2,3}^{\infty} \left[C_{S1} e^{\frac{m\pi y}{\omega_s}} + C_{S2} e^{\frac{-m\pi y}{\omega_s}} + \frac{\mu_0 \omega_s^{\,2} J_a(t)}{m^2 \pi^2} b_{m_n} \right] \sin\left(\frac{m\pi x}{\omega_s} \right). \tag{3.21}$$

where $C_1 - C_4$ are constants. By applying appropriate boundary conditions as explained in Appendix D, expressions for these constants can be derived as also given in Appendix D. The flux density in region II (the stator region) is then calculated by substituting (3.21) into (B.27) and (B.28); the results are given as

$$B_{xII} = \sum_{m=1,2,3}^{\infty} \left(\frac{m\pi}{\omega_s} \right) \left[C_{S1} e^{\frac{m\pi y}{\omega_s}} - C_{S2} e^{\frac{-m\pi y}{\omega_s}} \right] \sin\left(\frac{m\pi x}{\omega_s} \right). \tag{3.22}$$

and

$$B_{yII} = -\sum_{m=1,2,3}^{\infty} \left(\frac{m\pi}{\omega_s} \right) \left[C_{S1} e^{\frac{m\pi y}{\omega_s}} + C_{S2} e^{\frac{-m\pi y}{\omega_s}} + \frac{\mu_0 \omega_s^{\,2} J_a(t)}{m^2 \pi^2} b_{m_n} \right] \cos\left(\frac{m\pi x}{\omega_s} \right). \tag{3.23}$$

In Fig. 3.13 the analytical solution of (3.23) at $y = 0.5\ell_g$ (in the middle of the stator) is shown together with a FE solution of the same model. In Fig. 3.13(a) only the *b*-phase is excited, whereas in Fig. 3.13(b) all three phases are excited such that $i_b = -2i_a = -2i_c$. It is clear that the analytical and FE solutions are almost identical and hence verifies the accuracy of the analytical equations.

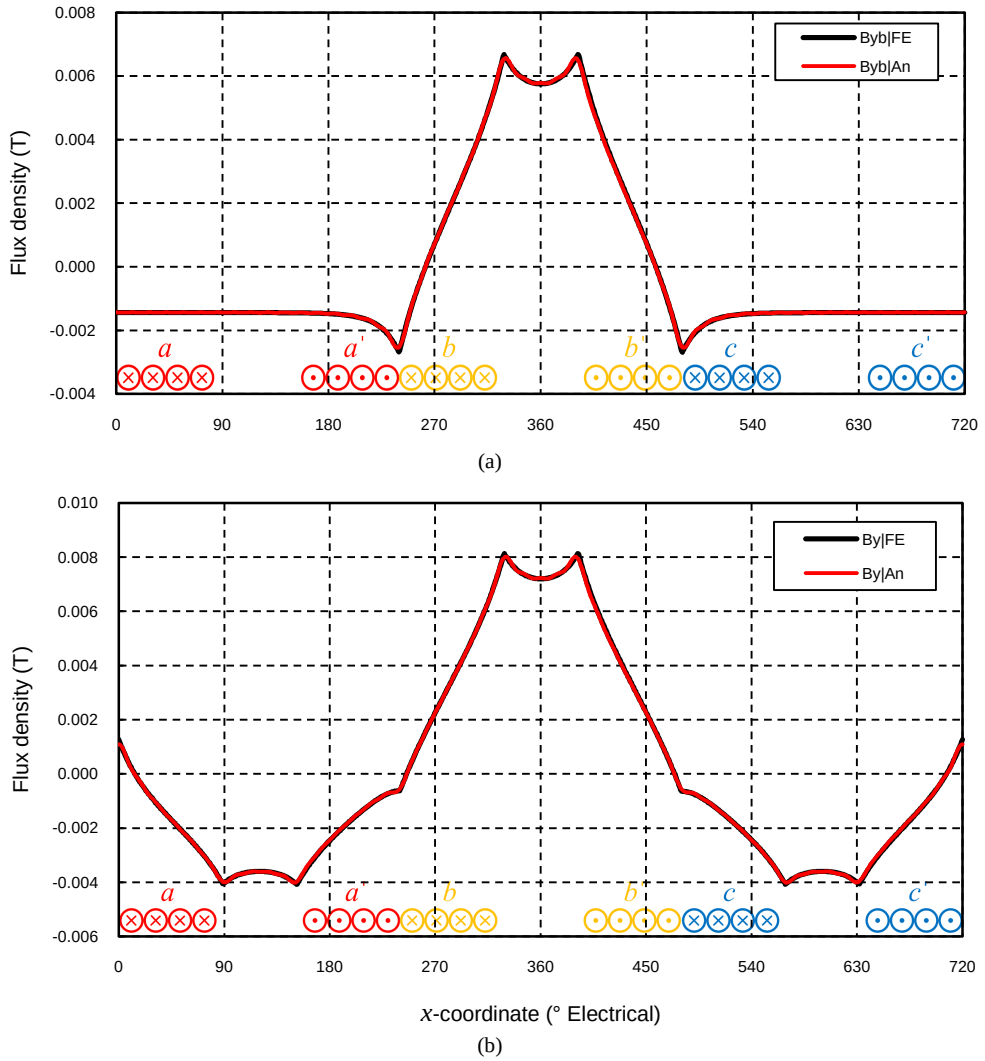

Fig. 3.13 Air gap flux density due to the stator current at $y = 0.5\ell_g$ (in the middle of the stator) as calculated analytically (red line) and with FEA (black line) with (a) only the *b*-phase energised and (b) all three phases energised such that $i_b = -2i_a = -2i_c$.

3.3.6 Inductance calculation

The flux linkages of a three-phase winding can be given in terms of the stator currents and inductances as

$$\begin{bmatrix} \lambda_a \\ \lambda_b \\ \lambda_c \end{bmatrix} = \begin{bmatrix} L_{aa} & L_{ab} & L_{ac} \\ L_{ba} & L_{bb} & L_{bc} \\ L_{ca} & L_{cb} & L_{cc} \end{bmatrix} \begin{bmatrix} i_a \\ i_b \\ i_c \end{bmatrix} \tag{3.24}$$

The self inductances, represented by L_{aa}, L_{bb} and L_{cc} in (3.24), is the ratio of the flux linkage per phase to the current in that same phase with zero current in all the other phases. All the other mutual inductances can be defined as the ratio of the flux linkage in one phase to the current in a different phase and when only that phase is energised. The inductance in the equivalent circuit of Fig. 3.3 is the synchronous inductance, defined as the ratio of the flux linkage per phase to the current in that same phase with all the other phases also conducting.

The flux linkage equation derived in Section 3.3.2 is based on a sinusoidal flux density distribution. As seen from Section 3.3.5, the flux density distribution due to the stator currents is not sinusoidal, and hence the same equation cannot be used. An alternative approach is to calculate the flux linkage of a coil directly from the vector potential of (3.21) as discussed in detail in Appendix E.

The flux linkage of one coil due to the vector potential generated by the current of that same coil only, is derived as

$$\lambda_{aa} = 2\omega_s \ell \sum_{m=1,2,3}^{\infty} b_{m_n} b_{mA_{zII}} \tag{3.25}$$

This is then simply divided by the current to give the self-inductance. The same approach is followed for the synchronous inductance; the vector potential due to all three phases is considered and gives the peak total flux linkage per phase as

$$\Lambda_{as} = 2\omega_s \ell \sum_{m=1,2,3}^{\infty} b_{m_n} b_{mA_{zII}} \left[1 - \cos\left(\frac{2\pi m}{3}\right)\right] \tag{3.26}$$

The synchronous inductance is then simply found as

$$L_{sa} = \frac{q\Lambda}{|i_a(t)|} \tag{3.27}$$

The analytical equation was again verified with the FEA model. The results of the analytical and FEA calculations are both shown in Table 3.1 and it is again clear that there is excellent agreement between the two. In the derivation in Appendix E, it is assumed that the entire winding is concentrated at $y = 0.5\ell_g$ in order to simplify the calculations. It is important to note that, since the stator windings are in reality spread over the total stator thickness and that the flux varies in the *y*-direction, a difference in the FEA and analytical solutions are expected. As the stator thickness increase, this difference in solutions can be expected to become more appreciable. For a conventional iron-cored machine with overlapping windings it can be shown that $L_{sa} = 1.5L_{aa}$ [72]. It is interesting to note that for the air-cored LG with DLNO windings, $L_{sa} = 1.33L_{aa}$.

It must of course also be noted that both the analytical and FE solutions are for a 2-D model and hence neither take the end winding inductance into account.

Table 3.1 Comparison between FEA and analytical solutions of the winding inductances.

	FE analysis	**Analytical analysis**	**Error (%)**
Self inductance (mH)	4.58	4.66	1.7
Synchronous inductance (mH)	6.10	6.17	1.1

3.4 Permanent magnet field

In order to calculate the induced voltage or EMF, and subsequently also the force, the PM-generated magnetic field must first be calculated. For simplicity of analysis and also for the eventual manufacturing process, only rectangular magnets (as seen in Fig. 3.5) are considered here.

3.4.1 Field solution

In order to calculate the magnetic fields due to the PM excitation, the Poisson equation (B.26) derived in Appendix B must be solved for each of the regions in of the Subdomain model shown in Fig. 3.5, similarly as was done for the stator winding excitation in Section 3.3.5. By "switching off" the stator currents and only considering the PM excitation, (B.26) can be simplified as

$$\nabla^2 A_{zI} = -\mu_0 \frac{\partial M_{ry}}{\partial x} \tag{3.28}$$

in regions **I** and **III** (PM regions) and

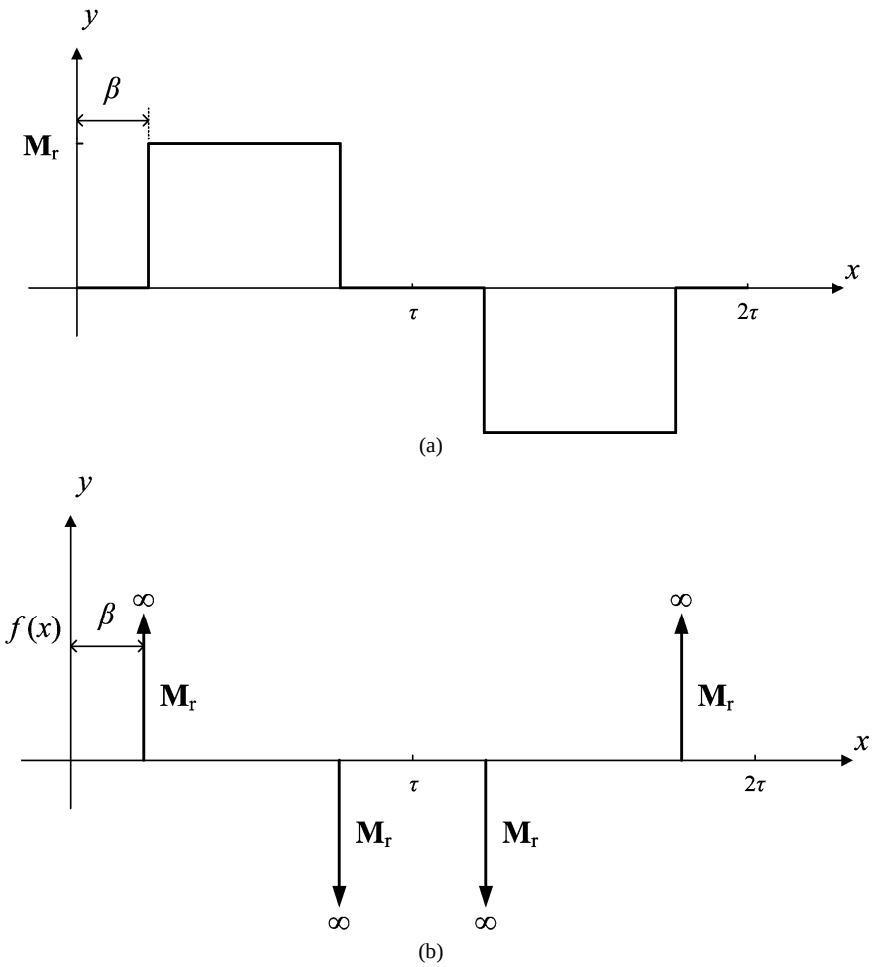

Fig. 3.14 (a) Distribution of the PM residual magnetisation and (b) the derivative of (a) with respect to *x*.

$$\nabla^2 A_{zII} = 0 \tag{3.29}$$

in regions **II** (stator region).

The magnetisation distribution in regions I and III can graphically be shown as in Fig. 3.14(a). From Fig. 3.14(a) it is easy to see that the derivative of M_{ry} with respect to x (as required in (3.28)) can be shown as in Fig. 3.14(b). The Fourier series expansion of this derivative, as derived in Appendix C, is given as

$$\frac{\partial M_{ry}}{\partial x} = \sum_{m=1,2,3}^{\infty} a_{m_M} \cos\left(\frac{m\pi x}{\tau}\right), \tag{3.30}$$

where

$$a_{m_M} = \left(\frac{4M_r}{\tau}\right)\cos(m\beta) \tag{3.31}$$

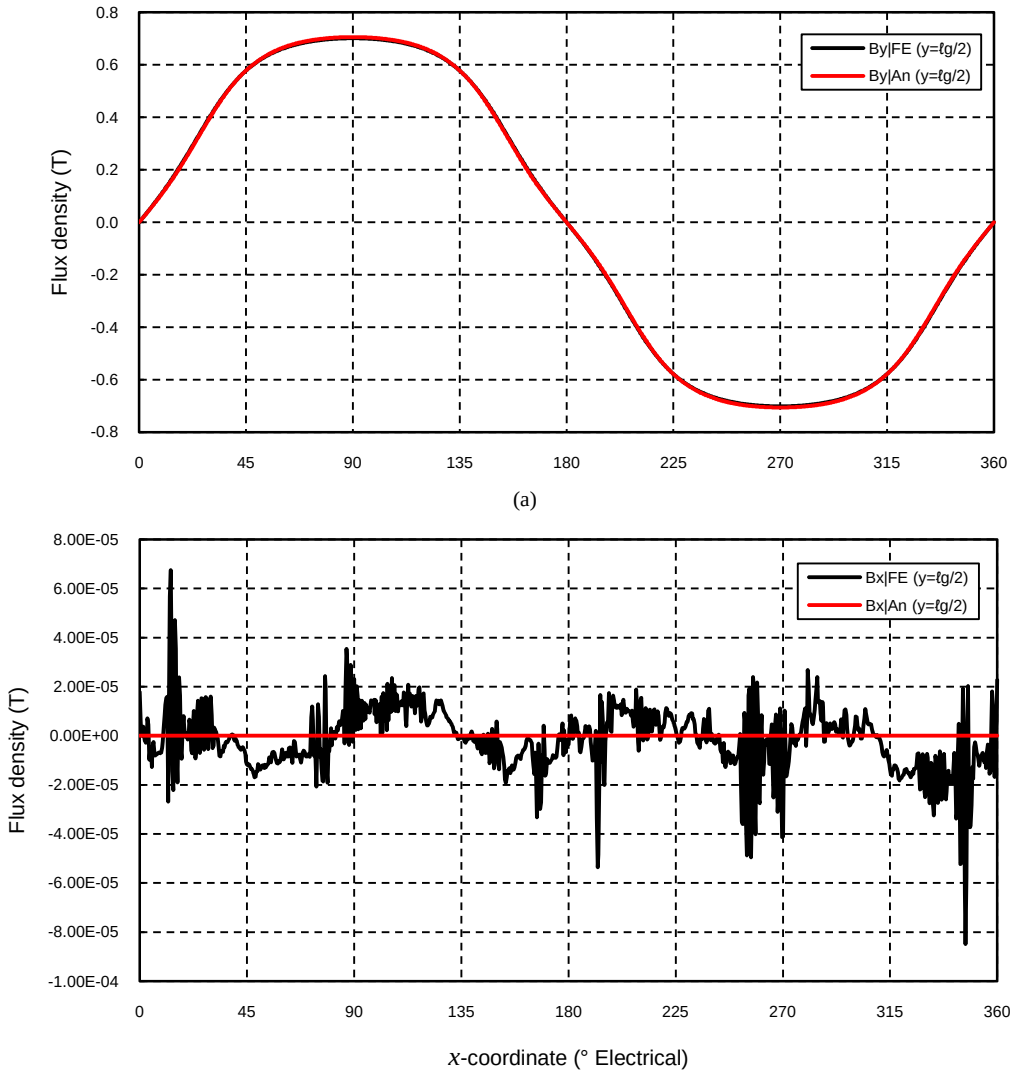

Fig. 3.15 Air gap flux density due to the permanent magnets at $y = 0.5\ell_g$ (in the middle of the stator) as calculated analytically (red line) and with FEA (black line): (a) the component across / normal to the air gap and (b) the component tangential to the air gap.

and

$$\beta = \frac{L}{p}\left(\frac{1-\tau_m}{2}\right). \tag{3.32}$$

and where τ_m is the per unit magnet width defined as $\tau_m = \theta_m/\theta_p$. Solutions for A_z in regions I and II is chosen as (as explained in Appendix D)

$$A_{zI} = \sum_{m=1,2,3}^{\infty}\left[C_{M1}e^{\frac{m\pi y}{\tau}} + C_{M2}e^{\frac{-m\pi y}{\tau}} + \frac{4B_r\tau}{m^2\pi^2}\sin\left(\frac{m\pi\tau_m}{2}\right)\right]\sin\left(\frac{m\pi x}{\tau}\right) \tag{3.33}$$

$$A_{zII} = \sum_{m=1,2,3}^{\infty}\left(C_3e^{\frac{m\pi y}{\tau}} + C_4e^{\frac{-m\pi y}{\tau}}\right)\sin\left(\frac{m\pi x}{\tau}\right) \tag{3.34}$$

By applying appropriate boundary conditions as explained in Appendix D, expressions for the constant terms can

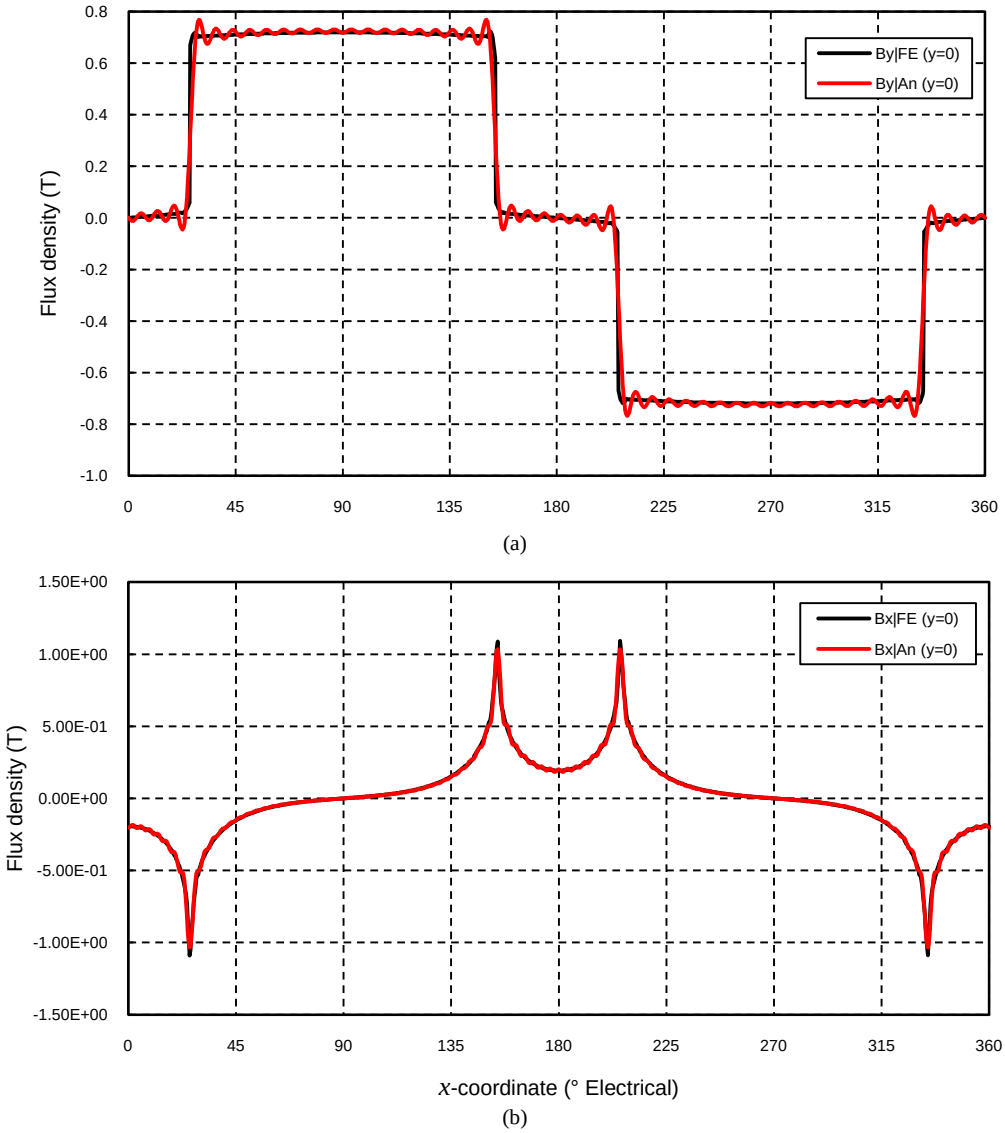

Fig. 3.16 Air gap flux density due to the permanent magnets at $y = 0$ (on the PM surface) as calculated analytically (red line) and with FEA (black line): (a) the component across / normal to the air gap and (b) the component tangential to the air gap..

be derived as also given in Appendix D. The flux density in region I (the PM region) is then calculated by substituting (3.33) into (B.27) and (B.28); the results are given as

$$B_{xI} = \sum_{m=1,2,3}^{\infty} \left(\frac{m\pi}{\tau}\right)\left[C_{M1}e^{\frac{m\pi y}{\tau}} - C_{M2}e^{\frac{-m\pi y}{\tau}}\right]\sin\left(\frac{m\pi x}{\tau}\right) \tag{3.35}$$

and

$$B_{yI} = -\sum_{m=1,2,3}^{\infty} \left(\frac{m\pi}{\tau}\right)\left[C_{M1}e^{\frac{m\pi y}{\tau}} + C_{M2}e^{\frac{-m\pi y}{\tau}} + \frac{4B_r\tau}{m^2\pi^2}\sin\left(\frac{m\pi\tau_m}{2}\right)\right]\cos\left(\frac{m\pi x}{\tau}\right). \tag{3.36}$$

In Fig. 3.15 the analytical solution of (3.35) and (3.36) at $y = 0.5\ell_g$ (in the middle of the stator) is shown together with a FE solution of the same model. It is clear that the analytical and FE solutions are almost identical for B_y and hence verifies the accuracy of the analytical equation. For B_x, the two solutions are rather different; this is however only due to the meshing of the FE model. In theory, B_x should be zero in the middle of the stator and hence the analytical solution is exact. The "noise" seen from the FE solution is the inevitable small inaccuracy resulting from the meshing of the model. As seen from the scale, this "noise" is indeed extremely small.

For interest, the solutions of B_x and B_y at $y = 0$ (on the PM surface) are also shown in Fig. 3.16. In Fig. 3.16(a) there is a small deviation in the two solutions. The FE solution here is more exact and the analytical solution shows small oscillations resulting from the addition of only a finite number of harmonics in (3.36). The nature of B_x in Fig. 3.16(b) is again such that the FE and analytical solutions render solutions matching very closely.

3.4.2 Harmonic analysis

The physical arrangement of the PMs will determine how sinusoidal the air gap flux density (and the back-EMF) is. Together with the stator current waveform this will also determine the magnitude of any ripple force. It is therefore important to try and configure the magnets in such a way as to minimise all harmonics in the flux den-

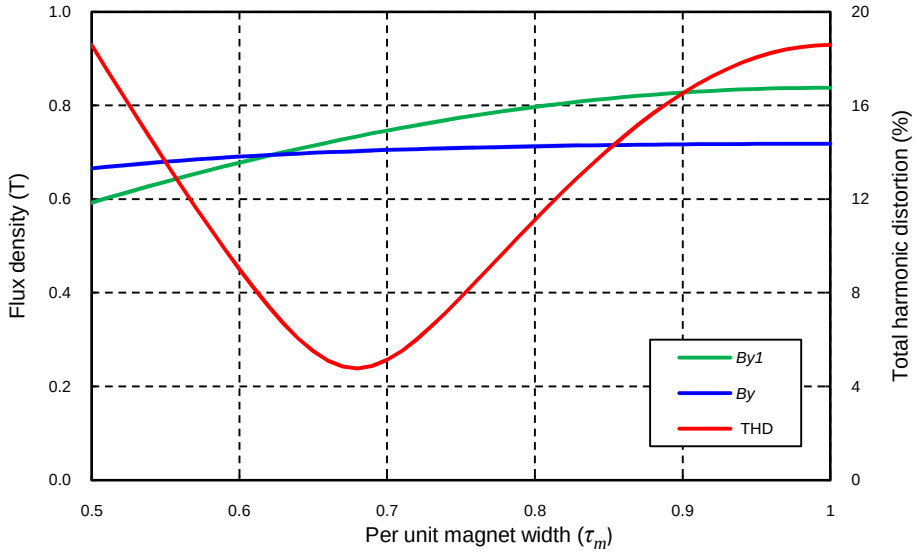

Fig. 3.17 Harmonic analysis of the PM flux density distribution in the middle of the air gap.

sity waveform. A study is done to see for which magnet to pole pitch ratio the total harmonic distortion, given as

$$THD = \frac{\sum_{n=2}^{\infty} B_{yn}^{\ 2}}{B_{y1}^{\ 2}}, \tag{3.37}$$

is the lowest. The peak flux density, the peak fundamental flux density and the THD is shown as a function of the per unit magnet width τ_m in Fig. 3.17. The peak flux density increases as τ_m increases, but it is clear that the THD is a minimum of about 4.5 % at $\tau_m \approx 0.68$.

3.4.3 EMF calculation

With the air gap flux density very close to sinusoidal, the back-EMF can simply be calculated from (3.6) - (3.9) with B_p equal to the peak value of B_{y1} from (3.36). For verification, the analytical solution is again compared to a FEA solution. The FEA solution is found by stepping the stator through the translator at a constant velocity and calculating the flux linkage at each step; the EMF is then calculated by taking the derivative of the flux linkage according to (3.6). The comparison is shown in Fig. 3.18. The difference in the two solutions is again almost negligible.

If there are significant harmonics present in the flux density waveform, the windings flux linkage can also be calculated from the magnetic vector potential as done in Section 3.3.6 for the inductance calculation. The equation in (3.9) is however very simple and requires far less computational power than a formula with the form of (3.25) or (3.26). This highlights a big advantage of choosing a per unit pole width that minimises the air gap flux density harmonics.

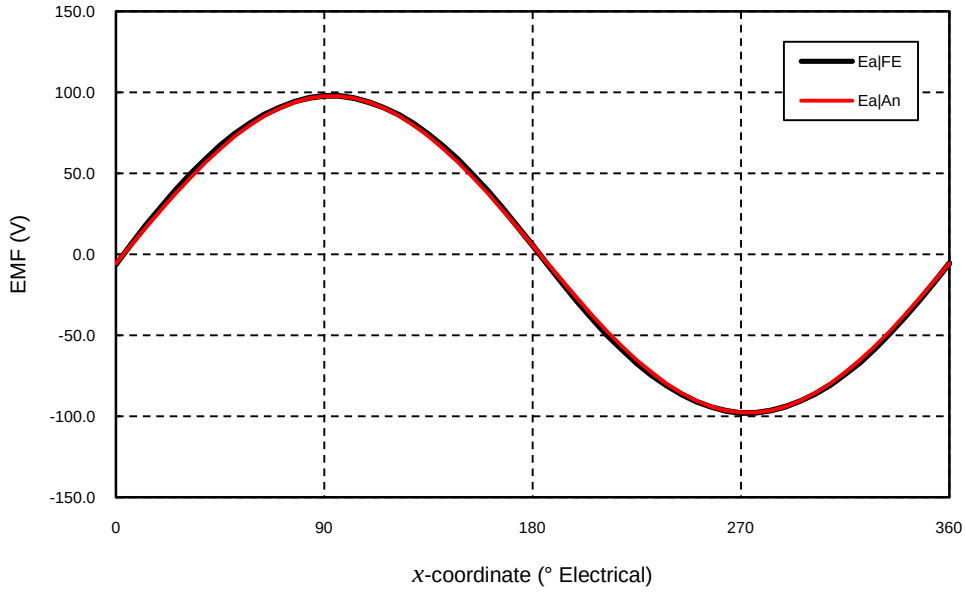

Fig. 3.18 EMF as calculated analytically (red line) and from FEA (black line).

3.4.4 One dimensional analysis

The flux density in electrical machines can also be calculated by modelling the magnetic circuits in the machine as lumped parameter circuits as mentioned in Section 3.2.1. This approach is for instance used in air-cored machines in [66], [80], [101] and very satisfactory results are obtained. In the previous section it was shown that only a single value of peak air gap flux density is necessary to very accurately calculate the back-EMF if the THD of the air gap flux density is low. This further motivates the use of a simplified, one-dimensional flux density calculation, as opposed to the more complicated and more computation expensive two-dimensional method discussed in Section 3.4.1. It is as such decided to also explore this method of analysis.

The lumped parameter circuit in Fig. 3.18 represents one PM and one air gap. It is assumed that there is no leakage flux, i.e. all the flux φ_m from the PM crosses the air gap. A constant reluctance value is used for both the PM (σ_m) and the air gap (σ_g), and is given as

$$\sigma_m = \frac{h_m}{\mu_{rec} A_m} \text{ and } \sigma_g = \frac{\ell_g}{\mu_0 A_g}, \tag{3.38}$$

where μ_{rec} is the PM recoil permeability, μ_0 is the permeability of air and A_m and A_g is the effective cross-sectional area of the PM and of the air gap between opposing PMs respectively. The assumption is therefore made that the MMF (F_m) across the PM and across the air gap is constant. The air gap flux density, between two opposing PMs, (B_p) and the flux density in the PM (B_m) are assumed to be uniform and is given as

$$B_p = \frac{\varphi_m}{A_g} \text{ and } B_m = \frac{\varphi_m}{A_m}. \tag{3.39}$$

The MMF F_m generated by a PM can be given as

$$F_m = H_c h_m, \tag{3.40}$$

where H_c is the PM coercivity. As was mentioned, the magnetic circuit seen in Fig. 3.19 represents one magnet and one air gap. To complete the magnetic circuit, n_s (the number of stator sections in the novel LG) of these circuits must be placed in series to represent the complete path through which the magnetic flux flows. Applying Kirchoff's voltage law to the circuit gives

$$n_s H_c h_m = n_s \varphi_m \left(\frac{h_m}{\mu_{rec} A_m} + \frac{\ell_g}{\mu_0 A_g} \right). \tag{3.41}$$

Substituting $\mu_{rec} = B_r/H_c$ and (3.39) into (3.41) and simplifying gives

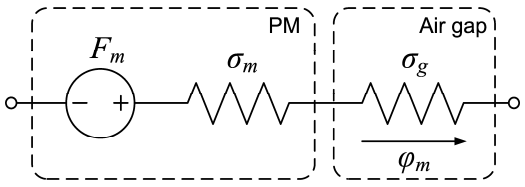

Fig. 3.19 Equivalent magnetic circuit diagram of one magnet and one air gap.

$$H_c h_m = B_m \left(\frac{H_c}{B_r} \right) h_m + B_p \left(\frac{1}{\mu_0} \right) \ell_g . \tag{3.42}$$

Studying Fig. 3.8 reveals that the peak air gap flux density occurs along the middle of the PM pitch as expected. It can also be noted from the flux lines that, at this point, B_p is basically the same as B_m. It is therefore valid to assume that $B_m = B_g$ in (3.42). Making this substitution and rearranging then gives the peak air gap flux density as

$$B_p = \frac{\mu_0 h_m B_r H_c}{\mu_0 h_m H_c + \ell_g B_r} . \tag{3.43}$$

Using this method to calculate the peak air gap flux density for the same dimensions used in Section 3.4.1 gives $B_p = 0.704$ T, whereas the two-dimensional method gives $B_p = 0.706$ T. It is remarkable how similar these results are and shows that the one dimensional flux density analysis can indeed be used with very good results. It must however be recognised that, as the air gap length increases with respect to the magnet height, that more fringing and leakage flux will be present and that the assumptions used for the one-dimensional analysis will become less valid. From (3.38), it is evident that the air gap reluctance is proportional to the air gap length. Hence, in order to minimise leakage flux and fringing, it is necessary to enforce dimensional constraints for a double-sided air cored machine such as done by Stegmann [66]:

$$h_m > \frac{1}{2} \ell_g , \tag{3.44}$$

and

$$\ell_{ipg} > \ell_g . \tag{3.45}$$

This ensures that the reluctance across the air gap is less than the reluctance between adjacent PMs and between the PM and the rotor yoke; most of the flux will then cross the air gap and ensure that (3.43) can be used to calculate the peak air gap flux density. For the novel LG, the dimensional constraint of (3.44) should be re-written as

$$h_m > \ell_g , \tag{3.46}$$

because there is only one PM per air gap, unlike a conventional double-sided machine which has two PMs per air gap. In terms of the novel LG dimensions, the constraint of (3.45) can be given as

$$\ell_{ipg} = \frac{L}{p} (1 - \tau_m) > \ell_g . \tag{3.47}$$

3.5 Varying magnet height

So far the 3-D effects in the novel LG have been ignored to simplify the analysis. Apart from the end-winding flux linkages, the most important of 3-D effects is the fact that the magnet height actually varies from a mini-

mum value at the inside diameter of the LG to a maximum value at the outside diameter as shown in Fig. 3.4(b). According to (3.43), the air gap flux density is a function of the magnet height, and hence it is expected to also vary from the inside to the outside diameter of the LG.

The average magnet height h_m is given approximately in terms of the outside and inside diameter and the number of stator section n_s as

$$\begin{aligned} h_m &= \frac{\pi}{n_s}\left(d_o - \ell\right) - \ell_g \\ &= \frac{\pi}{n_s}\left(d_i + \ell\right) - \ell_g . \end{aligned} \tag{3.48}$$

Alternatively the outer magnet height h_{mo} and inner magnet height h_{mi} can respectively be given as

$$h_{mo} = \frac{\pi}{n_s} d_o - \ell_g \tag{3.49}$$

and

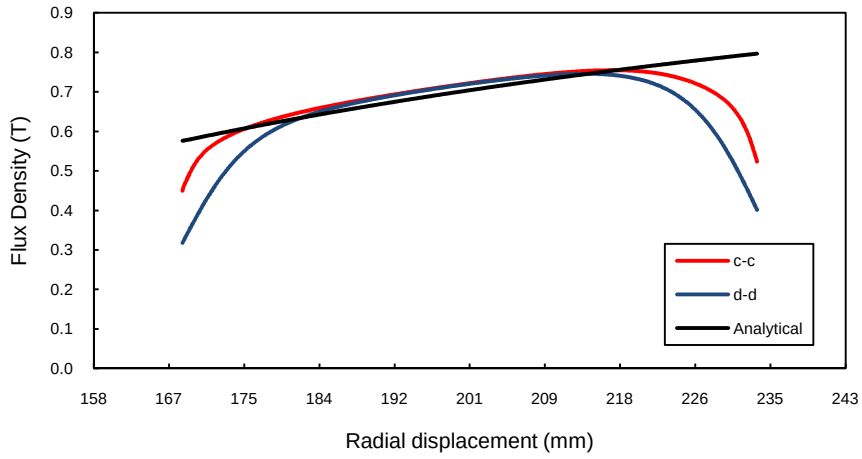

Fig. 3.20 Flux density along line c-c and d-d in Fig. 3.20 and as calculated from (3.45).

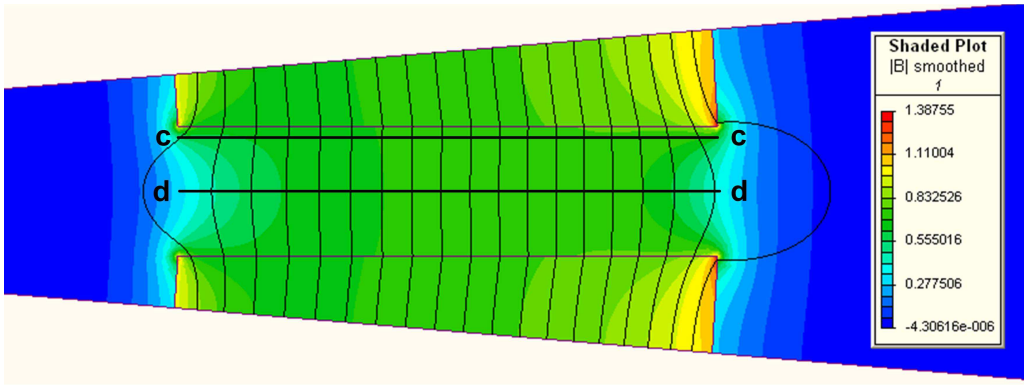

Fig. 3.21 Flux density colour and flux contour plot of one air gap as seen from the top in Fig. 3.4(b).

$$h_{mi} = \frac{\pi}{n_s} d_i - \ell_g . \tag{3.50}$$

From (3.48) – (3.50) it is clear there exist a definite relationship between ℓ, d_o, d_i and n_s (for a fixed h_m and ℓ_g constrained by (3.46) and (3.47)). This will be discussed in more detail in Section 3.8.

In Fig. 3.20 the air gap flux density is shown as analytically calculated from (3.43) from the inside to the outside diameter. The effect is almost a linear increase in flux density. Equation (3.43), however, does not take cognisance of the fringing effects at the ends of the magnets, and for this purpose a FEA model as shown in Fig. 3.21 is set up. From the flux density colour and contour plot it is easy to see the fringing effects at the ends of the magnets. Plots of the FEA-calculated flux density along line c-c (the middle of the air gap) and d-d (at the surface of the stator) are shown alongside the analytical solution in Fig. 3.20. The FEA shows an increase in flux density as the magnet height increases, and corresponds well with the analytical obtained results near the middle of lines c-c and d-d. It is however clear that the flux density rapidly decreases near the ends of the magnets due to fringing. The average analytical flux density is 0.7 T as per the design specifications, while the average flux density along line c-c and line d-d is 0.69 T and 0.65 T respectively. Initially this result may seem to suggest that the induced voltage in the stator winding may be less than expected. However, there are voltages induced in the end-windings which are not analysed with 2-D FEA and which to some extent make up for the lower flux density at the active windings.

3.6 Force calculation

Given the fairly straight forward calculation of the LG's EMF, it is decided to simply calculate the force from this EMF as

$$f = \frac{3E_p I_p}{2v}, \tag{3.51}$$

where the current depends on the LG load and velocity is determined by the waves. This gives a steady state value for the force. If it is necessary to analyse the force ripple, the Lorentz force law (B.1) can be used to calculate a force distribution from the flux density (3.36) and current density distributions (3.14). For the purpose of this thesis only a steady state force will be calculated from (3.51) and equation (2.10) as discussed in Chapter 2. In the next Chapter, where the design of the prototype LG is considered, FEA will be used to verify the force calculation and to analyse any ripple force effects.

3.7 Performance analysis

In this section the most important sources of losses in the air-cored LG will be discussed. This is important for calculating the electrical efficiency of the generator. From an economic perspective it is also necessary to know the cost per unit power generated by the LG. Since material prices are however fairly volatile and this LG is still in the beginning phases of development, it is rather decided to analyse the LG in terms of the required material

mass per unit power generated. In this way manufacturing, labour and material costs can be ignored for now, but easily added to the performance analysis at a more mature stage of the development.

3.7.1 Copper losses

Copper or conduction losses are usually the most dominant source of losses in air-cored electrical machines. As in [65], the phase resistance of a stator section can be derived as

$$R_s = \frac{N^2 q \rho_{cu} (2\ell + \ell_e)}{a^2 k_f hw}, \tag{3.52}$$

where w is the coils side width in meters, h is the coil thickness in meters, k_f is the copper fill factor, ρ_{cu} is the resistivity of copper and ℓ_e is the end winding length of the coils, which can be calculated as

$$\ell_e = \frac{2\theta_c L}{\pi p}(1 - 0.586\kappa). \tag{3.53}$$

The copper losses of the LG can now be calculated as

$$P_{cu} = 3I^2 R_s. \tag{3.54}$$

3.7.2 Eddy current losses

The changing magnetic flux induces unwanted eddy currents in the copper conductors according to Faraday's law of electromagnetic induction (B.6). From [62], the power loss resulting from these eddy currents can be calculated as

$$P_{ec} = 1.7 NQ n_c \frac{2\pi \ell d_w^{\,4} B_p^{\,2} \omega^2}{32\rho_{cu}}, \tag{3.55}$$

where, n_c is the number of parallel strands per conductor and d is the strand diameter. The eddy-loss resistance shown in Fig. 3.3 can then be calculated from (3.7) and (3.55) as

$$R_e = \frac{3E_p^{\,2}}{P_{ec}}. \tag{3.56}$$

It is important to note the factor $d_w^{\,4}$ in (3.55). Care must be taken in the design to avoid conductors of too large a diameter, as the eddy-current losses can quickly become very large. Due to this, stranded conductors, or *Litz* wires, must be used in air-cored machine windings.

3.7.3 Electrical efficiency

As discussed in Chapter 2, the average generated power in the LG at a constant velocity is given as

$$P_g = \frac{3E_p I_p}{2} \tag{3.57}$$

From (3.54), (3.55) and (3.57) the electrical efficiency of the LG can then be calculated as

$$\eta = \frac{P_g - P_{cu} - P_e}{P_g} \times 100. \tag{3.58}$$

3.7.4 Mass calculation

The mass of the different components in the LG is a function of their respective dimensions and material density. As mentioned before, the mass per unit generated power will be used as a figure of merit for the novel LG and will form the basis for an eventual economic figure of merit. For this analysis it is also decided to focus on the active material mass, i.e. the copper and magnet mass, as these are the most critical, and probably also the most expensive materials, in the machine.

From the LG dimensions given in Fig. 3.2 - 3.5, the PM mass is given as

$$M_m = n_s \gamma_{fe} \tau_m h_m \ell L \tag{3.59}$$

and the copper mass is given as

$$M_{cu} = n_s \gamma_{cu} \kappa k_f h \ell L (2 + \delta). \tag{3.60}$$

where γ_{fe} and γ_{cu} are the respective densities of the PM material and of copper and $\delta = \ell_e/\ell$.

3.8 Comparative study

When first considering this novel topology, it was thought that the power density (power per unit mass) may be improved over existing air-cored LGs. However, the LGs in literature with the most available data with regard to dimensions and performance measurements are the iron-cored LGs from Columbia Power Technologies (Chapter 2, Section 2.7.3) and from Seabased (Chapter 2, Section 7.2). Nevertheless, in order to get an early indication of how this machine would perform compared to these LGs, a comparative study is conducted.

3.8.1 Methodology

It is decided to design two versions of the novel topology, namely N1, for comparing with the 1 kW tubular LG of Columbia Power Technology (CPT) in [43], [85], and N2, for comparing with the 10 kW four sided LG of Seabased in [42], [70]. N1 and N2 are designed to be of a size comparable to the respective existing LGs in order to make a reasonable comparison. In general, the dimensions of these LGs (including number of poles and pole pitch) and other parameters like current density and velocity were imposed on N1 and N2 as far as possible; from this the generated power, efficiency and mass of the active materials (copper and magnet mass) are compared. The simplified one-dimensional PM field analysis as explained in Section 3.4.4 is used and, since the inductance of air-cored windings are usually very small, it is ignored in this study.

Table 3.2: Machine parameters which are common to N1 and N2.

Inside diameter d_i (m)	0.3	Turns per coil N	100
Outside diameter d_o (m)	0.6	Strands per turn n_c	10
Stator thickness h (mm)	10	Number of stators n_s	54
Air gap length ℓ_g (mm)	14	Copper fill factor k_f	0.45

The outside diameter is fixed at 0.6 m for both N1 and N2; the reason for this is that the air gap diameter of the CPT LG is about 0.6 m and a diameter of 0.6 m would also more or less enclose the active material of the Seabased LG. Previous work on air-cored machines has shown that a peak air gap flux density in the vicinity of 0.7 T is practically achievable [66], [96]. With the peak air gap flux density therefore set to B_p = 0.7 T, the stator height h is maximised, while staying within the constraint of (3.46) and (3.47); with a fixed magnetic loading and current density, maximising h effectively maximises the current loading, and hence also the shear stress of the machine according to (2.11). With the shear stress maximised, the effective air gap area must be maximised in order to maximise the shear force of the machine according to (2.10), and hence the power output according to (2.7). As the active length L is already matched to that of the iron-cored LGs, only the active winding length ℓ can be varied to change the air gap area, which is given as $A_g = \ell L$ for one stator section. With d_o fixed at 0.6 m, ℓ is a function of the number of stator sections n_s or the inside diameter d_i, from (3.48). It is shown in [105] that decreasing d_i increases ℓ and A_g, while decreasing n_s. The inside diameter can however not be too small, and a practical value of $d_i = 0.5d_o$ is chosen; this resulted in n_s = 54 for both N1 and N2, as calculated from (3.48). A wire diameter is chosen such that the eddy current losses are kept to a minimum. Parameters that are common to N1 and N2 are given in Table 3.2.

It must be noted that some of the parameters of the CPT and Seabased LGs are not directly available from literature and are calculated from the data that *is* available. The calculation of these parameters is explained in Appendix G. Also, the highest available NdFeB magnet grade is used (at the time of the study it was N48). This is chosen based on a study in [66], which shows that selecting the highest magnet grade significantly decreases magnet mass with only a marginal increase in costs (for a given air gap flux density). In the CPT LG, NdFeB magnets of grade N35 are used; the NdFeB grade used in the Seabased LG is unknown. It can however be assumed that a grade lower than N48 is used in the Seabased LG, as it was constructed a number of years prior to the study.

From the stated methodology, it is clear that an exact comparison between the different LGs is not possible. This is however not the purpose of this study. The aim here is simply to get a rough indication of the novel LG's performance compared to existing LGs.

3.8.2 Results

The results of the comparative study are given in Tables 3.3 and Table 3.4, and also shown in Fig. 3.22. The limited stator thickness of the air-cored LG limits its electric loading and its large effective air gap length limits its magnetic loading. As mention before, increasing the electrical loading by increasing the stator thickness will also reduce the magnetic loading and vice versa. However, it is clear to see that the novel topology succeeds in creat-

Table 3.3 Comparison of the novel LG topology with existing iron-cored machines.

Parameter	CPT	N1	Seabased	N2
Stator core	Iron	Air	Iron	Air
Air gap area A_g (m^2)	0.53*	1.56	2.08	7
RMS Air gap flux density B (T)	0.76	0.7/√2	1	0.7/√2
Current density J (A_{rms}/mm^2)	0.45*	0.45	1.8	1.8
Electric loading K (kA_{rms}/m)	3.26*	1.36	7.97*	5.5
Shear stress σ_s (kN/m^2)	2.48*	0.68	7.97*	2.7
Shear force f_g (kN)	1.315	1.06	16.57*	19.1
Power P_g (kW)	1	0.81	11.57	13.4
Copper losses P_{cu} (p.u.)	0.040*	0.040	0.09	0.16
Core losses P_c (p.u)	-	0.01	0.05	0.003
Efficiency η (%)	-	95	86	84
Copper mass M_{cu} (kg)	28.55	80	144*	315
Total stator mass M_s (kg)	181.58	106	949*	419
Magnet mass M_m (kg)	222	504	115	754
Total translator mass M_t (kg)	1446	607	547	903

* Parameters calculated from data given in literature (See Appendix G).

ing a much larger active air gap area (per volume) than the other topologies. From the shear force and power it is clear to see that the larger air gap area to some extent makes up for the shortcomings with the electrical and magnetic loading. For N1, the generated power is 19 % less than that of the CPT LG. The low current density however results in a high efficiency of 95 %. For N2, the generated power is actually 17 % higher than that of the Seabased LG, while the efficiency is two percent lower. It should be mentioned that N1 is slightly smaller than the CPT LG and N2 is probably slightly larger than the Seabased LG. Furthermore, the efficiencies of the different LGs are also different (or unknown). This makes a true comparison between the LGs impossible, although this is not the aim, as mentioned. In terms of a rough indication, the calculated figures indicate a power rating of the novel LG which is fairly similar to that of the iron-cored LGs.

It is a well-known fact that air-cored machines use much more magnet material that iron-cored machines [106]; this is confirmed by this study, as 560 % more magnet material is used in the novel LG compared to the Seabased LG, even though a higher PM grade is probably used. This has a big cost implication for the novel LG. In Table 3.4 and Fig. 3.22 this is highlighted, where the power per active mass of the LGs are given. It is clear that the power per copper and per magnet mass is much lower in the novel LG. The high copper mass of the novel LG may be inherent to the topology of the machine, where a large amount of copper is basically made to fit into a small space. Also, the end windings contribute a significant amount to the overall mass of the copper in the novel LG; this basically constitutes wasted copper mass and can be considered a drawback of this topology.

In comparing the power per total *active* mass of the stators and translators, the novel LG however performs much better than the iron-cored LGs. This is of course due to the lack of iron in both the stator and translator of the

Table 3.4 Comparison of the power density of the novel LG topology with existing iron-cored machines.

Parameter (W/kg)	CPT	N1	Seabased	N2
Power per copper mass	35	10	80	43
Power per magnet mass	4.5	1.61	101	18
Power per active stator mass	5.5	7.6	12	32
Power per active translator mass	0.69	1.33	21	15
Power per total active mass	0.61	1.14	7.7	10

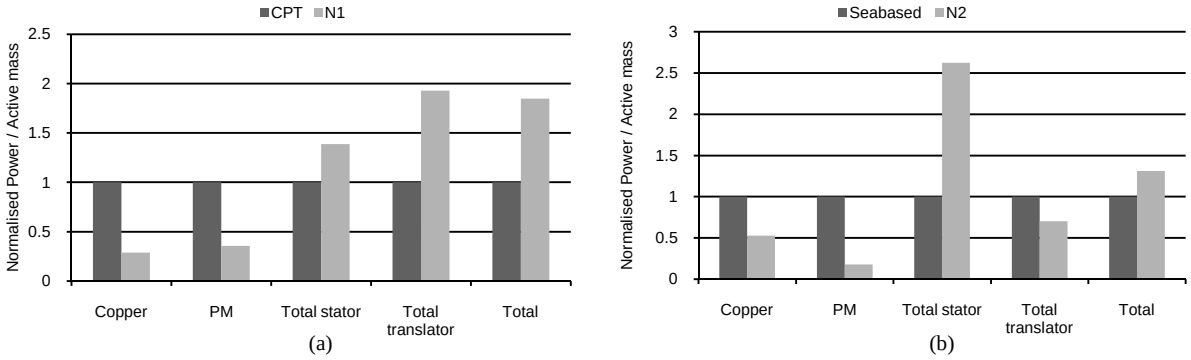

Fig 3.22 Normalised power per active mass of N1 and N2 compared to the LGs from CPT and Seabased.

novel LG. The mass in addition to the copper and PM material for N1 and N2 simply constitutes epoxy for the stator and a low density, non-magnetic support material for the PMs (e.g. a phenolic composite, such as Tufnol, or an engineering plastic). Some rough calculations indicate that the stator epoxy mass will be around 33 % of the copper mass and a typical engineering plastic would constitute around 20 % of the total magnet mass. Although these materials are not "active" as such, it is included in the total active stator and translator mass calculation, as it serves an essential role in supporting the copper and magnets.

It must be noted that the structural support material needed to keep the stator and translator apart is not considered in this study. For the iron-cored LGs, significant amounts of steel would be needed for this, whereas the structural material in the air-cored LG simply needs to carry the mass of the active material. The cost of the various materials is also not considered in this study. This is because material cost alone can be misleading. When considering costs, manufacturing and assembly costs should also be included. This information is of course not readily available, especially since these are all experimental machines. Furthermore, metal prices, and especially rare-earth material prices, are currently extremely volatile and including this as part of the study will therefore not be meaningful.

3.8.3 Conclusion

It must be acknowledged that the amount of active material, especially of the PM material, can be seen as a significant drawback of the novel LG. However, this study shows that the overall power per total active material of the novel LG is better than for comparably sized iron-cored LGs. Furthermore, as there are practically zero at-

traction forces in the novel LG, it is expected that much less structural material will be used. An improvement on the cost issue of the novel LG compared to iron-cored LGs is therefore expected. Construction and assembly procedures can be simplified due to the elimination of attraction forces. The winding of the stator can also be automated, as pre-formed coils are used. All of this will further reduce costs. The designs of N1 and N2 in this study are also not optimised. A design of the novel LG that is optimised for minimum active mass will therefore further improve the performance results obtained here.

Based on all the above mentioned aspects, the proposed novel LG can be considered as a viable alternative to current technology used for DD-WECs. The next step is to find an optimised design for a prototype LG which can be built and tested in a laboratory.

Chapter 4

Prototype linear generator design

In the previous chapter the analytical model of the novel LG is derived and verified with FEA. Two rough designs are done based on a simplified one-dimensional PM field analysis; this is done in order to conduct a comparative study such as to put the novel LG's performance into perspective. In this chapter the focus is on designing a prototype of the novel LG to satisfy certain performance specifications. Given the fairly straight forward analytical model of the machine, an exhaustive optimisation procedure is developed to find optimal dimensions for minimum active mass of the LG; some of this work has been published in [107], [108] and is given here again for completeness. Some mechanical design aspects are discussed, although the thermal modelling and design of the machine is not considered in this thesis.

4.1 Optimisation code

The analytical model of the novel LG is here manipulated into a form which is more appropriate for implementing in a computer programme for finding the optimal dimensions subject to the performance specifications. These specifications are defined in the next section. It is shown that all the machine dimensions can be calculated once values for only four variables are selected.

4.1.1 Performance specification

It has already been mentioned that the LG operates at a constantly varying velocity. In order to design for a certain average power, a constant average velocity and force, calculated from (2.8), are assumed. The LG specifications are here given in terms of the required average power P_g, average velocity V and efficiency η.

The dimensional parameters to be optimised are the generator active length L, winding active length ℓ, stator height h, average magnet height h_m and the inside and outside diameter d_i and d_o. These dimensions can be seen in Figs. 3.2, 3.4 and Fig. 3.5. The dimensional parameters depend on the choice of the number of stator sections n_s, the rms current density J and the number of active poles p; these additional parameters therefore also form part of the optimisation.

The performance parameters, dimensional parameters and the additional parameters to be optimised are now respectively defined in matrix-format by $\mathbf{U}$, $\mathbf{X}_1$ and $\mathbf{X}_2$ as

$$\mathbf{U}=\begin{bmatrix} P_g \\ V \\ \eta \end{bmatrix}; \qquad \mathbf{X}_1=\begin{bmatrix} L \\ \ell \\ h \\ h_m \\ d_i \\ d_o \end{bmatrix}; \qquad \mathbf{X}_2=\begin{bmatrix} n_s \\ J \\ p \end{bmatrix}. \tag{4.1}$$

By recognizing that each of the stator sections as defined in Fig. 3.2 are identical, the power P_{gi} generated in an individual stator section can be calculated as $P_{gi} = P_g/n_s$. Furthermore, two more required performance parameters, which are here also defined for an individual stator section, are the developed force F_{gi} and the copper losses P_{cui}. The performance specification can now be simplified as

$$\mathbf{G}=\begin{bmatrix} F_{gi}\left(\mathbf{X}_1,\mathbf{X}_2\right) \\ P_{cui}\left(\mathbf{X}_1,\mathbf{X}_2\right) \end{bmatrix}=\frac{1}{n_s}\begin{bmatrix} 1/V \\ k(1-\eta) \end{bmatrix}P_g, \tag{4.2}$$

where $k < 1$ is the ratio of the copper losses to the total losses in the machine. As explained before, only copper losses and the eddy-current losses in the stator windings need to be considered and hence k is given as

$$k=\frac{P_{cu}}{P_{cu}+P_{ec}}. \tag{4.3}$$

It can be seen from (3.55) that the determining factor for P_{ec} is the wire diameter d_w. The electrical angular frequency ω, which also has an effect on P_{ec}, depends on the wave speed and the magnet pole pitch. Due to constraints on the magnet pole pitch, as discussed in Chapter 3 and the inherent slow wave speed, ω is expected to be very low. Therefore, by adjusting the number of parallel strands in each coil turn, and so adjusting d_w, P_{ec} can be designed to be very small. Assuming a value of k then serves to reduce the complexity of the problem.

4.1.2 Thrust calculation

Similarly as derived in [65], the thrust developed per stator section can be expressed as

$$F_{gi}=k_w C_1 K_1. \tag{4.4}$$

The machine constant C_1 is given by

$$C_1=B_{p1}\sqrt{\frac{2\kappa k_f P_{cui}}{\rho_{cu}}}. \tag{4.5}$$

The variable K_1, which is a function of $\mathbf{X}_1$ only, is given by

$$K_1=\sqrt{\frac{h\ell L}{(2+\delta)}}. \tag{4.6}$$

It can be noted that K_1 can now be calculated from the required force of (4.2) and from (4.4) and (4.5) as

$$K_1 = \frac{F_{gi}}{k_w C_1}. \tag{4.7}$$

4.1.3 Copper loss calculation

The copper losses can be expressed as

$$P_{cui} = K_2 C_2, \tag{4.8}$$

where C_2 is another machine constant given by

$$C_2 = \kappa k_f \rho_{cu} J^2. \tag{4.9}$$

The machine constant K_2, which is also a function of $\mathbf{X}_1$ only, is given by

$$K_2 = h\ell L(2+\delta). \tag{4.10}$$

Similar to (4.7), K_2 can now be calculated from the required copper losses of (4.2) and from (4.8) and (4.9) as

$$K_2 = \frac{P_{cui}}{C_2}. \tag{4.11}$$

4.1.4 Dimensional parameter calculation

The equations from the previous two sections can be manipulated as in [107] to find the active stator winding length ℓ as

$$\ell = \frac{2\theta_c L}{\pi p(K_3 - 2)}(1 - 0.586\kappa) \tag{4.12}$$

where K_3 is defined as

$$K_3 = \frac{\sqrt{K_2}}{K_1}. \tag{4.13}$$

According to (4.12), and since the optimal values for θ_c and κ are known (discusses in Chapter 3), there exists a unique value of ℓ for a given combination of L, p, J and n_s. Hence, if L, p, J and n_s are chosen, ℓ can be determined from (4.12). Furthermore, with ℓ known, h can be determined from (4.6) or (4.10).

By rearranging (3.43), the average magnet height can be calculated as

$$h_m = \frac{B_p \ell_g}{\mu_0 H_c \left(1 - B_p / B_r\right)}. \tag{4.14}$$

The required value of B_p is selected in the design, as is also done in Chapter 3.8.

With the values of ℓ, h, and h_m already calculated from (4.12), (4.6) and (4.14), d_o and d_i can then easily be found by rearranging (3.48).

4.1.5 Active mass calculation

The active mass consists of the PMs and the stator copper and can be calculated from (3.59) and (3.60). By substituting (4.10) into (3.60), the copper mass is given as

$$M_{cu} = n_s \gamma_{cu} \kappa k_f K_2. \tag{4.15}$$

Substituting first (4.11) and then (4.9) into (4.15) gives

$$M_{cu} = \frac{n_s P_{cui} \gamma_{cu}}{\rho_{cu} J^2}. \tag{4.16}$$

It can be noted that the copper mass is independent of $\mathbf{X}_1$ of (4.1) and only a function of n_s and J of $\mathbf{X}_2$ of (4.1).

With all the parameters of $\mathbf{X}_1$ and $\mathbf{X}_2$ known, the active mass of the generator can be calculated from (3.60) and (4.16).

4.1.6 Dimensional constraints

In addition to the constraints given in (3.46) and (3.47), for minimum leakage flux, an additional constraint is defined to limit the minimum magnet height h_{mi} to a certain minimum value. This is for construction purposes, as the minimum magnet height must be greater than the spacer height h_s, from Fig. 3.4(a), as

$$h_{mi} > h_s. \tag{4.17}$$

A typical value for the per unit magnet width τ_m that can be used in the design is $\tau_m = 0.7$ [63], [66]. This is in agreement with the findings in Chapter 3, Section 4.2, where $\tau_m \approx 0.68$ is found to give the minimum THD.

4.1.7 Optimisation procedure

The objective function, $F(\mathbf{X}_1, \mathbf{X}_2)$, that has to be minimised in the design optimisation, subject to the performance constraints of (4.1) and the dimensional constraints of (3.46), (3.47) and (4.17), can now be expressed as

$$F(\mathbf{X}_1, \mathbf{X}_2) = w_1 M_m(\mathbf{X}_1, \mathbf{X}_2) + w_2 M_{cu}(\mathbf{X}_2), \tag{4.18}$$

where w_1 and w_2 are weighting factors. By assigning the price per kg of the PM material and copper to w_1 and w_2 respectively, the objective function represents the active material cost of the machine. This approach of minimising the active material cost is followed for linear machines in [49] and [88]. It may however also be necessary to factor in the labour costs associated with the copper and magnet mass, such as winding the copper onto the stator and fixation of the magnets. For instance, even though PM material is much more expensive than copper, stator winding could be considerably more expensive than magnet fixation, depending on the specific type of machine. To factor in these costs requires foreknowledge of manufacturing procedures and times; this information is

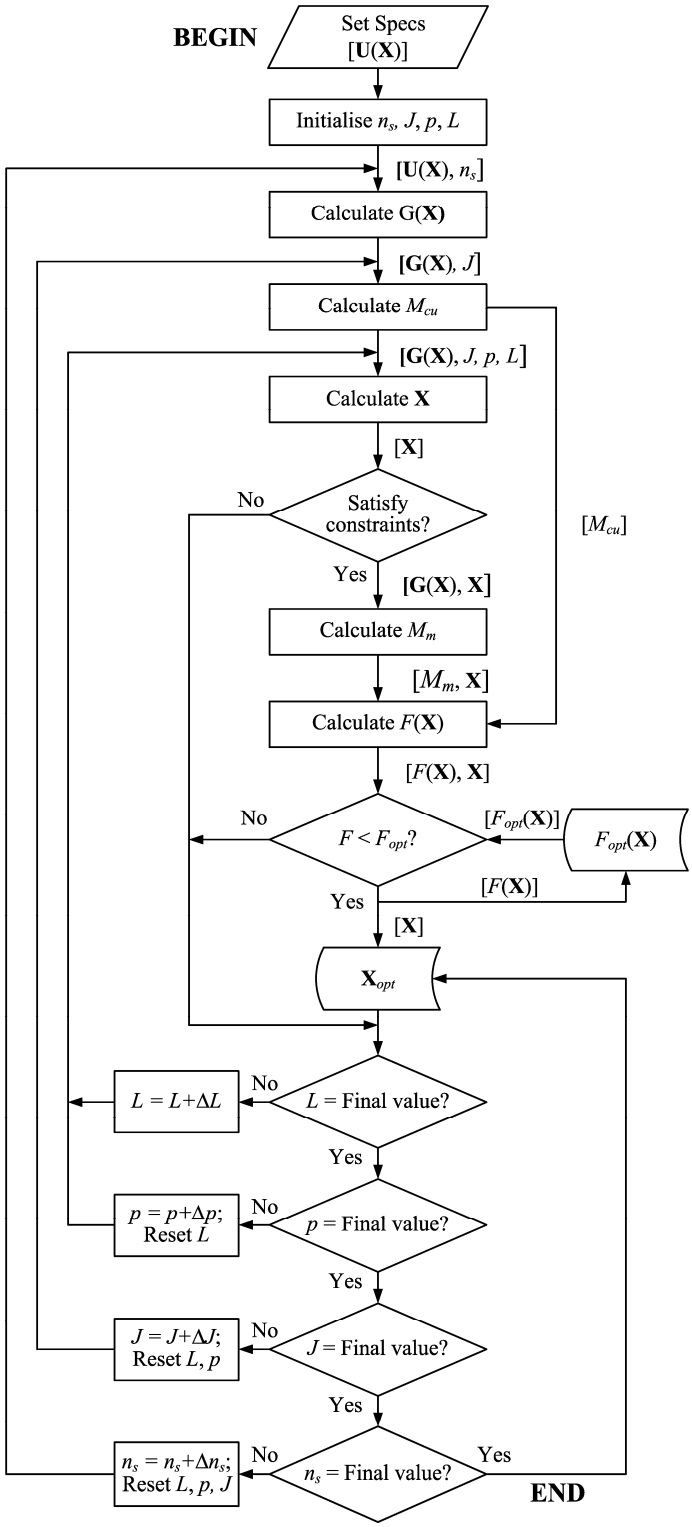

Fig. 4.1 Optimisation procedure flow diagram (**X** represents both $\mathbf{X_1}$ and $\mathbf{X_2}$ of (4.1)).

hardly ever available at the development stage, but should be considered where possible. As also mentioned in Chapter 3, due to the current price volatility of PM and copper material, factoring in material costs is not considered meaningful at this stage.

It is clear from (4.1) – (4.18) that all the dimensional parameters of $\mathbf{X}_1$, from (4.1), and the objective function of (4.18) can be determined for a given value of $\mathbf{X}_2$ and L. The relatively straight forward analytical model allows for optimal dimensions to be obtained by way of an exhaustive optimisation procedure. Such a procedure iterates through all the possible combinations of the input variables ($\mathbf{X}_2$ and L), within limits, to find the minimum value of the objective function. A program to do this was implemented in the Python programming language. For each combination of the input variables, the constraints of (3.46), (3.47) and (4.17) are checked; the objective function is only calculated if the constraints are not violated. Through each valid iteration the values of $\mathbf{X}_1$ and $\mathbf{X}_2$ are stored if $F(\mathbf{X}_1,\mathbf{X}_2)$ is less than in the previous iteration. The optimal dimensions are therefore simply retrieved from memory when the program terminates. The flow diagram of the program is shown in Fig. 4.1.

It is worth pointing out that this procedure is different to other optimisation procedures in that each iteration finds the machine dimensions which exactly satisfy the performance specifications of (4. 1). If any of the solutions do not satisfy the constraints of (3.46), (3.47) and (4.17), it is simply discarded. The procedure then basically finds the solution with the minimum value of $F(\mathbf{X}_1,\mathbf{X}_2)$ from all the valid solutions. There are therefore no problems with distinguishing between local and absolute maxima like in other optimisation algorithms.

4.2 Design specifications

It is decided to design a 1 kW LG with an efficiency of 85 %. The average translator velocity is chosen as 0.75 m/s, similar to the typical wave conditions in [43]. This gives

$$\mathbf{U}=\begin{bmatrix} P_g \\ V \\ \eta \end{bmatrix}=\begin{bmatrix} 1000\,\mathrm{W} \\ 0.75\,\mathrm{m/s} \\ 85\,\% \end{bmatrix}. \tag{4.19}$$

The value of $\mathbf{G}$ of (4.2) depends on n_s, which is a variable in the optimisation; $\mathbf{G}$ will thus be calculated for a range of different values of n_s.

4.2.1 Design constants

From experience, k of (4.3) is taken as $k = 0.95$. For the windings, $\kappa = 0.37$ and $\theta_c = 4\pi/3$ are selected according to the discussion in Chapter 3.3, and $k_f = 0.45$ is also selected from experience. For the PMs, NdFeB magnets of grade N48 are chosen, as discussed in Chapter 3.8. As a point of attachment for the magnets, the spacer height h_s is kept constant at 10 mm. It is expected that the spacers will support a very small mechanical load, so this is

Table 4.1 – Constant design parameters.

ρ_{cu} (Ωm)	1.7×10^{8}	B_r (T)	1.37
γ_{fe} (kg/m^3)	7580	H_c (kA/m)	1021
γ_{cu} (kg/m^3)	8230	B_p (T)	0.7
κ	0.37	g (mm)	2
k_f	0.45	τ_m (mm)	0.7
k_{w1}	0.875	h_s (mm)	10

Table 4.2 – Optimal dimensions.

Weighting	$w_1 = w_2$	d_o (mm)	466
M_m (kg)	50.73	d_i (mm)	262
M_{cu} (kg)	32.81	ℓ (mm)	65
n_s	38	h (mm)	11.5
J (A/mm^2)	1.45	h_m (mm)	17.5
p	4	h_{mo} (mm)	23
L (mm)	224	h_{mi} (mm)	12

considered sufficient for the prototype. Some of the other constant parameters used in the design are given in Table 4.1.

4.2.2 Optimisation

The optimisation procedure discussed in Section 1.7 is used to find the optimal dimensions of the machine, subject to the performance specifications of (4.19). For the weighting factors, $w_1 = w_2$ is used in the optimisation; by doing this the material prices are ignored as discussed. The results of the optimisation are given in Table 4.2.

In Fig. 4.2 the PM mass for different valid solutions calculated in the optimisation procedure, i.e. solutions satisfying the dimensional constraints are shown. It is interesting to note that for the optimal combination of $p = 4$ and $J = 1.45$ A/mm^2, only one valid solution exists. As J is decreased and/or p is increased, more valid solutions exist. The maximum allowable valid value of J therefore gives both the minimum M_m and M_{cu} (from (4.16)) and therefore also the minimum value of the objective function. What is even more interesting is that, due to this, when the optimisation is repeated with $w_1 = 4.5w_2$ (to reflect the active material price at the time of construction) in the optimisation, the same optimum dimensions is returned as before. The optimum dimensions can therefore be obtained by minimising only the PM or only the copper mass (or cost).

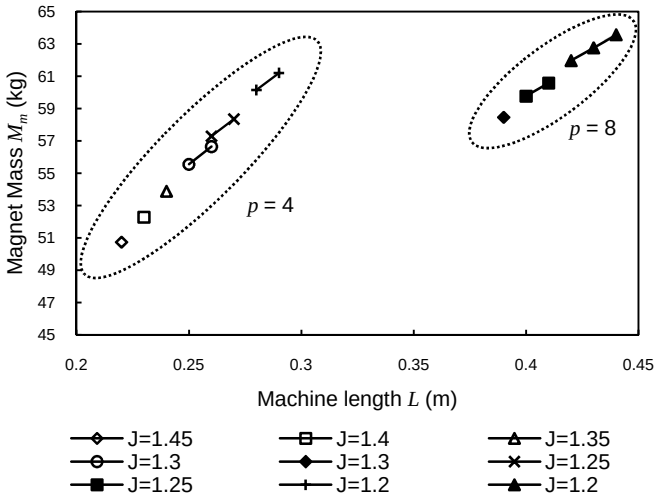

Fig. 4.2 PM mass as a function of active LG length L, number of poles p and current density J. Only valid solutions are shown for $p = 4$ and $p = 8$.

For the final design, the stator height was changed from h = 11.5 (given in Table 4.2) to h = 11 to provide more leniency on manufacturing and assembly tolerances. This effectively increased the mechanical air gap either side of the stator from g = 2 (given in Table 4.1) to g = 2.25. Inevitably this causes a reduction in output and an increase in copper losses for the given current density. The recalculated power is found as P_g = 956 W and the copper losses as P_{cu} = 0.147 p.u.

4.3 Winding design

From the design optimisation, the number of stator sections and the number of coils per section has been determined. The dimensions of the coils have also been determined. The winding design as described in this section entails selecting the number of parallel coils a, number of coil turns N, the number of parallel strands in the wire n_c and the wire diameter d_w. The most important constraints on the choice of these parameters are the required eddy current losses of (3.55), and the induced voltage (3.9). Other important constraints are also the maximum practical wire diameter (wire with diameters greater than about 1 mm^2 becomes difficult to strand and wind) and the length of the wire. Stranding of the wire is done in-house; a maximum wire length of about 25 m can be stranded with the available space.

By the choice of efficiency in the performance specifications of (4.19), and the choice of k in (4.3), the eddy current losses must be limited to 0.0075 p.u.. The required output voltage is determined by the intended load. Plans for the LG include testing with an active rectifier with a dc–bus voltage of 300 V. It is as such decided to limit the output phase voltage to below 150 V. By ignoring the internal voltage drop and limiting the peak EMF of (3.9) at the peak velocity to below 150 V, an added degree of safety exists. The converter is discussed in more details in the next chapter.

With 38 stator sections, and one coil per phase per stator section, there are only four possible options for parallel circuits, namely a = 1, 2, 19 or 38. By selecting a value for a and N, the peak induced voltage can be determined from (3.9). With a = 1, choosing N = 40 results in E_p = 128 V at the maximum velocity of V_p = 1.06 m/s. This is well within the limit of 150 V as specified. The resulting wire length is also calculated as ℓ_w = 10 m, which is also well within the limit of 25 m. With E_p known, the peak rated current can also be calculated from (2.6) as I_p = 9.96 A. The rms induced voltage and current is calculated from (2.8) as E_g = 64 V and I = 5 A.

With chosen values of a and N, The choice of n_c now determines the eddy-current losses and the required wire diameter. Care must be taken to select a value of n_c which results in a practical wire diameter as mentioned before. In this case, with n_c = 16, a wire diameter of 0.52 is obtained, while the resulting eddy-current losses are

Table 4.3 – Different options for the winding design.

Parallel circuits a	1	2	19	38
Turns per coil N	40	80	760	1520
Wire length ℓ_w	10	20	188	376
Parallel strands per coil turn n_c	16	9	1	1
Wire diameter d_w (mm)	0.52	0.49	0.48	0.34
Eddy current losses P_e (p.u.)	0.007	0.006	0.006	0.003
Efficiency η (%)	84.6	84.7	84.7	85.0

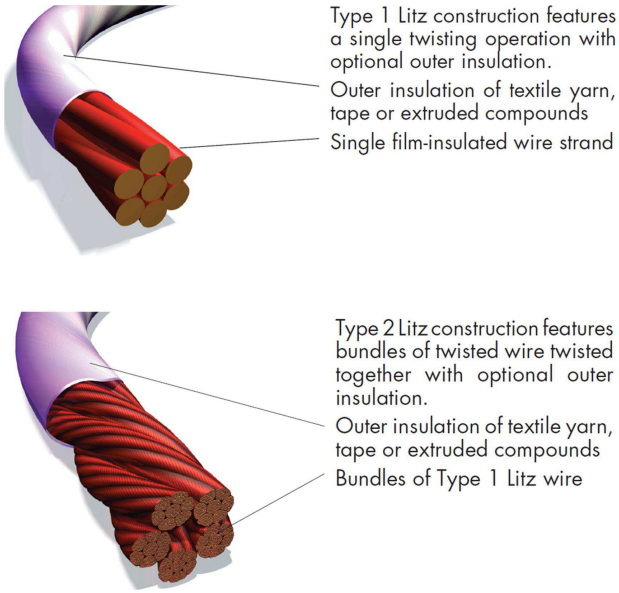

Fig 4.3 Type 1 (above) and Type 2 (below) litz wire used to minimise eddy current losses in the windings [109].

0.007 p.u. The wire diameter is slightly larger than the readily available and easy to work with size of 0.5 mm and 16 strands can easily be stranded as a type 2 Litz wire with 4 bundles of 4 strands each, as shown in Fig. 4.3 [109]. The eddy current losses are within the originally calculated limit; however, with the copper losses higher than initially calculated, the overall efficiency is 84.6 %, only slightly less than the specified η = 85 %. The other options for the windings are given in Table 4.3.

The options with a = 19 and 38 are discarded due to the huge number of coil turns and also the long wire length required; these aspects will make manufacturing very laborious. In terms of performance there are not much difference between options with a = 1 and a = 2. The former is chosen simply because fewer coil turns are required and, more importantly, because no coils will have to operate in parallel; coils operating in parallel simply increase the risk of additional losses due to circulating currents.

4.4 Translator length

It is normally desirable for the stator winding to be within the PM generated field at all times, as is the case for normal rotary machines. If part of the stator winding is outside the PM field, it becomes inactive and only contributes to conduction losses. For the whole stator winding to be active during the entire stroke length, as shown for Case A in Fig. 4.4, the translator length must be

$$L_t = L_{st} + L, \tag{4.20}$$

where L_{st} is the stroke length and L is the stator (active) length. The stator length for the novel LG is determined in the analytical design where it is assumed that the whole stator winding is active all the time. Furthermore, the stroke length is determined by the wave height of the intended installation site for the WEC. From (4.20) it can therefore be appreciated that the translator can be very long and expensive if the stator winding is to be active all the time.

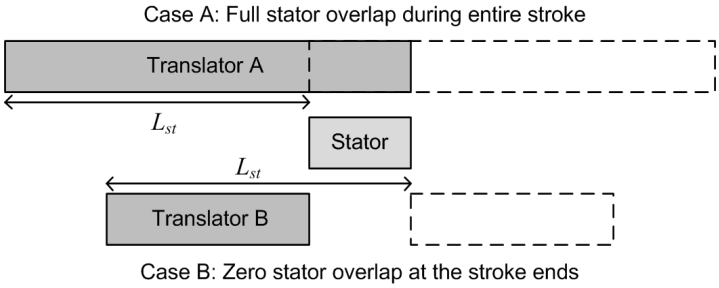

Fig. 4.4 For a fixed stroke and stator length, the difference in translator length is illustrated here where full stator–translator overlap is maintained during the entire stroke (Case A) and where zero overlap is allowed at the stroke ends (Case B).

An alternative approach followed for the air-cored LGs in [48] and [56] is to purposefully make the translator shorter than the stator in order to save on PM cost. Measures are however needed to switch the inactive coils out of the circuit such that they do not contribute to conduction losses. In [48] a displacement transducer is used to determine when to switch each stator coil in or out with a triac. In [56] all the stator coils are paralleled onto a common dc-bus through individual boost converters; the converters effectively isolate inactive coils from the dc-bus. The large number of power electronic components needed for these schemes is however a drawback.

For the novel LG it is decided to follow a different approach. Since the translator velocity is at its lowest at the stroke ends, the instantaneously generated power at the stroke ends is also at its lowest and makes a very small contribution to the overall average power. It is therefore theorised that by allowing the translator to move beyond the stator windings at the stroke ends, as shown for Case B in Fig. 4.4, a saving can be made on the translator cost with a small sacrifice in performance; it is therefore expected that the power-to-weight ratio of the LG can overall be improved this way. For Case B, the translator length is then given as

$$L_t = L_{st} - L. \tag{4.21}$$

From (4.20) and (4.21) it is clear that, for a given stator and stroke length, the translator can be significantly shorter, and cheaper, in Case B than in Case A. For the novel LG it is therefore decided to investigate Case B. Since the prototype is only intended for laboratory testing, the stroke length is chosen based on the drive system, rather than any specific wave climate. From (4.21), the drive system allows for a translator length of $2L$, giving L_t = 448 mm and L_{st} = 672 mm. Details of this drive system are discussed in Chapter 5.

For the average power as given in Chapter 2.5, full stator-translator overlap during the entire stroke is assumed. The affect of the chosen configuration on the generated power, among other things, is investigated with finite element analysis in the next section.

4.5 Finite element method verification

As mentioned in Chapter 3.2, the PMs in the prototype LG have small indentations on both sides to facilitate fixation. This is explained in more detail in Section 4.7 and in Chapter 6. These indentations have an effect on the air gap flux density distribution, and hence on the induced EMF. In the subdomain model developed in Chapter 3.2.1, these indentations are ignored in order to avoid over complicating the model. In the FEA model used

for verification in Chapter 3.2.2, the indentations are also neglected; the reason for this is that the subdomain model itself is there verified and comparing the result to reality is not of concern. In this section the air gap flux density, induced EMF and force is calculated from an FEA model taking the indentations into account to get a better indication of the actual performance which is to be expected.

4.5.1 Air gap flux density

The air gap flux density (in the middle of the air gap) calculated from the new as built FEA model is shown in Fig. 4.5(a) together with the FEA solution from Chapter 3 (with not PM indentations). It is clear that there is a slight deviation in the shape of the two solutions. In general, however, there is still good agreement between the two solutions and the two peak values of 0.695 T and 0.701 T respectively are almost equal and also very close to the one dimensional solution of 0.7 T. The fundamental component of the as built FEA calculated air gap flux density is shown in Fig. 4.5(b); it is calculated by doing a Fast Fourier Transform (FFT) and it is found that $B_{p1} = 1.034B_p$. The quality of the air gap flux is further analysed indirectly by calculating the EMF induced by the flux.

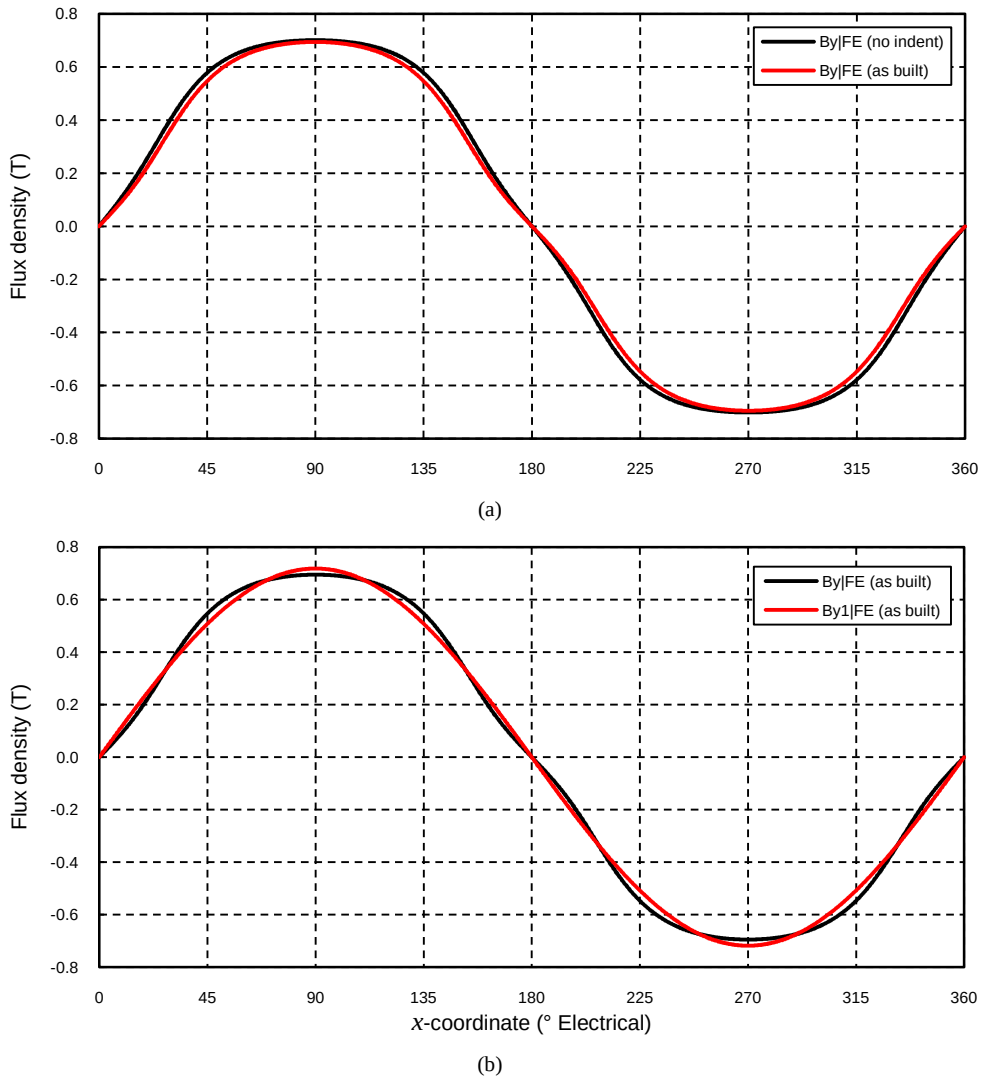

Fig. 4.5 Flux density along line a-a in Fig. 3.8(b). (a) A comparison of the models with and without the PM indentations, and (b) the fundamental component compared to the total air gap flux density of the as-built model.

4.5.2 Constant velocity simulations

Simulations at a constant velocity of 0.75 m/s are conducted in order to verify the analytical design; for this reason full stator–translator overlap is at all times assumed for the constant velocity simulations.

4.5.3 Induced EMF

In order to find the EMF induced in the stator windings, the stator flux linkage, $\lambda(x)$, is calculated at different positions (x) of the stator relative to the translator. The induced voltage is then calculated as

$$e_g(t) = \frac{d\lambda(t)}{dt} = \frac{d\lambda(x)}{dx} \times \frac{dx}{dt} = \frac{d\lambda(x)}{dx} \times v(t), \tag{4.22}$$

The translator is stepped through π electrical radians, and the flux linkage calculated by FEA at each step. The EMF is then calculated from (4.22) and the resulting EMF for 38 stators in series is shown in Fig. 4.6. The peak value of the FEA-simulated EMF is found as E_p = 95.7 V (with E_g = 95.7 / √2 = 68 V), which is about 6 % higher than the analytically obtained value of E_g = 64 V. This can possibly be partly attributed to the slightly higher peak air gap flux density closer to the magnet surface and voltages induced in the end-windings. Furthermore, it can be observed that the EMF is very close to sinusoidal. The actual calculated total harmonic distortion (THD) for the simulated waveform is less than 0.1 %.

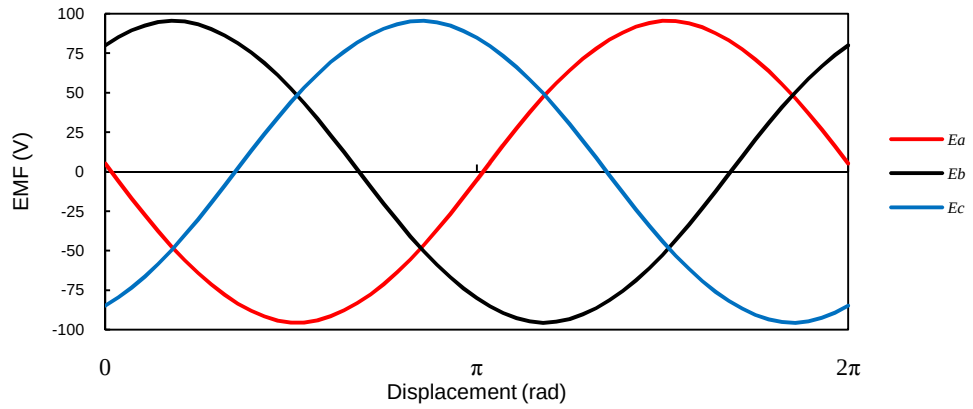

Fig. 4.6 Simulated three-phase stator EMFs for a constant velocity of V = 0.75 m/s.

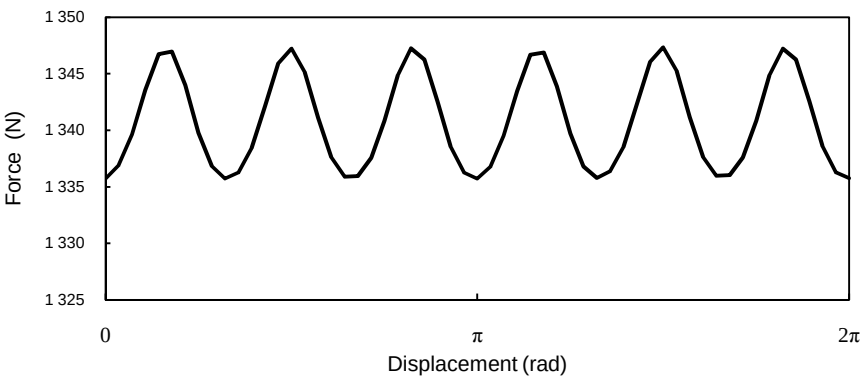

Fig. 4.7 Simulated generator force with V = 0.75 m/s.

4.5.4 Developed force

The developed force is obtained directly from the FEA by injecting the rated current (I = 5 A) on the q-axis (i.e. forcing the current in phase with the EMF). The translator is again stepped through π electrical radians and the resulting force is shown in Fig. 4.7. A small ripple, as can be expected from a three-phase excitation, is evident. The average force obtained is F_g = 1342 N and is also about 6 % higher than the analytically calculated value of 1275 N; this is probably due to the same reason as explained for the higher EMF found above. The ripple is calculated as less than 1 % of the average force.

4.5.5 Impedance calculation

The FEA model is also used to verify the resistance and inductance calculations. Using the known end-winding length, from (3.53), the FEA resistance calculation is scaled up to include the end-winding resistance; the result is the same as the analytically calculated value of 1.9 Ω. This equates to a per unit value of R_s = 0.17 p.u, which is rather high. The reason for this is the increased active material (copper, in this case) needed to compensate for the low speed of DD-WECs.

The inductances are calculated from FEA as also done in Chapter 3.3.6. No provision is made for an analytical calculation of the inductance with the one-dimensional analysis used for the prototype design. The FEA solution can hence only be used to verify an analytical inductance solution obtained from subdomain analysis or it can here be used to obtain the inductance values where it is not known.

The synchronous inductance is calculated as 6.1 mH. At the average speed of V = 0.75 m/s, the synchronous reactance of the novel LG is given as

$$X_s = \omega L_s = \left(\frac{\pi p}{L}\right) V L_s, \tag{4.23}$$

and results in a per unit value of X_s = 0.026 p.u. It is clear that the phase reactance is significantly smaller than the phase resistance. The resulting load angle is 8.7°.

As mentioned before, the end windings are not modelled in the 2-D FEA model, and their effect on the inductance is therefore not taken into account. In [63], the end-winding inductance is calculated with an analytical equation after the active winding inductance was also calculated from FEA; the same approach can be used here, however, since the reactance as calculated here is so small, it is decided to ignore the end-winding inductances.

4.5.6 Discussion

A summary of the FEA calculated parameters of the novel LG is given in Table 4.4 along with the analytically calculated values. Overall there is very good agreement between the two sets of results; this, to some extent, verifies the analytical design.

Table 4.4 Analytical and FEA obtained parameters for the prototype novel LG. All analytical values are calculated from the one-dimensional analysis, except for the synchronous inductance, which is calculated from subdomain analysis.

v = 0.75 m/s	Analytical	FEA
Peak air gap flux density B_p (T)	0.7	0.69
RMS induced voltage E_g (V)	64	68
Phase resistance R_s (Ω)	1.9	1.9
Synchronous inductance L_s (mH)	6.17	6.1
Total developed force F_g (N)	1275	1342
Total generated power P_g (W)	956	1007
Copper losses P_{cu} (p.u.)	0.146	0.146
Eddy-current losses P_{ec} (p.u.)	0.007	-
Efficiency η (%)	84.7	-

There are, however, inherent 3D effects in this machine which the 2-D model ignores. This includes the flux circulating transversely around the machine, the varying magnet thickness and the end-windings. The 2-D FEA model shown in Fig. 3.21 tries to analyse some of these aspects to some extent, but 3-D FEA would be more accurate in predicting the novel LG's performance. The increased processing power and time needed for 3-D simulation is for now however not considered worthwhile.

4.6 Sinusoidal velocity simulations

Since the translator length is such that the stator-translator overlap will vary (from Section 4.4), analytical solutions for the actual EMF and force is difficult to calculate; this is especially true when the translator is reciprocating with a sinusoidal displacement profile. FEA is hence also used to get an indication of the novel LG's output under sinusoidal translator displacement and to study the effects of the varying stator-translator overlap.

4.6.1 Induced EMF

The same procedure as explained in Section 5.3 is also followed to calculate the EMF for a sinusoidal velocity. However, the translator is this time stepped through its entire stroke length to gain an idea of what the actual waveform of the LG will look like. The simulation is done for the case where there is full stator-translator overlap during the entire stroke (Fig. 4.8, Case A from Section 4.4) and also for the case where there is zero stator-translator overlap at the stroke ends (Fig. 4.9, Case B from Section 4.4). The wave form for Case B is the same as for Case A during the middle of the stroke when all the stator windings are within the PM field. However, the EMF clearly reduces to zero sooner as the stator–translator overlap decreases to zero at the stroke ends. In this particular LG, the unbalance between the phase voltages are also evident at the stroke ends.

4.6.2 Generated Power

The generated instantaneous power during a full stroke length is calculated from the induced EMF and the current forced through the windings. The current is again forced in phase with and directly proportional to the EMF; the constant of proportionality is calculated as

$$k_r = \frac{I}{E_g} = \frac{5}{68} = 0.074. \tag{4.24}$$

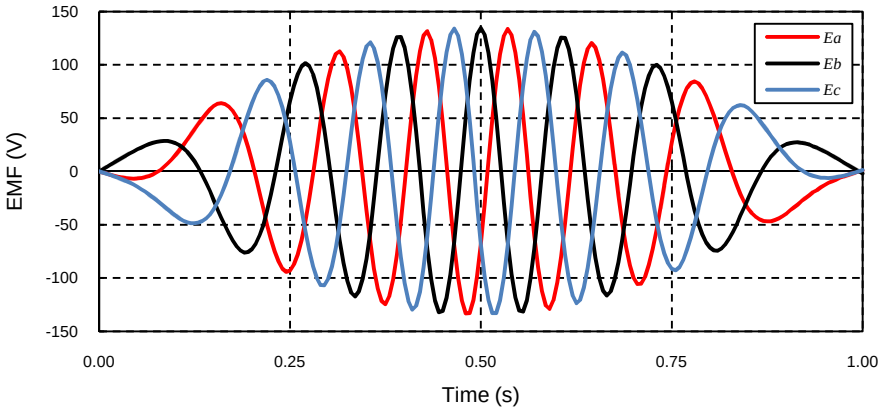

Fig. 4.8 Case A: Stator EMF for a sinusoidal velocity with V_p = 1.06 m/s with full stator-translator overlap during the entire stroke.

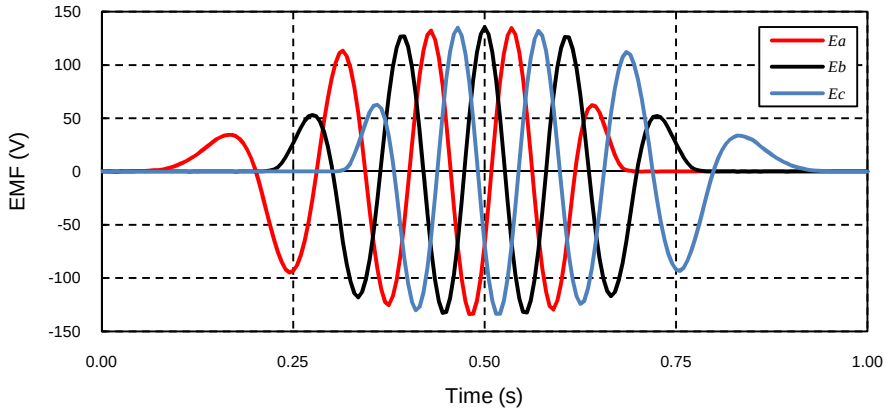

Fig. 4.9 Case B: Stator EMF for a sinusoidal velocity with V_p = 1.06 m/s with zero stator-translator overlap at the stroke ends.

In Fig. 4.10 the instantaneous power for both Case A (P_{gA}) and Case B (P_{gB}) are shown. For Case A the average power over the stroke equals P_{gA} = 1005 W and resembles the shape of a squared sinus as is expected. For Case B, large dips in power occur at the stroke ends; this is because only one phase becomes active at first, with the other two phases becoming active in turn thereafter. With the currents assumed in phase with and proportional to the EMFs as is done here, the average power over the stroke equals P_{gB} = 734 W. Taking the per unit power per translator mass as unity in Case A, the per unit power per translator mass in Case B is 1.46 p.u., as given in Table 4.5. Although the length of this LG is not designed for a real sea state, this result shows that, from a cost perspective, it can make sense to allow for zero overlap between stator and translator at the stroke ends.

The loss of translator control at the stroke ends will need to be taken into account though. Careful consideration should be given to whether this situation is allowable for an actual DD-WEC installation. Furthermore, a large degree of phase unbalance is observed near the stroke ends in Fig. 4.9, which causes large dips in power as shown in Fig. 4.10. This is of course highly undesirable and is made worse by the particular prototype stator winding layout, which has only one concentrated coil per phase along the whole length of the stator. However, for a larger LG, it is expected that more coils per phase will be distributed along the length of the stator which will considerably reduce the dips in power observed in Fig. 4.10.

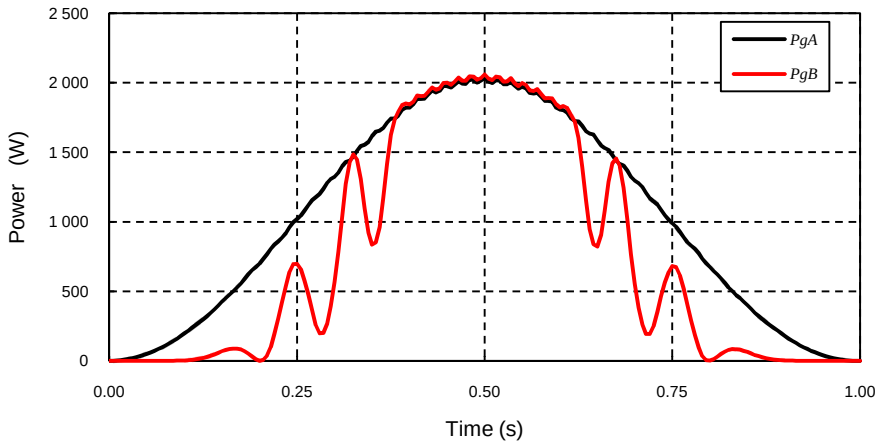

Fig. 4.10 Simulated LG generated instantaneous power for Case A (P_A) and Case B (P_B).

Table 4.5 Comparison of LG generated average power for Case A and Case B.

$v = \sqrt{2}\times 0.75\sin(\omega t)$ m/s	Case A	Case B
Generated power (p.u.)	1	0.73
Translator mass (p.u.)	1	0.5
Power / translator mass (p.u.)	1	1.46

4.7 Mechanical design aspects

A detailed structural and thermal design is beyond the scope of this work. Inherent to the novel topology is the ideal elimination of magnetic attraction forces between the stator and translator, as well as ideal elimination of forces between the PMs in the translator. Furthermore, the small scale of the prototype and the low current density of 1.45 A/mm^2 negate the need for thorough thermal design at this stage. Further work in these areas is needed though. This section only serves to outline the construction and assembly plan for the novel LG.

4.7.1 Stator design

Air-cored stator windings have been manufactured at Stellenbosch University for a number of years. Stranding and winding the coils are rather straightforward. The challenge for a novel machine topology is in designing an appropriate mould for casting the coils into epoxy resin. The epoxy primarily serves as mechanical support for the windings, but also functions as electrical insulation between coils and between individual turns and strands of windings.

The mould needs to allow for easy insertion of the windings, access for casting the epoxy into the mould and for easy removal of the finished stator section. The mould itself also needs to be robust enough to be re-used numerous times. Experience has shown that manufacturing the mould in separate parts makes inserting coils and removal of the stator sections afterwards the easiest. However, the different parts of the mould must fit together very precisely for each stator section to be the same.

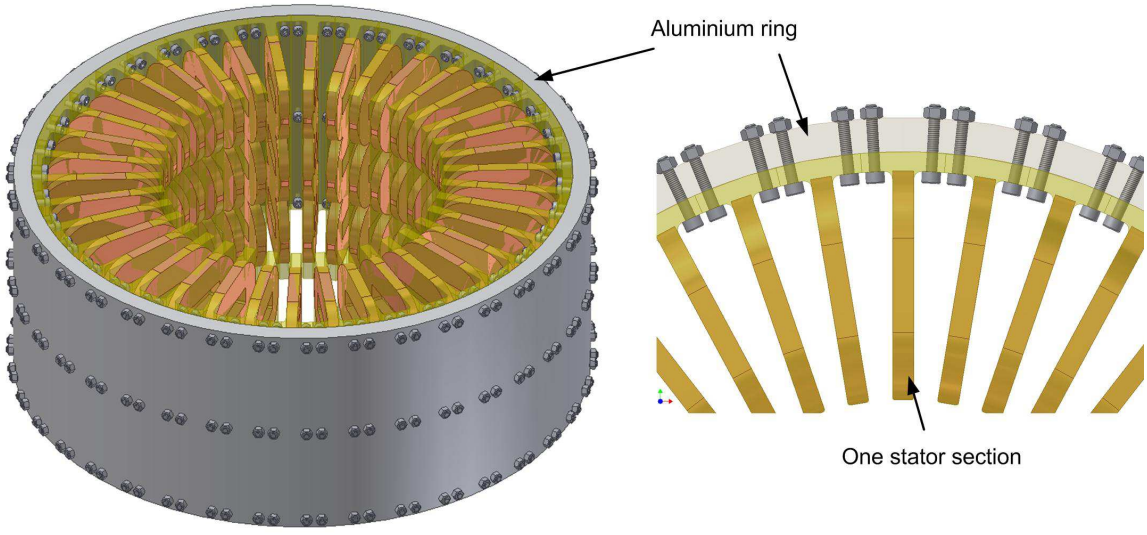

(a) (b)

Fig. 4.11 CAD model of the stator showing (a) a 3-D view and (b) the stator section fixation as viewed from the top.

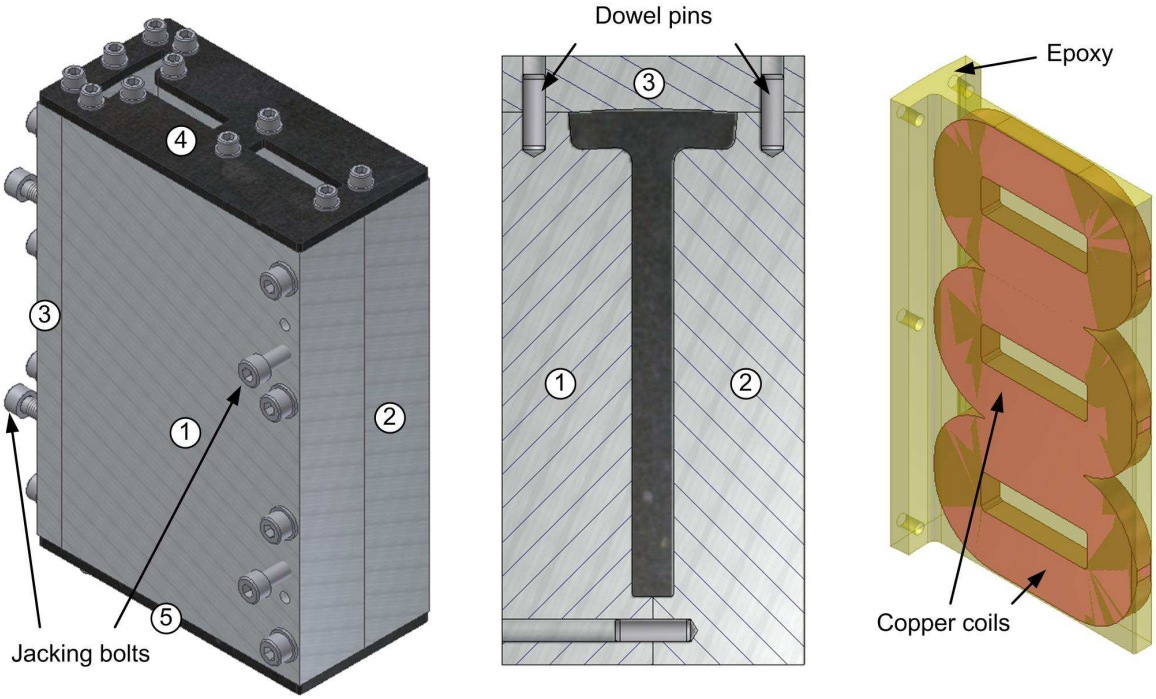

(a) (b) (c)

Fig. 4.12 (a) A 3-D CAD model of the stator mould, (b) a sectional view of the stator mould and (c) one stator section.

In the novel LG, all the different stator sections must be bolted to the inside of an aluminium ring as shown in Fig. 4.11. The different sections therefore need to fit flush against the inside surface of the ring, with a shoulder on either side where the stator section can be bolted to the ring as shown in Fig. 4.11(b). The mould design is shown in Fig. 4.12. It consists of 5 parts. Parts 1 - 3 shown in Fig 4.12(a) and (b) form the bulk of the mould and is manufactured from solid blocks of aluminium by computer numeric control (CNC). Aluminium, although more expensive than steel, is much less costly to machine into intricate shapes, as is required here. The top and

bottom parts (4 and 5) are laser-cut from steel and keep the coils in place. An opening in the shape of a stator section profile is cut in part 4; this allows the resin to be cast into the mould and also for air to escape. The different sections are located relative to each other with dowel pins (as shown in Fig 4.12(b)), for repeated accurate assembly, and bolted together. Jacking bolts as shown in Fig. 4.12(a) are used to aid in opening the mould after the resin is cured.

4.7.2 Translator design

The translator has a rather intricate shape. For mass-production, moulding the translator into shape may be the easiest, although it is too expensive for a prototype. In concept, the translator basically consists of number of identical layers in the longitudinal directional; it is therefore decided to also manufacture it as such. Layers of non-magnetic material are cut into shape, as shown in Fig. 4.13, by waterjet. These layers are all stacked over a centre column. Layer one serves as a spacer between consecutive magnet layers, layer two and three serves to position the magnet at the correct radial depth and layer four gives structural support for the magnets. Although there are in theory no attraction forces between magnets, manufacturing and assembly tolerances will cause a small net attraction force in either direction. Layer four is therefore manufactured from non-magnetic stainless steel (Stainless steel 316) to provide good structural integrity. The other layers are manufactured from polyethylene terephthalate (PET), a kind of engineering plastic with excellent rigidity and dimensional stability.

The magnets are ordered from a manufacturer in China in the shape as shown in Fig. 4.14. The grooves at the top

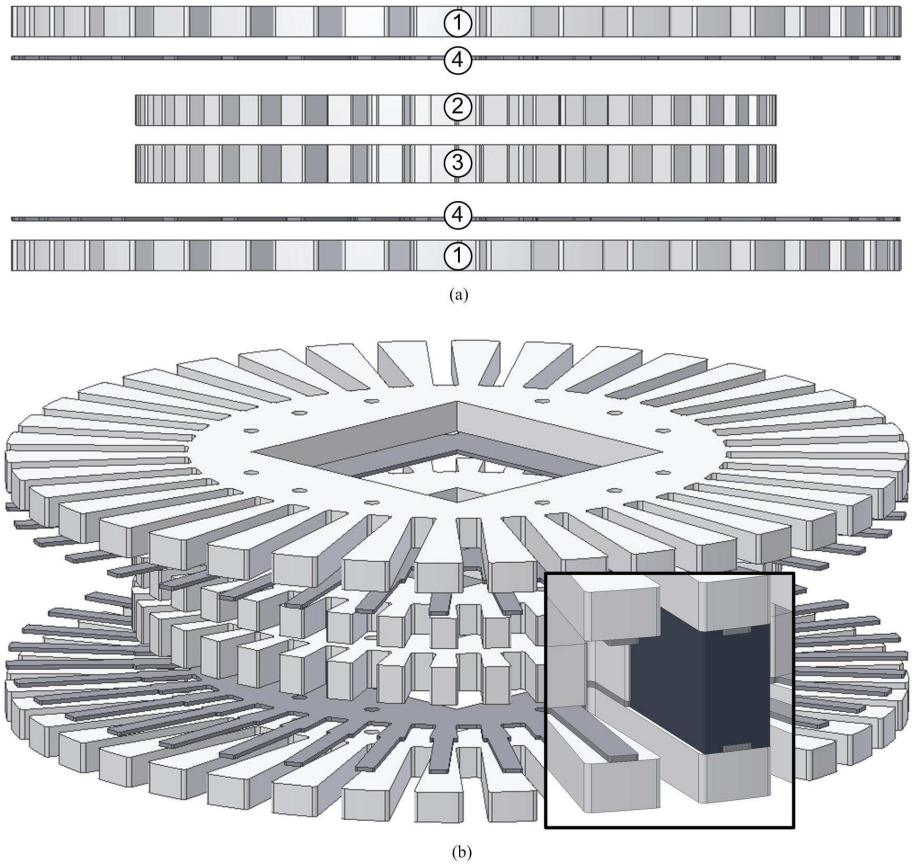

Fig. 4.13 3-D CAD model of the different layers of the translator. The insert shows one magnet inserted into the translator.

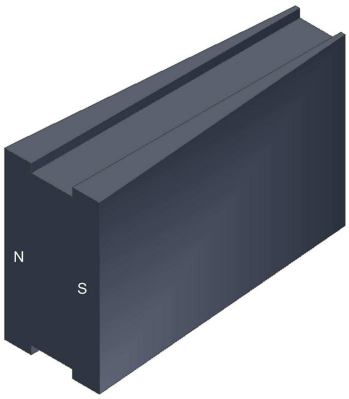

Fig. 4.14 3-D CAD model of one magnet, indicating the magnetic poles.

and bottom fit over the stainless steel layers as shown in the insert in Fig. 4.13; the magnets are therefore supported for a net attraction force in either direction. After the different translator layers are assembled, the magnets are simply slid into place from the outside. The magnets are therefore not bolted into place and no adhesives are used. Due to the flux circulating transversely around the machine, all the magnets are also pulled towards the centre of the machine, which further serves to keep the magnets in place. The three-dimensional CAD assembly of the entire translator is shown in Fig. 4.15. Two non-magnetic stainless steel plates are added to the two ends of the translator stack. The end plates extend slightly beyond the other layers in the radial direction. Stainless steel rods are inserted through these extensions at each row of magnets. This helps to secure the different layers and magnets together and the resultant “cage” provides a degree of mechanical protection to the magnets.

4.8 Conclusion

The analytical modelling and design optimisation presented in this chapter enables optimal dimensions for minimum active mass to be found quickly. FEA enables verification of this design, as well as additional insight into aspects which are difficult to analyse analytically; this specifically include voltage and power waveforms for a varying stator–translator overlap. Together, analytical and FE analysis are sufficient tools for the 1 kW prototype design. For larger machines, however, a thorough mechanical design would also be required.

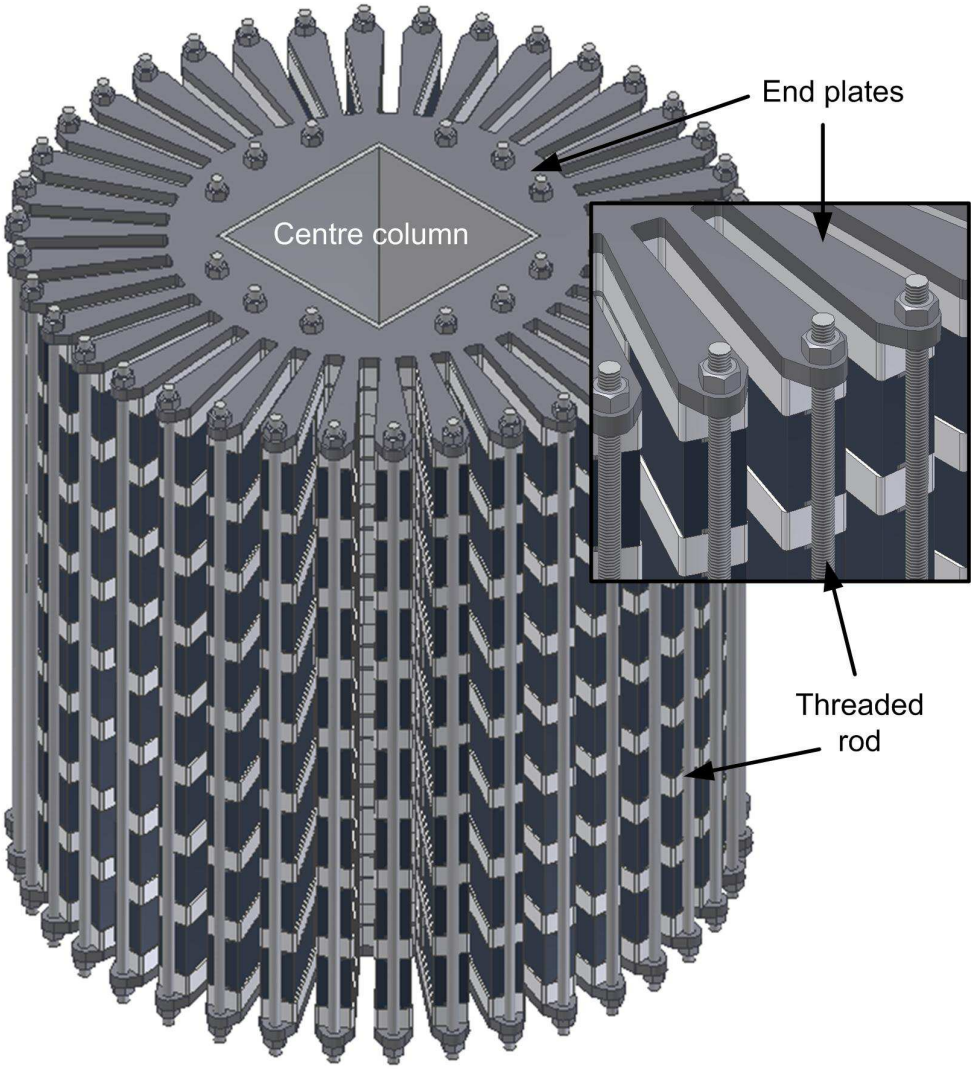

Fig. 4.15 3-D CAD model of the fully assembled translator.

Chapter 5

Drive system and control design

A suitable test rig to enable laboratory testing of the prototype LG is needed. In this chapter an overview of existing test rigs for LGs are given and a suitable system for the prototype LG is designed. An overview of current LG control schemes is also given where after an alternative control scheme is considered for the novel LG control. The control scheme is simulated in Ansys Simplorer for verification. This work has been published in [118], [119] and is given here again for completeness.

5.1 Existing LG test rigs

Electrical machine laboratories are commonly equipment with a standard induction motor and drive which can be used to test any kind of rotary generator. Linear test rigs are however less commonplace. Different stroke lengths and displacement profiles for different applications also mean that one test rig is less likely to be suitable for other applications. This is evident when looking at the custom test rigs that were developed for laboratory testing of LGs in [43], [48], [53], [56] and [58]; these include vertical [43], [112], and horizontal [48] hydraulic drive systems, cable-and-pulley systems [53], [58], a rotary-to-linear crankshaft mechanism [80] and a VSD with a worm-and-ball gear [56]. In addition to these prime movers, control hardware and software are also needed to simulate wave motion under a varying generator load. Developing a drive system for testing LGs can thus become a project on its own with considerable cost.

5.2 Proposed test rig

It is decided to mount the translator horizontally on a test bench with its stator suspended on linear tracks. Horizontal translation avoids having to continually oppose gravity when reciprocating and, since the stator is much lighter than the translator, it is easier to move rather than the translator. The test rig has to provide the stroke length of 0.672 m (from Chapter 4, Section 4) and input power in excess of the peak instantaneous LG power of 2 kW. Furthermore, as the design simulations are done at a sinusoidal velocity, the prime mover displacement must be controlled to be sinusoidal under a varying LG load in order to verify and compare with the simulations. Lastly, cost is also an important consideration and as such it is decided to try and make use of existing equipment where possible.

These considerations all led to the decision to use a rotary-to-linear crank mechanism. This is because an experimental 20 kW 40-pole PM wind turbine generator (WTG) was available for use; the project where it was used had come to an end and there was no other use for it. The WTG conveniently has an outside diameter of about 0.7 m, which is more than sufficient to achieve the necessary stroke length, and a rating far in excess of the peak LG rating. Furthermore, back-to-back 2-level IGBT voltage source converters (VSCs) with a digital signal controller (DSC), which were used for grid-connection of the WTG, were also available. One side of the con-

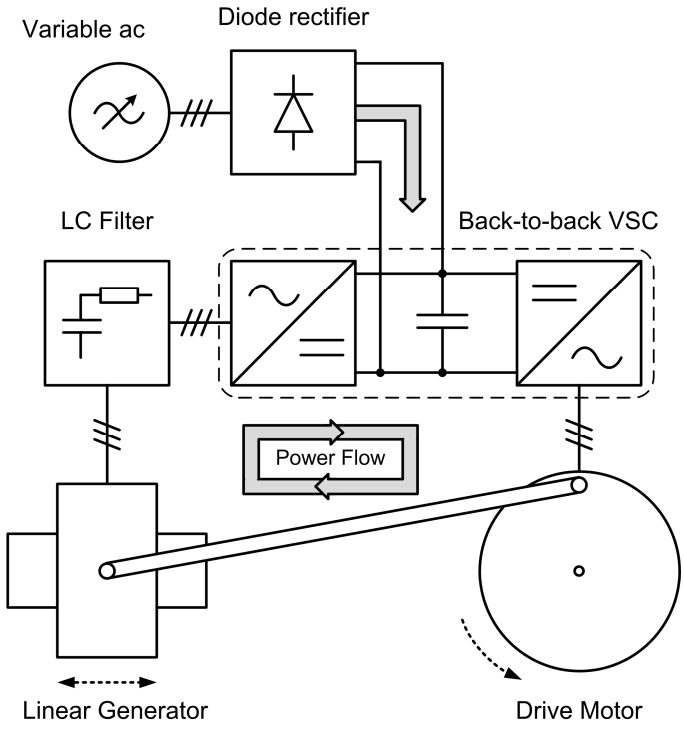

Fig. 5.1 Schematic representation of the proposed test setup.

verter can therefore be used as an inverter to control the WTG's speed and the other side can be used as an active rectifier for the LG control. All the requirements of the test rig are therefore met with existing equipment, and a converter for the LG control is also included.

A few minor modifications to the system are needed though. The first of these is to fit a crankshaft between the LG and the WTG (or the "drive motor" as it will be referred to from now on). The energy in the system is effectively circulated through the drive motor, the LG and the dc-bus. In order to account for the losses in the system, a diode rectifier is added to the dc-bus. A variable three-phase ac supply can then be used to charge up the dc-bus through the diode rectifier and also to feed the losses in the system. The system schematic is shown in Fig. 5.1, with a more detailed layout of the VSCs shown in Fig. 5.2.

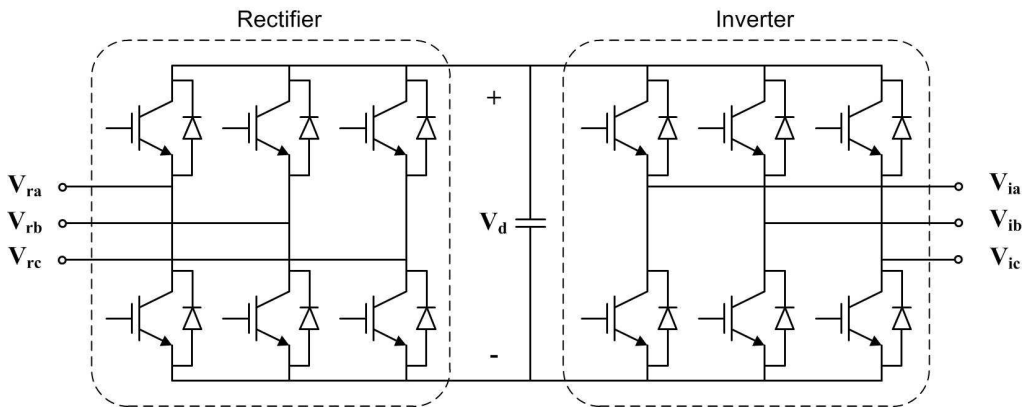

Fig. 5.2 Topology of the two-level back-to-back IGBT voltage source converters.

A filter is installed between the active rectifier and the LG. The main reason for this is that the LG's terminal voltage must be measured in the control strategy described in Section IV.B, and hence the high switching frequency must be filtered out. There are however also a number of other reasons why the use of a filter is justified. PWM voltages applied to machines have been shown to cause a number of undesirable effects, as for instance discussed in [112], [113], [114]; this includes excessive winding insulation stress due to high *dv*/*dt* and voltage reflections when the cable between the machine and drive is long. Radiated and conducted electromagnetic interference (EMI), which can respectively cause malfunction of electronic devices and additional systems losses, are also problematic. These unwanted effects can be reduced, if not eliminated, with a filter. A simple LC-filter is a robust and cost-effective solution [113] and is hence used here. Since the LG operates at very low frequencies, the voltage drop across the filter is expected to be almost negligible.

It should be noted that no provision is made for grid connection of the LG output. In a real wave power plant, the power from a number of DD-WECs will probably feed onto a common dc-bus from where it will then be inverted to the grid [45], [46]. Connecting the output from one LG to the grid is therefore deemed as an unnecessary exercise here.

5.3 DD-WEC control issues

The problems with current DD-WEC control strategies are briefly outlined in the problem statement in Chapter 1. A more comprehensive overview is given here. Keep in mind, as this is a direct drive WEC (i.e. with no intermediate mechanical energy conversion stages), it is assumed that the power absorbed by the WEC is also the power transferred to the LG. It is therefore assumed that there are no losses in the mechanical to electrical energy conversion process in the DD-WEC. This process is depicted in Fig. 5.3.

5.3.1 Energy conversion from the waves to the WEC

The mechanics of energy conversion from the *ocean waves to the WEC* are discussed in Appendix A. For opti-

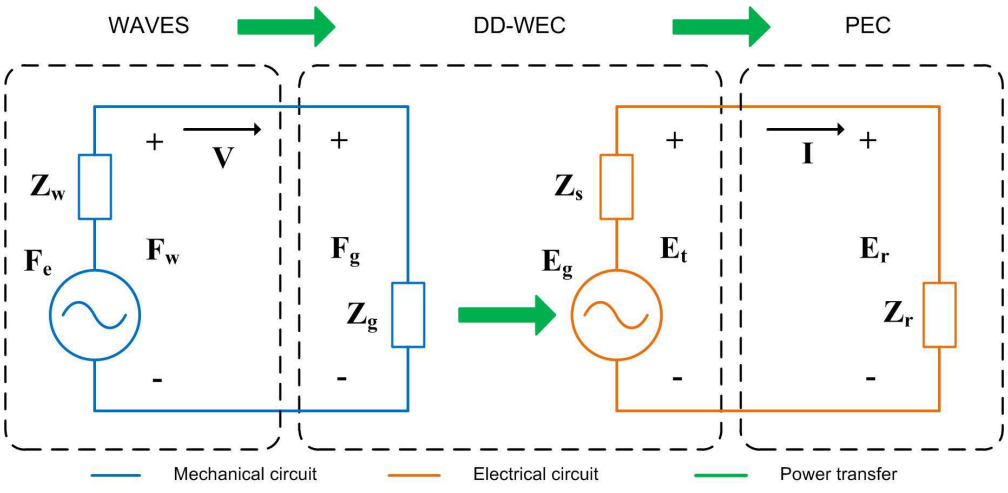

Fig. 5.3 The energy conversion process from the waves to the PEC for a DD-WEC.

mal energy conversion in this process, an effective resonance condition is needed in the system; this translates into the WEC velocity having the correct amplitude while also being in phase with the incident wave force. This can be achieved by adjusting the WEC's mechanical impedance ($\mathbf{Z_g}$ in Fig 5.3), and hence the WEC reaction force $\mathbf{F_g}$, to equal the complex conjugate of the wave impedance ($\mathbf{Z_w}$ in Fig 5.3), either by mechanical actuators, or electrically.

Much research on phase and amplitude control of point absorbers were done since the 1970s and is summarised in [13], [21], [115], [116]; mechanical actuators were envisaged in the control of the WEC impedance, either with hydraulic or pneumatic machinery. The AWS is a fairly recent example of where mechanical control was exercised to adjust the air-pressure and volume inside the device, and hence the mechanical impedance, to always maintain resonance [40]. Adjusting the mechanical impedance (or reaction force) by controlling the LG current is investigated, more recently, in [57], [58], [59]. Device reaction force control, as it is called in [57], [58], is achieved with a PEC and has obvious advantages over mechanical actuators, e.g. faster operation, lower maintenance and greater flexibility. However, a fundamental problem with this method of control is discussed in the next section.

5.3.2 Energy conversion from the WEC to the load

Since the LG output varies in amplitude, frequency and phase sequence (for a three-phase generator), a PEC is always needed for grid connection of a LG. It is therefore safe to assume that the LG load will always be a PEC. Whatever the load though, the electrical system is, in concept, basically the same as the mechanical system, as shown in Fig. 5.3: the PEC is used to control the load (active rectifier) voltage $\mathbf{E_r}$ (analogous to reaction force $\mathbf{F_g}$) such that the current $\mathbf{I}$ (analogous to velocity $\mathbf{V}$) has the correct amplitude and is in phase with the generator EMF $\mathbf{E_g}$ (analogous to excitation force $\mathbf{F_e}$).

It has been shown that device reaction force control (as explained in Section 5.3.1) will always cause a phase difference between the LG's EMF and current, as reactive power needs to be returned to the wave during part of the wave period [12], [57], [58]; this can be seen as the reactive component of the power needed to establish the imaginary component of $\mathbf{Z_g}$, as explained before. The point, though, is that the condition for maximum power transfer between the LG and load is now compromised, as the LG's EMF and current is forced to have a phase difference.

5.3.3 Practical control issues

Contrary to device reaction force control, the mechanical energy conversion stage (from the waves to the WEC) is ignored in some sources and the only focus is on energy transfer between the LG and the load [56], [60]. Whatever approach is used, an estimation of the generator EMF is always needed for the control strategies; this is because the EMF is constantly changing with the changing translator velocity. Obviously, the EMF cannot readily be measured while on load. In [44], [58], [60], [117], sense coils are mounted on the stator, and in [56], sense coils are wrapped around the stator winding, for EMF estimation. Linear position feedback is also used in [53], [59] for *dq*-transformation of the voltage and current.

The authors of [60] admit that the use of sense coils is a cumbersome practice and that sensorless methods should rather be investigated. Linear position sensors would also be expensive and difficult to install for long stroke lengths needed for real LGs; these should therefore also be avoided as far as possible.

5.4 Proposed control strategy

The novel LG is not device specific, meaning that it can potentially be installed in any type of DD-WEC as shown in Chapter 1. Because of this, and also because the drive system does not cater for it, optimal mechanical energy capture is not considered here and the focus will only be on controlling power transfer between the LG and load. As far as can be determined, predictive control, an inherently digital type of control, has never been investigated for LG control in DD-WEC applications. With the availability of the DSC it is therefore decided to investigate predictive control for the novel LG.

5.4.1 Predictive control principle

In this paper a dead-beat control strategy, as discussed in [118], [119], is proposed for the LG current control. Dead-beat control is a type of predictive control [120]; the principle of this inherently digital type of control is to calculate the PEC voltage necessary to force the measured current to its reference value by the following modulation period [118], [120]. Calculation of the PEC voltage reference must be based on an accurate system model and accurate knowledge of the system parameters such as resistance and inductance [118].

Similar to predictive control, the system model is also used to calculate the stator flux linkage in one type of position-sensorless control [121]. Instead of using a position sensor, the calculated stator flux-linkage is then used to derive position information which can be used in the chosen control strategy. Predictive control can therefore be seen as one way of achieving sensorless control, as for instance in [122]. In this paper a similar approach is also used to calculate the EMF without the use of position feedback or estimation; this is further discussed in the next section.

Space vector pulse width modulation (SV-PWM), which is ideally suited to digital control, is used to generate the IGBT gating signals as discussed in [123]. For this, the measured current and voltages should first be transformed to the stationary two-coordinate $\alpha\beta$-reference frame. It is often preferred to transform measured quantities to the synchronously rotating dq-reference frame where all electrical quantities are constant at steady-state [124]. For the constantly changing translator velocity of a LG there is however no steady-state and hence even in the dq-reference frame electrical quantities are constantly changing, as for instance shown in [59]. In addition, translator position feedback or estimation and decoupling transformations are needed in order to do control calculations in the dq-reference frame. In order to avoid especially the translator position feedback or estimation, control calculations are here done in the $\alpha\beta$-reference frame. The same approach is followed for predictive control in [118], [125], [126]. In [126], control calculations are done in both the $\alpha\beta$ and dq-reference frame and similar results are demonstrated in both cases.

5.4.2 Predictive control implementation

A single line diagram of the LG connected to the active rectifier through the LC-filter is shown in Fig. 5.4. It is assumed that only the switching frequency currents flow through the filter capacitor C_f; these currents are ignored and it is as such assumed that the measured active rectifier current **I** is the same as the LG current. In terms of the measured instantaneous LG terminal voltage $e_t(t)$ and instantaneous active rectifier current $i(t)$, the active rectifier voltage $e_r(t)$ is given as

$$e_r(t) = e_t(t) - L_f \frac{di(t)}{dt}, \tag{5.1}$$

where L_f is the filter inductance. Writing this as a difference equation for digital implementation gives

$$e_r[k] = e_t[k] - \frac{L_f}{T_s}\left(i[k+1] - i[k]\right), \tag{5.2}$$

where T_s is the switching period. If the current error is given as $\varepsilon_i[k] = i^*[k]$ - i[k], the dead-beat condition gives $\varepsilon_i[k+1] = 0$ [119]. This means that $i[k+1]$ must equal the reference current $i^*[k]$. Substituting this into (5.2) then gives the active rectifier voltage needed to achieve the deadbeat condition as

$$e_r^*[k] = e_t[k] - \frac{L_f}{T_s}\left(i^*[k] - i[k]\right). \tag{5.3}$$

From Fig. 5.4 the LG model is given as

$$\begin{aligned} e_t(t) &= \frac{d\lambda_t(t)}{dt} - i(t)R_s \\ &= e_g(t) - L_s\frac{di(t)}{dt} - i(t)R_s, \end{aligned} \tag{5.4}$$

where λ_t is the total stator flux linkage. As mentioned before, position information can be derived from the stator flux linkage which can be found by rearranging and integrating (5.4) as

$$\lambda_t(t) = \int\left[e_t(t) + i(t)R_s\right]dt. \tag{5.5}$$

In this application only the instantaneous EMF is required for the current reference calculation from (4.23) and not the position. This greatly simplifies the required calculation. Furthermore, since the synchronous inductance of the novel LG is negligible compared to the phase resistance (from Chapter 4, Section 5.5), the LG's EMF can

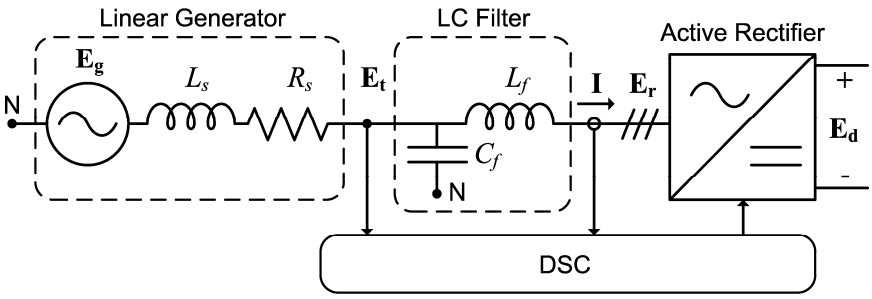

Fig. 5.4 Single line diagram of the LG, filter and active rectifier.

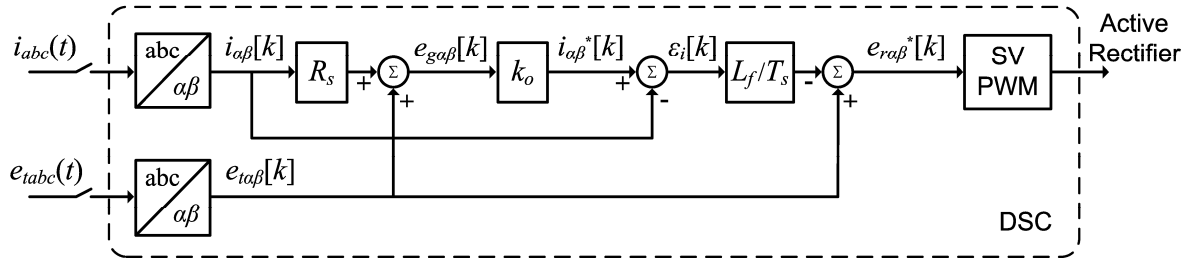

Fig. 5.5 Predictive control calculation and SV-PWM as implemented in the DSC.

then simply be calculated from (5.4) as

$$e_g[k] = e_t[k] + i[k]R_s. \tag{5.6}$$

By substituting (5.6) into (4.23), the reference current in (5.3) can now be calculated as

$$i^*[k] = k_r\left(e_t[k] + i[k]R_s\right). \tag{5.7}$$

The control strategy is shown schematically in Fig. 5.5. Take note that the reference current can be obtained from the calculated EMF, from (5.6), and the average input (wave) power. For the prototype LG, the average input power is assumed constant as per the design, and hence the current scaling factor k_r is used. For a real installation, the power will need to be measured or estimated and the current reference continually updated.

5.5 Drive motor control

The analytical design and simulations are all done with the assumption that the translator velocity is perfectly sinusoidal, even under a varying generator load (which is not perfectly sinusoidal); this is especially true for where the overlap between the stator and translator changes at the stroke ends, as shown in Chapter 4.6.2 and 6. To emulate this behaviour in the test rig, the drive motor speed is simply controlled at a fixed speed. This reference speed is calculated by considering the required displacement profile as

$$z(t) = Z\sin(\omega_m t), \tag{5.8}$$

where Z is the stroke length (peak-to-peak displacement) divided by two and ω_m is the drive motor speed. The translator velocity is then given as

$$\begin{aligned} v(t) &= \dot{z}(t) \\ &= \omega_m Z\cos(\omega_m t) \\ &= V_p\cos(\omega_m t). \end{aligned} \tag{5.9}$$

With the peak velocity and displacement known,

$$\begin{aligned} \omega_m^* &= V_p / Z \\ &= \sqrt{2}\,(0.75\ \text{m/s})/(0.672\ \text{m}/2) \\ &= 3.16\ \text{rad/s} \\ &= 0.50\ \text{rev/s}. \end{aligned} \tag{5.10}$$

Controlling the motor velocity is done with the well-established field-oriented control (FOC) strategy as described in [127]. A resolver fitted on the rotor shaft provides position feedback which is used to transform the measured *abc* motor currents to the synchronously rotating *dq* – reference frame and also used to calculated the rotor speed. The *q*-axis current, which is in phase with the motor EMF, is controlled to equal the reference value obtained from the outer speed control loop, while the *d*-axis current is controlled equal to zero. A single line diagram of the inverter and motor is shown in Fig. 5.6 and the control strategy is shown schematically in Fig. 5.7.

5.6 Simulation

The LG, filter and active rectifier, as shown in Fig. 5.4, are implemented in the multi-domain simulation package Ansys Simplorer® 8 for verification. The data from the FE simulated EMFs shown in Fig. 4.8 is stored in a lookup table and used as reference for ideal voltage sources representing the LG's EMFs; by using the FE simulated data, it is assumed that the drive motor control is working correctly; the FOC of the drive motor is hence not simulated. The active rectifier is modelled with ideal switches representing the IGBTs, and an ideal dc voltage source is used to represent the dc-bus. The parameters of the active rectifier, as used in the simulation, are given in Table 5.1. Simplorer® includes a VHDL-AMS solver, and therefore the control and SV-PWM calculations are implemented with VHDL code as described in [128]. The complete Simplorer® model is shown and described in Appendix H.

In Fig. 5.8(a) the simulated currents injected to the active rectifier during one stroke is shown. The current amplitudes deviate from the ideal sinusoidal envelope at the stroke ends; this can be expected when considering the EMFs shown in Fig. 4.15. In Fig. 5.8(b), the *c*-phase EMF, terminal voltage and current are shown. During the first part of the stroke, the *a*-phase and *b*-phase become active first. It can be seen that, since the three-phase cur-

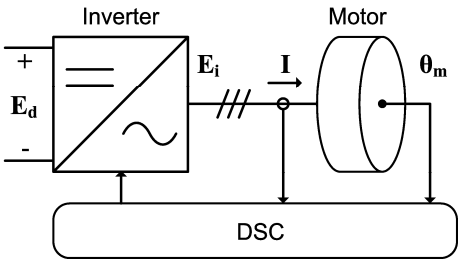

Fig. 5.6 Single line diagram of the inverter and drive motor.

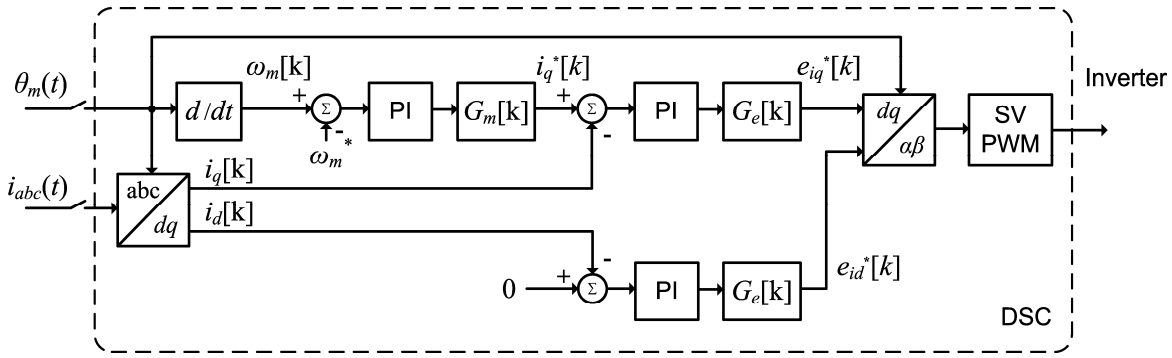

Fig. 5.7 Field oriented control for the drive motor speed control as implemented in the DSC.

Table 5.1 – Rectifier parameters as used in the control simulation.

Switching frequency f_s (kHz)	20
Filter inductance L_f (mH)	1.3
Filter capacitor C_f (µF)	23.5
Filter cut-off frequency f_c (Hz)	911
DC-bus voltage E_d (V)	300

rents are balanced, current from the *a*- and *b*-phases are conducted through the *c*-phase before it becomes active itself, i.e. while the *c*-phase EMF is still zero. This current can be seen to be 180° out of phase with the terminal voltage during this time and therefore only constitutes losses. As the *c*-phase becomes active, the current and terminal voltage can be seen to track the EMF. The current is in phase with the EMF as required. The terminal voltage is also basically in phase with the EMF and highlights the small effect of the synchronous inductance.

The *c*-phase current (i_c) is shown in Fig. 5.8(c) together with the ideal reference current (i_{cr}), as scaled from the actual EMF, and the reference current (i_{crc}) calculated in the control algorithm from (5.4)-(5.5). The return currents from the *a* and *b*-phase during the start of the stroke cause the calculated reference to deviate from the ideal reference. It can be seen that the simulated current follows the calculated reference current almost exactly.

The ideal three-phase power generated (p_{gi}, the same as shown in Fig. 4.16), the simulated power generated (p_g) and the power transferred (p_t) from the LG to the load is shown in Fig. 5.8(d). The simulated power p_g deviates slightly from the ideal waveform of p_{gi} at the stroke ends due to the additional losses incurred by the transitional phase currents. The average value of p_g is P_g = 700 W, almost 5 % less than P_{gi}. The efficiency is calculated as 86 % (ignoring eddy-current losses) with the average power transferred to the converter calculated to be 602 W.

5.7 Conclusion

Predictive control is here shown to work well in terms of forcing the current to follow the calculated reference very closely. During the transitional phase where the stator-translator overlap is changing, the calculated reference however deviates slightly from the ideal reference, which is scaled from the actual EMF. This results in a 5 % loss in power from the ideal generator power calculated in Chapter 4.6.2. Take note, however, that this loss is incurred after the previously mentioned increase in power-to-weight ratio gained by allowing for zero stator-translator overlap at the stroke ends (Chapter 4, Section 6). Apart from this small deviation, predictive control appears to work well, even during the transition from zero to full stator–translator overlap. Predictive control can therefore be a viable alternative to control strategies currently investigated for LGs in DD-WECs, especially also because no EMF sensing or linear position feedback is used. More conclusions on the predictive control will be drawn after the experimental evaluation in Chapter 6.

Also take note of the fact that the velocity is assumed sinusoidal here, but in a real world situation the translator velocity will deviate from this due to the irregular load the generator will place on the incident wave force. Furthermore, with zero stator-translator overlap, no control can be exerted on the generator's reaction force to the waves. These aspects are not further investigated in this work, but must be kept in mind for an actual WEC installation.

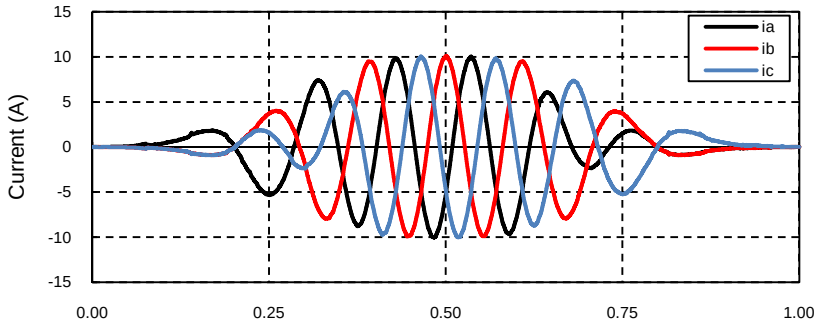

(a)

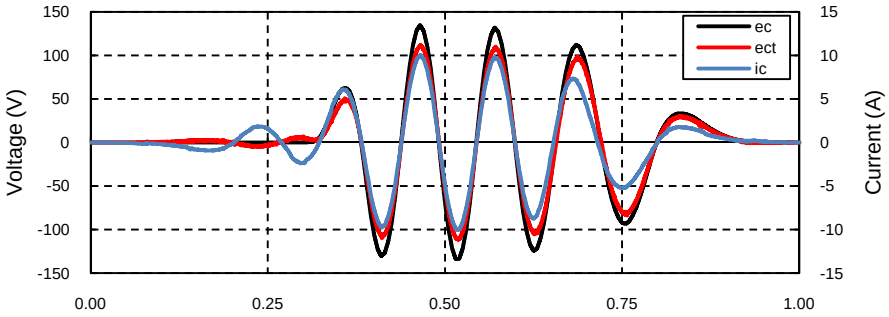

(b)

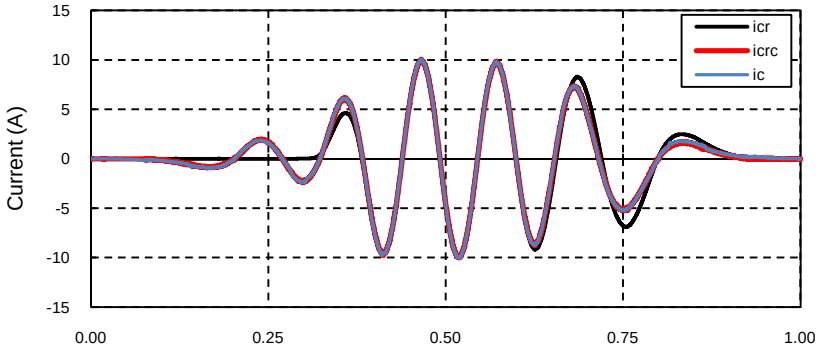

(c)

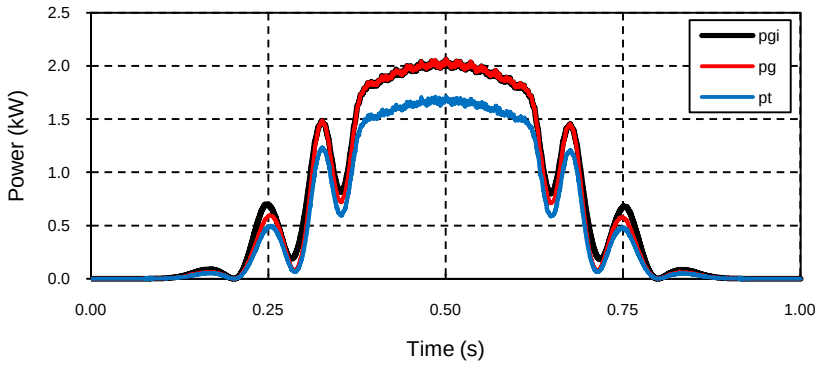

(d)

Fig. 5.8. Simulation of the predictive control strategy yields (a) the three-phase currents injected to the rectifier; (b) *c*-phase emf (ec), terminal voltage (etc) and current (ic); (c) *c*-phase ideal reference current (icr), reference current as calculated in the control (icrc) and the simulated current (ic); and (d) the ideal instantaneous three-phase generated power (pgi), the actual instantaneous three-phase generator power (pg) and instantaneous power transferred to the rectifier (pt).

Chapter 6

Experimental evaluation

The prototype LG, test setup and control strategy described until now were practically implemented in the Electrical Machines Laboratory at Stellenbosch University. In this chapter the construction and test results obtained from the implementation is analysed in order to verify the theoretical and simulated results and to help establish the LG's suitability for DD-WECs.

6.1 Prototype LG construction

6.1.1 Translator construction

As mentioned before, it was decided to mount the translator horizontally and suspend the stator on linear bearings. Horizontal translation means avoiding the effects of gravity on the reciprocation. Furthermore, since the stator is much lighter than the translator, it is easier to move, rather than the translator. The steel centre column

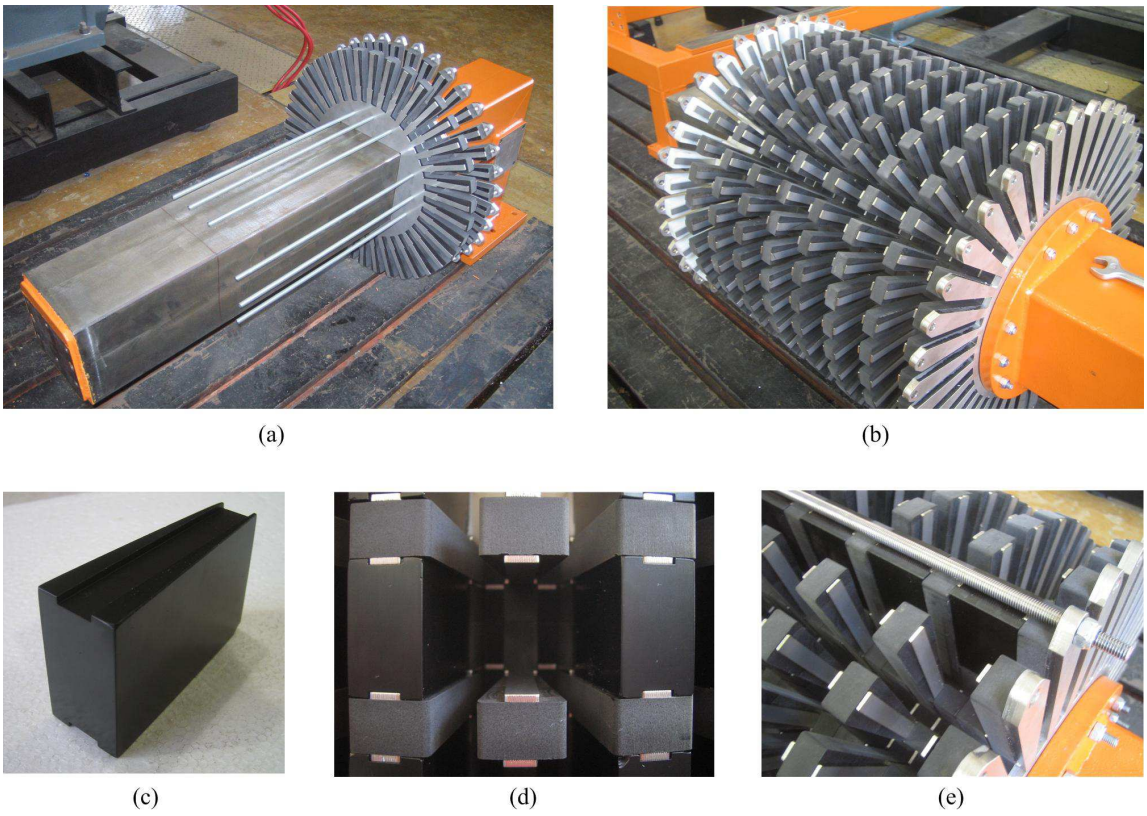

Fig. 6.1 Construction of the prototype LG translator. (a) The different translator layers being assembled onto the centre column. (b) All the layers assembled, ready for the magnets to be inserted. (c) One of the tapered magnets with grooves at the top and bottom. (d) Close-up of the translator showing two inserted magnets and an open space, ready for another magnet to be inserted. (e) One row of magnets inserted in the translator with the stainless steel (SS 316) rod securing the different layers and magnets in place.

of the translator is mounted on a test bench as shown in Fig. 6.1(a); the different layers of the translator, as discussed in Chapter 4.7.2, is seen as it is being assembled onto the centre column. In Fig. 6.1(b) the translator is shown with all the layers, including the end plates, assembled together and ready for the magnets to be inserted. One of the custom manufactured magnets is shown in Fig. 6.1(c). In Fig. 6.1(d) a close-up of the translator is shown with all but one magnet inserted; the stainless steel layers and how these fit into the grooves in the magnets are clearly visible here. The stainless steel rod securing one row of magnets is shown in Fig. 6.1(e). Finally, the completed translator is shown in Fig. 6.2. The configuration of the supporting steel frame and the bearings rails for the stator can also be seen.

6.1.2 Stator construction

The stator was almost entirely manufactured in-house. Only the manufacture of the aluminium ring and the stator mould had to be done by outside companies. The stator coils were stranded and machine wound in the lab. In Fig. 6.3(a), three coils are shown as they are laid-up in the mould. Glass-fibre cloth is wrapped around the coils for added strength of the finished stator section as shown in Fig. 6.3(b). In Fig. 6.3(c) the fully assembled mould with the coils inside is shown, ready for epoxy to be cast into the opening at the top. In Fig. 6.4(a) the complete stator is shown with all 38 stator sections bolted to the inside of the aluminium ring. The connections between the stator sections, shown in Fig. 6.4(b), are heat-shrink insulated.

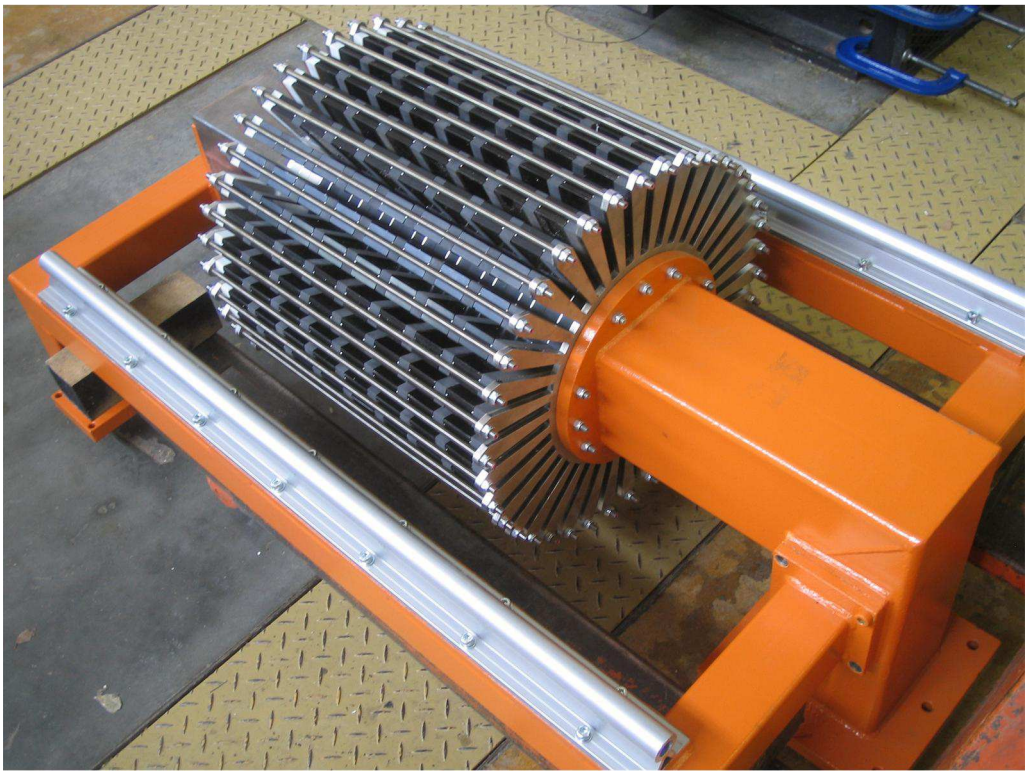

Fig. 6.2 The completed translator, mounted horizontally on a steel frame; the linear bearings for the stator is mounted on the sides of the frame.

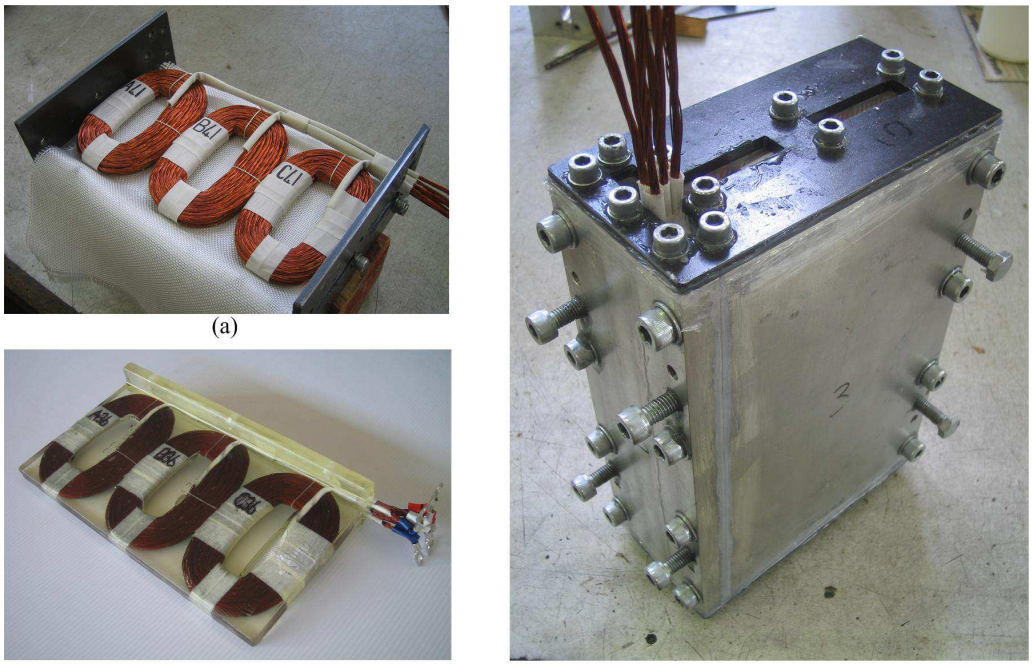

(a) (b) (c)

Fig. 6.3 (a) Three stator coils laid-up in the mould, (b) a finished stator section and (c) the fully assembled mould, ready for casting epoxy into the opening at the top.

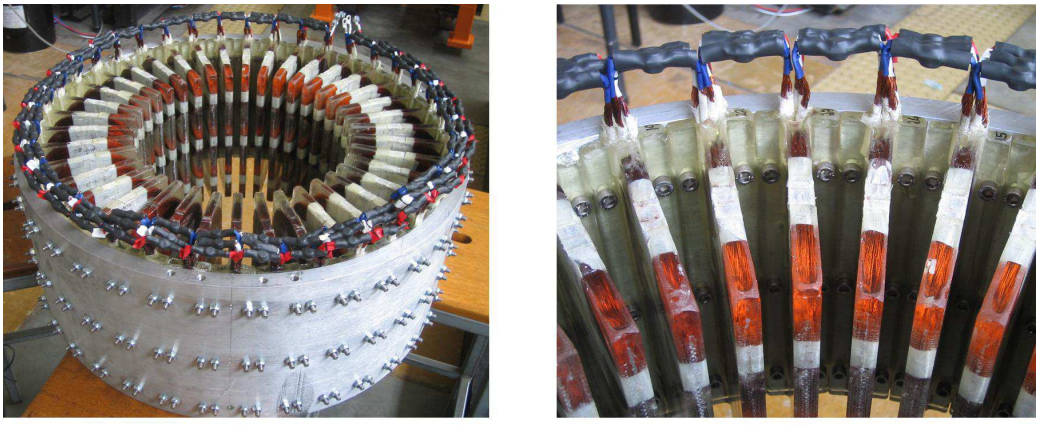

(a) (b)

Fig. 6.4 (a) The completed stator with all 38 stator sections bolted to the inside of the aluminium ring and (b) a close-up of the connections between the different stator sections.

6.1.3 Impedance measurement

During the stator construction, the impedance of each individual stator section was measured. The resistance was measured with a micro-ohm meter and the inductance with an LCR meter. The average phase resistance and self inductance of one stator section was found to be R_{si} = 59.5 mΩ and L_{xxi} = 119.2 μH. Multiplying this by 38 results in a total phase resistance and inductance of R_s = 2.26 Ω and L_{xx} = 4.53 mH (Method 1). Once the stator was completed and all the stator sections connected, the phase resistance and self inductance were again measured as before. This resulted in measurements of R_s = 2.07 Ω and L_{xx} = 8.06 mH (Method 2). The phase resis-

Table 6.1: Measured values of the stator phase impedance.

Method	R_s	L_{xx}	L_s
Method 1	2.26	4.53	-
Method 2	2.07	8.06	-
Method 3	2.26	7.91	-
Method 4	2.18	-	7.95

tance and inductance was also calculated by applying a 50 Hz ac voltage to each of the phase windings *in turn* and measuring the current. The impedance is then calculated as **Z** = **V**/**I** (Method 3). This resulted in measurements of R_s = 2.26 Ω and L_s = 7.91 mH. The synchronous impedance was finally determined by applying three-phase ac voltages to the three phases of the novel LG and calculating the impedance as with Method 3. The value of the synchronous impedance is given in Table 6.1 together with the other calculated values.

It is clear that the flux coupling between the coils of the same phase in the different stator sections is significant. This is proven by the fact that when the stator sections are all connected in series in the novel LG, the resultant self-inductance almost doubles compared to the sum of the individual inductances (as calculated with Method 1). To some extent this effect can be expected when considering the close proximity of the different stator sections; the different coils of the same phase together almost resemble a toroid. The measured self inductance of the completed stator is also significantly higher that the calculated value of 4.66 mH. The most obvious reason for this is the relatively large end windings of the prototype LG. Since the end windings are large compared to the active windings and since the end windings are neglected in both the analytical and FE model, a difference in the measured and calculated values is to be expected. Interestingly the difference between the measured self- and synchronous inductances are negligible. The large end-windings may again be a contributing reason for this. It may be that, due to the large end windings in addition to the close proximity of the stator sections, more flux links with the coils of the same phase rather that cross-linking with coils of different phases. To better investigate these effects a 3D FE model should be used. However, the resulting synchronous reactance, calculated at the average velocity of 0.75 m/s as X_s = 0.034 p.u., is still rather low compared to the phase resistance. It is hence decided not to do 3D FE modelling at this stage.

The measured phase resistance is also up to 20 % higher that calculated in Chapter 4. There are a number of factors which can contribute to the increased measured resistance, including the increased wire length due to twisting of the strands and the connections between the different stator sections, which were not taken into account in the design.

6.1.4 Mass distribution

During construction, the mass of each of the components was measured in order to gain an idea of the overall mass of the LG. The total mass of the LG (excluding the linear bearings and the steel frame used for mounting the generator on the test bench) amounts to 256.5 kg. The breakdown of this mass is given in Table 6.2 and is also shown in Fig. 6.5. The measured copper and magnet mass correspond well with the design values.

Table 6.2: Measured mass of the novel LG.

Part	Mass (kg)
Stator	**67.3**
Copper	34.6
Epoxy	13
Aluminium	19.7
Translator	**189.2**
Magnet	99.1
Steel	49.7
Plastic	40.4
TOTAL	**256.5**

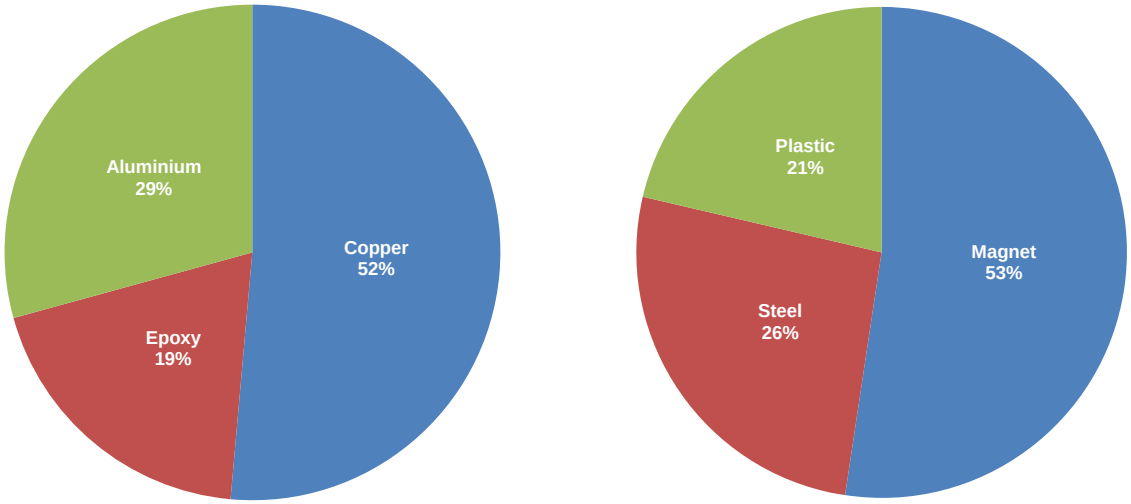

(a) (b)

Fig. 6.5 Mass distribution of the (a) stator and the (b) translator. The mass of the bearings and steel frame is excluded.

It can be noted that the copper and magnet mass make out more than half of the overall LG mass. The additional mass can be considered as structural mass. This result supports the initial assumption than very little structural mass is needed for the novel topology. Furthermore, the steel mass of the translator is probably much more than is needed. It is expected that a thorough structural design optimisation will reduce the steel mass significantly.

It must also be noted that the chosen bearing arrangement is by no means considered to be the most optimum, and was only chosen as it best suited the requirements of the test setup. In a real installation, where the translator will most probably be the moving part, a sliding surface on the inside of the centre column may be more suitable, and possibly even less expensive. As such, the mass of the bearings are not included as part of the LG at this stage.

6.2 Test setup

The overall test setup with the completed LG and the drive motor with the crankshaft are shown in Fig. 6.6. The LG and drive motor are both star connected and cabled to a test bench which houses the variable ac supply, the PEC and a variable resistor bank. The PEC is shown in more detail in Fig. 6.7. Two Mitsubishi PM50CLA60 intelligent power modules (IPMs), which contain the 600 V, 50 A IGBTs for each VSC, form the basis of the PEC. A Texas Instruments eZdsp^{TM} F28335 stand-alone developer board, which houses a TMS320F28335 DSC, is used to store and execute the control instructions and to generate the IGBT gating signals. CTs are used to measure the currents at the connections to the IPMs. The speed reference for the drive motor is set with a knob on the converter as shown in Fig. 6.7. The parameters of the PEC are given in Table 6.3.

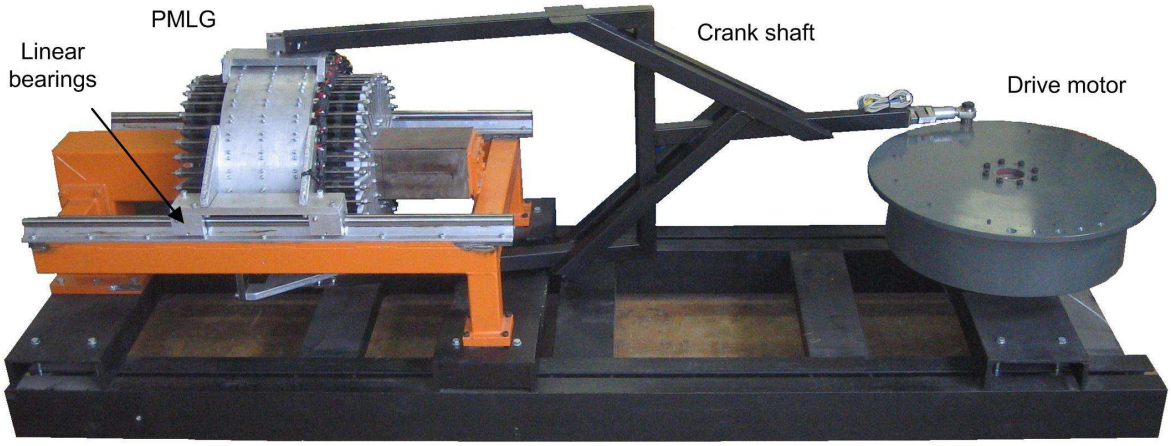

Fig. 6.6 Complete test setup showing the novel LG and the drive motor and crank shaft.

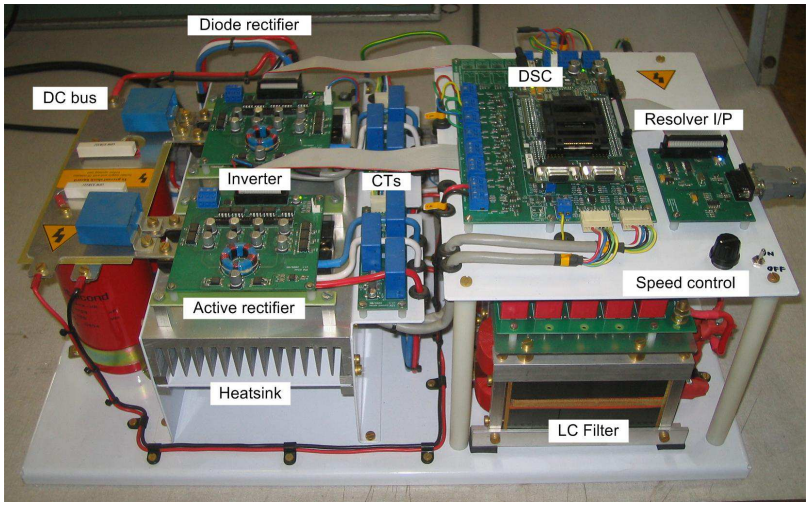

Fig. 6.7 The back-to-back voltage source converters; also shown is the diode rectifier, LC-filter and digital signal controller.

Table 6.3: Converter and LC-filter parameters.

DC bus voltage E_d (V)	300
Dc bus capacitance C_d (μF)	9400
Filter inductance L_f (mH)	1.3
Filter capacitance C_f (μF)	23.5
Filter cut-off frequency (Hz)	911
Switching frequency (kHz)	20

6.3 Test results

All the results presented in this section are measured while the drive motor is controlled at the design speed of 30 rev/min (0.5 rev/s). This results in sinusoidal reciprocation at the LG with a peak velocity of 1.06 m/s (rms velocity of 0.75 m/s) under no-load and load conditions.

6.3.1 Open circuit voltage

The open circuit voltage, or the EMF, of the LG is measured and shown in Fig. 6.8(a). There is a clear resemblance to the FEA simulated waveform in Fig. 4.9. The sinusoidal envelope suggests the correct functioning of

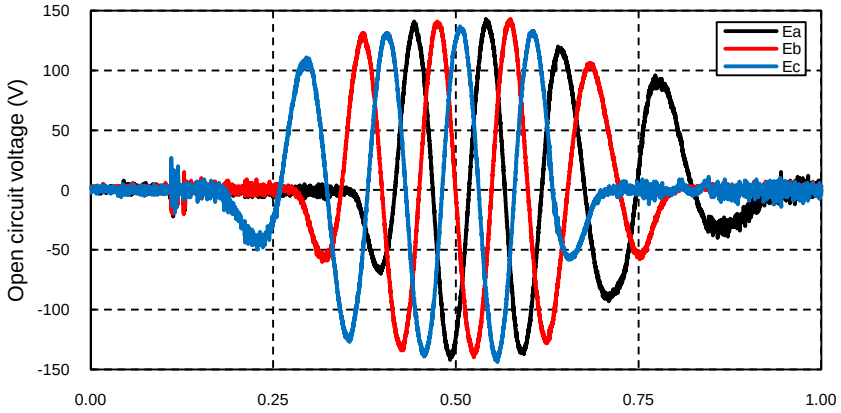

(a)

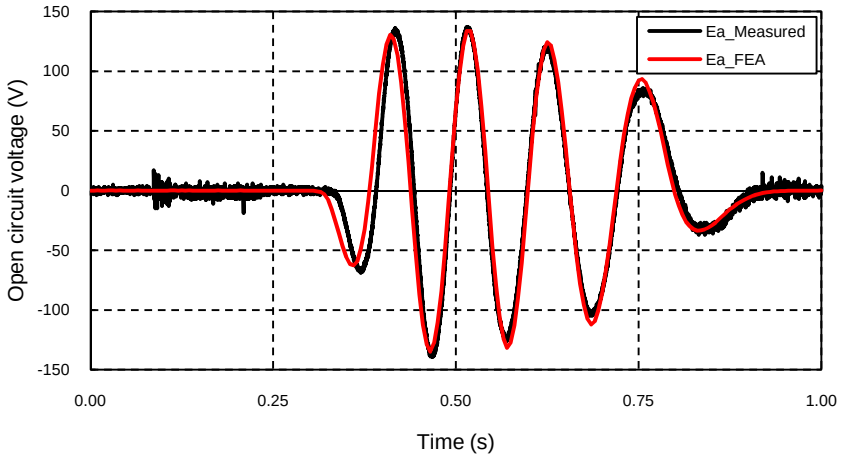

(b)

Fig. 6.8 (a) Measured open circuit voltages (EMFs) at V = 0.75 m/s and (b) a comparison of the measured and FEA simulated a-phase EMF.

the drive motor control, at least without loading the LG. For a better comparison of the measured and simulated EMFs, the *a*-phase measured and simulated EMF waveforms are shown on the same graph in Fig. 6.8(b). It is clear that the measured open circuit voltage very closely matches the simulated EMF and hence confirms the validity of the 2-D FEA model of the LG. The peak measured voltage is 140 V, which is 3 % higher than the peak simulated voltage.

6.3.2 Resistive load tests

Prior to testing the LG control strategy, the LG is loaded with the star connected three-phase resistor bank. This serves to confirm the correct functioning of the drive motor control under a varying load. In order to draw the rated current, a resistive load of R_l = 11 Ω is needed. Setting the resistor bank to this value proved problematic for the drive motor, as the speed could not be kept constant. The drive motor speed could be properly regulated again when the load was reduced to 30 Ω; the measured *a*-phase current and LG terminal voltage for this load are shown in Fig. 6.9. It is clear that the current and LG terminal voltage is in phase, hence confirming the small influence of the inductance at the design velocity. Furthermore, at the end of the stroke, there is still current flowing through the *a*-phase, even though the terminal voltage is negligible, i.e. when the *a*-phase winding has moved out of the PM field. This is of course the currents from the still active *b*- and *c*-phase windings returning through the *a*-phase as also observed in the simulations in Chapter 5.6.

It is unfortunate that problems with the drive system prevented full load testing of the LG. The source of the problems could unfortunately not be solved by the time of writing. However, testing at part-load is still sufficient to verify the modelling and design and the correct functioning of the LG and the control strategy. The control tests are presented next.

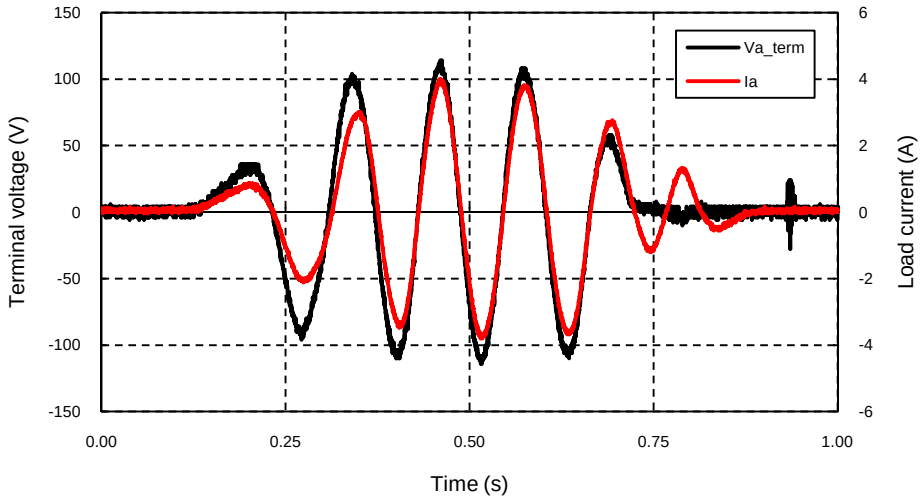

Fig. 6.9 Measured LG *a*-phase terminal voltage and currents at V = 0.75 m/s with a load resistance of R_l = 30 Ω.

6.3.3 Predictive control tests

The LG is connected to the active rectifier as shown schematically in Fig. 5.4. From the resistive load tests the maximum load at which the drive motor control correctly works is determined; in terms of the LG control, this load translates into a current scaling factor of k_r = 0.031. To provide some room for error, the scaling factor was reduced by 25 % to k_r = 0.023 for the predictive control strategy. The measured LG three-phase currents under predictive control with k_r = 0.023 are shown in Fig. 6.10(a). For comparison, the simulations of Chapter 5.6 are repeated with the same k_r. In Fig. 6.10(b) a comparison between the simulated and measured *a*-phase current is shown. The similarity between the two wave forms indicates that the practically implemented predictive control strategy functions as expected.

Even though rated conditions could not be tested, the test results show that the predictive control works as expected. The fact that the LG's phase resistance can be measured fairly accurately and that the synchronous in-

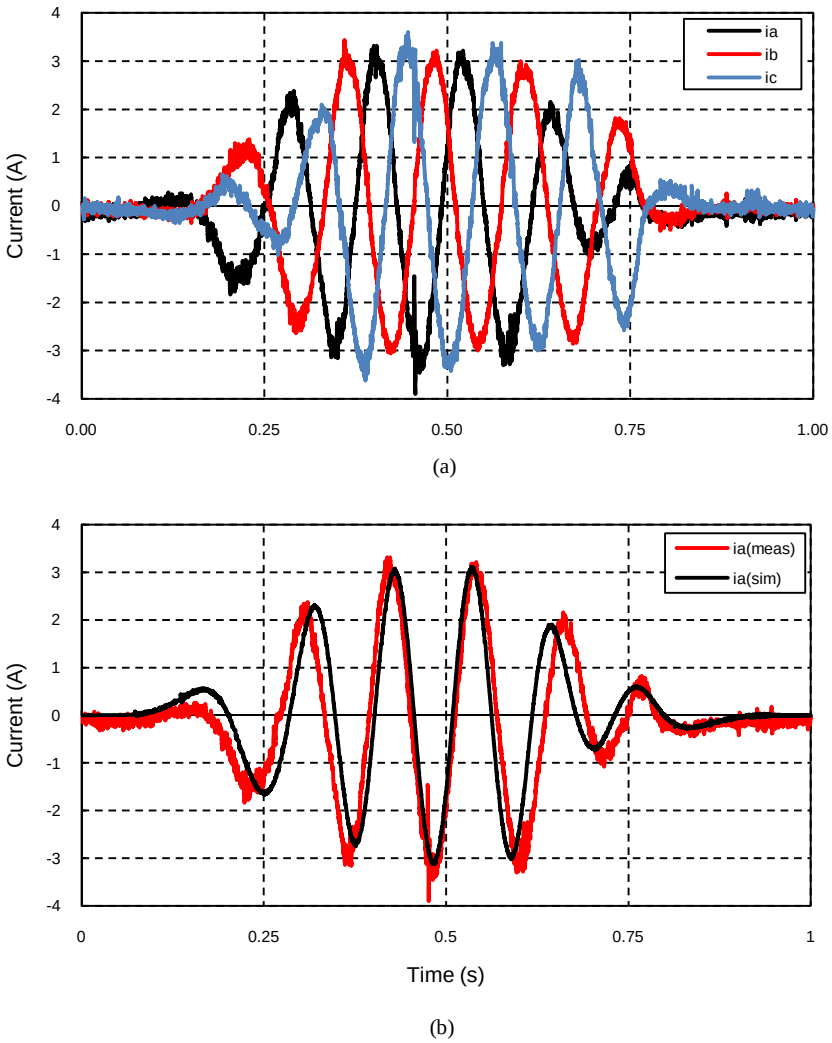

Fig. 6.10 (a) Measured three-phase LG currents under predictive control with k_r = 0.023 and V = 0.75 m/s. (b) A comparison between the simulated and measured *a*-phase current.

ductance is negligibly small, clearly aids in easy and accurate calculation of the LG's EMFs (and hence the reference currents). For iron-cored LGs the effect of the inductance in (5.4), which is generally much higher than in air-cored machines, will have to be taken into account. Translator position estimation may also be necessary depending on the degree of position dependency of the inductance, which in turn very much depends on the PM translator structure [121]. In this case the straight-forward control calculations as presented in Chapter 5, Section 4, will become more complex. Furthermore, parameter sensitivity is a well documented issue in predictive control. This issue is not addressed here and will have to be investigated in more detail in the future. Methods have been proposed to make dead-beat control more robust against parameter mismatch [118], [119], [125] and some of these methods could be incorporated here.

The prototype LG was designed for nominal velocity and the test setup was designed to verify the LG operation specifically at nominal velocity. A real DD-WEC will however be subjected to a large variation in both stroke length and velocity and future work should focus on evaluating the LG for these varying conditions. This also includes the working of the control strategy.

6.3.4 Efficiency

Apart from the problems with the drive system as discussed, one other limitation in the test setup is the inability to measure the mechanical input power, and hence to accurately measure the LG efficiency. From the drive motor speed, a good estimation of the linear velocity of the LG can be found. However, since the input force to the LG is achieved by means of a crankshaft, for which the angle of incidence is constantly changing, measuring the linear force is difficult. A loadcell was installed in the crankshaft to try and estimate the linear force from the axial force in the crankshaft, but it proved impractical to connect the loadcell cable to measurement apparatus while constantly rotating with the drive motor.

The efficiency of the LG is here calculated based on the known (calculated and measured) LG parameters. It is assumed that the eddy-current losses are as given in Table 4.5. The efficiency can be given as a function of the load resistance as

$$\eta = \frac{R_l}{R_l + \left(R_s / k\right)}, \tag{6.1}$$

where k is the ratio of copper losses to total losses as defined in (4.3). A plot of (6.1) is shown in Fig. 6.11, where it can be seen that at full load, the LG efficiency is about 83 %; this is slightly less than the rated 85 %, and is due to the LG phase resistance being higher than calculated in the design. At the test load, the efficiency is 93 %.

6.4 Conclusions

A small scale prototype of the novel topology is constructed and test results are presented in this Chapter. In the first place, the feasibility of constructing the novel topology is confirmed, if only on a small scale. During the concept development, it was theorised that very little structural material would be needed for keeping the magnets in place; this theory is confirmed by the prototype as constructed and tested. It is also expected than a

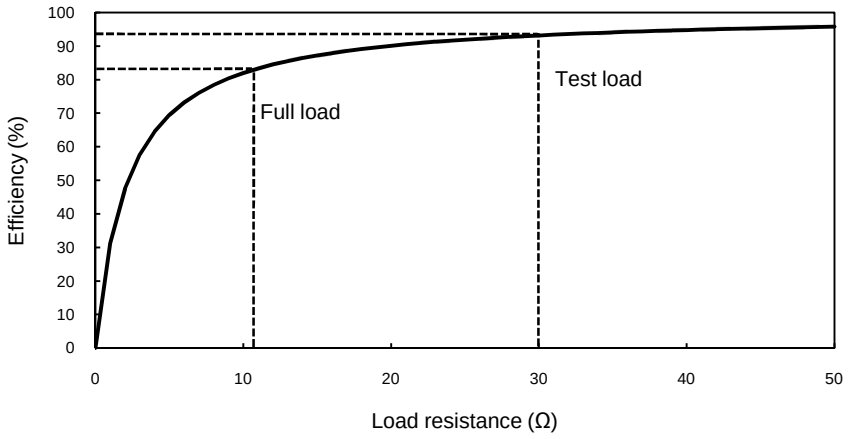

Fig. 6.11 Calculated LG efficiency as a function of load resistance.

thorough mechanical design optimisation will even further reduce this mass. Construction of the stator proved a little cumbersome, although assembly of the different parts of the LG were easy, as there are no attraction forces between the stator and translator. The particular design of the translator also provides for quick and easy insertion of the magnets.

A unique test setup for testing the LG in a laboratory setting is also demonstrated. Although there are some limitations with the drive system's control, enough measurements are done to confirm the correct functioning of the LG and the predictive control strategy. Furthermore, excellent agreement between the measurements and simulation results are demonstrated. These results serve to confirm the validity of the chosen modelling and design methodology used for the novel LG. Although the laboratory setup only simulates ideal monochromatic wave conditions, the results are a good foundation for suggesting that the novel LG and predictive control are viable solutions for DD-WECs and that research in this area should be continued.

Chapter 7

Conclusion and recommendations

The conclusions which can be drawn from the work presented in this thesis and the specific research contributions are discussed in this final chapter. A number of recommendations for further research are also discussed.

7.1 Conclusions

7.1.1 Novel LG concept

A number of problems with current LG topologies are identified in Chapter 1.4. As a means to solve at least some of these problems, a novel air-cored PM topology for a LG, developed from a LDS topology, is proposed, developed and evaluated in this thesis. The transverse flux paths in the novel topology eliminates pair-wise flux coupling found in longitudinal flux LGs, and together with this eliminates a potential uneven air gap flux density distribution which leads to increased cogging forces. In fact, due to the air-cored stator, there are zero cogging forces and also a very sinusoidal voltage waveform, which is advantageous for measurement and control. Also, due to the air-cored stator, attraction forces between the stator and translator, one of the biggest problems with more conventional iron-cored LGs, is eliminated. Furthermore, the attraction forces between the opposing translator sides of LDS machines are also ideally eliminated with the novel topology. The elimination of magnetic attraction forces means a large reduction in structural mass can be expected.

Air-cored stators are also characterised by low inductance; coupled with the low frequencies at which DD-WECs operate, the synchronous reactance is very low. A high power factor (or low load angle) is therefore another advantage of air-cored windings. This is an important advantage for LGs used in DD-WECs. In [42] it is shown how an inherently low load angle at nominal power results in better voltage regulation at overload conditions (which are frequently experienced in the sea). It of course also eliminates the need for phase compensation equipment such as capacitors. In [60], for instance, a very much overrated active rectifier is used for phase compensation of a LG with a high load angle.

A non-overlapping stator winding is proposed for the novel topology. The numerous advantages of this type of winding are outline in Chapter 3, Section 3.1; some of these include increased efficiency and potentially automated construction. For the novel topology, the modularity of the stator is a particular advantage. In the case of a coil failure, only one stator sections needs to be replaced. If a spare stator section is not available, the faulty section can simply be bridged out (in the case of series connected sections) or simply disconnected from the other sections (in the case of parallel connected stator sections), while the LG can continue operating.

There are however some disadvantages to this topology. A rough comparison to existing experimental iron-cored LGs in Chapter 3.8 points out that a very large amount of PM material and copper is needed. The large amount

of PM material is due to the large effective air gap created by the air-cored stator. The large amount of copper mass can partly be attributed to the short active length of the coils (compared to the coil pitch); the short active length means that the end-windings, which don't contribute to the LG force, contributes a much larger portion of the total copper mass. However, it is expected that a very big reduction in structural mass will be achieved with this topology. An estimation in the study in Chapter 3.8 reveals that the total stator and translator mass of the novel LG compares more favourably with that of the iron-cored LGs. This is of course due to the lack of active steel in the novel topology. When the structural steel is added to these figures, it is expected that the novel topology will perform significantly better in terms of power density. Due to the volatility of PM and copper prices, no conclusion can yet be made about the cost per unit power of the novel topology.

7.1.2 Modelling and design

Since the novel LG topology is based on the LDS topology, existing analytical modelling techniques are easily applied to the novel LG. Subdomain modelling is used to solve the appropriate Laplace and Poisson equations in conventional air-cored LDS machines in [94], [95]; these models are adapted for the novel LG to calculate the air gap flux density and winding flux linkages and is verified with finite element analysis. The very accurate analytical equations for the flux density help to quickly analyse the effect of the pole width on the flux density harmonics and an optimal pole width for minimum THD of the flux density can quickly be found.

A simplified analytical model based on a one dimensional magnetic circuit model is also used and shown to be sufficiently accurate under given constraints. This model is manipulated into a form from which an exhaustive optimisation procedure is developed in Chapter 4. For specified performance specifications and dimensional constraints, the optimisation procedure finds the LG dimensions and average current density for minimum active mass (copper and magnet mass). Since the optimisation is based on relatively simple analytical equations, optimal dimensions are very quickly obtained with this method. It is worth stressing the fact that local minima / maxima are also not a problem with this procedure; all possible combinations of input variables are considered (within limits), and all valid solutions (adhering to the specifications and constraints) are evaluated for the optimum combination.

An interesting result from the optimisation is that optimal dimensions for the LG are obtained at the maximum allowable current density and minimum allowable number of poles. At this particular combination of current density and poles, only one solution exist which satisfy the dimensional constraints and gives both the minimum magnet and copper mass. It can therefore be concluded that the optimal dimensions can be obtained by minimising only the magnet or only the copper mass.

FEA is further used to verify the constant velocity analytical design and also to simulate and analyse the LG output for sinusoidal reciprocation. Good agreement between the analytical and FEA obtained results established confidence in both methods of analysis. Since only 2D FEA is done, results are again obtained very quickly. Analysing the LG output for sinusoidal reciprocation and for varying amounts of overlap between the stator and translator is very easily done. It can therefore be concluded that FEA is a very useful and indeed an indispensible tool in the development of the novel LG.

It was decided to design the LG to have zero stator-translator overlap at the stroke ends. Since the translator velocity, and hence the power output, is at its lowest at the stroke ends, it was theorised that doing this could result in a significant cost saving with a relatively small sacrifice in performance. From FEA simulations in Chapter 4.6.2, it is shown that for this particular LG, a 46 % increase in power density over a LG with full stator-translator during the entire stroke was achieved. To some extent, the theory is therefore proven, although it must be mentioned that this LG and its stroke length was not designed for real wave heights. This result shows that savings may be possible though, and that this may be an option for future designs. The lack of control when there is no overlap between the stator and translator must also be taken into account; this is addressed in Section 7.1.5.

7.1.3 Prototype construction

A functional small scale prototype of the novel topology was constructed as described in Chapter 6.1. This proved the feasibility of constructing the novel topology, at least on a small scale. Although constructing the stator was straightforward, manually repeating the same process for each of the 38 stator sections proved rather time consuming, with the coil winding and waiting for the epoxy to cure taking the most time. Multiple moulds and increased automation in the process will reduce construction time, but will also increase costs. In contrast, the translator construction proved to take significantly less time. Sliding the translator layers over the centre column and inserting the magnets from outside for this particular prototype was done in only one day. As mentioned, the manufacturing and construction methods presented for the prototype LG may not be applicable for larger machines; other methods may have to be investigated for larger machines.

The prototype LG, as built, proved that little structural mass is needed for magnet support. This is despite the fact that a proper structural design optimisation was not performed for the prototype. It is expected that the structural mass can be much reduced if a proper structural design optimisation is performed.

7.1.4 Drive system and measurements

A unique drive system, which effectively circulates energy from the dc-bus, through the drive motor and LG and back onto the dc-bus was developed. Existing equipment in the form of a WTG and back-to-back VSCs were used to construct the system, hence saving on costs. The drive system functions as desired for small loads on the LG, but cannot effectively control the drive motor speed when the LG load approaches full load. This is unfortunately an ongoing problem of which the cause could not yet be determined.

Despite the aforementioned problems, the drive system enabled sufficient test results to be obtained such that the correct functioning of the LG could be confirmed and the analytical and FE models of the LG could be verified. Controlling the drive motor speed at a constant value enabled the LG output, under variable loading, to be verified against the design and simulations which were done with the assumption of sinusoidal translator displacement.

In terms of the measurements, overall good agreement between the design / simulated values and the measured values was observed. Practically zero phase displacement between the LG current and terminal voltage was ob-

served with the resistive load tests; this confirmed the negligible effect of the stator inductance. An interesting result was that, when all the stator sections were assembled and connected together in the finished stator, the total self-inductance is almost double the sum of the self-inductances of the individual stator sections; this shows a significant amount of flux coupling between the phase coils of the individual stator sections. Despite this, the overall effect of the inductance is still very small. Furthermore, very little cross-coupling of flux between the three phases are observed; this was confirmed by the fact that the measured synchronous phase inductance is basically the same as the phase self-inductances. It is suspected that the large end-windings in the prototype play a significant part in these observations with respect to the inductances, although further investigation with 3D FEA will be necessary to better understand this.

7.1.5 Control strategy

As an alternative for existing control strategies for energy transfer between the LG and the load, dead-beat predictive control is proposed for the first time, as far as can be determined. Predictive control is an inherently digital type of control with a very fast response and is a form of position sensorless control, i.e. no cumbersome linear position feedback or EMF sensing techniques are needed. The LG current is controlled to be in phase and proportional to the LG's EMFs for maximum energy transfer to the load. To achieve this, the EMFs, reference currents and required active rectifier voltages are calculated from measured electrical quantities and the rectifier IGBTs are switched accordingly. Simulation results of the control strategy are given in Chapter 5.6; practical measurements are given in Chapter 6.3.3 and agree very well with the simulated waveforms.

The control is also tested specifically for the case of zero stator–translator overlap at the stroke ends. In this particular LG, during the beginning and ending of the stroke when there is only partial overlap between the stator and translator, transitional phase currents flow in some of the phases with zero back EMF which causes unwanted losses. Despite this, the control strategy stays stable and continues to function as expected. Due to the transitional currents flowing, the calculated EMFs however deviate from the actual EMFs, and hence the controlled current also deviates slightly from the desired currents during the transitional phase. Overall, a 5 % reduction in the generated power is observed due to these transitional phase currents. It must be noted that while there is not complete stator–translator overlap, some degree of control is sacrificed; and all control is sacrificed while the overlap is zero. For a real installation, careful consideration will be required for whether this situation will be allowable.

It is important to note that the constant (linear), low reactance of the air-cored LG makes the control strategy as presented in this thesis possible. For iron-cored LGs, the strategy will have to be adapted to include the effect of the higher and more variable reactance and will hence increase the complexity of the control problem. It must also be noted that the low reactance requires the use of a filter to achieve smooth current waveforms when connected to the active rectifier. However, the use of a filter also has additional advantages in terms of preventing possible over voltages and high frequency losses and may in fact be required for iron-cored machines as well.

7.1.6 Final remarks

The work presented in this thesis is only a first step towards developing a novel concept air-cored PMLG. A huge amount of work is needed to take this LG from concept to a commercially viable product, if indeed it will be commercially viable. The same can be said for the proposed control strategy, which focuses on only one part of the energy conversion control process. Nevertheless, limited in scope as this project may be, a significant amount of work has gone into these first steps and it is believed that a valuable contribution has been made to the available body of knowledge on LGs for DD-WECs. The specific research contributions made in this work are outlined in Chapter 1; a more detail discussion of these contributions follows.

7.2 Contributions

1) A completely novel air-cored PMLG topology which improves on some of the problems associated with more traditional LG topologies is proposed, developed and evaluated. Pair-wise flux coupling, as analysed in [51], [70], is eliminated in this design. The air-cored stator ensures zero attraction forces between stator and translator and ideally also eliminates the attraction forces between the two opposing translator sides of double-sided air-cored machines, such as those in [48], [94].
2) It is shown that the novel topology can largely be analysed very accurately with existing methods used for ordinary linear doubles-sided machines. A two-dimensional subdomain analytical model, in particular, is developed to calculate the stator and PM generated fields for the novel LG from Maxwell's equations; from this, equations for calculating the winding flux linkages directly from the magnetic vector potential is derived, similarly as done for radial flux machines in [104]. This is used to accurately calculate the winding inductances, which is usually considered very difficult to calculate accurately for air-cored windings [63].
3) A simplified one–dimensional magnetic circuit model is also developed for the novel LG. Dimensional constraints to minimise leakage flux so as to accurately apply this model are established. Furthermore, the one-dimensional analysis assumes a sinusoidal air gap flux density distribution and only calculates the peak of this distribution. Subdomain analysis is used to establish the per unit pole width for minimum THD of the air gap flux density such that this assumption is justified.
4) The relatively simple one-dimensional analytical model is used to develop an exhaustive optimisation procedure for quickly finding optimal dimensions for minimum active mass of the novel LG.
5) The feasibility of constructing the novel LG topology, at least on a small scale, is demonstrated. It is confirmed that a relatively small amount of structural material is required for the novel topology, even without a mechanical design optimisation. Test results from the prototype LG generally also confirm the validity of the modelling and design methods used.
6) A unique test rig which simulates ideal monochromatic wave conditions for testing the LG under active control and while subjected to variable loading is developed. This enables verification of the design and simulations which are done under the assumption of perfect sinusoidal displacement.
7) The PM translators of LGs are usually longer than the stator such that the stator winding is active during as much of the stroke as possible [40], [42], [43], [44]. In this study, the translator is made shorter, and hence cheaper, such that the stator is completely in-active at the stroke ends where the generated power is very

small. It is shown that allowing the situation of zero overlap between the stator and translator at the stroke ends increases the power-to-weight ratio of the novel LG. The result can also be applicable to other LGs.

8) Dead-beat predictive control, as a position sensorless alternative to current LG control strategies for DD-WECs, is proposed, simulated and practically evaluated for LGs for DD-WECs for the first time. This inherently digital type of control eliminates the need for any kind of EMF sensing or linear position feedback in the control as used in [44], [53], [56], [58].
9) In addition to the known advantages of the low inductance, as outlined in Section 7.1.1, an important new advantage is established in terms of the chosen predictive control strategy. A requirement for accurate predictive control is accurate knowledge of system parameters [118]. The fact that the filter inductance and the LG's phase resistance can be measured fairly accurately and that the LG's synchronous inductance is negligible, therefore makes the predictive control accurate. For instance, in [118], [119], techniques are proposed for making predictive control more robust against inductance mismatches between the actual load and the model. This is particularly relevant for iron-cored machines where the synchronous inductance is dominant and also has a significant transient component. In the novel air-cored LG, the dominant phase resistance stays very constant as the relatively low current density together with natural cooling will keep the temperature variation to a minimum; improved cooling will also be possible if the LG is to be installed in the sea. As there is no possibility of saturation in the air-cored stator, the inductance is also very constant, and therefore stays negligible during all operating conditions. The air-cored stator is hence shown to have significant advantages for LGs in DD-WECs, not just in mechanical terms, but also in terms of possible control strategies.

7.3 Recommendations

There are a number of areas where further research can be focussed as discussed in this section.

7.3.1 Mechanical design and optimisation

The work in this thesis focuses mostly on the electromagnetic design of the LG. This is acceptable due to the small size of the prototype LG. However, for larger LGs, and to further reduce structural material, a thorough mechanical design and optimisation methodology should be developed. This should include both structural and thermal design of the LG, and should, if possible, be integrated with the electromagnetic design optimisation as is done in [48], [93].

As part of a thorough mechanical design, construction methods should be investigated for large scale LGs. Waterjet cutting and assembling layers of engineering plastic will probably not be very economical or practical for large machines. Furthermore, the linear bearings used for the LG was chosen as a simple solution in the chosen test setup, and is by no means the most optimal solution for the LG. A sliding surface or bearings on the inside of the translator may be a better option. A thorough study should be conducted to find the best bearing solution.

7.3.2 Test setup

The current test setup works well for verifying the design to a large extent. Further confidence in design methods will be established if the current problems can be solved to enable full load and also overload testing of the LG.

However, to enable testing of a variety of LGs and also to simulate more realistic wave conditions, a new test setup should be developed. The test setup should provide for accurately measuring the mechanical input power to the LG in order to measure the LG efficiency. If possible, a control system should be able to independently control the translator displacement and the excitation force to match that of actual recorded wave data. The LG control strategy can then be tested under more realistic conditions. The linear test bed at Oregon State University [43] is currently probably the most advance LG test system and serves as a good example for further development. Development of such a system can be expected to incur considerable cost, and should as such be generic enough to enable testing of a variety of LGs.

Before wave tank or sea trials will be a possibility, the LG must be integrated into an actual WEC. For this, a new WEC should be developed, or the possibility of integrating the novel LG into an existing WEC (see Chapter 1.3.3) should be investigated. There may be the possibility of cooperating with an existing WEC developer to further the development of the LG and then to also integrate the LG into their WEC. This option should be seriously considered if this LG is ever to be commercially viable.

7.3.3 Electrical and Electromagnetic design

The analytical and FEA models presented in this thesis are accurate enough for calculating the relevant magnetic and electrical parameters of the LG and further work in this area is not a priority. 3D FEA can be used to better understand the flux paths and inductances in the machine, although the inductances are already small enough to be negligible, and hence this is not strictly necessary. A more detailed analysis of the magnetic attraction forces between the magnets may however be necessary. This will tie into the more detailed mechanical design of the machine as mentioned above. It would be particularly relevant to study the effect of manufacturing and assembly inaccuracies and the effect this may have on the required structural material.

The control strategy is shown to work well under changing circumstances, such as the constantly changing translator velocity and the varying stator – translator overlap. However, a more complete strategy will also cater for abnormal circumstance such as network faults or stormy seas and is something which should also be investigated.

The design for the prototype LG was done at a single average velocity. For LGs which will be used in the sea, more consideration needs to be given to the actual sea conditions in which the LG will operate. This will include finding optimal dimensions for a large variety of operating conditions, including extreme sea conditions.

7.3.4 General

Work which has more recently been published explores interesting new methods of increasing power density, and hence reducing the cost, of LGs for DD-WECs. This include increasing the translator speed via a non-linear PTO [129] and via magnetic gearing [130], or increasing the power density by using high temperature superconducting (HTS) excitation as an alternative to PMs, as well as HTS stator windings [131], [132], [133]. It is possible that these ideas can be incorporated into future work done on the novel LG of this thesis.

Appendix A

Wave energy absorption

As part of the background for the work in this thesis, it is necessary to have an understanding of the basic principles of ocean wave energy conversion. The theory presented in this Appendix is covered in more detail by McCormick [21] and Falnes [13], [115], [116]; these sources give a good overview of the large amount of work which have been done in this area since the early 1970s. It must be noted that the physical phenomena in the sea is infinitely more complex than presented here. However, for deep water waves (when the depth is greater than half the wavlength λ_w) with sufficiently small wave height H_w (when $H_w/\lambda_w < 1/50$) the wave dynamics can be approximated with linear theory with good accuracy. This basic understanding then forms a good foundation for understanding more complex phenomena.

A.1 A simplified explanation

The theory of wave energy conversion is most often explained in terms of a floating buoy with motion restricted to the heave (up and down) direction. A floating buoy can generally be assumed to be a point absorber (from Chapter 1.3.2) and is therefore particularly applicable for DD-WECs. The DD-WEC of [42], for instance, uses exactly this concept, i.e. a LG directly driven by a heaving buoy. In this Appendix, the buoy is assumed to be two-dimensional, symmetrical and restricted to sinusoidal heave motion.

The energy per unit surface area of a wave is given as

$$W_w = \frac{\gamma_{sw} g_a H_w^{\,2}}{16}, \tag{A.1}$$

where γ_{sw} is the water density and g_a is the gravitational constant. In terms of the wave properties, it is clear that the energy is proportional to the square of the wave height. In order to decrease (or absorb) some, or all, of this energy, the WEC needs to create a wave which destructively interferes with this incident wave. In Fig. A.1(a) and (b) the incident wave and created wave are respectively shown; note that the symmetrical buoy radiates identical waves both to the left and to the right. The resultant sea-level elevation of the buoy interacting with the incident wave is then obtained by the superposition of the waves in Fig. A.1(a) and (b) and is shown in Fig A.1(c). The optimum amount of energy is absorbed by the WEC when the created wave height is half of the incident wave height and when the two waves are in phase; the mathematical proof of this follows in the next section. From the smaller wave height to the right of the WEC in Fig. A.1 (c) it is clear that the energy in the incident wave has been reduced (or absorbed by the buoy).

It is important to note that energy is required in order to absorb more energy. If the incident wave energy is proportional to $H_w^{\,2}$, the required energy from the WEC for optimum energy conversion is proportional to $2(H_w/2)^2 = 0.5H_w^{\,2}$ for optimum energy absorption (one wave travelling left and one travelling right). A maximum of 50 % of the wave energy can therefore be absorbed.

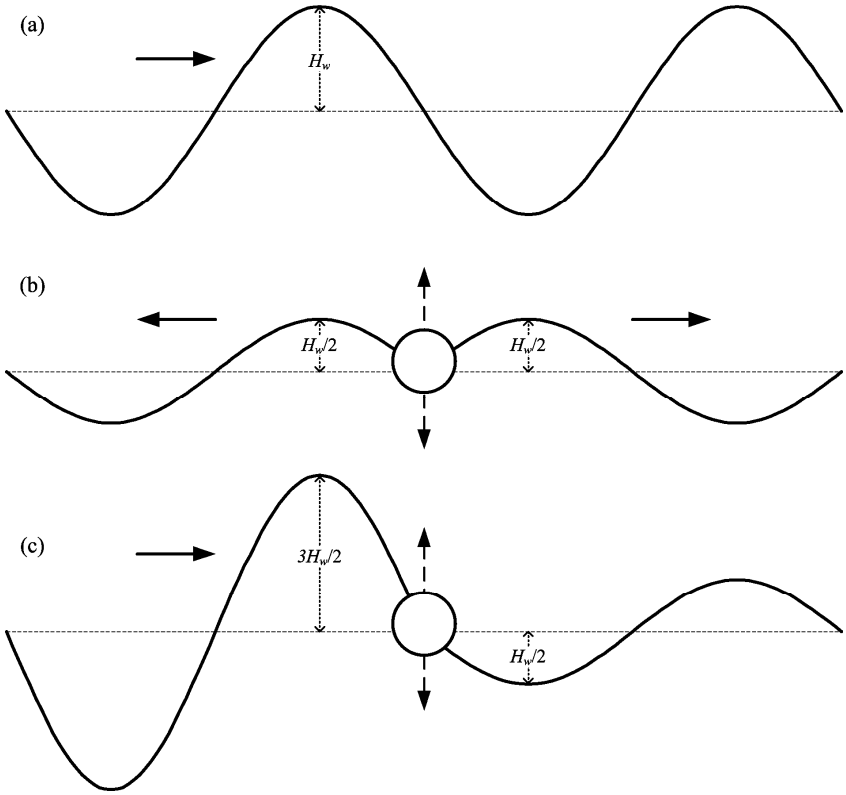

Fig. A.1 Optimum energy absorbed by a two-dimensional, symmetrical, heaving buoy. (a) The incident wave with height H_w travelling to the right, (b) the waves radiated by the buoy in both directions and (c) the superposition of the two former waves. It can be seen that the wave height to the right of the buoy has decreased, indicating that energy was removed (absorbed) from the wave.

A.2 Modelling

The dynamics of a heaving buoy point absorber connected to a LG as load and subjected to an incident wave can be modelled as simple mass-spring-damper system as shown in Fig. A.2, and as also done in [57]. The wave excitation force, $f_e(t)$, acts on the buoy of mass M, while the combined effects of the friction and viscous losses, the radiated wave and the buoy load (LG force) is modelled as a spring with constant c and damper with constant b. The spring constant c is given as

$$c = c_h + c_g, \tag{A.2}$$

where c_h represents the hydrostatic buoyancy stiffness and c_g represents the load (LG) stiffness. The damper constant b is given as

$$b = b_f + b_r + b_g, \tag{A.3}$$

where b_f is represents friction and viscosity resistance, b_r represents the wave radiated by the buoy and b_g represents the load (LG) resistance. The mass M consists of the system's physical mass plus a component called the "added mass", which is caused by the radiated wave. Newton's third law gives

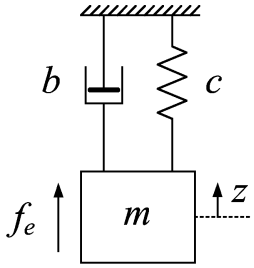

Fig. A.2 A spring-mass-damper model of a heaving buoy subject to a wave excitation force.

$$\begin{aligned}\sum f_z(t) &= M\ddot{z}(t) \\ &= f_e(t) - cz(t) - b\dot{z}(t),\end{aligned} \tag{A.4}$$

where $z(t)$ is the vertical displacement of the buoy. The sinusoidal excitation force is given as

$$f_e(t) = F_e \cos(\omega_w t), \tag{A.5}$$

where ω_w is the the angular wave frequency. The particular solution for the buoy displacement can now also be assumed to be sinusoidal with the same frequency as that of the excitation force, given as [132]

$$z(t) = Z \cos(\omega_w t - \chi), \tag{A.6}$$

By substituting (A.5) and (A.6) into (A.4), the amplitude Z and phase χ of $z(t)$ can respectively be found as [132]

$$Z = \frac{F_e/c}{\sqrt{\left[(\omega_w/\omega_o)^2 - 1\right]^2 + \left[(2\varsigma\omega_w)/\omega_o\right]^2}} \tag{A.7}$$

and

$$\chi = \tan^{-1}\left[\frac{2\zeta(\omega_w/\omega_o)}{1-(\omega_w/\omega_o)^2}\right], \tag{A.8}$$

where ω_o is the natural frequency of the system defined as

$$\omega_o = \sqrt{\frac{c}{M}} \tag{A.9}$$

and ζ is the damping factor of the system defined as

$$\zeta = \frac{b}{2M\omega_o}. \tag{A.10}$$

The velocity of the buoy can be calculated as

$$\dot{z}(t) = \omega_w Z \cos(\omega_w t - (\chi - \pi/2)) = V_p \cos(\omega_w t - \psi). \tag{A.11}$$

Multiplying (A.4) through by $\dot{z}(t)$ gives

$$f_e(t)\dot{z}(t) = M\ddot{z}(t)\dot{z}(t) + b\dot{z}^2(t) + cz(t)\dot{z}(t). \tag{A.12}$$

Each of the terms in (A.12) represents power. The wave excitation power can be simplified as[1]

$$p_e(t) = f_e(t)\dot{z}(t) = \frac{F_e V_p}{2}\left[\cos(\psi) + \cos(2\omega t + \psi)\right], \tag{A.13}$$

where the first term represents the average power and the second term a sinusoidal oscillation about the average power. It is clear that maximising V_p and minimising ψ will maximise the average power in the system. From (A.8) and (A.11), $\psi = 0$ when $\omega_o = \omega_w$. For this condition, V_p [from (A.7) and (A.11)] is also maximised (assuming a fixed value of ζ). This condition is known as resonance and will occur when ω_w happens to equal ω_o, or when ω_o is controlled to match ω_w.

A.3 Electrical circuit equivalent

The differential equation of (A.4) can be compared to the differential equation obtained by applying Kirchoff's voltage law to an electrical circuit. Then, $f_e(t)$ is the voltage, $\dot{z}(t)$ is the current, $z(t)$ is the charge on the capacitor, M is inductance, $1/c$ is capacitance, and b is resistance. From the electrical circuit analogy, the resonance condition is perceived slightly differently. In order for the current to be in phase with the voltage, the reactance in the circuit must sum to zero as

$$\omega_w M - \frac{c}{\omega_w} = 0. \tag{A.14}$$

Rearranging this results in (A.9) and hence confirms the equivalence between the two approaches. Substituting (A.2) into (A.14) and rearranging gives

$$c_g = \omega_w^2 M - c_h. \tag{A.15}$$

In a phase control scheme, (A.15) serves as the reference value for the load (LG) stiffness.

Phase control on its own is the first step to maximising the power absorbed by the *whole system*. In addition, the power absorbed by the *load* should also be maximised. From classical electric circuit theory, the condition for maximum power transfer to a load is given as

$$\mathbf{Z_g} = \mathbf{Z_w}^*, \tag{A.16}$$

where $\mathbf{Z_g}$ is the load impedance and $\mathbf{Z_w}^*$ is the complex conjugate of the source impedance. For the system in Fig. A.3,

[1] Simplification done by using the trigonometric identity $\cos A \cos B = (1/2)\left[\cos(A-B) + \cos(A+B)\right]$.

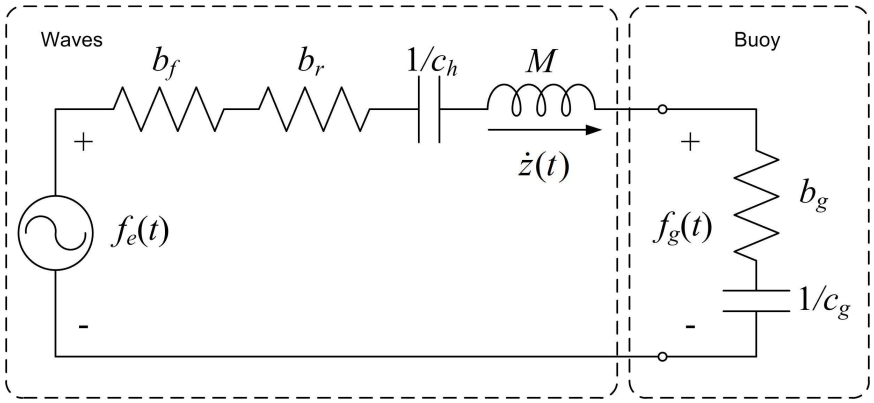

Fig. A.3 An electrical circuit equivalent model of a heaving buoy subject to a wave excitation force.

$$\mathbf{Z_g} = b_g - \mathrm{j}\frac{c_g}{\omega_w} \text{ and } \mathbf{Z_w} = b_r + b_f + \mathrm{j}\left(M - \frac{c_h}{\omega_w}\right). \tag{A.17}$$

The condition for maximum power transfer then gives

$$b_g = b_w = b_r + b_f \tag{A.18}$$

and (A.15). Satisfying (A.16) therefore achieves both phase and amplitude control of the velocity. For amplitude control, (A.18) serves as the reference value of the load (LG) resistance. b_g and c_g can be controlled mechanically (e.g. with hydraulic or pneumatic actuators), or electrically by controlling the LG current.

The maximum active load power, as dissipated in b_g, can be expressed, from (A.12) and (A.18), or from the electrical circuit in Fig. A.3, as

$$\begin{aligned} P_{g(\max)} &= \tfrac{1}{2} V_p{}^2 b_w \\ &= P_e - \tfrac{1}{2} V_p{}^2 b_w \\ &= \tfrac{1}{2} P_e . \end{aligned} \tag{A.19}$$

Therefore, as mentioned before, the maximum power that can be extracted from the waves is 50 % of the excitation power.

Appendix B

Electromagnetic theory

In order to understand the conversion of mechanical energy to electrical energy, a thorough grasp of the physical laws pertaining to electricity and magnetism is necessary. In this Appendix an overview of electromagnetic theory is given, as found in [144]. It can be difficult to explain exactly what an electric and magnetic field is. One way to form a concept of such a field is to see it as the mechanisms by which a charge can perform work on another charge over a distance. These fields can then be defined mathematically in terms of the force **f** exerted on a test charge q moving at a velocity **v**. This force is given in terms of the electric field intensity **E** and the magnetic flux density $\mathbf{B} = \mu_0\mathbf{H}$ as

$$\mathbf{f} = q\left(\mathbf{E} + \mathbf{v} \times \mu_0\mathbf{H}\right), \tag{B.1}$$

where μ_0 is the permeability of free space and **H** is the magnetic field intensity. From (B.1) it can be seen that the force induced on the charge is composed of two components: one independent of the velocity and one proportional and orthogonal to the velocity. The equation in (B.1) is known as the *Lorentz force law*.

B.1 Maxwell's equations

Charge is the source of electric fields, while charge in motion, or current, is the source of magnetic fields. Charge and current is most often defined in terms of their respective densities. Charge density ρ is the charge per unit volume and current density **J** is the time rate of change of charge per unit area given by

$$\mathbf{J} = \rho\mathbf{v}. \tag{B.2}$$

The so called *Maxwell's equations* relate electric and magnetic fields to these sources and to each other. The first of these is *Gauss' law*, which relates the electric field to the charge density. It states that the net charge within an arbitrary volume V that is enclosed by surface S is related to the net electric flux through that surface by

$$\oint_S \varepsilon_0\mathbf{E} \cdot d\mathbf{a} = \int_V \rho dv, \tag{B.3}$$

where ε_0 is the permittivity of free space. The term $\varepsilon_0\mathbf{E}$ is called the electric displacement flux density, **D**. From (B.3), there must be a net displacement flux from a region containing net charge.

Secondly, *Ampère's law* relates the magnetic field to the current density. It states that the line integral, or circulation, of the magnetic field around a closed contour is related to the net current passing through the surface spanning the contour plus the time rate of change of the net displacement flux density through the surface by

$$\oint_C \mathbf{H} \cdot d\mathbf{s} = \int_S \mathbf{J} \cdot d\mathbf{a} + \frac{d}{dt}\int_S \varepsilon_0 \mathbf{E} \cdot d\mathbf{a}. \tag{B.4}$$

The second term on the right of (B.4) is also called the displacement current.

By applying Ampère's law to a closed surface and substituting Gauss' law into it, the relationship between the charge and current density is found as

$$\oint_S \mathbf{J} \cdot da + \frac{d}{dt}\int_V \rho dv = 0. \tag{B.5}$$

This is known as the *law of charge conservation*. Strictly, (B.5) is not considered as one of the Maxwell's Laws, but of course follows from the Laws and provides further insights to the relationship between the two sources of the fields. It shows that the net charge density enclosed in a volume must be decreasing with time in order for there to be a net current out of the volume.

The relationship between the electric and magnetic field is defined by *Faraday's integral law*, which is often also referred to as *Faraday's law of electromagnetic induction*. This law states that the circulation of the electric field around a closed contour is related to the time rate of change of the flux through the surface spanning the contour by

$$\oint_C \mathbf{E} \cdot d\mathbf{s} = -\frac{d}{dt}\int_S \mathbf{B} \cdot d\mathbf{a}. \tag{B.6}$$

The net flux density through the enclosed surface in (B.6) is also referred to as the *flux linkage* λ.

The definition of electromotive force (EMF) is related to Faraday's integral law in (B.6). EMF along a certain path between points *a* and *b* is defined as

$$EMF_{ab} = \int_a^b \mathbf{E} \cdot d\mathbf{s}. \tag{B.7}$$

If the EMF between the two points is path independent it is referred to as the voltage between the two points.

Lastly, the *magnetic flux continuity law* states that the net magnetic flux out of a region must be zero and is given as

$$\oint_S \mu_0 \mathbf{H} \cdot d\mathbf{a} = 0. \tag{B.8}$$

For the two dimensional case this means that the flux lines form closed paths [70].

The integral laws of Maxwell are summarised in Table B.1. These laws are rather remarkable in the fact that they apply to any combination of volume and enclosed surface or surface and enclosing contour. It is by associating the relevant volumes, surfaces and contours with conductors and other magnetic materials that the basic laws of electric and magnet *circuits* are formulated. It however becomes exceedingly difficult to calculate the fields with

the integral laws if the geometry is not highly symmetrical, hence making the integral laws difficult to apply in realistic applications.

In order to help overcome this, the integral laws are rewritten in differential form. In order to do this, Gauss' and Stoke's integral theorems are used to derive the differential laws also given in Table B.1 alongside its equivalent integral form.

Table B.1 Maxwell's and the charge conservation law in integral and equivalent differential forms.

Law	Integral law	Differential law
Gauss' Law	$\oint_S \varepsilon_0 \mathbf{E} \cdot d\mathbf{a} = \int_V \rho dv$	$\nabla \cdot \varepsilon_0 \mathbf{E} = \rho$
Ampère's Law	$\oint_C \mathbf{H} \cdot d\mathbf{s} = \int_S \mathbf{J} \cdot d\mathbf{a} + \frac{d}{dt}\int_S \varepsilon_0 \mathbf{E} \cdot d\mathbf{a}.$	$\nabla \times \mathbf{H} = \mathbf{J} + \frac{\partial \varepsilon_0 \mathbf{E}}{\partial t}.$
Faraday's Law	$\oint_C \mathbf{E} \cdot d\mathbf{s} = -\frac{d}{dt}\int_S \mu_0 \mathbf{H} \cdot d\mathbf{a}.$	$\nabla \times \mathbf{E} = -\frac{\partial \mu_0 \mathbf{H}}{\partial t}.$
Magnetic Flux Continuity Law	$\oint_S \mu_0 \mathbf{H} \cdot d\mathbf{a} = 0.$	$\nabla \cdot \mu_0 \mathbf{H} = 0$
Charge Conservation Law	$\oint_S \mathbf{J} \cdot da + \frac{d}{dt}\int_V \rho dv = 0.$	$\nabla \cdot \mathbf{J} + \frac{\partial \rho}{\partial t} = 0.$

B.2 Continuity (Boundary) conditions

For each of the laws in Table 1 there exists a continuity condition which describes the relationship between fields on either side of a surface (or a boundary between different materials). Understanding these continuity laws are essential in order to successfully analyse the fields in electrical machines, where a number of different materials are used. The most important of these continuity conditions for the work in this thesis are the ones associated with Ampère's Law and with the Magnetic Flux Continuity Law.

B.2.1 Ampère's continuity condition

Consider the boundary between material 1 and 2 shown in Fig. B.1. By selecting a surface S spanned by contour $c = c_1 + c_2$ such that c_1 is on material 1's side of the boundary and c_2 is on material 2's side of the boundary, we can write Ampère's Law (B.4) as

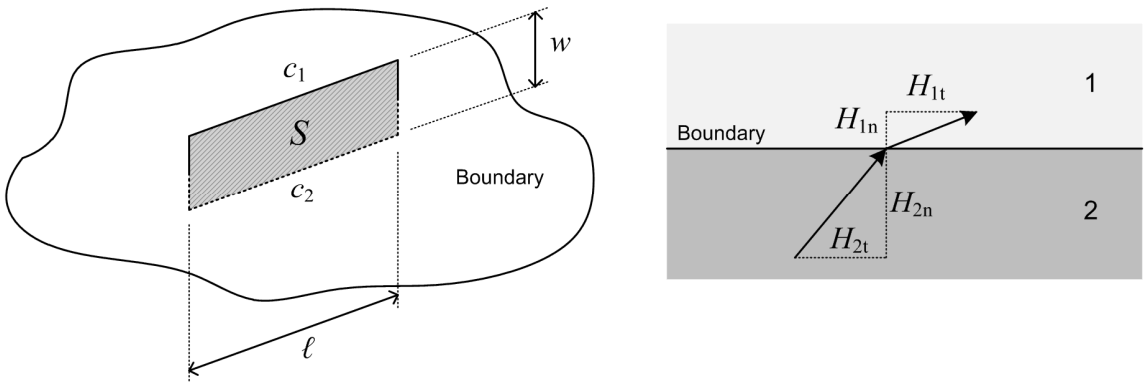

Fig. B.1 Ampère's continuity condition shows that the tangential components of the magnetic field intensity are equal at the interface between material 1 and 2, but only when there is no surface current density present.

$$\oint_{c_1} \mathbf{H}_1 \cdot d\mathbf{s} + \oint_{c_2} \mathbf{H}_2 \cdot d\mathbf{s} = \int_S \mathbf{J} \cdot d\mathbf{a} + \frac{d}{dt}\int_S \varepsilon_0 \mathbf{E} \cdot d\mathbf{a} \tag{B.9}$$

By assuming that there are no current densities or displacement current densities, and by also assuming *w* in Fig. B.1 is infinitely small, (B.9) can be reduced to

$$\ell \mathbf{i_t} . \left(\mathbf{H}_1 - \mathbf{H}_2 \right) = 0, \tag{B.10}$$

where $\mathbf{i_t}$ is a unit vector tangential to the boundary and in the plane of surface *S*. Simplifying (B.10) then gives

$$H_{1t} = H_{2t}. \tag{B.11}$$

This shows that the tangential components of the magnetic field intensities at the boundary must be equal as also shown in Fig. B.1. Note that this only applies when there is no surface current density.

B.2.2 Magnetic flux continuity condition

Consider the boundary between material 1 and 2 shown in Fig. B.2. By selecting a cylindrical volume which spans both materials and by making the cylinder side *w* infinitely small in such a way that the cylinder's two end surfaces, S_1 and S_2, are still within the two different materials, the Flux Continuity Law (B.8) can be given as

$$\begin{aligned} \oint_{S_1} \mu_1 \mathbf{H}_1 \cdot d\mathbf{a} + \oint_{S_2} \mu_2 \mathbf{H}_2 \cdot d\mathbf{a} &= \oint_{S_1} \mathbf{B}_1 \cdot d\mathbf{a} + \oint_{S_2} \mathbf{B}_2 \cdot d\mathbf{a} \\ &= 0. \end{aligned} \tag{B.12}$$

Further assuming that $\mathbf{B_1}$ and $\mathbf{B_2}$ are finite everywhere on S_1 and S_2 and that the areas of S_1 and S_2 have direction normal to the boundary, (B.12) can be reduced to

$$A\mathbf{i_n} . \left(\mathbf{B}_1 - \mathbf{B}_2 \right) = 0, \tag{B.13}$$

where *A* is the area of S_1 and S_2 and $\mathbf{i_n}$ is a unit vector normal to the boundary. From (B.13) it then follows that

$$B_{1n} = B_{2n}. \tag{B.14}$$

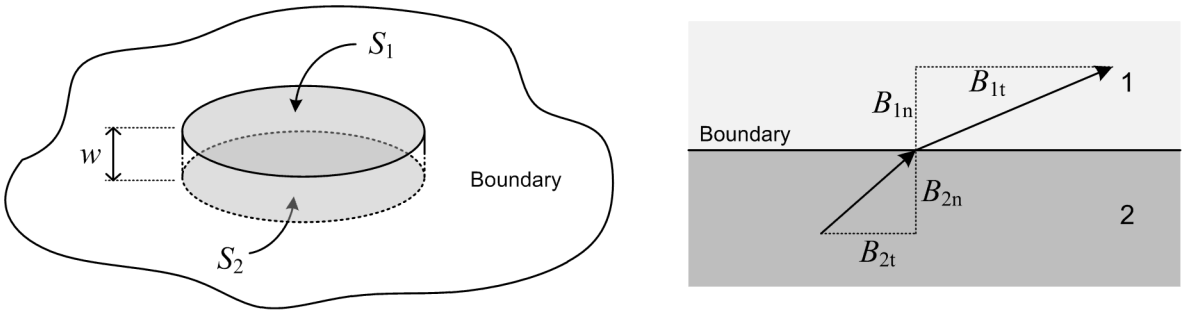

Fig. B.2 The magnetic flux continuity condition shows that the normal components of the magnetic flux densities are equal at the interface between material 1 and 2.

The normal component of the flux density in material 1 is hence equal to the normal component of flux density in material 2 at the boundary between the two materials as also shown in Fig B.2.

B.3 Quasistatics

Two special cases of Maxwell's equation exists where either the displacement current in Ampere's law or the magnetic induction in Faraday's law can be ignored (basically, the time rate of change terms are ignored) such that

$$\nabla \times \mathbf{H} = \mathbf{J} \tag{B.15}$$

and

$$\nabla \times \mathbf{E} = 0. \tag{B.16}$$

These two conditions are respectively referred to as magnetoquasistatic (MQS) and electroquasistatic (EQS) and are realised when the time rate of change of the respective fields are small enough such that the wavelengths are much greater than the physical dimensions of the relative physical objects. In effect, a snapshot of the field source distribution at that time is sufficient to determine the actual field distribution as well; the previous state of the source distributions hence does not have much of an influence of the current state of the field distributions.

When both EQS and MQS are applicable, some consideration must be given as to which condition takes precedence. There are two aspects to consider. First, it must be noted that it can be shown that a vector is determined if the curl and divergence of that vector is specified. Second, the sources of the fields must be understood for the particular problem. For example, if ρ is given, both Gauss' Law (see Table 1) and the EQS form of Faraday's law (B.16) are specified. Both the curl and divergence of **E** are hence specified and **E** is so determined. **H** and **J** are then a "consequence" of **E** and the EQS condition takes precedence. However, if **J** is given, the curl and divergence of **H** are respectively specified in the MQS form of Ampere's law (B.15) and the flux continuity condition (See Table B.1) and hence **H** is so determined. **E** and ρ are then a "consequence" of **H** and the MQS condition takes precedence.

Electrical machines must be designed such that an EMF can be induced in the stator windings according the Faraday's exact law (B.6) and can hence not be EQS. Furthermore, the current density in the windings must be well defined and controlled. Also, at normal power system frequencies of 50-60 Hz, electromagnetic waves have wavelengths of 5 - 6×10^6 m, which are of course many orders of magnitude larger than any realistic machine. It is hence safe to assume a MQS condition and make use of the reduced form of Ampere's law (B.15) in the analysis and design of electrical machines.

B.4 Magnetic materials

The current density **J**, which has so far been described as the source of the **H** field, is more accurately described as the *free* current density; this refers to unpaired electrons freely flowing through a conducting material, for instance. There is, however, also another important source of magnetic fields in the form of electrons circulating

around the atomic nuclei of materials. These circulating "currents" give rise to magnetic dipoles. If all these dipoles are aligned, usually because of an externally applied magnet field **H**, a resultant magnetic field **M**, called the magnetisation, is created. For magnetically linear materials, the magnetisation is dependent on **H** such that

$$\mathbf{M} = \chi_m \mathbf{H}, \tag{B.17}$$

where χ_m is the magnetic susceptibility. The effect of the magnetisation is taken into account in the flux density such that

$$\begin{aligned} \mathbf{B} &= \mu_0 \left(\mathbf{H} + \mathbf{M} \right) \\ &= \mu_0 \left(1 + \chi_m \right) \mathbf{H} \\ &= \mu_0 \mu_r \mathbf{H} \end{aligned} \tag{B.18}$$

where μ_r is termed the relative permeability of the material.

Permanent magnets are created when a residual magnetisation, $\mathbf{M_r}$, remains present in the material after the externally applied field is removed. The total magnetisation of a permanent magnet is then given as

$$\mathbf{M} = \mathbf{M_i} + \mathbf{M_r}, \tag{B.19}$$

where $\mathbf{M_i}$ is the induced magnetisation. Substituting (B.19) into (B.18) gives

$$\begin{aligned} \mathbf{B} &= \mu_0 \left(\mathbf{H} + \mathbf{M_i} + \mathbf{M_r} \right) \\ &= \mu_0 \left(1 + \chi_m \right) \mathbf{H} + \mu_0 \mathbf{M_r} \\ &= \mu_0 \mu_r \mathbf{H} + \mathbf{B_r} \end{aligned} \tag{B.20}$$

where $\mathbf{B_r} = \mu_0 \mathbf{M_r}$ is called the remanent flux density of the PM; this is a measure of the flux density in the magnet without any external field applied. A typical B–H curve for a magnetic material is shown in Fig. B.3 where the B_r value is seen at $H = 0$. The flux density can only be reduced to 0 by applying an external field of $-H_c$,

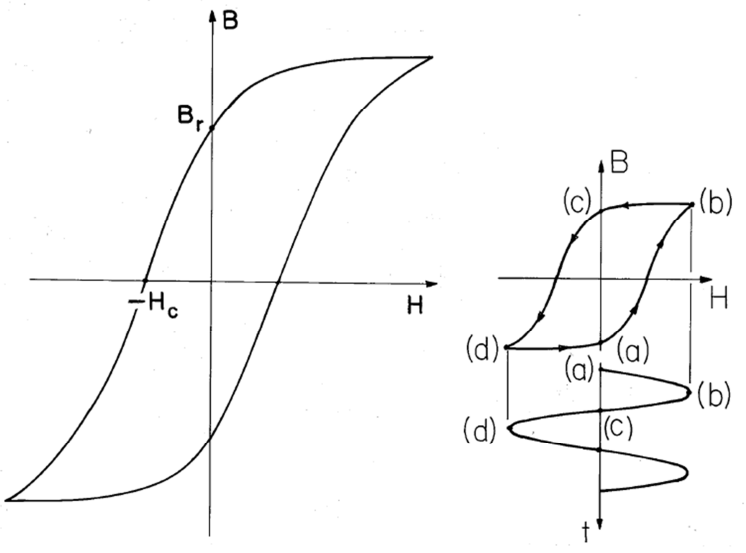

Fig. B.3 B-H curve for a typical ferromagnetic material.

called the coercive field strength, to the PM. This is referred to as demagnetizing the PM.

The areas where the curve saturates is when there are no more dipoles left to align with the applied field. In other words, μ_r reduces from its "normal" value to about 1 in the saturated areas. The slope of the B-H curve therefore in effect decreases from $\mu_r \mu_0$ for small values of **H** to only μ_0 for large values of **H**. This non-linear behaviour is very prominent in ferromagnetic materials which have very high values of μ_r in the linear region; the different types of steel used in the manufacturing of electrical machines are all ferromagnetic in nature.

B.5 Magnetic vector potential

In order to start using Maxwell's equations to solve for **B**, it is necessary to manipulate the equations into a slightly more usable form. In order to do this, the magnetic flux density is expressed as the curl of another vector, **A**, called the magnetic vector potential, such that

$$\mathbf{B} = \nabla \times \mathbf{A}. \tag{B.21}$$

This can be seen as a way of specifying some vector in terms of the existing, known value of **B** (except that it is *not* actually known at this stage and this new vector is created in order to assist with the calculation of **B**). However, in order to completely define **A**, its divergence must also be specified. The value of its divergence can be chosen and should be chosen to make the ensuing field calculations more convenient. Choosing this specification is termed *gauging*. The value at which the gauge should be set will become clear next.

The equation in (B.21) can be seen as the integral of the Magnetic Flux Continuity Law (B.8). Ampère's Law (B.15) contains the source of the magnetic flux, **J**, and attention is hence naturally shifted to this equation next. Rearranging and substituting (B.20) into (B.15) gives an expression of **B** in terms of the field source **J** such that

$$\nabla \times \left(\mathbf{B} - \mu_0 \mathbf{M}_r \right) = \mu_0 \mu_r \mathbf{J} \tag{B.22}$$

Furthermore, substituting (B.21) into (B.22) and simplifying gives

$$\nabla \times \left(\nabla \times \mathbf{A} \right) - \mu_0 \left(\nabla \times \mathbf{M}_r \right) = \mu_0 \mu_r \mathbf{J} \tag{B.23}$$

The identity,

$$\nabla \times \left(\nabla \times \mathbf{A} \right) = \nabla \left(\nabla . \mathbf{A} \right) - \nabla^2 \mathbf{A} \tag{B.24}$$

can be substituted into (B.23). At this point it is recognised that setting the gauge such that div A = 0, the identity in (B.24) can be simplified significantly. This gauge is called the *Coulomb Gauge*. Setting this gauge, substituting (B.24) into (B.23) and rearranging then gives

$$\nabla^2 \mathbf{A} = -\mu_0 \mu_r \mathbf{J} - \mu_0 \left(\nabla \times \mathbf{M}_r \right), \tag{B.25}$$

which is in the form of a vector Poisson equation. This equation basically gives **A** in terms of two known and controllable parameters, namely the current density (which would usually only be in the stator windings) and the residual magnetisation of the chosen PMs (which is specified by the manufacturer in terms of B_r).

For the linear electrical machine model in Fig. 2.15, **J** only has a *z*-directed component and it is assumed that $\mathbf{M_r}$ only has a *y*-directed component. Furthermore, **B** only has a *x*- and *y*-component; expanding (B.21) then gives

$$\begin{aligned} B_x\mathbf{i_x} + B_y\mathbf{i_y} &= \begin{vmatrix} \mathbf{i_x} & \mathbf{i_y} & \mathbf{i_z} \\ \frac{\partial}{\partial x} & \frac{\partial}{\partial y} & \frac{\partial}{\partial z} \\ A_x & A_y & A_z \end{vmatrix} \\ &= \left(\frac{\partial A_z}{\partial y} - \frac{\partial A_y}{\partial z}\right)\mathbf{i_x} - \left(\frac{\partial A_z}{\partial x} - \frac{\partial A_x}{\partial z}\right)\mathbf{i_y}. \end{aligned} \tag{B.26}$$

Since the model is two-dimensional there is no change in **A** in the *z*-direction and B_x and B_y can respectively be given as

$$B_x = \frac{\partial A_z}{\partial y} \tag{B.27}$$

and

$$B_y = -\frac{\partial A_z}{\partial x}. \tag{B.28}$$

The magnetic vector potential defined in (B.21) can hence be assumed to only have a *z*-directed component.

Due to all the above, the vector Poisson equation in (B.25) can then be reduced to

$$\nabla^2 A_z = -\mu_0\mu_r J_z\mathbf{i_z} - \mu_0\left(\frac{\partial M_{ry}}{\partial x}\mathbf{i_z} - \frac{\partial M_{ry}}{\partial z}\mathbf{i_x}\right), \tag{B.29}$$

Further simplifications of (B.29) are possible, depending on the specific problem domain. This is discussed in Chapter 3 for the LG of this thesis. Once A_z is calculated from (B.29), the result can be substituted back into (B.21), or (B.27) and (B.28), to calculate the magnetic flux density **B**.

B.6 Finite element analysis

B.6.1 Overview

Analytical solutions to (B.25) can be very difficult, if not impossible, to find. This is especially true when the geometry in the study area (the machine) is complicated and when the non-linearity of the permeability of magnetic materials plays an important role. A solution to (B.25) can however also be found numerically by the Finite Element Method (FEM) as described in [147], [145], [146]. With the FEM, a 2-D problem domain is divided into a mesh of triangular elements as shown in Fig. 3.7. The magnetic vector potential in each element is then

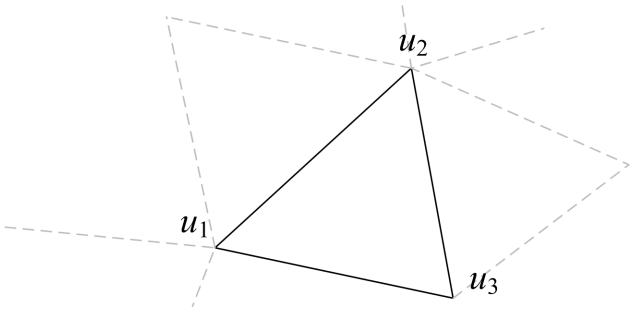

Fig. B.4 A triangular element in a finite element mesh.

approximated with a polynomial. A first order polynomial approximation for A_z in the element in Fig B.4 is given as [148]

$$A_z(x,y) = \alpha_1 + \alpha_2 x + \alpha_3 y = N_1 u_1 + N_2 u_2 + N_3 u_3, \tag{B.26}$$

where N_i are position functions and u_i are the unknown values of the potential at the nodes (triangle vertices).

Since the nodes of the neighbouring triangles overlap/correspond, the equations of the different triangles can be inter-related to form a set of simultaneous equations; these equations must be solved to find the coefficients of (B.26) for each of the elements. The result is a piece-wise continuous approximation of the magnetic vector potential for the entire problem domain. The magnetic flux density can then be obtained from (B.21).

An iterative process is used to deal with non-linear permeability. At the start of the process, the initial permeability from the B-H curve (Fig. B.3) is assigned to each element. Once the flux density is calculated as explained above, the permeability is updated from the B-H curve and the process is repeated until the permeability converges to within a given specification. The Newton iteration method is commonly used.

It is important to realise that FEM does not produce an exact solution. The solution error can however be made negligibly small by making the elements sufficiently small or by using higher order polynomial approximations in (B.26). The convergence tolerance for non-linear calculations can also be adjusted. All these strategies however increase the problem size and the required processing power and time. There is therefore a clear trade-off between computing power/time and solution accuracy with FEM.

B.6.2 Boundary conditions

In order to solve the abovementioned equations it is necessary to know how the field behaves beyond the boundaries of the problem domain. For 2-D problems, these boundaries form closed curves around the problem geometry where field properties must be specified as boundary conditions. The two most common boundary conditions are:

- The Dirichlet, or *flux tangential*, boundary condition. The flux function is constant over any part of the boundary, and hence the boundary forms part of a flux line.

- The Neumann, or *field normal*, boundary condition. The magnetic flux density is normal to any part of the boundary, and hence the flux lines are at right angles to the boundary.

Assigning a Dirichlet boundary around a model is equivalent to placing the model in a cavity with zero permeability, i.e. such that no flux can escape from the model. This is an effective boundary for high permeability objects such as the back-iron of an electrical machine. Assigning a Neumann boundary around a model is equivalent to placing the model in a cavity of infinite permeability. Instead of containing flux like the Dirichlet boundary, the Neumann boundary has the effect of drawing flux out of the model. The Neumann boundary is typically used to reduce a problem's size by exploiting symmetry.

Magnetic fields in electrical machines typically have a periodic structure, where the fields in one part of the machine are identical or symmetrical to the fields in another part. This means that only one such a representative part of the machine needs to be modelled. The periodic nature of the machine is modelled by a constraint between the field values at either end of the part. This constraint is called a *periodic boundary condition*. If the field values of the two ends are equal in magnitude and direction, it is called an *even periodic* boundary condition. If the field values of the two ends are equal in magnitude but opposite in direction it is called an *odd period* boundary condition.

For the work in this thesis, the commercial FEM package Infolytica MagNet 7 is used. This software has been in development since 1978 and is based on the finite element method as presented by Silvester & Ferrari [146]; it so happens that Silvester is also one of the co-founders of Infolytica corporation. MagNet is a good example of the many additional features of which FEA packages are currently also capable. Some of these features include calculation with non-linear materials, automatic mesh adaption for increased accuracy, transient solutions and motional effects in 2-D and 3-D, coupling with electric circuits and mechanical and thermal models, utilisation of multicore processors, parameterisation for "what if"–analysis, design optimisation and integrated visualisation and graphing tools.

Appendix C

Fourier series expansions

The distributions of conductor density, current density and PM magnetisation given in Chapter 3 are fairly intuitively represented graphically. However, in order to calculate the resulting magnetic fields, these distributions have to be represented mathematically; this involves calculating their Fourier series expansions as explained in [149]. The derivations of these Fourier series expansions are here given in more detail.

C.1 Overview of the Fourier Series expansion

Jean Baptiste Joseph Fourier discovered that a periodic function, $f(t)$, can be represented by an infinite sum of harmonically related sine and cosine functions such that

$$f(t) = a_0 + \sum_{m=1}^{\infty} a_m \cos(m\omega_0 t) + b_m \sin(m\omega_0 t), \tag{C.1}$$

where ω_0 is the fundamental frequency of $f(t)$ and m is the integer sequence 1, 2, 3,... Each of the Fourier coefficients, a_0, a_m and b_m can respectively be determined as

$$a_0 = \frac{1}{T}\int_0^{t_0+T} f(t)dt, \tag{C.2}$$

$$a_m = \frac{2}{T}\int_0^{t_0+T} f(t)\cos(m\omega_0 t)\,dt, \tag{C.3}$$

$$b_m = \frac{2}{T}\int_0^{t_0+T} f(t)\sin(m\omega_0 t)\,dt, \tag{C.4}$$

where $T = 1/\omega_0$, and k is the kth coefficient in the integer sequence 1, 2, 3... The derivation of these coefficients is the subject of most undergraduate engineering degree programmes (as for instance given in [149]) and is not further discussed here. The coefficient a_0 is the dc component, or average value, of $f(t)$. All of the waveforms discussed in this Appendix have no dc component and it will henceforth be assumed that a_0 is always equal to zero.

The effect of symmetry in $f(t)$ has the effect of further simplifying the calculation of the remaining two coefficients in (C.3) – (C.4). For even function symmetry, where $f(t) = f(-t)$,

$$a_m = \frac{4}{T}\int_0^{T/2} f(t)\cos(m\omega_0 t)\,dt \text{ and} \tag{C.5}$$

$$b_m = 0, \text{ for all } m. \tag{C.6}$$

Likewise, for odd function symmetry, where $-f(t) = f(-t)$,

$$a_m = 0, \text{ for all } m \text{ and} \tag{C.7}$$

$$b_m = \frac{4}{T}\int_0^{T/2} f(t)\sin(m\omega_0 t)\,dt. \tag{C.8}$$

If an even or odd function also has half-wave symmetry, where $f(t) = -f(t - T/2)$, all the even coefficients of either a_m or b_m respectively are also zero. Furthermore, if a half-wave symmetric function is also symmetric about $T/2$ (called quarter-wave symmetry), (C.5) further reduces to

$$a_m = \frac{8}{T}\int_0^{T/4} f(t)\cos(m\omega_0 t)\,dt \tag{C.9}$$

for even functions and (C.8) reduces to

$$b_m = \frac{8}{T}\int_0^{T/4} f(t)\sin(m\omega_0 t)\,dt. \tag{C.10}$$

for odd functions.

C.2 Conductor density distribution

The conductor density is represented graphically as shown in Fig. 3.11 and repeated here in Fig. C.1 for clarity. The "period" of the distribution is the distance between successive coils from the same phase as indicated in Fig. C.1. From Fig. C.1 it is also easy to see that $n(x) = -n(-x)$ and that $n(x)$ is hence an odd function. The distribution does not have half-wave symmetry and hence, by definition also does not have quarter wave symmetry, even though it is symmetric about "$T/2$". From Section C.1 it follows that

$$n(x) = \sum_{m=1}^{\infty} b_m \sin\left(\frac{m\pi x}{w_s}\right), \tag{C.11}$$

with

$$b_m = \frac{2}{w_s}\int_0^{w_s} n(x)\sin\left(\frac{m\pi x}{w_s}\right). \tag{C.12}$$

The magnitude of the conductor density is known from (3.10); this term is removed from (C.12) and then simplified as

$$b_{m_n} = \frac{2}{w_s}\int_{(w_s/3)(1-2\kappa)}^{w_s/3} \sin\left(\frac{m\pi x}{w_s}\right). \tag{C.13}$$

Integrating (C.13) gives

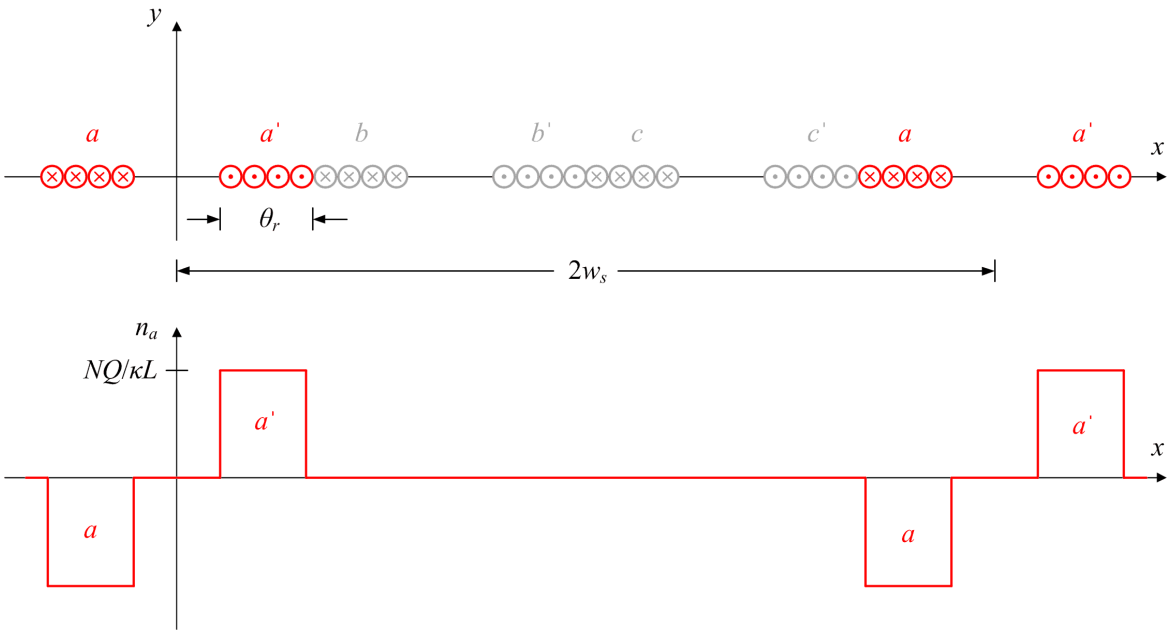

Fig. C.1 Graphical representation of the conductor density distribution.

$$\begin{aligned} b_{m_n} &= \frac{-2}{m\pi}\left[\cos\left(\frac{m\pi}{3}\right)-\cos\left(\frac{m\pi(1-2\kappa)}{3}\right)\right] \\ &= \frac{4}{m\pi}\sin\left(\frac{m\pi\kappa}{3}\right)\sin\left(\frac{m\pi(1-\kappa)}{3}\right). \end{aligned} \tag{C.14}$$

The *a*-phase conductor density is then given as

$$n_a(x) = |n_a|\sum_{m=1}^{\infty} b_{m_n}\sin\left(\frac{m\pi x}{w_s}\right), \tag{C.15}$$

where $|n_a|$ is the magnitude of the conductor density calculated from (3.10).

C.3 Current density distribution

The current density distribution has exactly the same shape as the conductor density and hence the derivation is also the same as for the conductor density. The *a*-phase current density can hence be given as

$$J_a(x) = J_a(t)\sum_{m=1}^{\infty} b_{m_n}\sin\left(\frac{m\pi x}{w_s}\right), \tag{C.16}$$

with b_{mn} the same as in (C.14) and $J_a(t)$ the time-dependent current density magnitude calculated from (3.13).

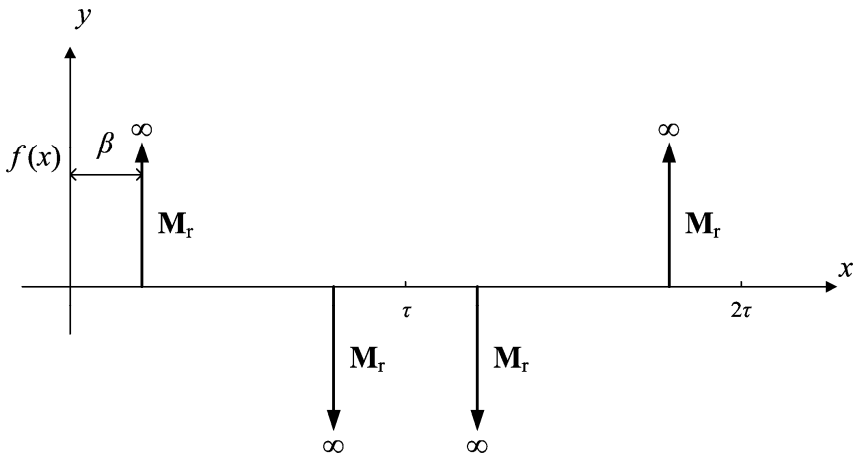

Fig. C.2 Distribution of the derivative of the PM residual magnetisation distribution with respect to *x*.

C.4 Magnetisation

In (3.28) it is necessary to express the derivative of the magnetisation distribution with respect to *x* as a Fourier series expansion in order to find the particular solution for the magnetic vector potential due to the PMs. The distribution of the derivative of the magnetisation is shown in Fig. 3.14(b) and repeated here in Fig. C.1 for clarity. The distribution is basically an even period function with quarter-wave symmetry and consists only of impulses (dirac-delta functions). From Section C.1, the distribution can hence be given as

$$\frac{\partial M_r(x)}{\partial x} = \sum_{m=1,3,5,\ldots}^{\infty} a_m \cos\left(\frac{m\pi x}{\tau}\right), \tag{C.17}$$

with

$$\begin{aligned} a_m &= \frac{4}{\tau}\int_0^{\tau/2} M_r \delta(x-\beta)\cos\left(\frac{m\pi x}{\tau}\right). \\ &= \frac{4M_r}{\tau}\cos\left(\frac{m\pi\beta}{\tau}\right). \end{aligned} \tag{C.18}$$

Appendix D
LG magnetic field solutions

The general theory surrounding subdomain analysis as used for calculating magnetic fields in electrical machines is discussed in Chapter 3, Section 2.1. This method is applied to the novel LG where the resulting equations for the air gap magnetic flux density are given and verified by means of FEA. More detail about the choice of the general and particular solution to the Laplace and Poisson equations and the solution of the constants are given in this Appendix.

D.1 General solution

In order to solve the magnetic vector potential from the Laplace and Poisson equations of (3.18) and (3.19), a general solution for the vector potential with unknown constants must be "guessed". The shape of the magnetic flux density in the air gap is well known from FEA and can also fairly intuitively be derived; a relationship between the magnetic flux density and the vector potential is also defined in equations (B.27) and (B.28). This is therefore used as a starting point in deriving a general solution for A_z.

The magnetic flux density across the air gap, between opposing PM faces, is shown in Fig. D.1. It is clear that the flux density decreases away from the PM face until it reaches a minimum value in the middle of the air gap. Mathematically this shape can be described by the hyperbolic cosine function. It follows that B_y is proportional to cosh such that (from (B.28))

$$B_y = \frac{\partial A_z}{\partial x} \propto \cosh\left(\frac{\pi y}{\tau}\right), \tag{D.1}$$

Furthermore, the PMs are purposefully arranged as they are to establish at least a quasi-sinusoidal air gap flux

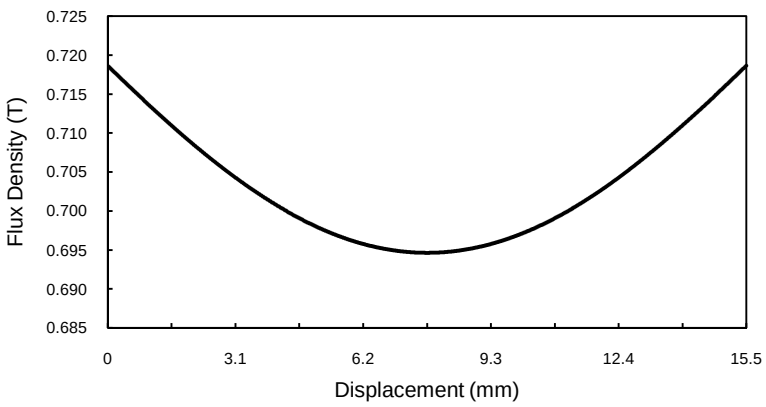

Fig. D.1 The flux density across the air gap, between opposing PM faces (along line b-b in Fig. 3.8(b)).

density in the *x*-direction, and hence (from (B.27))

$$B_x = \frac{\partial A_z}{\partial y} \propto \sin\left(\frac{m\pi x}{\tau}\right), \tag{D.2}$$

From (D.1) and (D.2), and considering all the harmonics, it can therefore be assumed that

$$A_z = \sum_{m=1,2,3}^{\infty}\left[C_{M1}e^{\frac{m\pi y}{\tau}} + C_{M2}e^{\frac{-m\pi y}{\tau}}\right]\sin\left(\frac{m\pi x}{\tau}\right), \tag{D.3}$$

where

$$e^{\frac{m\pi y}{\tau}} + e^{\frac{-m\pi y}{\tau}} = 2\cosh\left(\frac{m\pi y}{\tau}\right) \tag{D.4}$$

and C_{M1} and C_{M2} are unknown constants (the factor 2 in (D.4) is absorbed in the constants C_{M1} and C_{M2} in (D.3)). Equation (D.3) can be substituted back into (D.1) and (D.2) to verify that it is indeed correct. It is preferred to use the form of (D.3) with the exponential functions instead of the hyperbolic cosine function to make later differentiation easier and more readable.

The stator fields of course do not have the exact same form as the PM field, but, since there is also a decay in flux density away from the stator (in the *y*-direction) and a periodic shape along the air gap (in the *x*-direction), the general solution to the stator fields is assumed to be of the same form as the PM field. It is however expected that the harmonic content of the stator field solution will be much higher due to its very non-sinusoidal form.

D.2 Particular solutions

Particular solutions for the magnetic vector potential can be found from the governing Poisson equations in Region I and III for the PM fields (3.28) and in Region II (3.19) for the stator fields. These are easily found by "inspection" and checked by substituting back into the Poisson equation.

D.2.1 PM Field particular solution

Substituting $B_r = \mu_0 M_r$, from (B.20), into (3.28) and expanding the left hand side gives

$$\frac{\partial^2 A_{zI}}{\partial x^2} + \frac{\partial^2 A_{zI}}{\partial y^2} = \left(\frac{4B_r}{\tau}\right)\sum_{m=1,2,3}^{\infty}\cos(m\beta)\cos\left(\frac{m\pi x}{\tau}\right), \tag{D.5}$$

Integrating twice with respect to *x* gives

$$A_{zI} = -\left(\frac{4B_r\tau}{m^2\pi^2}\right)\sum_{m=1,2,3}^{\infty}\cos(m\beta)\cos\left(\frac{m\pi x}{\tau}\right), \tag{D.6}$$

Substituting this back into (D.5) confirms that it is an appropriate particular solution. Combining this with the general solution then gives

$$A_{zI} = \sum_{m=1,2,3}^{\infty}\left[C_{M1}e^{\frac{m\pi y}{\tau}} + C_{M2}e^{\frac{-m\pi y}{\tau}} + \frac{4B_r\tau}{m^2\pi^2}\sin\left(\frac{m\pi\tau_m}{2}\right)\right]\sin\left(\frac{m\pi x}{\tau}\right) \tag{D.7}$$

as given in (3.33).

D.2.2 Stator field particular solution

In region II, substituting (3.12) and (3.14) into (3.19) and expanding the left hand side gives

$$\frac{\partial^2 A_{zII}}{\partial x^2} + \frac{\partial^2 A_{zII}}{\partial y^2} = J_a(t)\sum_{m=1}^{\infty}\left(\frac{4\mu_0}{m\pi}\right)\sin\left(\frac{m\pi\kappa}{3}\right)\sin\left(\frac{m\pi(1-\kappa)}{3}\right)\sin\left(\frac{m\pi x}{\omega_s}\right), \tag{D.8}$$

The particular solution to A_{zII} is again found by twice integrating and finding

$$A_{zII} = -J_a(t)\sum_{m=1,2,3}^{\infty}\left(\frac{4\mu_0\omega_s^{\,2}}{m^3\pi^3}\right)\sin\left(\frac{m\pi\kappa}{3}\right)\sin\left(\frac{m\pi(1-\kappa)}{3}\right), \tag{D.9}$$

Substituting this back into (D.8) confirms that it is an appropriate particular solution. Combining this with the general solution then gives

$$A_{zII} = \sum_{m=1,2,3}^{\infty}\left[C_{S1}e^{\frac{m\pi y}{\omega_s}} + C_{S2}e^{\frac{-m\pi y}{\omega_s}} + \frac{\mu_0\omega_s^{\,2}J_a(t)}{m^2\pi^2}b_{m_n}\right]\sin\left(\frac{m\pi x}{\omega_s}\right), \tag{D.10}$$

with

$$b_{m_n} = \left(\frac{4}{m\pi}\right)\sin\left(\frac{m\pi(1-\kappa)}{3}\right)\sin\left(\frac{m\pi\kappa}{3}\right). \tag{D.11}$$

as also given in (3.12).

D.3 Solutions

Four constants must be solved for each of the two sets of equations in (3.33) and (3.34) and in (3.20) and (3.21) (for the PM and stator fields respectively). Four simultaneous equations are needed to solve four unknowns; these equations are found by relating the two equations for magnetic vector potential by means of the boundary conditions, from Appendix B, Section 2, between the different regions in the subdomain model shown in Fig. 3.5. As explained Chapter 3, Section 2.1, there exists symmetry both about the middle of the PMs (at $y = -h_m/2$) and about the middle of the stator (at $y = \ell_g/2$). At these "symmetry boundaries" (or Neumann boundaries from Appendix B, Section 6.2) it is intuitively known that $H_x = 0$ on either side of the boundary.

D.3.1 PM field solution

In the middle of the stator (at $y = \ell_g/2$), it is known that $H_x = 0$ and hence

$$\begin{aligned} H_x &= \frac{B_x}{\mu_0} = \left(\frac{1}{\mu_0}\right)\frac{\partial A_{zII}}{\partial y}\bigg|_{y=\ell_g/2} \\ &= \sum_{m=1,2,3}^{\infty}\left(\frac{m\pi}{\mu_0\tau}\right)\left(C_{M1}e^{\frac{m\pi\left(\ell_g/2\right)}{\tau}} - C_{M2}e^{\frac{-m\pi\left(\ell_g/2\right)}{\tau}}\right)\sin\left(\frac{m\pi x}{\tau}\right) \\ &= 0 \end{aligned} \tag{D.12}$$

This is then simplified to

$$C_{M1} = C_{M2}e^{\frac{-2m\pi\left(\ell_g/2\right)}{\tau}} \tag{D.13}$$

At the interface between Region I and II, $H_{xI} = H_{xII}$ and $B_{yI} = B_{yII}$. From the former it follows that

$$\begin{aligned} H_{xI} &= \frac{B_{xI}}{\mu_0} = \left(\frac{1}{\mu_0}\right)\frac{\partial A_{zI}}{\partial y}\bigg|_{y=0} \\ &= \sum_{m=1,2,3}^{\infty}\left(\frac{m\pi}{\mu_0\tau}\right)\left(C_{M1} - C_{M2}\right)\sin\left(\frac{m\pi x}{\tau}\right), \end{aligned} \tag{D.14}$$

and

$$\begin{aligned} H_{xII} &= \frac{B_{xII}}{\mu_0} = \left(\frac{1}{\mu_0}\right)\frac{\partial A_{zII}}{\partial y}\bigg|_{y=0} \\ &= \sum_{m=1,2,3}^{\infty}\left(\frac{m\pi}{\mu_0\tau}\right)\left(C_{M3} - C_{M4}\right)\sin\left(\frac{m\pi x}{\tau}\right), \end{aligned} \tag{D.15}$$

Equating (D.14) and (D.15) and simplifying then gives

$$\sum_{m=1,2,3}^{\infty} C_{M1} - C_{M2} = \sum_{m=1,2,3}^{\infty} C_{M3} - C_{M4}. \tag{D.16}$$

From the second condition at the boundary between Regions I and II it follows that

$$\begin{aligned} B_{yI} &= \frac{\partial A_{zI}}{\partial x}\bigg|_{y=0} \\ &= \sum_{m=1,2,3}^{\infty}\left(\frac{m\pi}{\tau}\right)\left[C_{M3} + C_{M4} + \frac{4B_r\tau}{m^2\pi^2}\sin\left(\frac{m\pi\tau_m}{2}\right)\right]\cos\left(\frac{m\pi x}{\tau}\right), \end{aligned} \tag{D.17}$$

and

$$\begin{aligned} B_{yII} &= \left.\frac{\partial A_{zII}}{\partial x}\right|_{y=0} \\ &= \sum_{m=1,2,3}^{\infty}\left(\frac{m\pi}{\tau}\right)\left(C_{M1}+C_{M2}\right)\cos\left(\frac{m\pi x}{\tau}\right), \end{aligned} \tag{D.18}$$

Equating (D.17) and (D.18) and simplifying then gives

$$\sum_{m=1,2,3}^{\infty}\left(C_{M1}+C_{M2}\right)=\sum_{m=1,2,3}^{\infty}\left[C_{M3}+C_{M4}+\frac{4B_r\tau}{m^2\pi^2}\sin\left(\frac{m\pi\tau_m}{2}\right)\right], \tag{D.19}$$

The boundary condition at $y = -h_m/2$ (through the middle of a PMs) again gives $H_{xI} = 0$, as in the middle of the air gap. This results in

$$\begin{aligned} H_{xI} &= \frac{B_{xI}}{\mu_0} = \left(\frac{1}{\mu_0}\right)\left.\frac{\partial A_{zI}}{\partial y}\right|_{y=-h_m/2} \\ &= \sum_{m=1,2,3}^{\infty}\left(\frac{m\pi}{\mu_0\tau}\right)\left(C_{M3}e^{\frac{-m\pi\left(h_m/2\right)}{\tau}}-C_{M4}e^{\frac{m\pi\left(h_m/2\right)}{\tau}}\right)\sin\left(\frac{m\pi x}{\tau}\right) \\ &= 0 \end{aligned} \tag{D.20}$$

and further simplifying gives

$$C_{M3}=C_{M4}e^{\frac{2m\pi\left(h_m/2\right)}{\tau}}. \tag{D.21}$$

By substituting (D.13) and (D.21) into (D.16) and rearranging, C_{M4} can be expressed in terms of C_{M2} as

$$C_{M4}=\frac{\left(e^{\frac{-2m\pi\left(\ell_g/2\right)}{\tau}}-1\right)}{\left(e^{\frac{2m\pi\left(h_m/2\right)}{\tau}}-1\right)}C_{M2}. \tag{D.22}$$

Substituting (D13), (D.21) and (D.22) into (D.19) and rearranging then gives a value for C_{M2} of

$$C_{M2}=\frac{\frac{4B_r\tau}{m^2\pi^2}\sin\left(\frac{m\pi\tau_m}{2}\right)}{\left(e^{\frac{-2m\pi\left(\ell_g/2\right)}{\tau}}+1\right)+\left[\frac{\left(-e^{\frac{-2m\pi\left(\ell_g/2\right)}{\tau}}+1\right)\left(e^{\frac{2m\pi\left(h_m/2\right)}{\tau}}+1\right)}{\left(e^{\frac{2m\pi\left(h_m/2\right)}{\tau}}-1\right)}\right]}. \tag{D.23}$$

D.3.2 Stator field solution

The exact same process is here followed for the stator fields. The boundary conditions are of course the same and only the governing equations in the different regions changes. For completeness each step is again shown here.

In the middle of the stator (at $y = \ell_g/2$), it is known that $H_{xII} = 0$ and hence

$$\begin{aligned} H_{xII} &= \frac{B_{xII}}{\mu_0} = \left(\frac{1}{\mu_0}\right)\left.\frac{\partial A_{zII}}{\partial y}\right|_{y=\ell_g/2} \\ &= \sum_{m=1,2,3}^{\infty}\left(\frac{m\pi}{\omega_s}\right)\left(C_{S1}e^{\frac{m\pi\left(\ell_g/2\right)}{\omega_s}} - C_{S2}e^{\frac{-m\pi\left(\ell_g/2\right)}{\omega_s}}\right)\sin\left(\frac{m\pi x}{\omega_s}\right) \\ &= 0. \end{aligned} \tag{D.24}$$

This is then simplified to

$$C_{S1} = C_{S2}e^{\frac{-2m\pi\left(\ell_g/2\right)}{\omega_s}}. \tag{D.25}$$

At the interface between region I and II, $H_{xI} = H_{xII}$ and $B_{yI} = B_{yII}$. From the former it follows that

$$\begin{aligned} H_{xI} &= \frac{B_{xI}}{\mu_0} = \left(\frac{1}{\mu_0}\right)\left.\frac{\partial A_{zI}}{\partial y}\right|_{y=0} \\ &= \sum_{m=1,2,3}^{\infty}\left(\frac{m\pi}{\mu_0\omega_s}\right)\left(C_{S1} - C_{S2}\right)\sin\left(\frac{m\pi x}{\omega_s}\right), \end{aligned} \tag{D.26}$$

and

$$\begin{aligned} H_{xII} &= \frac{B_{xII}}{\mu_0} = \left(\frac{1}{\mu_0}\right)\left.\frac{\partial A_{zII}}{\partial y}\right|_{y=0} \\ &= \sum_{m=1,2,3}^{\infty}\left(\frac{m\pi}{\mu_0\omega_s}\right)\left(C_{S3} - C_{S4}\right)\sin\left(\frac{m\pi x}{\omega_s}\right). \end{aligned} \tag{D.27}$$

Equating (D.26) and (D.27) and simplifying then gives

$$\sum_{m=1,2,3}^{\infty} C_{S1} - C_{S2} = \sum_{m=1,2,3}^{\infty} C_{S3} - C_{S4}. \tag{D.28}$$

From the second condition at the boundary between Regions I and II it follows that

$$\begin{aligned} B_{yI} &= \left.\frac{\partial A_{zI}}{\partial x}\right|_{y=0} \\ &= \sum_{m=1,2,3}^{\infty}\left(\frac{m\pi}{\omega_s}\right)\left(C_{S3} + C_{S4}\right)\cos\left(\frac{m\pi x}{\omega_s}\right), \end{aligned} \tag{D.29}$$

and

$$\begin{aligned} B_{yII} &= \left.\frac{\partial A_{zII}}{\partial x}\right|_{y=0} \\ &= \sum_{m=1,2,3}^{\infty}\left(\frac{m\pi}{\omega_s}\right)\left(C_{S1}+C_{S2}+\frac{\mu_0\omega_s{}^2 J_a(t)}{m^2\pi^2}b_{m_n}\right)\cos\left(\frac{m\pi x}{\omega_s}\right). \end{aligned} \tag{D.30}$$

Equating (D.29) and (D.30) and simplifying then gives

$$\sum_{m=1,2,3}^{\infty}\left(C_{S1}+C_{S2}+\frac{\mu_0\omega_s{}^2 J_a(t)}{m^2\pi^2}b_{m_n}\right)=\sum_{m=1,2,3}^{\infty}\left(C_{S3}+C_{S4}\right). \tag{D.31}$$

The boundary condition at $y = -h_m/2$ (through the middle of a PMs) again gives $H_{xI} = 0$, as in the middle of the air gap. This results in

$$\begin{aligned} H_{xI} &= \frac{B_{xI}}{\mu_0} = \left(\frac{1}{\mu_0}\right)\left.\frac{\partial A_{zI}}{\partial y}\right|_{y=-h_m/2} \\ &= \sum_{m=1,2,3}^{\infty}\left(\frac{m\pi}{\mu_0\omega_s}\right)\left(C_{S3}e^{\frac{-m\pi\left(h_m/2\right)}{\omega_s}}-C_{S4}e^{\frac{m\pi\left(h_m/2\right)}{\omega_s}}\right)\sin\left(\frac{m\pi x}{\omega_s}\right) \\ &= 0. \end{aligned} \tag{D.32}$$

and further simplifying gives

$$C_{S3}=C_{S4}e^{\frac{2m\pi\left(h_m/2\right)}{\omega_s}}. \tag{D.33}$$

By substituting (D.25) and (D.33) into (D.28), C_{S4} can be expressed in terms of C_{S2} as

$$C_{S4}=\frac{\left(e^{\frac{-2m\pi\left(\ell_g/2\right)}{\omega_s}}-1\right)}{\left(e^{\frac{2m\pi\left(h_m/2\right)}{\omega_s}}-1\right)}C_{S2}. \tag{D.34}$$

Substituting (D.25), (D.33) and (D.34) into (D.31) then gives a value for C_{S2} of

$$C_{S2}=\frac{\frac{\mu_0\omega_s{}^2 J_a(t)}{m^2\pi^2}b_{m_n}}{\left[\frac{\left(e^{\frac{-2m\pi\left(\ell_g/2\right)}{\omega_s}}-1\right)\left(e^{\frac{2m\pi\left(h_m/2\right)}{\omega_s}}+1\right)}{\left(e^{\frac{2m\pi\left(h_m/2\right)}{\omega_s}}-1\right)}\right]-\left(e^{\frac{-2m\pi\left(\ell_g/2\right)}{\omega_s}}+1\right)}. \tag{D.35}$$

Appendix E

Inductance calculation

The derivation for the stator winding inductance is given in this appendix. This derivation is based on a similar derivation of the stator winding inductance for a radial flux air cored PM machine done by Randewijk [104]. It entails deriving an equation for the flux linkage directly from the magnetic vector potential and conductor density as calculated in Chapter 3 (with details in Appendix B and C).

E.1 Flux linkage derivation

Consider a single coil in a magnetic field (i.e. the air gap of the novel LG) as shown in Fig. E.1(a). For simplicity it is assumed the coil is rectangular. From (B.6) and (B.21) we can express the flux linkage of the coil as

$$\begin{aligned}\lambda_t &= \int_S \mathbf{B}d\mathbf{a} \\ &= \int_S (\nabla \times \mathbf{A})\, d\mathbf{a}\end{aligned} \tag{E.1}$$

Using Stoke's Theorem [144], the surface integral in (E.1) can be change to a line integral such that

$$\begin{aligned}\lambda_t &= \int_C \mathbf{A}d\mathbf{l} \\ &= \int_{C_{12}} \mathbf{A}d\mathbf{l} + \int_{C_{23}} \mathbf{A}d\mathbf{l} + \int_{C_{34}} \mathbf{A}d\mathbf{l} + \int_{C_{41}} \mathbf{A}d\mathbf{l},\end{aligned} \tag{E.2}$$

where C_{12}, C_{23}, C_{34}, and C_{41}, denotes the four sides of the turn as shown in Fig. E.1(a). From (B.26) - (B.29), $\mathbf{A} = A_z\mathbf{i_z}$, and hence (E.2) can be reduced to

$$\lambda_t = \int_{C_{12}} \mathbf{A}d\mathbf{l} + \int_{C_{34}} \mathbf{A}d\mathbf{l}. \tag{E.3}$$

Furthermore, assuming that A_z is uniform in the z-direction, (E.3) can be reduced to

$$\lambda_t = A_z(x_1, y_1)l - A_z(x_2, y_2)l, \tag{E.4}$$

where (x_1, y_1) and (x_2, y_2) are the positions of the respective turn sides C_{12} and C_{34}. Since the magnetic field is produced by the current in the turn itself, the magnetic vector potential is symmetrical about the coil axis. In Fig. E.1(b) a finite element solution of A_z is shown. It is clear that there exists odd symmetry about the coil axis, and hence (E.4) can be written as

$$\begin{aligned}\lambda_t &= 2A_z(x_1, y_1)l \\ &= -2A_z(x_2, y_2)l.\end{aligned} \tag{E.5}$$

The flux linkages for all the turns in a coil must be added to get the total flux linkage for the coil. In order to do this, the number of turns and their respective positions are required to calculate A_z. This is where the conductor

density as calculated in Chapter 3 (and Appendix C) is used directly. By multiplying (E.5) with the conductor density (3.11) and integrating over one coil side (remember, as derived above, A_z of only one side of each turn is required), the total flux linkage of a coil can be calculated. This flux linkage is then given as

$$\lambda_{ta} = 2l\int n_a(x)A_{za}(x)dx \tag{E.6}$$

It is here assumed that all the conductors in the coil are concentrated at $y = 0.5\ell_g$, which is in the middle of the air gap. This assumption implies that A_z does not vary significantly over the height of the coil. In reality this is not true; in Chapter 3 the solution is checked against an FEA solution to determine the validity of this simplification.

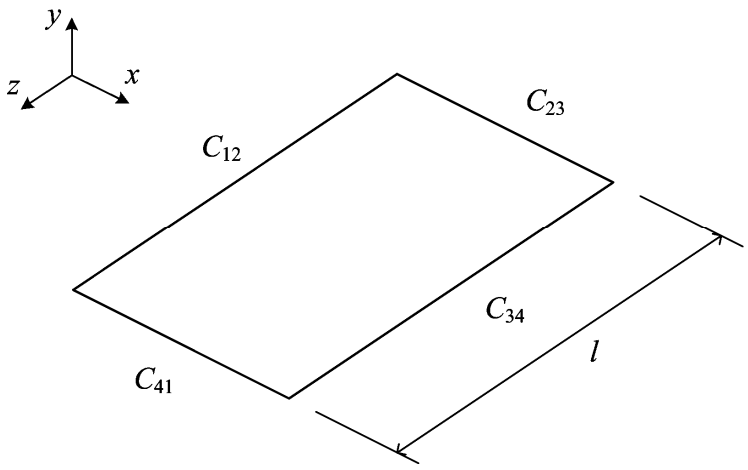

(a)

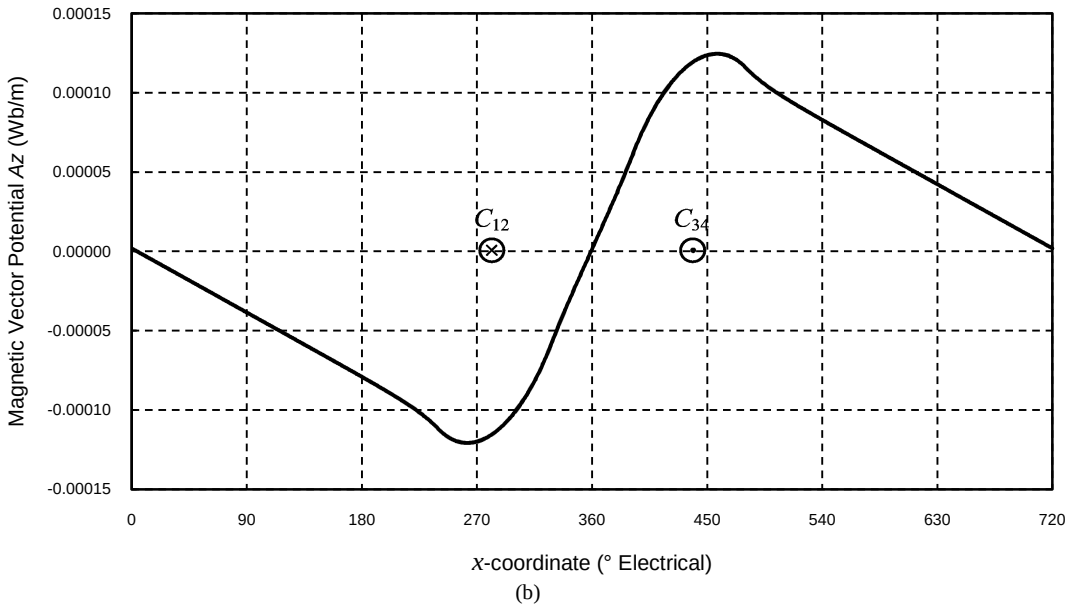

(b)

Fig. E.1 (a) A single turn of a coil with its different sides labelled. (b) The magnetic vector potential (as calculated with FEA) due to the current in the turn has odd symmetry about the midpoint of the coil.

Substituting (3.11) and (3.21) into (E.6) gives

$$\begin{aligned}\lambda_{ta} &= 2l|n_a|\int\left[\sum_{m=1,2,3}^{\infty} b_{m_n}\sin\left(\frac{m\pi x}{\omega_s}\right)\right]\left[\sum_{n=1,2,3}^{\infty} b_{Az}\sin\left(\frac{n\pi x}{\omega_s}\right)\right]dx \\ &= 2l|n_a|\sum_{m=1,2,3}^{\infty}\sum_{n=1,2,3}^{\infty} b_{m_n}b_{Az}\int \sin\left(\frac{m\pi x}{\omega_s}\right)\sin\left(\frac{n\pi x}{\omega_s}\right)dx,\end{aligned} \tag{E.7}$$

where b_{mn} is given in (3.12) and

$$b_{Az} = C_{S1}e^{\frac{n\pi y}{\omega_s}} + C_2 e^{\frac{-n\pi y}{\omega_s}} + \left(\frac{\mu_0\omega_s^2 J_a(t)}{n^2\pi^2}\right)b_{m_n} \tag{E.8}$$

Unless $n = m$, the integral in (E.7) evaluates to zero. In the case that $n = m$, the integral evaluates to $\omega_s/2$ and

$$\lambda_{ta} = l\omega_s|n_a|\sum_{m=1,2,3}^{\infty} b_{m_n}b_{Az}. \tag{E.9}$$

E.2 Self inductance

The self inductance of a coil is simply the flux linked due to the flux induced by the current in that same coil divided by the current as explained in Chapter 3.3.6. The total self inductance due to q coils per phase can therefore very easily be calculated from (E.9) and (3.13) as

$$\begin{aligned}L_{aa}(t) &= \frac{q\lambda_t(t)}{i_a(t)} \\ &= \frac{Qql\omega_s|n_a|}{\kappa g L J_a(t)}\sum_{m=1,2,3}^{\infty} b_{m_n}b_{Az}.\end{aligned} \tag{E.10}$$

It must be noted that inductances in electrical machines are usually position-dependent (and hence time-dependent) as reflected in (E.10). Saturation and varying reluctances due to stator teeth causes the ratio of flux linkage to current to change with position / time. In the novel LG there is no iron in either the stator or the translator, and hence saturation and varying reluctances are not an issue; a very linear relationship hence exist between the flux linkage and current and consequently the inductance is constant at any load.

E.3 Synchronous inductance

In the equivalent circuit diagram of an electrical machine (see Fig. 3.3) it is required to calculate the synchronous inductance. This means that the flux linkage of a winding due to all three phase currents (in a three-phase machine) needs to be considered. In order to calculate this flux linkage, the magnetic vector potential due to all three phases must be considered in (E.6), such that

$$\lambda_{ta} = 2l\int n_a(x)\left[A_{za}(x) + A_{zb}(x) + A_{zc}(x)\right]dx \tag{E.11}$$

In order to simplify the calculation in (E.11), the specific operating point where i_a is at its peak and $i_b(t) = i_c(t) = -0.5i_a(t)$ is chosen; the assumption is of course made that the currents are balanced. In this case the calculated flux linkage will be the peak flux linkage. As mentioned before, any operating point can be chosen for calculating the inductance due to the linear behaviour of the air-cored machine. The peak flux linkage is hence given as

$$\begin{aligned}\Lambda_{ta} = 2l|n_a|\int &\left[\sum_{m=1,2,3}^{\infty} b_{m_n}\sin\left(\frac{m\pi x}{\omega_s}\right)\right] \\ \times &\left[\sum_{n=1,2,3}^{\infty} b_{Aza}\sin\left(\frac{n\pi x}{\omega_s}\right) - \frac{1}{2}b_{Aza}\sin\left(\frac{n\pi\left(x-{}^{L}\!/_{Q}\right)}{\omega_s}\right) - \frac{1}{2}b_{Aza}\sin\left(\frac{n\pi\left(x+{}^{L}\!/_{Q}\right)}{\omega_s}\right)\right]dx\end{aligned} \tag{E.12}$$

By using known trigonometric identities, (E.12) can be reduced to

$$\Lambda_{ta} = 2l|n_a|\int \left[\sum_{m=1,2,3}^{\infty} b_{m_n}\sin\left(\frac{m\pi x}{w_s}\right)\right]\left[\sum_{n=1,2,3}^{\infty} b_{Aza}K_\lambda\sin\left(\frac{n\pi x}{w_s}\right)\right]dx \tag{E.13}$$

where K_λ is given by

$$K_\lambda = 1-\cos\left(\frac{2m\pi}{3}\right) \tag{E.14}$$

Equation (E.13) is of the same form as (E.7) and can hence similarly be reduced to

$$\Lambda_{ta} = l\omega_s|n_a|\sum_{m=1,2,3}^{\infty} b_{m_n}b_{Az}K_\lambda. \tag{E.15}$$

It can be noted that (E.15) is the same as (E.9), but with the additional factor K_λ.

The total synchronous inductance due to q coils per phase is now simply calculated as

$$L_{as} = \frac{q\Lambda_{ta}}{|i_a(t)|} \tag{E.16}$$

E.4 Mutual inductance

It is possible to calculate the mutual inductances of each phase from first principles as done for the self and synchronous inductances in the previous two sections. However, assuming, due to symmetry, that the mutual inductances in (3.18) are equal and given by L_m, the synchronous inductance can be expressed as

$$\begin{aligned}L_{as} &= \frac{\lambda_{ta}}{I_a} \\ &= \frac{L_{aa}I_a + L_mI_b + L_mI_c}{I_a}\end{aligned} \tag{E.17}$$

Assuming further that the currents are balanced such that $I_a = I_b = I_c = 0$, (E.17) is reduced to

$$L_{as} = \frac{L_{aa} I_a - L_m I_a}{I_a} \tag{E.18}$$

Simplifying and rearranging (E.18) then gives the mutual inductance in terms of the synchronous and self inductances as

$$L_m = L_{aa} - L_{as}. \tag{E.19}$$

It is hence not necessary to derive a separate formula for the mutual inductance once the self and synchronous inductances have been calculated.

Appendix F

Average power derivation

The average power for a reciprocating LG, as given in (2.5), is derived in this Appendix. In this derivation it is assumed that the whole stator winding is active during the entire stroke.

The instantaneous LG EMF and current for phase *a* are assumed to be in phase and respectively given as

$$e_{ga}(t) = E_p \cos(\omega t)\cos(\omega_w t) \tag{F.1}$$

and

$$i_a(t) = I_p \cos(\omega t)\cos(\omega_w t), \tag{F.2}$$

where ω is the electrical frequency of the LG, which varies with the translator velocity, and ω_w is the constant wave frequency. The instantaneous generated power for phase *a* is then given as

$$\begin{aligned} p_{ga}(t) &= e_{ga}(t) i_a(t) \\ &= E_p I_p \cos^2(\omega t)\cos^2(\omega_w t). \end{aligned} \tag{F.3}$$

The system is balanced and hence the power for phase *b* and phase *c* can similarly be expressed as

$$p_{gb}(t) = E_p I_p \cos^2(\omega t - 120°)\cos^2(\omega_w t). \tag{F.4}$$

and

$$p_{gc}(t) = E_p I_p \cos^2(\omega t + 120°)\cos^2(\omega_w t). \tag{F.5}$$

The total instantaneous generated power is the sum of the instantaneous power from each phase as

$$p_g(t) = p_{ga}(t) + p_{gb}(t) + p_{gc}(t). \tag{F.6}$$

Substituting (F.3) – (F.5) into (F.6) gives[1]

[1] Using the trigonometric identity $\cos^2(\theta) = \frac{1}{2}\left[1 + \cos(2\theta)\right]$.

$$\begin{aligned} p_g(t) &= \frac{E_p I_p}{2}\cos^2(\omega_w t)\left[1+\cos(2\omega t)\right] \\ &+ \frac{E_p I_p}{2}\cos^2(\omega_w t)\left[1+\cos(2\omega t-240°)\right] \\ &+ \frac{E_p I_p}{2}\cos^2(\omega_w t)\left[1+\cos(2\omega t+240°)\right]. \end{aligned} \tag{F.7}$$

Simplifying and rearranging (F.7) gives

$$\begin{aligned} p_g(t) &= \frac{3E_p I_p}{2}\cos^2(\omega_w t) \\ &+ \frac{E_p I_p}{2}\left[\cos(2\omega t)+\cos(2\omega t-240°)+\cos(2\omega t+240°)\right]. \end{aligned} \tag{F.8}$$

The second term in (F.8) contains three balanced phasors which has a sum of 0; hence

$$\begin{aligned} p_g(t) &= \frac{3E_p I_p}{2}\cos^2(\omega_w t) \\ &= \frac{3E_p I_p}{4}\left[1+\cos(2\omega_w t)\right]. \end{aligned} \tag{F.9}$$

From (F.9) it is now clear that the instantaneous LG generated power oscillates about an average value of

$$P_g = \frac{3E_p I_p}{4} \tag{F.10}$$

at double the wave frequency.

Appendix G

Comparative study calculations

The parameters used for comparing the LGs are already given in Table 3.2 and is repeated here for clarity in Table G.1. The parameters are not all directly available from literature for the LGs from CPT and Seabased. Enough detail is however given to the extent where those parameters not available from literature can be calculated fairly accurately. It must be mentioned that a good *estimation* of these parameters would be sufficient for this exercise as the aim is only to obtain a rough indication of the performance of the novel topology compared to existing iron-cored topologies.

G.1 Columbia Power Technologies

The parameters used for this LG is given in Table G.2 and is taken from [85] and [43]. The rating of this LG is given as 1 kW, which can be calculated from the given velocity and shear force according to (2.7), i.e. 0.76 m/s × 1316 N = 1 kW. The given rated current and voltage of this LG does however not give the rated power according to (2.7), i.e. 3 × 245 V × 2.95 A = 2.2 kW ≠ 1 kW; this probably means that the rated values are rated maxima. This could therefore not be used in the calculations of average electrical loading. The given current density of 2.25 A/mm^2 also does not correspond with the rated current of 2.95 A and the copper wire cross sec-

TABLE G.1 Comparison of the novel LG topology with existing iron-cored machines.

Parameter	CPT	N1	Seabased	N2
Stator core	Iron	Air	Iron	Air
Air gap area A_g (m^2)	0.53*	1.56	2.08	7
Air gap flux density B_g (T)	0.76	0.7/√2	1	0.7/√2
Current density J (A_{rms}/mm^2)	0.45	0.45	1.8	1.8
Electric loading K (kA_{rms}/m)	3.26*	1.36	7.97*	5.5
Shear stress σ_s (kN/m^2)	2.48*	0.68	7.97*	2.7
Shear force f_s (kN)	1.315	1.06	16.57	19.1
Power P (kW)	1	0.81	11.57	13.4
Copper losses P_{cu} (p.u.)	0.040*	0.040	0.09	0.16
Core losses P_c (p.u)	-	0.01	0.05	0.003
Efficiency η (%)	-	95	86	84
Copper mass M_{cu} (kg)	28.55	80	144*	315
Total stator mass M_s (kg)	181.58	106	949*	419
Magnet mass M_m (kg)	222	504	115	754
Total translator mass M_t (kg)	1446	607	547	903

*

tional area of 2.08 mm^2, i.e. 2.95 A / 2.08 mm^2 ≠ 2.25 A/mm^2; and 2.08 mm^2 × 2.25 A/mm^2 = 4.68 A. There is therefore some confusion regarding these rated values.

Since the actual dimensions, including the slot dimensions, of the LG are available, it was decided to calculate the current density corresponding to the rating of 1 kW. The total active air gap area of the LG can be calculated as

$$\begin{aligned} A_g &= \pi d_g L \\ &= \pi(0.6121)(0.274) = 0.53 \text{ m}^2. \end{aligned} \tag{G.1}$$

where d_g is the air gap diameter and L the active length of the LG. L is taken as 12 times the slot pitch plus one tooth width, which is more or less the stator length. The shear stress can then be calculated as $\sigma_s = f_s / A_g$.

The average air gap flux density is given as B_g = 0.76 T. From (2.10) the electrical loading can then be calculated. The slot area is given as 299 mm^2 which equals $w_s \times h$ in (2.12). The total copper area is taken as the given copper wire area times the given number of turns per slot (77). The fill factor is then calculated as

$$k_f = \frac{(2.08)(77)}{299} = 0.54. \tag{G.2}$$

The winding factor, as explained in Chapter 2, Section 4, consists of the distribution and pitch factor. The distribution factor for this LG is unity, as the coil sides are concentrated in only one slot. The coil pitch, however, is equal to 0.917 times the magnet pole pitch, or 0.917π radians. From [72], the pitch factor is therefore given as

$$k_p = \sin\left(\frac{0.917\pi}{2}\right) = 0.99. \tag{G.3}$$

This means the overall windings factor is also k_w = 0.99. With the given slot pitch of 22 mm and calculated

TABLE G.2: Given parameters for the CPT LG which are used for further parameter calculations.

Rated power (kW)	1	Rated velocity v (m/s)	0.76
Slot area $A_s = w_s \times h.$ (mm^2)	299	Rated force f_s (kN)	1.316
Slot pitch τ_s (mm)	22	Average flux density B_g	0.76
Pole pitch τ_m (mm)	72	Turns per slot N	77
Wire area A_w (mm^2)	2.08	Winding factor k_w	0.99
Air gap diameter d_g (m)	0.6121	Phase resistance R_s (Ω)	4.6

TABLE G.3: Given mass for different parts of the CPT LG.

Copper mass	28.55	Magnet mass	222
Lamination mass	139.40	Lamination mass	1215
Epoxy mass	12.63	Stainless steel mass	2
		Epoxy mass	7
Total stator mass	**180.58**	**Total translator mass**	**1446**

winding factor of 0.99, the current density can then be calculated from (2.12) as J = 0.45 mm^2. This current density is used for N1 in the comparative study. This current density is used to calculate the average current; together with the given phase resistance, the copper losses as given in Table G.1 is then calculated.

The breakdown of stator and translator mass is given in Table G.3. These figures are directly available in the literature.

G.2 Seabased

Details for this LG was obtained from [42] and [70]. The rated voltage and current correspond to the rated power as √3 × 200 V × 28.9 A = 10 kW. The rated current density could therefore be calculated from the rated current and given cross-sectional area of the cable. The shear stress could also be calculated from the given active air gap area. From (2.11) and the given air gap flux density, the electrical loading could be calculated. The copper losses, eddy current losses, hysteresis losses and the efficiency of the generator are also given in the literature. These losses are added to the rated 10 kW to obtain the total generated power of 11.57 kW.

The mass of the stator and translator steel and the PM mass are given in the literature. The copper mass was calculated from the given cable length and the cross sectional area of the cable as

$$\begin{aligned} M_{cu} &= A_w \ell_c \gamma_{cu} \\ &= (16\times10^{-6})(1096)(8230) = 144 \text{ kg}, \end{aligned} \tag{G.4}$$

where γ_{cu} is the density of copper. From a local manufacturer of stranded PVC insulated cables, the specific mass of 16 mm^2 cable is given as 16.7 kg / 100 m. The total mass of this cable, including the PVC insulation, can therefore be estimated as (1096 / 100) × 16.7 = 183 kg. The breakdown of the stator and translator masses is given in Table G.5.

TABLE G.4: Given parameters for the Seabased LG which are used for further parameter calculations.

Rated power (kW)	10	Rated velocity v (m/s)	0.7
Rated voltage (V)	200	Average flux density B_g	1
Rate current (A)	28.9	Cable length ℓ_c (m)	1096
Air gap area d_g (m^2)	2.08	Wire area A_w (mm^2)	16

TABLE G.5: Given mass for different parts of the Seabased LG.

Copper mass	144		Magnet mass	115
PVC mass	39		Steel mass	432
Steel mass	766			
Total stator mass	**949**		**Total translator mass**	**547**

Appendix H

Simplorer simulation model

The Simplorer simulation model used to simulate the predictive control together with a brief description is given in this Appendix.

The Simplorer model can be seen in Fig. H.1. The LG is modelled with ideal voltage sources, resistances and inductances as discussed in Chapter 3 (Fig. 3.3). The FE-obtained waveforms shown in Fig. 4.9 are stored in lookup tables (DATAPAIRS1 – 3 in Fig. H.1) and used as reference for the ideal voltage sources (E1 – E3). By doing this, sinusoidal displacement of the LG translator is assumed; the drive motor control is hence assumed to work correctly and is not part of the simulation.

The active rectifier is modelled with generic diodes (D1 - D6) and ideal switches (S1 – S6) representing the IGBTs. The dc-bus is represented by an ideal dc voltage source (E4). The LC-filter is modelled with ideal inductors, capacitors and resistors to represent the series resistance of the inductors.

Sample-and-hold blocks (SAH1 – 6) are used to simulate the current and voltage measurements as done by the digital signal controller (DSC). The sampled values are inputs to the “Deadbeat” VHDL block, which contains the deadbeat predictive control calculations, which calculates the reference active rectifier voltages. The reference voltages are then passed to the “SVPWM” VHDL block, where the appropriate duty cycles for each of the active rectifier switches are calculated. The duty cycles are passed to the comparators (COMP1 – 3), which compares the duty cycle with a unity amplitude triangular wave generator’s output in order to create the PWM switching signals for the active rectifier switches.

Results from the simulations are shown and discussed in Chapter 5, Section 6.

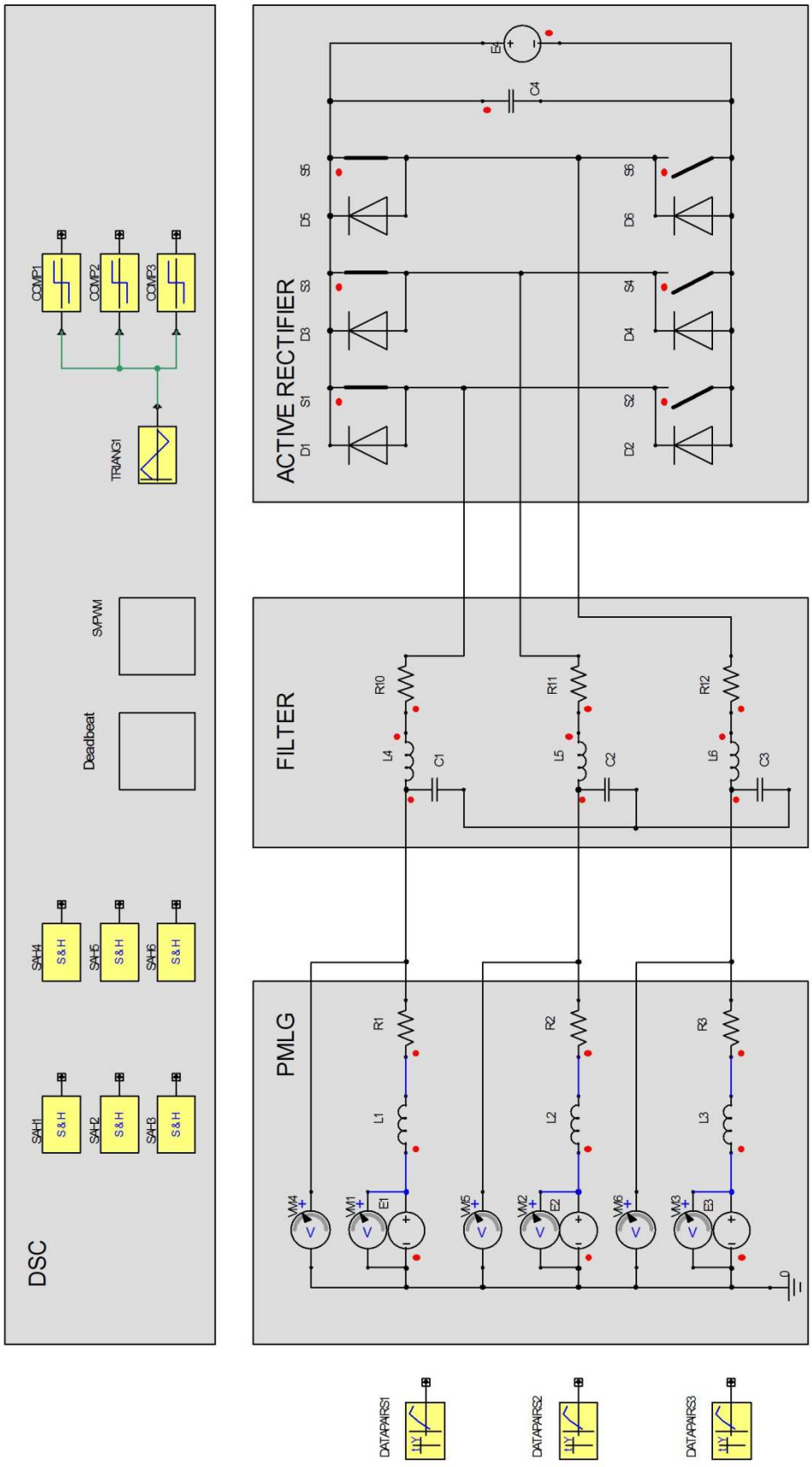

Fig H.1 Simplorer model for simulating the predictive control strategy.

Appendix I

List of patents

A list of international patents with reference to the LGs discussed In Chapter 2, Section 7, is given in Table I.1 below. The full patents are available from the World Intellectual Property Organisation's website [140].

TABLE I.1: List of international patents related to the LGs discussed in Chapter 2, Section 7.

Patent No.	Description	Inventors	Date
Archimedes Wave Swing			
WO9517555	Wave energy transformer	-Fred Ernest Gardner	29/06/1995
WO9911926	Device for energy conversion from wave movement	-Fred Ernest Gardner -Rudolfus Gerardus van Schie	11/03/1999
Uppsala / Seabased			
WO2003058055	Wave-power unit and the use of a wave-power unit for production of electric power, a method of generating electric power and a system of components for manufacturing a linear generator for a wave-power unit.	-Hans Bernhoff -Mats Leijon	17 /07/2003
WO2004085842	Wave power assembly	-Mats Leijon -Hans Bernhoff	07/10/2004
WO2004085843	Wave power assembly	-Mats Leijon -Hans Bernhoff	07/10/2004
WO2004090324	Wave power assembly provided with an electromagnetic damping means.	-Hans Bernhoff -Mats Leijon	21/10/2004
WO2007111546	A system for generating electric energy	-Karin Thorburn -Mats Leijon	04/10/2007
WO2008130295	A wave power unit, a buoy, use of a wave power unit and a method for producing electric energy.	-Mats Leijon -Erland Stromstedt	30/10/2008
WO2010024741	A wave-power unit	-Mats Leijon -Magnus Stålberg -Andrej Savin	04/03/2010
WO2010024745	A wave-power unit, and a use of a such	-Mats Leijon -Stefan Gustafsson	04/03/2010
WO2010085188	A wave power unit	-Mats Leijon -Cecilia Boström -Erik Lejerskog -Magnus Rahm -Olle Svensson	29/07/2010
WO2011149396	A wave power unit with guiding device	-Mats Leijon -Andrej Savin -Robert Leandersson -Rafael Waters -Magnus Rahm	01/12/2011
WO2011149397	A wave power unit, a use of a such and a method of generating electric energy	-Mats Leijon -Kalle Haikonen	01/12/2011
WO2011149398	Stator frame for a submerged linear generator	-Mats Leijon -Erik Doré -Fredrik Axelsson -Rafael Waters	01/12/2011

Patent No.	Description	Inventors	Date
WO2012078084	An electric device and a method for a wave power plant.	-Mats Leijon -Cecilia Boström -Mikael Eriksson	14/06/2012
Oregan State University / Columbia Power Technologies			
WO2006113855	Methods and apparatus for power generation	-Emmanuel Agamloh -Ken Rhinefrank -Alan Wallace -Manfred Dittrich -Annette von Jouanne	26/10/2006
WO2008109062	Methods and apparatus for power generation	-Kenneth Rhinefrank -Annette von Jouanne -Joseph Prudell -Alphonse Schacher -Alexandre F.t. Yokochi -Ted Brekken -David Elwood -Chad Stillenger -Robert K. Paasch	12/09/2008
WO2010096195	Direct drive rotary wave energy conversion	-Kenneth Rhinefrank -Bradford Lamb -Joseph Prudell -Alphonse Schacher	26/08/2010
WO2012106558	Method and system for wave energy conversion	-Kenneth Edward Rhinefrank -Alphonse Schacher -Joseph Horan Prudell -Erik Joel Hammagren	09/08/2012
WO2012138725	A mechanical assembly for maintaining an air gap between a stator and rotor in an electro-mechanical energy converter.	-Kenneth Rhinefrank -Joseph Prudell -Alphonse Schacher -Erik Hammagren	11/10/2012
Trident Energy			
WO0106118	Apparatus for protecting a wave energy converter	-Hugh-Peter Granville Kelly	25/01/2001
WO0106119	Sea wave to electric energy conversion plant	-Hugh-Peter Granville Kelly	25/01/2001
WO200501272	Method of operation for a self-protecting wave energy conversion plant.	-Hugh-Peter Granville Kelly	10/02/2005
WO2006075147	Improvements to tubular electrical generators	-Hugh-Peter Granville Kelly	20/07/2006
WO2007042793	Support structure for sea wave energy farms	-Malcolm van den Bergh -Hugh-Peter Granville Kelly	19/04/2007
WO2007042800	Float for sea wave energy conversion plant	-Hugh-Peter Granville Kelly	19/04/2007
WO2010061199	Low cost linear generator wave energy converters	-Hugh-Peter Granville Kelly	03/06/2010
Edinburgh University / NGenTec			
WO2007104976	Generator and magnetic flux conducting unit	-Markus Mueller -Kenneth Ochije	20/09/2007
WO2009034302	Magnetic flux conducting unit	-Markus Mueller -Alasdair Steward McDonald	19/03/2009
Ocean Power Technologies			
WO2005089281	Circuitry for increasing efficiency of a linear electric generator	-David B. Stewart -Henry I. Schanzer	29/09/2005
WO2005089283	Coil switching circuit for linear electric generator	-David B. Stewart -Paul Smalser -Henry I. Schanzer	29/09/2005
WO2005089284	Wave energy converter (WEC) with magnetic braking	-David B. Stewart -George W. Taylor	29/09/2005
WO2005089295	Wave energy converters (WECs) with velocity multiplication	-Thomas Sabol -David B. Stewart	29/09/2005

WO2005089378	Wave energy converters (WECs) with linear electric generators (LEGs)	-David B. Stewart -George W. Taylor	29/09/2005
WO2005089379	Antirotational structure for wave energy converters	-Thomas Sabol	29/09/2005

References

[1] African Crisis. (2008, Jan.) South Africa orders mines closed: world gold, platinum markets hit all-time high.. [Online]. http://www.africancrisis.co.za/Article.php?ID=21866&

[2] T. Creamer, "$2,7bn smelter becomes power-crunch casualty," *Engineering News, Creamer Media*, vol. Avialable Online [www.engineeringnews.co.za], Oct. 2009.

[3] Energize, EE Publishers. (2010, Mar.) Anglo to enter the power generation industry?. [Online]. http://www.eepublishers.co.za/view.php?sid=20745

[4] "White paper on renewable energy," Department of Minerals and Energy, RSA, 2003.

[5] "South Africa renewable energy feed-in tariff," National Energy Regulator of South Africa (NERSA), 2009.

[6] Department of Energy, "Integrated resource plan for electricity 2010 - 2030," *Government Gazette*, vol. 551, no. 34263, May 2011.

[7] Department of Energy (RSA). (2012, Sep.) Renewable energy independent power producer procurement programme. [Online]. http://www.ipprenewables.co.za

[8] J. R. Joubert and J. L. van Niekerk, "Recent developments in wave energy along the coast of southern Africa," in *European Wave Tidal Energy Conference*, Uppsala, Sweden, 2009, pp. 1096-1100.

[9] "2008 Anual Report: Implementing Agreement of Ocean Energy Systems," International Energy Agency, 2008.

[10] J. Khan, G. S. Bhuyan, and A. Moshref, "Potential opportunities and differences associated with integration of ocean wave and marine current energy plants in comparison with wind energy," Report by Powertech Labs for IEA-OES Annex III T0311, 2009.

[11] A. Clément, et al., "Wave energy in Europe: current status and perspectives," *Renewable and Sustainable Energy Reviews*, vol. 6, pp. 405-431, 2002.

[12] A. F. d. O. Falcão, "Wave energy utilisation: A review of the technologies," *Renewable and Sustainable Energy Reviews*, vol. 14, pp. 899-918, 2010.

[13] J. Falnes, "A review of wave-energy extraction," *Marine Structures*, vol. 20, pp. 185-201, 2007.

[14] Engineering Committee on Oceanic Resources (ECOR), *Wave energy conversion. Elsevier ocean engineering series volume 6*, R. Bhattacharyya and M. E. McCormick, Eds. Oxford, UK: Elsevier, 2003.

[15] J. Cruz, "Introduction," in *Ocean wave energy: Current status and future perspectives*, J. Cruz, Ed. Berlin, Germany: Springer-Verlag, 2008, ch. 1, pp. 1-6.

[16] Centre for Renewable Energy Sources, "Ocean Energy Conversion in Europe: Recent advancements and prospects," European Commission, 2006.

[17] "2011 Anual Report: Implementing Agreement of Ocean Energy Systems," International Energy Agency, 2011.

[18] International Energy Agency. (2012, Sep.) Ocean Energy Systems online library. [Online]. http://www.ocean-energy-systems.org/library/

[19] (2012, Sep.) European marine energy centre. [Online]. http://www.emec.org.uk/about-us/

[20] D. Peacock, "TC144 Marine Energy - wave, tidal and other water current converters," International Electrotechnical Commission Strategic Business Plan SMB/4555/R, 2011.

[21] M. E. McCormick, *Ocean Wave Energy Conversion*. USA: John Wiley & Sons, Inc., 1981.

[22] R. Shaw, *Wave energy: a design challenge*. Chichester: Ellis Horwood, 1982.

[23] D. Ross, *Energy from the waves*, 1st ed. Oxford, UK: Pergamon Press, 1979.

[24] D. Ross, *Power from the waves*, 1st ed. Oxford, UK: Oxford University Press, 1995.

[25] J. Falnes, *Ocean waves and oscillating systems: linear interactions including wave energy extraction*. Cambridge University Press, 2005.

[26] J. Cruz, Ed., *Ocean wave energy: current status and future perspectives*. Berlin, Germany: Springer-Verlag, 2008.

[27] J. Falnes. (2012, Jul.) Books on wave energy. [Online]. http://folk.ntnu.no/falnes/w_e/books_wave_energy.htm

[28] T. W. Thorpe, "Wave Energy: 2007 Survey of energy resources," World Energy Council, Sep. 2007.

[29] T. W. Thorpe, "A brief review of wave energy: A report produced for The UK Department of Trade and Industry.," ETSU-R120, May 1999.

[30] "2007 survey of world energy resources," World Energy Council ISBN: 0 946121 26 5, 2007.

[31] "Oceanlinx Wave Energy Technology," Oceanlinx Available Online [http://www.oceanlinx.com/images/Technology/oceanlinxpresentation.pdf], Accessed 22 Apr 2010.

[32] M. A. Mueller, H. Polinder, and N. Baker, "Current and novel electrical generator technology for wave energy converters," in *Proc. IEEE IEMDC*, vol. 2, Antalya, Turkey, 2007, pp. 1401-1406.

[33] Oceanlinx. (2011, Aug.) [Online]. www.oceanlinx.com

[34] Emerging Energy Research. (2010, Oct.) Global Ocean Energy Markets and Strategies: 2010–2030. [Online]. www.emerging-energy.com

[35] "Pelamis P-750 Wave Energy Converter," Pelamis Wave Power, Available Online [http://www.pelamiswave.com/media/pelamisbrochure.pdf], Accessed 22 April 2010.

[36] K. Rothenhagen, M. Jasinski, and M. P. Kazmierkowski, "Grid connection of multi-megawatt clean wave energy power plant under weak grid conditions," in *EPE Power Electronics and Motion Control Conference*, Poznań, Poland, 2008, pp. 1904-1910.

[37] P. Frigaarda, J. Tedda, J. P. Kofoeda, and E. Friis-Madsenb, "3 years experience with energy production on the Nissum Bredning Wave Dragon prototype," in *Coordinated Action of Ocean Energy (CA-OE) Workshop*, Lisbon, Portugal, 2006, p. 7.

[38] V. L. Neuenschwander, "Wave activated generator," USA Patent US4539485, Sep. 3, 1985.

[39] O. Danielsson, K. Thorburn, and M. Leijon, "Direct drive - linear generators," in *Ocean wave energy - Current status and future perspectives*, J. Cruz, Ed. Berlin, Germany: Springer-Verlag, 2008, ch. 6.2, pp. 220-240.

[40] H. Polinder, M. E. C. Damen, and F. Gardner, "Linear PM generator system for wave energy conversion in the AWS," *IEEE Trans. Ener. Conv.*, vol. 19, no. 3, pp. 583-589, Sep. 2004.

[41] H. Polinder, M. E. C. Damen, and F. Gardner, "Design, modelling and test results of the AWS PM linear generator," *Euro. Trans. Electr. Power*, vol. 15, pp. 245-256, 2005.

[42] O. Danielsson, M. Eriksson, and M. Leijon, "Study of a longitudinal flux permanent magnet linear

generator for wave energy converters," *Int. J. Energy Res.*, vol. 30, pp. 1130-1145, May 2006.

[43] J. Prudell, M. Stoddard, E. Amon, T. K. A. Brekken, and A. von Jouanne, "A permanent-magnet tubular linear generator for ocean wave energy conversion," *IEEE Trans. Industry Applications*, vol. 46, no. 6, pp. 2392-2400, Nov. 2010.

[44] P. C. J. Clifton, R. A. McMahon, and H. P. Kelly, "Design and commissioning of a 30 kW direct drive wave generator," in *Proc. IET 5th Int Conf. Power Electron., Mach. and Drives*, Brighton, UK, 2010, p. 6.

[45] K. Thorburn and M. Leijon, "Farm size comparison with analytical model of linear generator wave energy converters," *Ocean Engineering*, vol. 34, pp. 908-916, 2007.

[46] B. Das and D. C. Pal, "Voltage control performance of AWS connected for grid operation," *IEEE Trans. Energy Convers.*, vol. 21, no. 2, pp. 353-361, Jun. 2006.

[47] D. O'Sullivan and G. Dalton, "Challenges in the grid-connection of wave energy devices," in *European Wave and Tidal Energy Conference.*, Uppsala, Sweden, 2009, pp. 12-20.

[48] N. Hodgins, O. Keysan, A. S. McDonald, and M. A. Mueller, "Design and testing of a linear generator for wave energy applications," *IEEE Trans. Ind. Electron.*, vol. PP, no. 99, 2011.

[49] H. Polinder, B. C. Mecrow, A. G. Jack, P. G. Dickinson, and M. A. Mueller, "Conventional and TFPM Linear Generators for Direct-Drive Wave Energy Conversion," *IEEE Trans. Ener. Conv.*, vol. 20, no. 2, pp. 260-267, Jun. 2005.

[50] K. Nilsson, O. Danielsson, and M. Leijon, "Electromagnetic forces in the air gap of a permanent magnet linear generator at no load," *Journal of Applied Physics*, vol. 99, p. 5, 2006.

[51] O. Danielsson and M. Leijon, "Flux distribution in linear permanent magnet synchronous machines including longitudinal end effects," *IEEE Trans. on Magnetics*, vol. 43, no. 7, pp. 3197-3201, Jul. 2007.

[52] M. A. Mueller and N. J. Baker, "Modelling the performance of a vernier hybrid machine," *IEE Proc. Electr. Power Appl.*, vol. 150, no. 6, pp. 647-654, Nov. 2003.

[53] V. D. Colli, P. Cancelliere, F. Marignetti, and R. Di Stefano, "A tubular-generator drive for wave energy conversion," *IEEE Trans. Industrial Electronics*, vol. 53, no. 4, pp. 1152-1159, Aug. 2006.

[54] D. M. Joseph and W. A. Cronje, "Design and analysis of a double-sided tubular linear synchronous generator with particular application to wave-energy conversion," in *Proc. IEEE PES PowerAfrica*, Johannesburg, South Africa, Jul. 2007, p. 8.

[55] M. A. Mueller, et al., "Experimental tests of an air-cored PM tubular generator for direct drive wave energy converters," in *IET 4th Int. Conf. Power Electronics, Machines and Drives*, York, UK, 2008, pp. 747-751.

[56] L. Ran, et al., "Power conversion and control for a linear direct drive permanent magnet generator for wave energy," *IET Renewable Power Generation*, vol. 5, no. 1, pp. 1-9, 2011.

[57] J. K. H. Shek, D. E. Macpherson, M. A. Mueller, and J. Xiang, "Reaction force control of a linear electrical generator for direct drive wave energy conversion," *IET Renew. Power Gener.*, vol. 1, no. 1, pp. 17-24, 2007.

[58] J. K. H. Shek, D. E. Macpherson, and M. A. Mueller, "Experimental verification of linear generator control for direct drive wave energy conversion," *IET Renewable Power Generation*, vol. 4, no. 5, pp. 395-403, 2010.

[59] F. Wu, X. .-P. Zhang, P. Ju, and M. J. H. Sterling, "Optimal control for AWS-based wave energy conversion system," *IEEE Trans. Power Systems*, vol. 24, no. 4, pp. 1747-1755, Nov. 2009.

[60] P. R. M. Brooking and M. A. Mueller, "Power conditioning of the output from a linear vernier hybrid permanent magnet linear generator for use in direct drive wave energy converters," *IEE Proc.-Gener. Transm. Distrib.*, vol. 152, no. 5, pp. 673-681, Sep. 2005.

[61] H. Polinder, M. A. Mueller, M. Scuotto, and M. Goden de Sousa Prado, "Linear generator systems for wave energy conversion," in *Proc. 7th European Wave and Tidal Energy Conf.*, Porto, Portugal, 2007.

[62] R.-J. Wang and M. J. Kamper, "Calculation of eddy current loss in axial field permanent-magnet machine with coreless stator.," *IEEE Trans. Energy Convers.*, vol. 19, no. 3, pp. 532-538, Sep. 2004.

[63] R.-J. Wang, M. J. Kamper, K. van der Westhuizen, and J. F. Gieras, "Optimal design of coreless stator axial flux permanent-magnet generator," *IEEE Trans. on Magnetics*, vol. 41, no. 1, pp. 55-64, Jan. 2005.

[64] M. J. Kamper, R.-J. Wang, and F. G. Rossouw, "Analysis and performance of axial flux permanent-magnet machine with air-cored nonoverlapping concentrated stator windings," *IEEE Trans. Industry Applications*, vol. 44, no. 5, pp. 1495-1504, Sep. 2008.

[65] M. J. Kamper, "Comparison of linear permanent magnet machine with overlapping and non-overlapping air-cored stator windings," in *Proc. IET 4th Int. Conf. Power Electronics, Machines and Drives*, York, UK, 2008, pp. 767-771.

[66] J. A. Stegmann and M. J. Kamper, "Design aspects of double-sided rotor radial flux air-cored permanent

magnet wind generators," *IEEE Trans. Ind. Appl.*, vol. 47, no. 2, pp. 767-778, Mar. 2011.

[67] J. F. Gieras and Z. J. Piech, *Linear synchronous motors: Transportation and automation systems*. Boca Raton, Florida, USA: CRC Press LLC, 2000.

[68] I. Boldea and S. A. Nasar, *Linear electric actuators and generators*. New York, USA: Cambridge University Press, 1997.

[69] T. J. E. Miller, *Brushless permanent-magnet and reluctance motor drives*. New York, United States: Oxford University Press, 1989.

[70] O. Danielsson, "Linear Synchronous Permanent Magnet Generator," Ph.D. dissertation, Dept. Engineering Sciences, Uppsala University, Sweden, 2006.

[71] T. J. E. Miller and A. Hughes, "Comparative design and performance analysis of air-cored and iron-cored synchronous machines," *Proc. IEE*, vol. 124, no. 2, pp. 127-132, Feb. 1977.

[72] A. E. Fitzgerald, C. Kingsley Jr, and S. D. Umans, *Electric Machinery*, 4th ed. Singapore: McGraw-Hill, 1988.

[73] J. R. Hendershot Jr and T. J. E. Miller, *Design of brushless permanent-magnet motors*. Hillsboro / New York, USA: Magna Physics Publications / Oxford University Press, 1994.

[74] J. Cros and P. Viarouge, "Synthesis of high performance PM motors with concentrated windings," *IEEE Trans. Energy Conversion*, vol. 17, no. 2, pp. 248-253, Jun. 2002.

[75] F. Magnussen and C. Sadarangani, "Winding factors and joule losses of permanent magnet machines with concentrated windings," in *IEEE International Electrical Machines and Drives Conference*, Madison, USA, 2003, pp. 333-339.

[76] M. J. Kamper, A. J. Rix, D. A. Wills, and R.-J. Wang, "Formulation, Finite-Element Modeling and Winding Factors of Non-Overlap Winding Permanent Magnet Machines," in *Proc. 18th Int. Conf. Electrical Machines*, Vilamoura, Portugal, 2008, pp. 1-5.

[77] J. J. Germishuizen and M. J. Kamper, "Classification of symetrical non-overlapping three-phase windings.," in *Int. Conf. Electrical Machines*, Rome, Italy, 2010, p. 6.

[78] J. D. Glover and M. S. Sarma, *Power system analysis and design*, 3rd ed. USA: Brooks/Cole, 2002.

[79] M. A. Mueller, "Electrical generators for direct drive wave energy converters," *IEE Proc. Generation,*

Transmission & Distribution, vol. 149, no. 4, pp. 446-456, Jul. 2002.

[80] A. S. McDonald, M. A. Mueller, and J. G. Jeffrey, "Development of a novel permanent magnet linear generator topology for direct-drive wave energy converters," in *Proc. IET 4th Int. Conf. Power Electronics, Machines and Drives*, York, 2008, pp. 81-85.

[81] M. G. de Sousa Prado, F. Gardener, M. Damen, and H. Polinder, "Modelling and test results of the Archimedes Wave Swing," *Proc. Institution of Mechanical Engineers: Journal of Power and Energy*, vol. 220 Part A, pp. 855-866, Dec. 2006.

[82] J. Sa da Costa, P. Pinto, A. Sarmento, and F. Gardner, "Modeling of an ocean wave power device AWS," in *Proc. IEEE Conf. Control App* , Istanbul, Turkey, 2003, pp. 618-623.

[83] M. Prado and H. Polinder, "Direct drive in wave energy conversion - AWS full scale prototype case study," in *IEEE Power and Energy Society General Meeting*, Detroit, USA, 2011, p. 7.

[84] B. Mols, "Wave power," *Delft Outlook*, no. 1, pp. 12-17, 2005.

[85] AWS Ocean Energy. (2011, Aug.) [Online]. www.awsocean.com

[86] O. Danielsson, M. Leijon, and E. Sjöstedt, "Detailed study of the magnetic circuit in a longitudinal flux permanent-magnet synchronous linear generator," *IEEE Trans. Mag.*, vol. 41, no. 9, pp. 2490-2495, Sep. 2005.

[87] Seabased AB. (2011, Nov.) [Online]. www.seabased.com

[88] J. H. Prudell, "Novel Design and Implementation of a Permanent Magnet Linear Tubular Generator for Ocean Wave Energy Conversion," M.S. Thesis, Oregan State University, Oregan, 2007.

[89] Columbia Power Technologies. (2011, Nov.) [Online]. www.columbiapwr.com

[90] M. A. Mueller and N. J. Baker, "A low speed reciprocating permanent magnet generator for direct drive wave energy converters," in *Proc. IEE Power Electronics, Machines & Drives Conf.*, Bath, UK, 2002, pp. 468-473.

[91] N. J. Baker, M. A. Mueller, and E. Spooner, "Permanent magnet air-cored tubular linear generator for marine energy converters," in *IEE 2de Int. Conf. Power Electronics, Machines and Drives*, Edinburgh, UK, 2004, pp. 862-867.

[92] R. Crozier and M. Mueller, "Modelling and first order optimisation of the air-cored tubular PM machine

using polynomial approximation," in *Proc. Int. Conf. Elec. Mach.*, Vilamoura, Portugal, Sep. 2008, p. 6.

[93] Trident Energy. (2011, Nov.) [Online]. www.tridentenergy.co.uk

[94] J. R. Bumby and R. Martin, "Axial-flux permanent-magnet air-cored generator for small-scale wind turbines," *IEE Proc. Electr. Power Appl.*, vol. 152, no. 5, pp. 1065-1075, Sep. 2005.

[95] J. R. Bumby, N. Stannard, J. Dominy, and N. McLeod, "A permanent magnet generator for small scale wind and water turbines," in *Proc. Int. Conf. Electrical Machines*, Vilamoura, Portugal, 2008, p. 6.

[96] M. A. Mueller and A. S. McDonald, "A lightweight low-speed permanent magnet electrical generator for direct-drive wind turbines," *Wind Energy*, 2009.

[97] Parker Hannifin Corporation. (2010, Oct.) Trilogy linear motor engineering reference guide. [Online]. http://www.parkermotion.com

[98] N. Hodgins, A. McDonald, J. Shek, O. Keysan, and M. Mueller, "Current and Future Developments of the C-GEN Lightweight Direct Drive Generator for Wave & Tidal Energy," in *Proc. 8th European Wave and Tidal Energy Conference*, Uppsala, Sweden, 2009, pp. 352-359.

[99] NGenTec. (2011, Nov.) [Online]. www.ngentec.com

[100] A. S. McDonald, M. A. Mueller, and H. Polinder, "Structural mass in direct drive permanent magnet electrical generators," *IET Renewable Power Generation*, vol. 2, no. 1, pp. 3-15, 2008.

[101] K. Rhinefrank, et al., "Comparison of direct drive power takeoff systems for ocean wave energy applications," *IEEE Journal Oceanic Engineering*, vol. 37, no. 1, pp. 35-44, Jan. 2012.

[102] K. Rhinefrank, J. Prudell, and A. Schacher, "Development and characterization of a novel direct drive rotary wave energy point absorber," in *MTS/IEEE Oceans*, Biloxi, USA, 2009, p. 5.

[103] K. Rhinefrank, et al., "Scaled wave energy device performance evaluation through high resolution wave tank testing," in *IEEE Oceans*, Sydney, Australia, 2010, p. 6.

[104] (2012, Nov.) Ocean Power Technologies. [Online]. http://www.oceanpowertechnologies.com

[105] G.-H. Kang, J.-P. Hong, and G.-T. Kim, "A novel design of an air-core type permanent magnet linear brushless motor by space harmonics field analysis," *IEEE Trans. Magnetics*, vol. 37, no. 5, pp. 3732-3736, Sep. 2001.

[106] S. Vaez-Zadeh and A. H. Isfahani, "Multi-objective design optimisation of air-core linear permanent-magnet linear synchronous motors for improved thrust and low magnet consumption," *IEEE Trans. Magnetics*, vol. 42, no. 3, pp. 446-452, Mar. 2006.

[107] P. J. Randewijk, M. J. Kamper, and R. .-J. Wang, "Analysis and performance evaluation of radial flux air-cored permanent magnet machines with concentrated coils," in *IEEE Int. Conf. Power Elec. Drive Systems*, Bangkok, Thailand, 2007, pp. 189-195.

[108] J. A. Stegmann, "Design and analysis aspects of radial flux air-cored permanent magnet wind generator system for direct battery charging applications," MScEng Thesis, Stellenbosch University, 2010.

[109] N. F. Lombard and M. J. Kamper, "Analysis and performance of an ironless stator axial flux PM machine," *IEEE Trans Ener. Conv.*, vol. 14, no. 4, pp. 1051-1056, Dec. 1999.

[110] F. G. Rossouw, "Analysis and design of axial flux permanent magnet wind generator system for direct battery charging applications," MScEng Thesis, Stellenbosch University, 2008.

[111] Z. Q. Zhu, L. J. Wu, and Z. P. Xia, "An accurate subdomain model for magnetic field computation in slotted surface-mounted permanent-magnet machines," *IEEE Trans. Magn.*, vol. 46, no. 10, pp. 1100-1115, Apr. 2010.

[112] P. J. Randewijk, "Analysis of radial flux air-cored permanent magnet machine with a double-sided rotor and non-overlapping windings," PhD Dissertation, Stellenbosch University, 2012.

[113] R. Vermaak and M. J. Kamper, "Novel Permanent Magnet Linear Generator Topology for Wave Energy Conversion," in *IET Int. Conf. Power Electronics, Machines and Drives*, Brigthon, 2010, p. 6.

[114] M. J. Kamper, J. H. J. Potgieter, J. A. Stegmann, and P. Bouwer, "Comparison of air-cored and iron-cored non-overlap winding radial flux permanent magnet direct drive wind generators," in *IEEE Energy Conversion Congress and Exposition (ECCE)*, Phoenix, Arizona, 2011, pp. 1620-1627.

[115] R. Vermaak and M. J. Kamper, "Design of a novel air-cored permanent magnet linear generator for wave energy conversion," in *Proc. Int. Conf. Electrical Machines*, Rome, Italy, 2010, p. 6.

[116] R. Vermaak and M. J. Kamper, "Design aspects of a novel topology air-cored permanent magnet linear generator for direct drive wave energy converters," *IEEE Trans. Ind. Electron.*, vol. PP, no. 99, p. 12, 2011.

[117] New England Wire Technologies. (2011, Sep.) [Online]. www.newenglandwire.com

[118] R. Vermaak and M. J. Kamper, "Construction and control of an air cored permanent magnet linear generator for direct drive wave energy converters," in *Proc. Int. Electr. Mach. and Drives Conf. (IEMDC)*, Niagara Falls, Canada, 2011, pp. 1076-1081.

[119] R. Vermaak and M. J. Kamper, "Experimental evaluation and predictive control of an air-cored linear generator for direct drive wave energy converters," *IEEE Trans. Ind. Appl.*, vol. 48, no. 6, pp. 1817-1826, Nov. 2012.

[120] A. Ridge, P. Clifton, R. McMahon, and H.-P. Kelly, "Force ripple compensation in a tubular linear generator for marine renewable generation," in *Proc. IEEE Int. Electr. Mach. and Drives Conf. (IEMDC)*, Niagara Falls, Canada, 2011, pp. 490-495.

[121] A. von Jouanne and P. N. Enjeti, "Design considerations for an inverter output filter to mitigate the effects of long motor leads in ASD applications," *IEEE Trans Ind. Appl.*, vol. 33, no. 5, pp. 1138-1145, Sep. 1997.

[122] T. G. Habetler, R. Naik, and T. A. Nondahl, "Design and implementation of an inverter output LC filter used for dv/dt reduction," *IEEE Trans. Power Eletron.*, vol. 17, no. 3, pp. 327-331, May 2002.

[123] H. Akagi and T. Shimizu, "Attenuation of conducted EMI emissions from an inverter-driven motor," *IEEE Trans. Power Electron.*, vol. 23, no. 1, p. 282, Jan. 2008.

[124] J. Falnes. (1997) Principles for capture of energy from ocean waves. Phase control and optimum oscillation.. [Online]. http://folk.ntnu.no/falnes/web_arkiv/InstFysikk/phcontrl.pdf

[125] J. Falnes, "Optimum control of oscillation of wave energy converters," *Wave Energy Converters: Generic Technical Evaluation Study.*, pp. 1-12, Jun. 1993.

[126] J. K. H. Shek, D. E. Macpherson, M. A. Mueller, and J. Xiang, "Reaction force control of a linear electrical generator for direct drive wave energy conversion," *IET Renew. Power Gener.*, vol. 1, no. 1, pp. 17-24, 2007.

[127] L. Malesani, P. Mattavelli, and S. Buso, "Robust dead-beat current control for PWM rectifiers and active filters," *IEEE Trans. Industry Applications*, vol. 35, no. 3, pp. 613-620, May 1999.

[128] G. H. Bode, P. C. Loh, M. J. Newman, and D. G. Holmes, "An improved robust predictive current regulation algorithm," *IEEE Trans Industry Applications*, vol. 41, no. 6, pp. 1720-1733, Nov. 2005.

[129] P. Cortés, M. P. Kazmierkowski, R. M. Kennel, D. E. Quevedo, and J. Rodríguez, "Predictive control in power electronics and drives," *IEEE Trans. Ind. Electron.*, vol. 55, no. 12, pp. 4312-4324, Dec. 2008.

[130] P. P. Acarnley and J. F. Watson, "Review of position-sensorless operation of brushless permanent-magnet machines," *IEEE Trans. Ind. Electron.*, vol. 53, no. 2, pp. 352-362, 2006.

[131] M. Preindl and E. Schaltz, "Sensorless model predictive direct current control using novel second-order PLL observer," *IEEE Trans. Ind. Electron.*, vol. 58, no. 9, pp. 4087-4095, Sep. 2011.

[132] H. W. van der Broeck, H. .-C. Skudelny, and G. V. Stanke, "Analysis and realization of a pulswidth modulator based on voltage space vectors," *IEEE Trans. Industry Applications*, vol. 24, no. 1, pp. 142-150, Jan. 1988.

[133] S. Bolognani, S. Bolognani, L. Peretti, and M. Zigliotto, "Design and implementation of model predictive control for electrical motor drives," *IEEE Trans. Ind. Electron.*, vol. 56, no. 6, pp. 1925-1936, Jun. 2009.

[134] O. Kükrer, "Deadbeat control of a three-phase inverter with an output LC filter," *IEEE Trans. Power Electron.*, vol. 11, no. 1, pp. 16-23, Jan. 1996.

[135] A. Bouafia, J.-P. Gaubert, and F. Krim, "Predictive direct power control of three-phase pulsewidth modulation (PWM) rectifier using space-vector modulation (SVM)," *IEEE Trans. Power Electron.*, vol. 25, no. 1, pp. 228-236, Jan. 2010.

[136] Texas Instruments, "Field oriented control of 3-phase ac motors," Online: www.ti.com BPRA073, 1998.

[137] P. J. Randewijk, "Multi-domain system simulation and rapid prototyping of digital control algorithms using VHDL-AMS," in *Proc. IEEE Int. Conf. Power Electronics and Drive Systems*, Bangkok, Thailand, 2007, p. 8.

[138] R. Crozier, et al., "Hydrodynamic and electromechanical simulation of a WEC with a novel non-linear PTO," in *European Wave and Tidal Energy Conference (EWTEC)*, Southampton, UK, 2011, p. 8.

[139] W. Li, K. T. Chau, and J. Z. Jiang, "Application of linear magnetic gears for pseudo-direct-drive oceanic wave energy harvesting," *IEEE Trans Magnetics*, vol. 47, no. 10, pp. 2624-2627, Oct. 2011.

[140] Y. Du, K. T. Chau, M. Cheng, Y. Wang, and J. Li, "A linear doubly-salient HTS machine for wave energy conversion," *IEEE Trans. Applied Superconductivity*, vol. 21, no. 3, pp. 1109-1113, Jun. 2011.

[141] Y. Du, et al., "A linear stator permanent magnet vernier HTS machine for wave energy conversion," *IEEE Trans. Applied Superconductivity*, vol. 22, no. 3, p. 5, Jun. 2012.

[142] O. Keysan and M. A. Mueller, "A linear superconducting generator for wave energy converters," in *IET Int. Conf. Power Electron. Mach. Drives (PEMD) 2012*, Bristol, UK, 2012, p. 6.

[143] J. L. Meriam and L. G. Kraige, *Engineering Mechanics Volume 2: Dynamics*, 5th ed. USA: John Wiley & Sons, Inc., 2003.

[144] H. A. Haus and J. R. Melcher, *Electromagnetic Fields and Energy*. Englewood Cliffs, NJ, USA: Prentice-Hall, 1989.

[145] S. J. Salon, *Finite element analysis of electrical machines*, 1st ed. Norwell, USA: Kluwer Academic Publishers, 1995.

[146] P. P. Silvester and R. L. Ferrari, *Finite elements for electrical engineers*, 3rd ed. Cambridge, UK: Cambridge University Press, 1996.

[147] A. B. J. Reece and T. W. Preston, *Finite element methods in electrical power engineering*, 1st ed. New York, USA: Oxford University Press, 2000.

[148] S. Gerber, "A finite element based optimisation tool for electrical machines," MScEng Thesis, Stellenbosch University, 2011.

[149] J. W. Nilsson and S. A. Riedel, "Fourier series," in *Electric circuits*. Upper Saddle River, NJ, USA: Pearson Prentice Hall, 2005, ch. 16, pp. 756-803.

[150] World Intellectual Property Organization (WIPO). (2012, Nov.) Patentscope. [Online]. http://patentscope.wipo.int